UNIVERSIDAD DE GRANADA

PROGRAMA DE DOCTORADO EN BIOMEDICINA

Departamento de Química Farmacéutica y Orgánica

Doctoral Thesis

Chem-MDBp: Development of chemistry-based Multiplexing Diagnostic Beadplatforms

PhD Candidate

Antonio Delgado González

Thesis supervisors

Dr.Juan José Díaz Mochón

Dra. Rosario Mª Sánchez Martín

Granada, 13th of September of 2019

GenYo
PFIZER-UNIVERSIDAD DE GRANADA-JUNTA DE ANDALUCÍA
CENTRE FOR GENOMICS AND ONCOLOGICAL RESEARCH

Editor: Universidad de Granada. Tesis Doctorales
Autor: Antonio Delgado González
ISBN: 978-84-1306-311-9
URI: http://hdl.handle.net/10481/57528

A mi madre, a mi padre, a mi hermana, y a Lola,
porque sois el faro que me guía

“To observe without thinking is as dangerous as to think without observing”

Santiago Ramón y Cajal

AGRADECIMIENTOS

Una tesis doctoral es el fruto de muchos años de trabajo, de muchos momentos, tanto buenos como malos, de oportunidades, alegrías y fracasos. Cada momento de ese tiempo viene determinado por las circunstancias y las personas que participan de ella y que, de algún modo, dejan su huella y definen la tesis doctoral y al doctorando.

En primer lugar me gustaría agradecer a Juanjo y Rosario, mis directores de tesis, por permitirme trabajar con ellos durante estos más de cinco años. Porque han sido cinco años maravillosos en los que he crecido, tanto profesional como personalmente, de su mano. Porque llegué con mucha ilusión, pero muy perdido, y acabo con más ilusión todavía y con las cosas más claras. Durante estos años habéis estado ahí, enseñando, apoyando, ayudando, exigiendo, ilusionando… generando siempre nuevos retos. Nunca dais nada por perdido y transmitís pasión, esfuerzo, sacrificio y recompensa. Trabajar con vosotros es entender que todo es posible, y eso no se encuentra muy a menudo. Además, no se trata solo de una relación profesional, sino también personal, por ello solo puedo deciros una cosa, GRACIAS.

A mis compañeros y amigos de NanoChemBio, a los que están y a los que ya se fueron, todos vosotros sois parte de esta tesis doctoral, Angélica, Victoria, Javi, José, Agus, José Espejo, Belén, Patri, Mª Paz, Tere, Rafa, Juandi, Juan Antonio… y muchos más que habéis pasado por aquí. En especial a Angélica, porque eres una persona única y especial, una amiga de verdad, que está ahí en los momentos buenos y malos. Millones de gracias, de corazón. A todos, daros las gracias por ser como sois, por hacerme aprender algo nuevo todos los días, por hacerme sonreír… por hacer que cada uno de los días de la tesis hayan valido la pena. Vosotros habéis hecho que el día a día en el laboratorio sea maravilloso, y así, la verdad, da gusto ir a trabajar. Eso, y el momento en el que alguien dice “¿café?” y se para absolutamente todo lo que se esté haciendo para llenar una mesa entera del comedor y echar unas buenas risas. Se me hace la boca agua solo de pensar en el pedazo de desayuno que montamos de vez en cuando como el que no quiere la cosa: tostadas, yogur, cereales, bizcocho, fruta… todo un festín. Pero no todo es trabajar, también hemos compartido momentos maravillosos fuera de él, tomando unas cervezas o de comida en el “castillo” jajaja Son momentos que no se olvidan jamás.

A mis compañeros de DestiNA Genomica, Antonio Marín, Bárbara, Mavys, Pepo, Salvo, Antonio Fara, Quique, Hugh y Margaret, porque esto tampoco se puede entender sin vosotros. Han sido muchas horas compartidas de trabajo, de reuniones y de discusión para alcanzar los objetivos que con creces sobrepasáis. De vosotros he aprendido muchas

cosas, pero sobre todo que el esfuerzo, la constancia y la perseverancia son la clave del éxito.

A mi socia Lidia, a Tere, a Jose Heavy, a Angélica, a Alejandra, a Álvaro, a Rafa... por todos esos momentos que pasamos en los inicios de la tesis, tanto dentro como fuera de Genyo. Porque esa amistad permitió que fuéramos a visitar a Angélica a Edimburgo en noviembre… ¡con el frío que hacía! Esa misma amistad hizo posible que cuatro personas en cuatro lugares tan lejanos como Palo Alto, Nueva York y Granada, quedáramos en Las Vegas… en Las Vegas… ¡no tenemos remedio!

A mis compañeros y amigos de la sala 1 de predocs Joan, Orlando, Agus, Inma, Carlos, Alba, Silvia, Jose, Javi, Victoria y Diego, ¡porque sois los mejores! Esto sí que es una sala de verdad, ambiente de trabajo, buen humor, cotilleos, confesiones, y sobre todo muchas risas. Y ya desde que pusimos la máquina de café… ¡un gustazo auténtico trabajar ahí con vosotros! Para los Genyos con los que he compartido tantos y tan maravillosos momentos en los pasillos, en las fiestas, en las comidas, en las cervezas de los viernes, en la feria… Baliñas, Alex, Mati, Helena, Clara, Paola, Alba, Pili, Mariadel, Pablo… Y los que ya no están, Patri, Javi, Joel, Julia, Xio, Meri, César, Manu, Marina… ¡Ha sido un auténtico placer conoceros y compartir todos estos años con vosotros! También para el personal de Genyo, Fernando, Miguel Ángel, Jorge, Carmen, Lucía… Genyo es diferente al resto de centros de investigación, y los es por las personas que hacen Genyo. Lo es por vosotros.

A todas las personas de la Facultad de Farmacia que me han ayudado en todo momento. A Ángel Orte y Emilio por permitirme adentrarme en el apasionante mundo de la fluorescencia. A Guille, porque además de compañero de trabajo has sido compañero de aventuras en Edimburgo, pero, por encima de todo, por ser nuestro amigo.

A los doctores Garry P. Nolan y Marc Vendrell, por permitirme trabajar en sus laboratorios durante meses para crecer a nivel científico y personal. A la doctora Wendy J Fantl, al doctor Fabio de Moliner y a Ying, por guiarme y dirigirme durante mis estancias. A mis compañeros de Dynafluors Nicole, Sam, Jamie, Antonio, Fabio y Ramón, y a Belén y a Ana Mª, por hacer que mi estancia en Edimburgo haya sido espectacular, una auténtica pasada. A Pepe, Helen, Coco y su familia, porque desde que llegué me acogieron como uno más de los suyos e hicieron que, a pesar estar a casi 10,000 km de distancia de casa, me sintiera como en ella. A Xavi, María y Belén, por su magnífica acogida en Stanford, en especial a Xavi, que me supo guiar y ayudar en los momentos duros, estando ahí en todo momento.

A mis amigos, porque sois como mis hermanos, Fabio, Adri, Comu, Olmo, Pepe, Fran, Javi, Zori, Archilla, Guada, Gus… nos os puedo poner a todos jajaja Hemos pasado momentos inolvidables juntos, y más que van suceder, ¡cracks!

A mi familia, a mi madre, a mi padre, y a mi hermana. Siempre me habéis apoyado en las decisiones que he tomado. Siempre habéis estado ahí a pesar de la distancia. Me hacéis crecer como persona todos los días. Me queréis con mis virtudes y mis muchos defectos, y eso no tiene precio. Tengo a la mejor madre, al mejor padre y a la mejor hermana que se puede tener. Os quiero. Muchas gracias.

Y a ti, Lola, por todo.

El doctorando / *The doctoral candidate* Antonio Delgado González y los directores de la tesis / *and the thesis supervisors* Dr. Juan José Díaz Mochón y Dra. Rosario Mª Sánchez Martín.

Garantizamos, al firmar esta tesis doctoral, que el trabajo realizado por el doctorando bajo la dirección de los directores de tesis y hasta donde nuestro conocimiento alcanza, en la realización del trabajo, se han respetado los derechos de otros autores a ser citados, cuando se han utilizado resultados o publicaciones.

/

Guarantee, by signing this Doctoral Thesis, that the work has been done by the doctoral candidate under the direction of the thesis supervisors and, as far as our knowledge reaches, in the performance of the work, the rights of other authors to be cited (when their results or publications have been used) have been respected.

Lugar y fecha/ *Place and date*:

Granada, 13th of September of 2019

Directores de la tesis / *Thesis supervisors*		Doctorando / *Doctoral Candidate*
Juan José Díaz Mochón	Rosario Mª Sánchez Martín	Antonio Delgado González
Firmado / *Signed*	Firmado /*Signed*	Firmado / *Signed*

Quality criteria to apply for the degree of "International PhD" by the University of Granada

To apply for the mention of "International Doctorate", this Doctoral Thesis is supported by:

1. Two international internships:

1.1. Internship at the MRC/UoE Centre for Inflammation Research, at the University of Edinburgh (UK), under the supervision of Dr. Marc Vendrell, Senior Lecturer in Biomedical Imaging. This internship was performed from the 3rd of April to the 2nd of July of 2017 and was funded by Ayuda a la Movilidad para Estancias Breves y Traslados Temporales (2016) (Reference EST16/00637). Project: "Nucleic Acid detection by Dynamic Chemistry through real-time fluorescence approach".

1.2. Internship at the Centre for Clinical Science Research, at Stanford University (USA), under the supervision of Professor Garry P Nolan, Rachford and Carlota A. Harris Professor. This internship was performed from the 15th of October of 2018 to the 18th of January of 2019, and was funded by Convocatoria de Movilidad Internacional de estudiantes de programas de doctorado 2018-2019. Project: "Multiplexed determination of poor prognosis in ovarian cancer cells by Mass Cytometry based on levels of expression of specific antigens using a nanoparticle-based single-cell barcoding".

2. Two published scientific articles in relevant journals in the field of the Doctoral Thesis scope. These two published articles include part of the Doctoral Thesis results, and an international patent application.

2.1. **Antonio Delgado-Gonzalez**, Emilio Garcia-Fernandez, Teresa Valero, M. Victoria Cano-Cortes, Maria J. Ruedas-Rama, Asier Unciti-Broceta, Rosario M. Sanchez-Martin, Juan Jose Diaz-Mochon, and Angel Orte. Metallofluorescent nanoparticles for multimodal applications, ACS Omega, volume 3, pages 144 – 153, 2018. Impact factor (JCR 2018): 2.584. Multidisciplinary Chemistry: 76/172 (Q2).

2.2. **Antonio Delgado-Gonzalez**, Agustin Robles-Remacho, Antonio Marin-Romero, Simone Detassis, Barbara Lopez-Longarela, F. Javier Lopez-Delgado, Diego de Miguel-Perez, Juan J. Guardia-Monteagudo, Mario Antonio Fara, Mavys Tabraue-Chavez, Salvatore Pernagallo, Rosario M. Sanchez-Martin, Juan J. Diaz-Mochon. PCR-Free and Chemistry-based Technology for miR-21 rapid detection directly from tumour cells, Talanta, volume

200, pages 51 – 56, 2019. Impact factor (JCR 2018): 4.916. Chemistry, Analytical: 11/84 (Q1).

2.3. **Delgado González Antonio**, Sánchez Martín Rosario María, Díaz Mochón Juan José, Valero Griñán María Teresa, Orte Gutiérrez Ángel, García Fernández Emilio. Dual Probes for Flow Cytometry and Mass Cytometry. WO2018224719 (A1) — 2018-12-13 (Source: European Patent Office (EPO)).

3. According to the University of Granada criteria to obtain an "international doctorate" degree, this Doctoral Thesis has been written and will be later defended in English. Additionally and following the requirement of the University of Granada, some parts of the document (abstract and conclusions) have also been written in Spanish and the conclusions will be defended in Spanish.

Grants and funding

The doctoral candidate Antonio Delgado González is grateful to the funding sources that have been made this Doctoral Thesis possible:

- Ayuda para la Formación de Profesorado Universitario (FPU) 2014. Ministerio de Educación, Cultura y Deporte. Reference FPU14/02181.

- Ayuda a la Movilidad para Estancias Breves y Traslados Temporales (2016). Ministerio de Educación, Cultura y Deporte. Reference EST16/00637.

- Convocatoria de Movilidad Internacional de estudiantes de programas de doctorado 2018-2019. Universidad de Granada.

- This work has been funded by NanoChemBio group projects from Consejería de Economía, Innovación, Ciencia y Empleo of Junta de Andalucía (BIO-1778) and the Ministerio de Economía y Competitividad (BIO2016-80519-R and CTQ2014-56370-R).

- DestiNA Genomica S.L. for providing scientific material, assistance, and collaboration, during this PhD.

- Dynafluors from the University of Edinburgh, and Nolan Lab from Stanford University, for hosting and providing scientific material and assistance to the PhD candidate.

Index

Abstract

Biotechnology and nanotechnology are two fields in their splendour moments with excellent scientific publications, large and unprecedented investments, and technological developments that are constantly revolutionising science and impacting positively to society. The development and utilisation of smart materials and nanomaterials have meant a before and after in different scientific fields. Novel technologies have emerged as a consequence, generating an invaluable impact both in economic terms and knowledge. In this context, this Doctoral Thesis aims to take advantage of smart materials and novel technologies to create bead-based platforms, focusing on the diagnosis field, by enabling both cellular and molecular assays, using chemical-based technologies. These bead-based platforms which allow both type of assays, comprise polystyrene particles, novel nucleic acid and metal chemistries and different analytical platforms.

Regarding the molecular assays, the bead-based platform comprises commercially available polystyrene-based magnetic microparticles and Chem-NAT technology, which is a chemical-based PCR-free technology for nucleic acid detection with single base resolution. Chem-NAT technology employs peptide nucleic acids probes with an abasic position (DGL probes) whose sequences are fully complementary to the target nucleic acids. This is due to the fact that target nucleic acids act as template of a thermodynamically controlled and specific dynamic incorporation of the reactive aldehyde-modified nucleobases (Smart-NB) into the abasic position, through the formation of a reversible covalent bond, an iminium specie, that is thereupon reduced to a stable tertiary amine. Due to the thermodynamic control given by the target nucleic acid this technology is highly selective and specific, avoiding the presence of false positive results.

This Chem-NAT technology was used for both quantitative and qualitative applications:

(i) Quantitative application: The synthesis and optimisation of DGL probes for the direct detection and quantification of miR-21 using fluorescence-based readout platforms is presented through dynamic chemistry labelling (DCL). The DGL probes optimisation steps were performed on flow cytometry, whilst the direct detection and quantification was performed on a fluorescence-based microplate reader. MiR-21 was successfully profiled and quantified from tumour cells and from plasma from patients with non-small cell lung cancer (NSCLC) in advances stages. Moreover, it was assessed the multiplexing capability of the platform by distinguishing miR-21 and miR-122 within the same sample.

(ii) Qualitative approach: The capability of the bead-based platform for testing single nucleotides polymorphisms (SNP) of KRAS is presented. The KRAS WT sequence and the mutated G13C KRAS sequence were successfully identified, within the same sample, by flow cytometry.

On the other hand, the bead-based platforms designed for cellular based assays are presented. Monodispersed cross-linked amino-functionalised polystyrene nanoparticles were functionalised with a fluorophore and a metal, giving rise to metallofluorescent nanoparticles, to achieve multi-modal applications for diagnosis. This dual combination allowed the nanoparticles to be employed for imaging techniques, chemical reactions, and mass-based technologies. They were used as imaging probes for confocal microscopy and/or for flow cytometry. Furthermore, the properties of the fluorophore, like the fluorescence lifetime, allowed their employment as probes in fluorescence life-time imaging. Moreover, the presence of metals, especially palladium, confers additional features without quenching the fluorophore. For instance, palladium nanoparticles can act as catalysts since they are capable of catalysing chemical reactions. Finally, the nanoparticles can be used as mass-tag reagents for mass cytometry along with flow cytometry, what converts them in dual probes.

Through the combination of pure palladium isotopes, the metallofluorescent nanoparticles were employed as mass-tag reagents for mass cytometry barcoding. In the Doctoral Thesis the first proof of concept (PoC) of the mass-based barcoding with two different metallofluorescent nanoparticles, and the first assays for live cell barcoding using three different metallofluorescent nanoparticles were developed. These two assays demonstrate the high capability, the non-toxicity, the specificity, and resistance of the metallofluorescent nanoparticles to be used as live cell barcodes in mass cytometry and flow cytometry.

Resumen

La biotecnología y la nanotecnología se encuentran en su máximo esplendor a tenor de las excelentes publicaciones científicas que atesoran, las importantes inversiones de capital y los desarrollos tecnológicos derivados que están constantemente revolucionando la ciencia y la sociedad. El desarrollo y la utilización de los llamados materiales “smart”, así como los nanomateriales, han supuesto un antes y un después en la ciencia. Las tecnologías novedosas surgidas en consecuencia generan un impacto incalculable tanto a nivel económico como en el conocimiento. En este contexto, esta tesis doctoral tiene como objetivo el utilizar estos materiales “smart” y las tecnologías recientes para crear una plataforma enfocada en el diagnóstico y basada en partículas. Esta plataforma permite realizar tanto ensayos moleculares como ensayos celulares mediante la aplicación de la química. Para ello, se ha desarrollado una plataforma basada en partículas de poliestireno que combina ácidos nucleicos, metales y diferentes plataformas analíticas.

En cuanto a los ensayos moleculares, la plataforma de detección combina partículas magnéticas de poliestireno y la tecnología Chem-NAT, que es una tecnología que no precisa de amplificación por PCR y basada en química para la detección de ácidos nucleicos con resolución de una única base. Para ello se emplean ácidos nucleicos peptídicos con una posición libre de base (DGL) y cuyas secuencias son totalmente complementarias a las secuencias de los ácidos nucleicos de interés. Esto se debe a que los ácidos nucleicos actúan como un molde de una reacción de incorporación dinámica específica, y controlada termodinámicamente, de una nucleobase modificada con un grupo aldehído (Smart-NB) en la posición donde no hay nucleobase. En esta reacción se produce a través de la formación de un enlace covalente reversible, un iminio, que es posteriormente reducido a un enlace covalente irreversible, formando una amina terciaria. Debido al control termodinámico ejercido por el ácido nucleico de interés, esta tecnología es altamente selectiva y específica, evitando la presencia de falsos positivos.

Esta tecnología Chem-NAT ha sido usada tanto para aplicaciones cuantitativas como cualitativas:

(i) Aplicaciones cuantitativas: Se presenta la síntesis y optimización de sondas DGL para la detección directa y cuantificación de miR-21 mediante el uso plataformas basadas en fluorescencia, y a través de conjugación por química dinámica (DCL). La optimización de las sondas DGL se ha llevado a cabo por citometría de flujo, mientras que para la detección directa y cuantificación se ha utilizado un lector de placas basado en fluorescencia. MiR-21 ha sido detectado y cuantificado con éxito a partir de células tumorales y de plasma de

pacientes con cáncer de pulmón (NSCLC) en estadios avanzados. Además, también se ha evaluado la capacidad de la plataforma diagnóstica para realizar ensayos de “multiplexing” mediante la detección específica de miR-21 y miR-122 en la misma muestra.

(ii) Aplicaciones cualitativas: Se presenta la capacidad de la plataforma diagnóstica para detectar mutaciones de una única base en KRAS. La secuencia KRAS silvestre y la secuencia mutada G13C KRAS han sido identificadas con éxito en la misma muestra mediante citometría de flujo.

Por otro lado, la plataforma de diagnóstico basada en partículas para ensayos celulares también ha sido presentada en esta tesis doctoral. Nanopartículas de poliestireno reticuladas y amino-funcionalizadas fueron conjugadas con fluoróforos y metales, dando lugar a nanopartículas metalofluorescentes para aplicaciones multimodales en diagnóstico. La combinación dual de fluoróforo y metal permitió que las nanopartículas se utilizaran como sondas para técnicas de imagen y citometria, para catalizar reacciones químicas y como reactivos para técnicas basadas en masas. Además, las propiedades intrínsecas de los fluoróforos, como el tiempo de vida meda de fluorescencia, permitió su utilización como sondas para microscopía de tiempo de vida media de fluorescencia. Por otro lado, debido a la presencia de metales, especialmente paladio, las nanopartículas metalofluorescentes adquirieron unas interesantes características adicionales sin afectar a la fluorescencia. Por ejemplo, las nanopartículas metalofluorescente con paladio pueden actuar como catalizadores de reacciones químicas. Finalmente, debido a su naturaleza dual, las nanopartículas metalofluorescentes pudieron ser empleadas como reactivos tanto en citometría de masas como en citometría de flujo.

A través de la combinación de isótopos puros de paladio, las nanopartículas metalofluorescentes fueron empleadas como reactivos para codificación celular en citometría de masas. En esta tesis doctoral, por tanto, se presenta la primera prueba de concepto de codificación celular con dos nanopartículas metalofluorescentes, así como el primer ensayo para codificación de células vivas. En esta prueba de concepto se demuestra la alta capacidad, la inocuidad, la especificidad y la resistencia de las nanopartículas metalofluorescentes para su utilización como reactivos de codificación de células vivas para citometría de masas y citometría de flujo.

Abbreviations

2D	2 Dimensional
Ab	Antibody
BG	Background
Chem-NAT	Chemistry based Nucleic Acid Testing
CSM	Cell Staining Media
CTC	Circulating Tumour Cells
CV	Coefficient of Variation
CyTOF	Mass Cytometry by Fluidgm Corporation (US)
DCC	N,N'-Dicyclohexylcarbodiimide
DCL	Dynamic Chemistry Labelling
DCU	N,N'-Dicyclohexylurea
DGL	PNA probe with an abasic position
DIC	N,N'-Diisopropylcarbodiimide
DLS	Dynamic Light Scattering
DVB	Divinylbenzene
EDC	1-ethyl-3-(3′-dimethylamino)carbodiimide
EDX	Energy-Dispersive X-ray
FACS	Fluorescence-Activated Cell Sorter
FDA	Food and Drug Administration
FLIM	Fluorescence Lifetime Imaging
FRET	Förster resonance energy transfer
INDEL	Insertion – Deletion
HRSEM	High Resolution SEM
HRTEM	High Resolution TEM
LoD	Limit of detection
MFI	Mean Fluorescence Intensity
MNF50	Multiplicity of Nanofection 50%
mRNA	Messenger RNA
miRNA	Micro RNA
NA	Nucleic Acid
NPs	Nanoparticles
NSCLC	Non-Small Cell Lung Cancer
PBS	Phosphate Buffered Saline

PBMC	Peripheral Blood Mononuclear Cell
PEG	Polyethylene glycol
PFA	Paraformaldehyde
PNA	Peptide Nucleic Acid
PoC	Proof of Concept
RFU	Relative Fluorescence Units
ROS	Reactive Oxygen Species
RT	Room Temperature
RT-qPCR	Reverse Transcriptase Quantitative PCR
SEM	Scanning Electron Microscopy
SAPE	Streptavidin-R-Phycoerythrin
SbG	Streptavidin-β-Galactosidase
SD	Standard Deviation
siRNA	Silencing RNA
Smart-NB	Aldehyde modified Nucleobases
SNP	Single Nucleotide Polymorphism
SPPS	Solid Phase Peptide Synthesis
ssDNA	Single Stranded DNA
STEM	Scanning Transmission Electron Microscopy
TEM	Transmission Electron Microscopy
VBAH	Vinylbenzylamine hydrochloride
XPS	X-ray photoelectronic spectroscopy

Rationale

A rapid, accurate and easy diagnosis is the key for medicine success. In this sense, lots of diagnostic platforms have been developed over the years to enhance physician's diagnostic, making it easier and more efficient.

The aim of this project was to develop bead-based platforms for multiple applications, such as molecular- and cellular-based assays, with affordable reagents. Regarding the molecular-based assays, the main aim was to develop a bead-based platform for the direct detection and quantification of nucleic acids, without the need of PCR amplification not RNA extraction, by employing a chemistry-based technology, Chem-NAT. This chemical bead-based technology leads to not only the direct detection and quantification of miR-21 from tumour cells and patients plasma, but also to detecting punctual KRAS mutations by dynamic chemistry labelling (DCL). Thus, this bead-based platform enables a qualitative and quantitative approach for nucleic acid testing within the same technological concept.

Regarding the cellular-based assays, developing biocompatible probes is desired for enhancing the existent reagents and expanding current biomedical applications. Therefore, the aim of this part of the project was to develop new multi-modal polystyrene nanoparticles capable of acting as biological probes to be detected with current state-of-the-art technologies. Amongst them, the principal aim was to apply metallofluorescent nanoparticles as mass-tag reagents for live cell barcoding using mass cytometry. This would enable codifying live cells to perform multiplexing experiments such as drug assessment and protein expressions evaluation in a high-throughput way.

OBJECTIVES

Objectives

Objective 1. Development of a bead-based platform for the direct identification and quantification of nucleic acids using dynamic chemistry.

Specific aims of the objective 1:

1.1. Development of a platform comprising magnetic beads and Chem-NAT technology for the identification and quantification of miR-21.

1.1.1. Design and synthesis of a suitable and specific DGL probe complementary to miR-21 target.

1.1.2. DGL probe conjugation to the magnetic beads to afford a DGL-bead-based platform for miR-21 testing.

1.1.3. Evaluation of the DGL-bead-based platform specificity for exclusively targeting miR-21 and the Smart-NB efficient and specific incorporation.

1.1.4. Implementation of a fluorescent method for the direct detection and quantification of miR-21 from tumour cells and selection of the fluorescent detection platform.

1.1.5. Implementation and evaluation of the fluorescent method for the direct detection and quantification of circulating miR-21 in plasma samples from patients with cancer.

1.2. Development of a platform comprising magnetic beads and Chem-NAT technology for KRAS mutation testing.

1.2.1. Design and synthesis of a suitable and specific DGL probe to testing KRAS mutation using the DGL-bead-based platform.

1.2.2. Evaluation of the DGL-bead-based platform for the effective detection of KRAS punctual mutation through dynamic chemistry labelling.

1.2.3. Implementation of the DGL-bead-based platform for KRAS mutation testing in serum samples of patients.

Objective 2. Development of biocompatible polystyrene nanoparticles as multi-modal probes for cell-based assays.

Specific aims of objective 2:

2.1. Development of biocompatible metallofluorescent nanoparticles acting as multi-modal probes

2.1.1. Synthesis of fluorescent and metallofluorescent nanoparticles.

2.1.2. In-depth characterisation of metallofluorescent nanoparticles using suitable techniques.

2.1.3 Evaluation of the multimodal capabilities of the metallofluorescent nanoparticles by fluorescence-based and mass-based techniques.

2.1.4. Evaluation of the biological and chemical implications of the metallofluorescent nanoparticles.

2.2. Assessment of the metallofluorescent nanoparticles application as dual fluorescence and mass cytometry probes

2.2.1. Evaluation of the cellular toxicity and cellular response to metallofluorescent nanoparticles by fluorescence and mass cytometry.

2.2.2. Synthesis and characterisation of palladium-isotope-conjugated nanoparticles by mass cytometry.

2.2.3. Evaluation of the toxicity and the cellular uptake efficiency of the palladium-isotope-conjugated-nanoparticles by mass cytometry.

2.2.4. Evaluation of the application of the palladium-isotope-conjugated-nanoparticles as mass-tag reagents for live cell barcoding in mass cytometry.

CHAPTER I

Chapter 1. Introduction

1.1. Biotechnology

Biotechnology, term introduced in 1919 by the Hungarian agricultural engineer Karl Ereky, is a broad discipline in which biological processes, organisms, cells or cellular components are exploited to develop new technologies. The new tools and products developed under the biotechnology term have been revolutionary in many fields such as research, industry and the clinic. An example of this revolution was the serendipitous biotechnological discovery achieved by the British scientist Sir Alexander Fleming, who accidently discovered the first antibiotic, the Penicillin, in 1928, “When I woke up just after dawn on September 28, 1928, I certainly did not plan to revolutionize all medicine by discovering the world's first antibiotic, or bacteria killer” [1]. In fact, the discovery of Penicillin changed the world vision of how bacterial diseases should be treated; being Sir Alexander Fleming, Ernst Boris Chain and Sir Howard Walter Florey awarded the Nobel Prize in Physiology or Medicine in 1945.

It was not until the 1950’s when it was reported one of the key events in biotechnology, which is considered one of the scientific breakthroughs in history, the discovery of the molecular structure of DNA in 1953 by Francis H. C. Crick and James D. Watson, with the invaluable help of Rosalind Franklin [2]–[5]. For this discovery, Francis Harry Compton Crick, James Dewey Watson, and Maurice Hugh Frederick Wilkins were awarded the Nobel Prize in Physiology or Medicine in 1962. Then, a lot of discoveries took place, highlighting some of the most remarkable, such as the one in 1955, when Dr. Jonas Salk developed the first vaccine for poliomyelitis, receiving the US Congressional Gold Medal in 1975 for his achievements and contributions to the science. Also in 1955, Severo Ochoa and Marianne Grunberg-Manago discovered an enzyme capable of joining nucleotides and, thus, of building RNA and DNA blocks [6]. In 1956 and 1958, Arthur Kronberg identified the enzyme to that Ochoa and Grunberg-Manago referred to as the DNA polymerase, which is capable of synthesise DNA [7],[8]. These two discoveries resulted in Severo Ochoa and Arthur Kornberg being awarded the Nobel Prize in Physiology or Medicine in 1959. Later, in 1960’s, among others, the mRNAs were discovered [9]; the genetic code was cracked by Marshall W. Nirenberg and J. Heinrich Matthaei [10],[11], being Marshall W. Nirenberg, Robert W. Holley, and Har Gobind Khorana the Nobel Prize of Physiology or Medicine in 1968, for “their interpretation of the genetic code and its function in protein synthesis”. Osamu Shimomura discovered the green fluorescent protein (GFP) [12], for what he was awarded the Nobel Prize of Chemistry in 2008, jointly with Martin Chalfie and Roger Y. Tsien. ~~Dr. Samuel Katz~~

and Dr. John F. Enders received the Nobel Prize of Physiology or Medicine in 1954 jointly with Thomas Huckle Weller and Frederick Chapman Robbins for developing the first measles vaccine.

Moving to the 70's, restriction enzymes were discovered by Werner Arber, Daniel Nathans and Hamilton O. Smith who jointly received the Nobel Prize in Physiology or Medicine in 1978. They also discovered the DNA ligase, which enabled another scientific breakthrough by creating the first in vitro synthesis of DNA [13]. Stanley Cohen and Herbert Boyer performed the first DNA recombinant experiment in history [14], settling the basis of the genetic engineering. In this regards, in 1975, Georges J. F. Köhler and César Milstein developed the first monoclonal antibody [15], being awarded the Nobel Prize in Physiology or Medicine in 1984 jointly with Niels K. Jerne for "theories concerning the specificity in development and control of the immune system and the discovery of the principle for production of monoclonal antibodies". Moreover, Herbert Boyer created recombinant human insulin and the first vaccines for meningococcal meningitis and pneumonia were developed. Another major breakthrough occurring in the 1970's was the development of Sanger sequencing method [16], based on the use of dNTPs, ddNTPs, and DNA polymerase, which has been the most widely used DNA sequencing method until the apparition of the next-generation sequencing (NGS) methods. The Sanger sequencing method was developed by the British biochemist Frederick Sanger in 1977, for what he was awarded the Nobel Prize in chemistry in 1980, jointly with Paul Berg and Walter Gilbert. Curiously, Frederick Sanger was also awarded the Nobel Prize in Chemistry in 1958 "for his work in the structure of proteins, especially that of insulin", becoming the only person who has won twice the chemistry prize, and the fourth person awarded the Nobel Prize twice after Marie Sklodowska-Curie (1903, 1911), Linus Pauling (1954, 1962), and John Bardeen (1956, 1972).

From the 1980's until nowadays the scientific discoveries in biotechnology have exponentially increased, ranging from the development of new vaccines, the invention of the polymerase chain reaction (PCR) (Nobel Prize of Chemistry 1993 for Kary B. Mullis and Michael Smith), the FDA approval of recombinant products and treatments, the publication of the sequence of the human genome [17],[18], the creation of a cell with synthetic DNA [19], to the development of the revolutionary and vogue human gene-editing tool, CRISPR [20],[21]. Of especial interest has been the development of NGS platforms at the beginning of the 2000's, which allowed DNA and RNA sequencing in a rapid, accurate, and inexpensive way, revolutionising genomics and molecular biology and leading multiple biotechnological breakthroughs to happen. Besides, the Nobel Prize in Chemistry 2014 was awarded to Eric Betzig, Stefan W. Hell, and William E. Moerner for "the development of super-resolved fluorescence microscopy"; the Nobel Prize in Chemistry 2017 was awarded to Jacques

Dubochet, Joachim Frank and Richard Henderson "for developing cryo-electron microscopy for the high-resolution structure determination of biomolecules in solution"; and the Nobel Prize in Chemistry 2018 was awarded to Frances H. Arnold (half prize) “for the directed evolution of enzymes” and to George P. Smith and Sir Gregory P. Winter (quarter prize each) "for the phage display of peptides and antibodies”.

Regarding the scientific contributions, the actual impact of biotechnology remains clear, but it is also remarkable from an economical point of view, due to the high number of biotechs that are operating. The rise of such number of biotech companies cannot be understood without the investment of large amounts of money coming from venture capital or public market investors. In fact, according to the UK business intelligence firm Infirma the overall equity funding available, in 2018, reached $23–24 billions. This represents approximately 50% more than in 2017. It is noteworthy not only the increase in funding amounts but also in how this investment is performed. It seems that early mega-rounds have been increased, and A rounds have been accompanied with more generous funding. For instance, comparing the funding distribution, in 2010–2012, A rounds investing less than $20 million represented the 55–60% whilst A rounds exceeding $50 million accounted for 5% of them. In 2018, these data have turned around since A rounds investing under $20 million decreased to 20%, whereas A rounds investing more than $50 million actually account for one third of the investments. Remarkably, the amount of funding going to A rounds has nearly quadrupled since 2010 (Figure 1) [22].

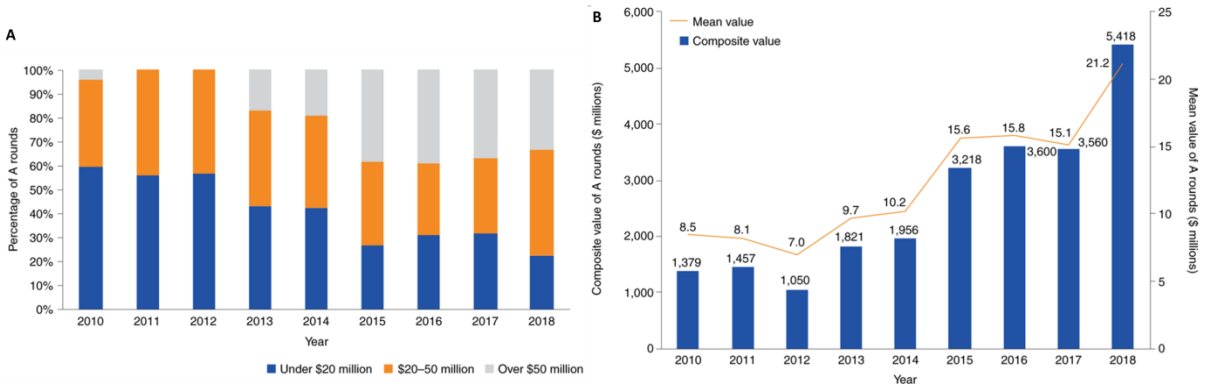

Figure 1. The evolution of A rounds. **A)** Distribution and amount of funding in A rounds; **B)** Total and average value of A rounds investment (Figure reproduced with permission from [22]).

1.2. Nanotechnology

Approximately, at the same time than biotechnology started to grow and to expand, a multidisciplinary technology involving the fields of biology, chemistry, physics and engineering, appeared. This technology, albeit sharing goals and perspectives with biotechnology, was exclusively focused on the small scale, being referred as nanotechnology.

According to the United States National Nanotechnology Initiative (Nano.gov), nanotechnology is science, engineering, and technology conducted at the nanoscale, which is about 1 to 100 nanometres. This institution also considers nanoscience and nanotechnology the study and application of extremely small things, and that they can be used across all the other science fields such as chemistry, biology, physics, material science, and engineering. The Nobel Laureate in Physics (1965), Richard Philips Feynman, brought the first ideas and concepts of nanotechnology to light in 1959. On the 29th of December, at the American Physical Society meeting at the California Institute of Technology (CalTech), Richard Feynman foresaw in his talk "There's plenty room at the bottom" that scientists would be able to control and manipulate at the small scale, even to rearrange atoms at their desire. However, the term "nanotechnology" would not be addressed until 1974, when the Japanese Professor Norio Taniguchi first defined it as: "'Nano-technology' mainly consists of the processing of separation, consolidation, and deformation of materials by one atom or one molecule".

1981 could be considered the key point for nanotechnology, when the Nobel Laureates in Physics (1986) Gerd Binnig and Heinrich Rohrer invented the Scanning Tunneling Microscope (STM), at IBM's Zurich Lab, what allowed to "see" individual atoms for the first time in history [23]. Moreover, in 1981, the American engineer Eric Drexler, often considered "the founding father of the nanotechnology", published his concept of nanotechnology [24], which established fundamental principles of molecular engineering and outlined the possible paths that advanced nanotechnologies could follow. In 1986, Eric Drexler opened the nanotechnology to the non-scientific audience with the publication of his scientific book "Engines of Creation: The Coming Era of Nanotechnology", which was reedited in 2007 to include recent publications. In 1991 he was awarded the first PhD in Molecular Nanotechnology from the Massachusetts Institute of Technology (MIT), publishing in 1992 a more technical book, "Nanosystems: Molecular Machinery, Manufacturing, and Computation", which was based on his PhD dissertation "Molecular machinery and manufacturing with applications to computation" [25].

Therefore, since 1981 there have been an increasing number of scientific discoveries regarding the nanotechnology research, moulding and defining the age of nanotechnology. Among these discoveries it is important to highlight the discovery in 1985 of buckminsterfullerene [26], which leaded to the Nobel Prize of Chemistry in 1996 for Professors Robert F. Curl Jr., Sir Harold W. Kroto, and Richard E Smalley; the discovery, also in 1985, of quantum dots by Professor Louis E. Brus [27], for what he was awarded the Kavli Prize in Nanoscience in 2008. The invention of the Atomic Force Microscope (AFM); the discovery of the Carbon Nanotubes (CNT) in 1991 by Professor Sumio Iijima [28], being awarded (shared) the Kavli Prize in Nanoscience in 2008; and the released of new insights on chemical bonding by Professor Wilson Ho and Hyojune Lee in 1999 [29] supposed a revolution in the 1990's. Lately in the 2000's, the creation of DNA-like robotic nanoscale assembly devices, between 2009 and 2010, by Nadrian Seeman [30]–[32], for what he was awarded (shared) the Kavli Prize in Nanoscience, in 2010; and the design and synthesis of molecular machines, the Nobel Prize in Chemistry in 2016, awarded jointly to the Professors Jean-Pierre Sauvage [33],[34], Sir J. Fraser Stoddart [35], and Bernard L. Feringa [36], represent clear examples of the deep impact of nanotechnology in science.

Regarding the nanotechnology field development, along with the scientific contributions, it was also very important the appearance of the first nanotechnology companies such as Nanophase Technologies in 1989, Helix Energy Solutions Group in 1990, Zyvex in 1997, and Nano-Tex in 1998, amongst others. In fact, the nanotechnology field has outstandingly expanded over the last decades. Nowadays, there are more than 13,000 patents registered in the U.S. Patent Office which include the word "nano" (US patent and trademark office source).

Despite the initial differences in the fields of study between biotechnology and nanotechnology, the evolution of science has made possible to fuse their goals and perspectives regarding biology and chemistry. In fact, it is clearly seen that as biotechnology has evolved, the discoveries and scientific researchers have been driven to the molecular level. Because of this molecular revolution, there have arisen the so-called smart materials, which are materials capable of tackling important biotechnological challenges. Smart materials are dynamic and responsible materials able to change their properties in response to stimuli. These stimuli can be light, pH, temperature, magnetic field or electrical field changes [37]. When the smart materials have a size in the nanometre range they are called smart nanomaterials, which are used as advanced diagnostics tools, imaging agents, and therapeutic modalities.

1.3. Smart nanomaterials

Polymers have gained special interest as smart materials since they can readily modify their properties in response to stimuli. Moreover, many of them are biocompatible, which enables their use in the biomedical field for uncountable applications. For instance, smart materials have been largely applied as diagnostic and therapeutic agents, but now, combining both diagnosis and therapy, smart materials are revolutionasing the theranostic field. In this regard, multimodal particles have reached an outstanding importance on the grounds of the plethora of different applications in which they can be applied. A rational design leads to multimodal particles carrying several biomolecules to expand their application to cutting edge technologies, apart from theranosis, like multimodal imaging [38]. The multimodal application allows combining the pros of the involved techniques and circumventing the cons. Nevertheless, the horizon of these applications is limited by the inner properties of the materials employed.

In this sense, nanomaterials represent a huge advance, especially nanoparticles (NPs). NPs are usually defined as particles of a size ranging from 1 nm to 100 nm regardless the shape: spheres, rods, wires, multipods, stars, etc. Nonetheless, there are also considered as NPs those particles with a size up to 1000 nm. The high surface-to-volume ratio, the high surface energy and their unique mechanical, thermal, magnetic and optical properties, amongst others, derived from their small size, are not found in bulk material particles [39]. These unique properties give rise to novel and highly valuable applications, making NPs suitable for biomedical applications. For instance, because of their small size, NPs can easily carry considerable amounts of cargoes, such as imaging agents or drugs, or even a combination of them as it happens with multifunctionalised NPs [38]. Similarly, controlling not only the size but also the shape and surface properties, NPs can improve their specificity towards certain: organs, tissues, whole cells and subcellular organelles [39]. Besides, an appropriate size and surface functionalisation of the NPs enhance the circulation time in the blood stream while reducing their uptake by the reticuloendothelial system (RES) [38], which is a major advantage in therapy. However, NPs unique features are also associated with certain risks as they can cause important toxicity effects that need to be taken into consideration when using in biomedical applications.

1.3.1.Type of NPs

There are many types of NPs that are currently employed in nanomedical applications. Table 1 shows the most popular NPs which can be divided into organic and inorganic NPs.

Table 1. Most employed NPs in nanomedicine.

Organic NPs	Inorganic NPs
Polymer NPs	Semiconductor NPs
Lipid-based NPs	Plasmonic nanostructures
Carbon nanostructures	Silica-based NPs
Magnetic polymeric NPs	Upconversion NPs
-	Magnetic NPs

1.3.1.1. Organic NPs

1.3.1.1.1. Polymeric NPs

Polymeric nanocarriers offer a great versatility in terms of size, shape, surface functionalisation and biodegradability, what allows their use in multiple applications such as bioimaging, sensing, diagnosis and therapy. Several of these polymers are made from polyesters, poly(amino esters), polyamides, or chitosan, to name just a few. One of the most known polymers is the poly lactide-co-glycolide (PLGA), which is one of the first polymers approved by the Food and Drug Administration (FDA) for clinical applications. These biopolymers present as main feature their biocompatibility on the grounds of their structural similarity with biological molecules, such as proteins or sugars, hence being able to be recognised and metabolised *in vivo*. This property makes them very promising biomedical tools. Besides, the relative ease of synthesis, in the majority of the cases, along with their wide chemical reactivity given by the large availability of functional groups, provide polymer NPs with highly interesting properties [39].

1.3.1.1.2. Lipid-based NPs

There are three different types: i) phospholipid-polymer nanomicelles, ii) lipid-bilayer vesicular nanostructure (liposomes), and iii) solid-lipid NPs (SLNs).

The polymer nanomicelles and liposomes usually employ phospholipids to create NPs of one or two lipid bilayers consisting of a polar core, a hydrophobic compartment, and a hydrophilic external part. This duality enables to load either hydrophilic or lipophilic molecules, or both, into lipid NPs. On the contrary, SLNs use high-melting lipids, triglycerides, which provide more stability [39].

1.3.1.1.3. Carbon nanostructures

Fullerenes, carbon dots (CDs), carbon nanotubes (CNTs), and graphene dots (GDs) are included in this group of organic NPs [39]. The fact of being made of carbon confers them unique electronic and luminescence properties for biomedical applications. For instance, CDs are very small, less than 10 nm, with tuneable fluorescent properties and can be functionalised to be used in aqueous media as sensing molecules, amongst others applications. In fact, their size and functionalisation modulate the CDs photoluminescent properties [40]. Similarly, CNTs have been widely used as imaging, sensing, diagnostic, therapeutic, and biotargeting probes. GDs, which consists of one single atomic layer of graphite with just two dimensions in nanoscale have recently emerged in biomedicine [39]. Their high photostability, tunable photoluminescence properties, good biocompatibility, and small size, enable GDs to be employed as bioimaging and biosensor molecules [41].

1.3.1.2. Inorganic NPs

1.3.1.2.1. Semiconductor NPs

Inorganic NPs are highly stable and resistant to enzymatic degradation, and exhibit intrinsic electronic, optical, and magnetic properties that can be controlled with the size, shape, composition, and surface functionalisation. On top of that, inorganic NPs possess an important grade of toxicity that limits their application with biomedical purposes [39].

Quantum dots (QDs) are included in this group. QDs range in size from 3 nm to 10 nm which provides quantum effects. The QDs emission is tunable and size-dependant because of the energy gap between the highest occupied level of the valence band and lowest unoccupied level of the conduction band which is determined by the QDs size [39]. QDs core is generally made of a combination of semiconductor elements from groups II – IV, such as CdSe or CdS, from groups III – V, such as InP or GaAs, or only semiconductor elements from group IV, such as Si or Ge. QDs are usually employed as imaging agents; nevertheless, their strong autofluorescence and the relative low light penetration are serious drawbacks [39].

1.3.1.2.2. Plasmonic nanostructures

Noble metals such as gold (Au) or silver (Ag) NPs exhibiting a strong localised surface plasmon resonance (LSPR) absorption peak are considered plasmonic NPs [42]. The LSPR absorption peak is a maximum in the optical absorption spectrum of the plasmonic nanomaterials that enables their use for two-photon luminescence bioimaging, photothermal bioimaging, photoaccustic bioimaging, and photothermal therapy [43]. Amongst the plasmonic NPs, gold NPs (AuNPs) are widely utilised since they exhibit low toxicity and great

versatility provided by their wide and ease functionalisation to proteins, oligonucleotides, and antibodies, giving rise to biocompatible bioconjugated AuNPs [44].

1.3.1.2.3. Silica-based NPs

Silica NPs contain a porous or mesoporous silica matrix produced by sol-gel chemistry which can be modulated to obtain tailored silica NPs of different pore and diameter sizes [45]. One of the major advantages of the silica NPs is their high biocompatibility that allows employing them as biosensors, delivery systems, or theranostics [39], amongst others [45]. In addition, the silica NPs surface can be functionalised to expand their applications.

An interesting type of silica NPs is the organically modified silica (ORMOSIL) which replaces one of the alkoxy arms of silicon for organic moieties to provide functional groups to enhance the biostability and to ease the bioconjugation [39].

1.3.1.2.4. Upconversion NPs

Upconversion NPs are diluted systems where trivalent lanthanides, such as Er^{3+} and Ho^{3+}, are dispersed in an appropriate dielectric lattice, like $NaYF_4$ [46]. Regarding upconversion, it is an anti-Stokes process wherein long-lived electronic states of lanthanides absorb two or more low energy photons (longer wavelengths), emitting a higher energy photon (lower wavelengths) [47]. This upconversion process generally takes place from the NIR range to the UV-VIS range, and it is unique to each lanthanide due to their unique electronic configuration and energy, regardless the size and the shape of the NPs. Furthermore, this upconversion process provides the NPs higher photostability, negligible photobleaching, absence of autofluorescence or lower toxicity, compared to traditional organic fluorophores or semiconductors QDs [46]. In addition, upconversion NPs can be easily engineered to accomplish a myriad of applications according to the lanthanides elements that can be incorporated. Amongst these multiple applications, it is noteworthy their use in multimodal imaging, biomarkers diagnosis, and drug release [39].

1.3.2. Bioconjugation chemistry

The chemical functionalisation of NPs provides them with physicochemical stability, stability to degradation, stability to undesired cross-reactions, biocompatibility, and opens-up their use in a large number of biomedical applications. However, the chemical modification of NP surfaces to give rise functionalised NPs could be challenging sometimes. Depending on the type of NPs and the functional groups presented on their surface, the ease and efficiency of the bioconjugation chemistry varies. Thus, in order to obtain biocompatible NPs with a specific aim for biomedicine, bioconjugation is required to enable chemical modifications of

functional groups. As aforementioned, the inclusion of functional groups onto the NPs surface guides the NPs applications to theranostic, such as tumour targeted imaging, multimodal imaging, and biosensing, amongst others [48].

Most bioconjugations to NPs of small molecules which can act as drugs, imaging agents and/or sensors, polymers, or biomolecules, are performed by either non–covalent interactions, mainly avidin-biotin partner recognition [49], or via covalent linking through chemical reactions (Figure 2), such as [39]:

(i) Reaction between an amine and a carboxylic acid group to form stable amide bonds. This reaction can be mediated by carbodiimides chemistry to enable carboxyl group to be activated prior reacting with the amine group. NHS-esters can also be used to activate the carboxylic acid group.

(ii) Reaction between a thiol and a maleimide group through Michael addition to give rise to a stable thioether bond at physiological pH (6.5 – 7.5) [50]. This strategy is very useful for proteins containing cysteine moieties.

(iii) Copper-catalysed Click chemistry to perform azide-alkyne cycloaddition [51]. Recently, it has emerged the use of copper-free Click chemistry which seems to present no apparent cytotoxicity [52]. This reaction takes advantage of the high reactivity between cyclooctynes and azides [53].

(iv) Reaction between an aldehyde and an amine group to give hemiaminal, which subsequently dehydrate to form substituted imines. The utilisation of glutaraldehyde to attach proteins is an example of this chemistry [54].

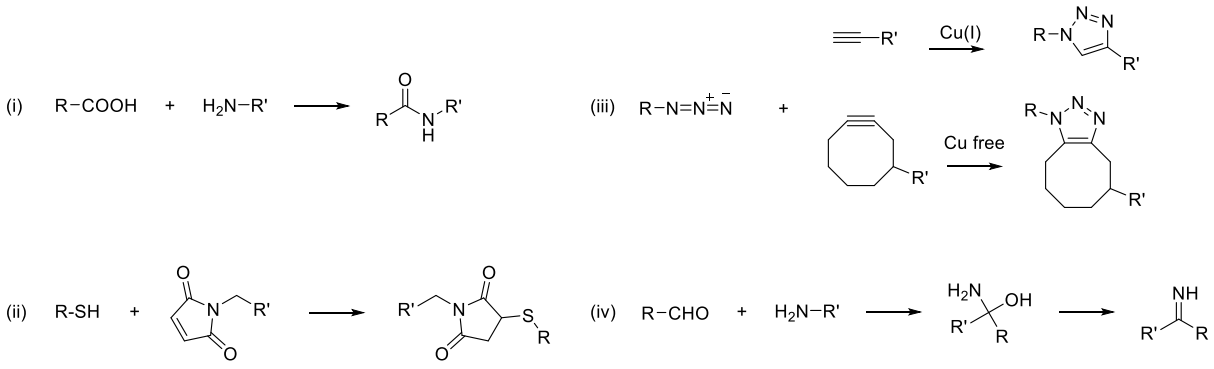

Figure 2. (i) Reaction between a carboxylic acid and an amine to form an amide; **(ii)** thioether formation via thiol and maleimide reaction; **(iii)** Click chemistry reaction mediated by Cu(I) or Cu free; and **(iv)** reaction between an aldehyde and an amine to give rise to an hemiaminal and, then, to an imine.

1.4. Magnetic particles

Magnetic particles contain iron oxide nano- and micro- particles, usually Fe_3O_4 (magnetite) and γ-Fe_2O_3 (maghemite), and sometimes α-Fe_2O_3 (ferrite), which provide paramagnetic properties [39]. Magnetic particles can be either organic, when the iron oxide NPs are dispersed in polymers or biopolymers, or inorganic, when the iron oxide NPs ranging from 5 to 50 nm in size are employed dispersed in an inorganic matrix [55].

The great importance of the magnetic particles lies in their paramagnetic properties which allow their use within biological material as the vast majority of them have diamagnetic properties. Therefore, the paramagnetic properties enable the efficient and selective separation of magnetic particles from biological material when a magnetic source is employed. Besides, the fact of having the iron oxide particles dispersed in polymers enables the immobilisation of a great variety of molecules such as oligonucleotides, proteins, antibodies, drugs, biomolecules or dyes, amongst others. Hence, the applications of magnetic particles, as long as they are biocompatible, such as the commercially available polystyrene-based magnetic particles MagPlex® and Dynabeads®, are countless [56]. For instance, one of the most common applications is the use of polymer-based biocompatible magnetic particles carrying streptavidin for specific biotinylated molecules binding and magnetic purification.

The commercially available polystyrene-based magnetic particles Dynabeads® (Dynal) were introduced in the 1980s and are widely employed nowadays since they are monodispersed (2.8 μm in size), robust, facile to handle, and biocompatible. In 2016, Life Technologies, now ThermoFisher, which in 2005 acquired Dynal for $300m, reported that "globally more than $2.5 billion laboratory tests are performed every year with Dynabeads® based immunodiagnostic assays". The variety of functionalised magnetic particles ensuring a specific capturing along with an affordable price has also contributed to their expansion. Depending on the target molecule and the selected capture approach, direct or indirect, the functionalisation of magnetic particles is chosen, thereby defining the magnetic particles application. In particular and regarding nucleic acids purification, magnetic particles allow the preparation of libraries for next generation sequencing (NGS), the capture of specific sequences and the immobilisation of either DNA or cDNA to run assays such as PCR.

Dynabeads® effective magnetic separation does not require centrifuge steps but just three simple steps. The first one consists of a specific binding between capture moieties attached to Dynabeads® and target molecules which are recognised by the capture groups. Secondly, Dynabeads® are easily and rapidly separated from the sample and subsequently

washed by employing a magnet, enabling magnetic purification and a gentle removal of the liquid phase. Finally, the target molecule is either eluted from Dynabeads® or kept bound to them, depending on the application.

Dynabeads® can be employed for cell isolation [57], T-cell activation and expansion [58], exosome isolation and detection [59], and protein and nucleic acid isolation and identification [60],[61], amongst others. In addition to the applications, the biocompatibility and low undesired cross-reactivity of Dynabeads® allow their translation to large number of detection platforms, such fluorescence-based readers and flow cytometers.

In this sense, magnetic particles have contributed to the development of multiplexing assays in flow cytometry, enabling the detection of multiple analytes in a single sample. Another example of the magnetic particles that contributed the most to the development is the MagPlex® microspheres for the xMAP technology (property of the Luminex Corporation, founded in 1995). These MagPlex® microspheres consist in polystyrene beads loaded with multiple dyes to enable the detection of up to 500 analytes simultaneously through a fluorescence assay. The concept of this assay, in brief, is that each MagPlex® microsphere contains a specific combination of dyes to provide unique fluorescent signal, and that each microsphere is conjugated to a unique capture reagent to measure multiple analytes at once. Then, a reporter fluorochrome (Streptavidin-phycoerythrin, SAPE) quantifies the target molecules bound to each type of MagPlex® microsphere [62]. The peculiarity of MagPlex® microspheres is that they can include iron oxide NPs within the polystyrene microspheres to comprise the features and advantages of their unique technology with the magnetic particles.

MagPlex® microspheres are superparamagnetic microspheres of 6.5 µm with the surface functionalised with carboxyl groups, which allows the labelling of biomolecules, such as peptides [63]. Interestingly, Luminex® introduced the MagPlex®-Avidin microspheres that contain a surface layer of avidin for binding biotinylated targets that enhance the performance since it separates the biomolecules from the microspheres surface [62].

In order to expand the molecular assays of the MagPlex® microspheres, Luminex® introduced the xTag® Technology, which is based on the universal array approach. Therefore, there were created the MagPlex-TAG™ microspheres which are conjugated to unique oligonucleotide probes (antiTAG) for capturing nucleic acid targets bearing the complementary TAG sequences [62]. The MagPlex-TAG™ microspheres have been employed in DNA-based assays for determining allele frequencies in a multiplex DNA-based assay [64], for developing multiplex single nucleotide polymorphism (SNP) mutation assays [65], or for a multiplexed detection and identification of respiratory pathogens [66]. Furthermore, they have been also employed for miRNA analysis and for protein-based and

immunoassays [67]–[69]. To have an idea about the economic impact of xMAP technology, in 2018 Luminex reported revenues of $50.15m in consumable sales and $156.71m in assays.

Thus, magnetic particles have been proved as versatile, suitable and valid tools for biomedical application since they can carry a wide variety of biomolecules for multiple approaches. Their high stability and capacity to chemically modify their surfaces makes them very attractive in combination with other existing technologies.

1.5. Toxicity

While so far, the huge potential of NPs in the biomedical field has been presented it is also important to note the downside of NPs, the toxicity which can be caused by NPs. The size, the surface functionalisation, the shape, and the chemical composition which are, in fact, directly responsible for their properties and dictate the behaviour of the NPs, also trigger their toxicity. Although a small size helps the NPs to avoid immunosurveillance and to infiltrate tissues, cells, and subcellular compartments, it also induces NPs accumulation that leads to toxicity. Furthermore, the chemical composition of the NPs determines one of their key properties in this respect, their biodegradability. For instance, those NPs having heteroatoms (–C–X–) instead of only carbons (–C–C–) in their structure tend to be biodegradable [39], reducing the risk of their accumulation in certain tissues, specially liver, and, hence, reducing the toxicity. On the other hand, being too easily hydrolysable could mean a considerable loss in their biodisponibility. Besides, whilst NPs as such might not be toxic, the by-products produced as a result of NPs degradation can cause toxicity, as it happens with the PLGA NPs. By-products produced by PLGA NP metabolism are lactic acid and glycolic acid, which cause mild to severe toxicity[39][38]. Likewise, NPs like quantum dots (QD) release carcinogenic heavy metals that are very toxic. Thus, in order to prevent undesired NPs degradation leading to toxic by-products, an appropriate surface coating, for instance with polyethilenglycol (PEG), is an option to be considered [39].

In this sense, the surface of the NPs is, perhaps, the aspect that influences the most their behaviour. Their modification thus drives to obtain more stable, less toxic, and more efficient NPs. The functionalisation of the NPs surface directly influences in the aggregation effect, the biochemical reactivity, the pharmacodynamics and biodistribution, the biodegradability, the cell entry, and the cellular localisation, to name just some effects. An appropriate surface functionalisation can modulate NPs, thereby reducing their toxicity by decreasing the high-surface energy, which is one of the main toxicity causes, along with NPs aggregation and the unspecific and undesired release of their cargo, especially when ions are included in the NPs

[39]. Moreover, an appropriate surface functionalisation not only reduces the toxicity of the NPs but also produces an enhancement in the NPs biological properties such as increasing their hydrophilicity. Therefore, the functionalisation of the surface of the NPs should balance the positive properties that can be exerted and the undesired toxicity that come with it.

NPs can induce toxicity through several ways: oxidative stress, genotoxicity, apoptosis and necrosis, immunogenicity and biofouling, which are the most common processes. The oxidative stress is related to the oxygen-containing molecules susceptible to undergo chemical reactions and, thereby, generating reactive oxygen species (ROS) within cells. Abnormal amounts of ROS produced as a consequence of NPs interaction with the oxygen-containing molecules leads to toxicity. One of the main causes for ROS production is NPs degradation due to an acidic environment in the endolysosomal vesicles inside the cells. This degradation is especially dangerous in those NPs carrying essencial ions such as Ca^{2+} or Fe^{3+}, or heavy metal ions like Hg^{2+} and Cd^{3+}. Genotoxicity refers to the damage produced in the DNA by either direct physical interaction, like DNA intercalation, or chemical interaction that leads to DNA mutations and malignant transformations. Also, NPs indirectly can induce cells to enter in apoptosis by generating ROS or genotoxicity, leading to cell death. Similarly, instead of producing a programmed death, NPs can also induce necrosis, a rapid and abrupt way of cell death, in which cell membranes are suddenly broken. On the contrary, immunogenicity does not induce the cells to die. In this case, NPs trigger the cell-mediated immune response as mechanism of defence because of recognition of the NPs as an unknown and invasive object. Thus, immunogenicity is characterised by the release of cytokines and pro-inflammatory proteins, which drives to an inflammatory process. Another way of causing immunogenicity is by the biofouling toxicity. Biofouling consists of the absorption of proteins over the surface of the NPs, forming a protein corona which alters the NPs biodistribution and changes how NPs interact with cells and biostructures. Consequently, the proteins biological functions are altered if compared as they were designed, affecting the cell signalling pathway and, hence, inducing the cell-mediated immune response [39].

CHAPTER II

Chapter 2. Development of bead-based technologies for molecular assays using Dynamic Chemistry

2.1. The importance of detecting nucleic acids

2.1.1. Nucleic Acids as Biormarkers

Biomarkers (biological markers) can be defined as biological substances which are specific and sensitive to a particular physiological or a pathological condition [70]. Thus, biomarkers are biological substances that are characteristic of predetermined conditions that, in case of an alteration of the conditions, would be modified in their expression, acting as indicators of such alteration. Biomarkers, therefore, can be of great value as diagnostic and prognostic tools to identify a pathological condition, monitor disease progression, evaluate the efficiency of a treatment, and predict disease progression. Moreover, the integration of biomarkers data using bioinformatics tools is currently increasing the understanding of biological pathways and regulatory mechanisms associated with diseases [71].

In order to be an ideal biomarker, the candidates should possess several features that make them specific, sensitive, predictive, robust, translatable, and non-invasive. The ideal biomarker should be specific of a tissue and not promiscuous, it should be easily differentiated in pathological conditions and should vary its expression according to the stage of the disease, it should predict a pathological condition by being stable in the time (long half-life), it should be identified with existing techniques and finally translated to clinic diagnostics. To conclude, the best biomarker should be accessible by non-invasive methods [70].

Despite the difficulty of finding biological substances matching with the ideal biomarkers characteristics, nucleic acids (DNA, RNA and miRNA) can tick most of the boxes of an ideal biomarkers [72],[73]. Moreover, as they can be found circulating in body fluids such as blood, urine and saliva, a new field, liquid biopsy, has strongly emerged. Modern techniques allow detecting these circulating nucleic acids and in 2015 MIT considered liquid biopsies as one of the top 10 breakthrough technologies which uses nothing more than a body fluid as sample [74].

Within blood samples, circulating nucleic acids can be found in different manners:

(i) as proper circulating nucleic acids, shed by tumours, as cell tumour DNA [74],[75] and circulating miRNA forming protein complexes with Ago-2 [73],[76] or HDL [73],[77];

(ii) inside circulating tumour cells (CTCs) shed to the bloodstream by solid tumours [74],[78], allowing their detection by isolating and breaking the CTCs;

(iii) inside of tiny vesicles ejected from the tumours called exosomes [74],[79], which contain mRNA and miRNA and it's a way of exchanging RNA between cells [80].

There may also be considered a fourth way of founding circulating nucleic acids in blood on the grounds that platelets contain tumour-derived RNA biomarkers, the so called tumour-educated platelets (TEPs) [81] due to their capability to swallow vesicles loaded with tumour RNA [74].

miRNAs were discovered 20 years ago and have been proposed as ideal biomarkers as they are found in body fluids coming from tissues with a long-life time. However, there are still limitations in the use of circulating miRNAs as biomarkers for clinical diagnosis. There are technical limitations for their quantification and their presence in both healthy individuals and cancer patients means that large patient populations are needed to develop robust clinical studies. Moreover, the differences in their expression levels between healthy people and patients are sometimes small, what makes challenging the process of distinguishing between both states, increasing the possibility of false negatives or positive diagnosis [82]. Furthermore, the biological role of certain miRNAs in diseases, especially in cancer, is quite complicated as they might have opposite behaviours, acting as oncomiR or having a suppressor role in different type of cancers. Thus, while the potential is out there, the discovery phase required to find the right miRNA panels needs to be done properly. Combining highly sensitive and specific miRNAs with other clinical indicators is highly required (Figure 3).

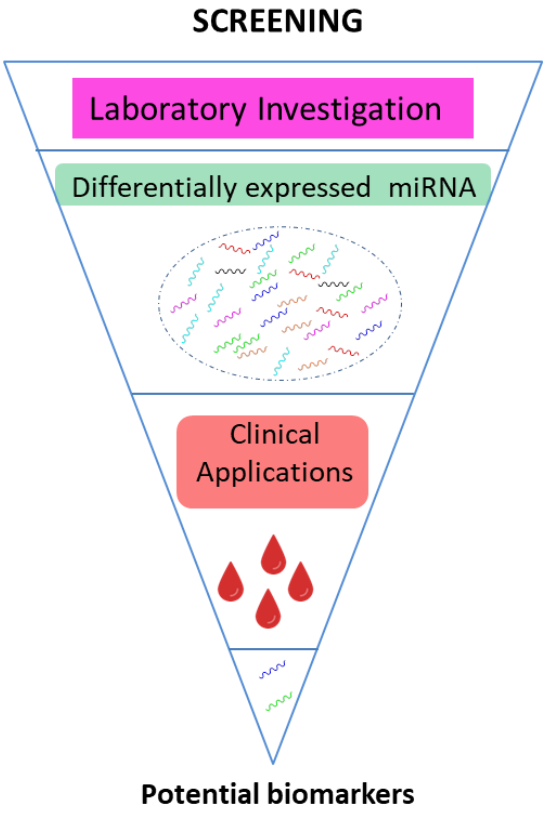

Figure 3. Work flow of how the screening of potential circulating miRNA biomarkers for clinical applications is done (Adapted from [82]).

Different studies have demonstrated the power of miRNA signatures for early diagnosis of cancer plus their power to identify the type of cancer. These have made them to be one of the most promising tools despite the current limitations of miRNA. The use of miRNAs as biomarkers is particularly important in those cancers wherein an early diagnosis is significantly difficult and crucial, as lung cancer, which is the most diagnosed cancer and the leading cause of cancer death worldwide [83], especially the non-small cell lung cancer (NSCLC) which represents, approximately, the 85% of lung cancer cases [84]. Additionally, the role of miRNA as diagnostic biomarker is also very interesting in breast cancer [85],[86], which is the second cause of cancer death and the most commonly diagnosed tumour in women [83]. The same apply in colorectal cancer (CRC) [87],[88] and prostate cancer [89],[90], which are also two of the most diagnosed cancers and two of the major causes of cancer death worldwide [83], amongst other cancers. Currently, the German company Hummingbird Diagnostics is developing miRNA-based assays for NSCLC and breast cancer and the Spanish company Amadix is doing the same for CRC and NSCLC.

2.1.2. miRNA-21

MicroRNAs (miRNAs) are small non-coding RNAs of 18-24 nucleotides in length that regulate gene expression by directly interacting with the 3' untranslated region (UTR) of a target gene's miRNA. This interaction leads to degradation and/or translational repression of that gene [91]–[94]. It is currently estimated that there are approximately 2,300 miRNAs encoded in the human genome and although they account for a minor fraction of the express genome [95], miRNAs are implicated in the regulation of cell growth, differentiation and apoptosis, and their deregulation is associated with multiple serious diseases [94], especially in the hallmark of cancer [96], as it is shown in Table 2.

Table 2. Examples of miRNAs involved in cancer. Table adapted from [96]

Type of cancer	Up-regulated miRNAs	Down-regulated miRNAs
Breast cancer	miR-21, miR-96, miR-182, miR-183, miR-141, miR-200a, miR-429	miR-139, miR-145
Lung cancer	miR-21, miR-187, miR-448, miR-200c	let7, miR-138, miR-383, miR-448
Prostate cancer	miR-21	miR-130b
Colorectal cancer	miR-21, miR-31, let7c, miR-99a, miR125-b, miR-6826, miR-6875, miR-19a	miR-148, miR-592, miR-545,
Ovarian cancer	miR-21, miR-9	miR-187
Pancreatic cancer	miR-21	miR-10b, miR-137, miR-7

MiRNAs are transcribed by RNA Polymerase II into large precursor RNAs, called pri-miRNA. Then, in the nucleus, these molecules (pri-miRNA) are processed by a member of the RNase III enzyme family, Drosha, along with the cofactor DGCR8/Pasha, after being capped and polyadenylated, resulting in stem-loop structures, the pre-miRNAs. Afterwards, exportin 5, a GTP-dependent transporter, exports the pre-miRNAs from the nucleus to the cytoplasm where they are process by another RNase III, Dicer. In this process step, the pre-miRNAs are shortened from approximately 70 nucleotides to approximately 22 nucleotides in length, and released as double-stranded RNA duplexes. Thereafter, the double-stranded RNA duplex is separated by helicases prior its incorporation into the miRNA-Induced

Silencing Complex (miRISC), which retains the mature miRNA strand to regulate the gene expression [94] (Figure 4).

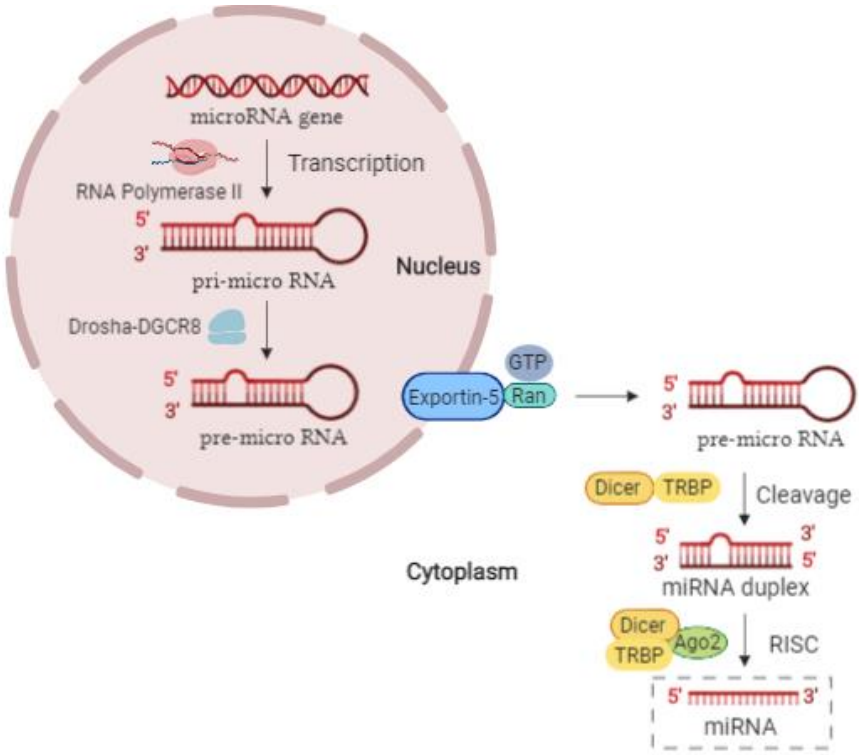

Figure 4. miRNA biogenesis and secretion. Adapted from [70] and created with Biorender.

One of the most studied and cited miRNAs is miR-21, a 22 nucleotide long single strand RNA located in the chromosome 17 [97] that presents two mature sequences: hsa-miR-21-5p, whose sequence is 5'–UAGCUUAUCAGACUGAUGUUGA–3' and hsa-miR-21-3p, whose sequence is 5'–CAACACCAGUCGAUGGGCUGU–3'. Whereas the 5p strand is present in the forward position (5'-3') in the pre-miRNA stem loop, the 3p strand is present in the reverse position (3'-5'). miR-21 has the spotlight, amongst other miRNAs, on the grounds of the high number of reports indicating that it is up-regulated in a lot of pathological conditions, being one of the most abundant miRNAs in cancer cells, and because miR-21 is capable of silencing tumour suppressor genes [97],[98]. Therefore, it is considered an oncomiR [99].

Regarding the implications of miR-21 in cancer, it is overexpressed in most human tumours and has emerged as one of the miRNAs most frequently associated with poor outcome in cancer, thus miR-21 is considered as a very promising diagnostic and therapeutic target for cancer [100],[101]. miR-21 is directly implicated in many human cancers [97] and amongst them, due to miR-21 high implication and the great importance of these cancers for the humanity in terms of frequency and mortality, it is interesting to highlight the glioblastoma

[102],[103], the breast cancer [104],[105], the ovarian cancer [106], the lung cancer [104], and the colorectal cancer [107]. As a matter of fact, extensive studies suggest that the up-regulation of miR-21 plays an important role in many processes of cancer such as tumourgenesis, progression (accounting for migration and invasion) and metastasis [108],[109]. Moreover, miR-21 has been reported to be involved in the generation of resistance to chemotherapy and radiotherapy in lung cancer [110], and resistance to chemotherapy in breast cancer [111] and in ovarian cancer [112], which usually increases patients morbidity and mortality [110]. For instance, it is found in the literature that miR-21 overexpression decreases the efficacy of chemotherapy drug treatment with placlitaxel in ovarian cancer [112]. It also produces resistance to cisplatin in aggressive A549 lung cancer cells, osteosarcoma, and ovarian cancer; to 5-Fluorouracil in colorectal cancer; to Gemcitabine in pancreatic cancer; to Teniposide in glioblastoma; to Gefinitib in NSCLC; and multidrug resistance in breast cancer [113]. Therefore, miR-21 possesses a great value as diagnostic biomarker but also as therapeutic target, as it evidences the antimiR-21 therapies that are being developed nowadays, especially the latest CRISPR/CAS9-based gene therapies [98],[112].

As a consequence of the major impact that miRNAs have in cancer, an accurate, specific, sensitive, precise and cost-effective detection and quantification of miRNA will represent a major advance and amelioration in diagnosis, along with real-time monitoring of miRNA, providing a high valuable knowledge to physicians, which is essential in personalised medicine [114],[115]. Nevertheless, this represents a challenge on the grounds of miRNA small size, low abundance, high homology sequences between different miRNA types, and high variation in their expression levels [116]–[118]. Hence, the ideal miRNA detection tool should be, as previously mentioned, sensitive enough to detect and quantify low amounts of miRNA, specific to discern similar miRNA sequences with single nucleotides differences, it also should be able to identify several miRNAs within the same sample in the same run (multiplexing), and it should be user-friendly and cost-effective.

To date, miRNA detection and quantification analyses are mostly done by RT-qPCR, which is the gold standard technique. RT-qPCR is based on the well-established polymerase chain reaction (PCR), combining the reverse transcription PCR (RT-PCR) with the quantitative PCR (qPCR). RT-qPCR consists of a first step wherein the miRNA are elongated and then are reverse transcribed into complementary DNA (cDNA) using a reverse transcriptase by forming a DNA/RNA hybrid that is transformed in single stranded DNA when the reverse transcriptase degrades the RNA portion of the duplex. Following this, cDNAs are amplified with a miRNA-specific forward primer and a universal reverse primer. The quantitative real-time detection, which enables miRNA quantification, can be performed by

different strategies. Employing a dsDNA binding dye, typically SYBR Green, which releases fluorescence in each cycle resulting in a fluorescence signal increase proportional to the amount of replicated DNA, is one of the most utilised. However, the strategy which is mostly used is the employment of fluorogenic probes, such as TaqMan® probes, which have a fluorophore and a quencher, resulting in fluorescence signal emission when the fluorophore and the quencher are separated in the amplification cycles [119].

However, the need to extract and purify miRNAs from their biological source, to elongate, to convert into cDNA, and to amplify by PCR makes these assays unsuitable to directly quantify the number of miRNAs per sample.

Lately, and because of the great importance of not only detecting but also quantifying the amount of miRNA, several platforms for the direct detection and quantification miR-21 have been developed. For instance, the platform that employs hydrogels functionalised with DNA probes complementary to the miRNA target contained within isolated well reactors [120], the platform that combines cyclic enzymatic amplification with microfluidic voltage-assisted liquid desorption electrospray ionization-tandem mass spectroscopy [121], the platform that comprises a microwell strip silicon photomultiplayer-based reader and a chemical-based method developed by DestiNA Genomics Ltd. (Chem-NAT) [122].

During this Doctoral Thesis, a novel protocol and reagents capable of quantifying miR-21 using a standard fluorescent microplate reader and Chem-NAT technology have been developed.

2.1.3. KRAS

The Ras proteins are small GTPases that, in response to extracellular stimuli, regulate several cellular responses such as proliferation, survival and differentiation, acting as signal switch molecules [123]–[125]. As Ras proteins are GTPases, they are activated when they bind to GTP, regulating a complex signalling network that modulates the cell behaviour by interacting with effector molecules, activating Ras-dependant signalling pathways [124]. Some of these Ras effector pathways involve apoptosis, cytoskeletal organisation, proliferation, survival, and vesicle trafficking, amongst others [126]. The Ras proteins are also known as “oncogenic Ras” due to they are usually expressed as mutant proteins in human cancers, resulting in abnormal cell signalling, proliferation, and survival [124],[127].

The Ras proteins are encoded by the Ras genes, which were firstly identified in the rat genome in 1981 and then found in the mouse [126],[128] and in the human genome [126]. The RAS genes have been described to be three: the Harvey sarcoma virus-associated oncogene (HRAS), the Kirsten sarcoma virus-associated oncogene (KRAS), and NRAS,

which was isolated from a human neuroblastoma. Likewise Ras proteins are considered oncogenic proteins, the human Ras genes KRAS, HRAS, and NRAS, are oncogenes and they are highly expressed and mutated in cancers. In fact, the Ras genes are the most frequently mutated oncogene in human cancers, appearing in 90% of the cases of pancreatic cancers, 35% of lung cancers, and 45% in colon cancers [129]. Besides, Ras genes are also expressed in many other frequent cancers such as ovarian cancer, melanoma or bladder, and low expressed in breast cancer or myeloid leukaemia, amongst others. When the appearance of the three Ras genes mutation frequency is analysed in separate, KRAS gene is found to be the prevalent isoform in pancreatic cancer, lung cancer and colorectal cancer, amongst others, whereas NRAS is the predominant mutated isoform in melanoma and myeloid leukaemia, and HRAS is the predominant isoform in bladder [129] (Table 3).

All these strong evidences came at the same time that new recombinant antibodies were developed by the biotech pharmaceutical companies as anticancer biopharmaceuticals. In particular, Cetuximab (Erbitux®), an antibody targeting the EGFR receptor, was demonstrated not to be very efficient in CRC patients who presented mutations in exon 2 of KRAS gen. In fact, in 2012, FDA approved Erbitux® conditionally to be used in combination with a FDA-approved companion diagnostic to determine whether the KRAS genes were mutated or wild type. Just to patients with wild type KRAS, Cetuximab is prescribed. At that moment, the therascreen KRAS test developed by DxS Diagnostics and commercialised by Qiagen was the first FDA-approved companion diagnostic for KRAS test. Currently, Cobas test by Roche is also FDA-approved.

All of this, along with the fact that KRAS genes are found as circulating DNA in patients with colorectal and pancreatic cancer, have converted KRAS in an interesting biomarker for diagnosis, companion diagnostic, prediction of recurrences and clinical outcome in the liquid biopsy field [130].

Table 3. HRAS, KRAS, and NRAS mutations in human cancer. Adapted from [124].

Cancer type	HRAS	KRAS	NRAS
Biliary tract	0%	33%	1%
Bladder	11%	4%	3%
Breast	0%	4%	0%
Cervix	9%	9%	1%
Colon	0%	32%	3%
Endometrial	1%	15%	0%
Kidney	0%	1%	0%
Liver	0%	8%	10%
Lung	1%	19%	1%
Melanoma	6%	2%	18%
Myeloid Leukemia	0%	5%	14%
Ovarian	0%	17%	4%
Pancreas	0%	60%	2%
Thyroid	5%	4%	7%

As aforementioned, KRAS gene is a major driver for lung adenocarcinoma, pancreatic cancer, and colorectal cancer, but it also works as a biomarker for diseases related to tobacco smoke since one of its mutations has been found in early lesions and metastases [129]. Regarding KRAS mutations, there exist more than 20 different mutations in total, being the mutations in codon 12 and 13 of exon 2 the most frequents, and less common the mutations in codon 61 of exon 3. In fact, in colorectal cancer, mutations in codon 12 and 13 account for, approximately, the 95% of all types of mutations, corresponding about the 80% to mutations in codon 12 and 15% to mutations in codon 13 [131]. KRAS mutations are single nucleotide point mutations where a nucleobase is changed by another nucleobase resulting in a different protein expression. Amongst all the KRAS mutations, the four most frequent mutations are G12D, G12V, G13D, and G12C, which account for the 83% of all KRAS mutations [132]. Particularly, in colorectal cancer, the most common pattern is G12D, G12V, G12A, G12R, G12C, G12S, and G13D [131]. In lung cancer, the most commonly reported KRAS mutation is the transversion mutation G12C, but it is also widely reported the implication of the transversion mutations G12V, G12A, and G12R, the transition mutations

G12D and G12S, along with the mutations G13D and G13C, though they are less common [133]. The principal mutations of KRAS are shown in Figure 5.

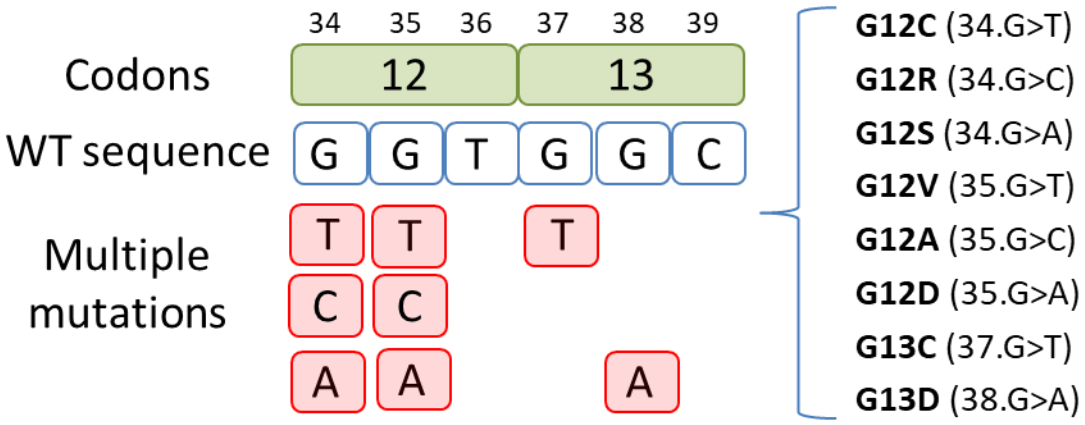

Figure 5. Principal mutations of KRAS.

On the grounds of the high number of KRAS mutations, their high expressions and implications in developing and progression of cancers, which are also some of the most frequent and lethal cancers within the human population, the KRAS genes testing has become a key aspect in the clinic. As a matter of fact, a KRAS external quality protocol in 59 laboratories across 8 European countries was established [134]. Currently, a great number of methods can be used for KRAS mutation testing which vary in sensitivity, turnaround time, and cost. The traditional methods are based on hybridisation and DNA sequencing, however, they are time consuming and have large and complexes protocols [131]. On this basis, the emerging of PCR revolutionised the DNA mutation studies, becoming the PCR-based technologies the most utilised methods at this moment. Amongst them it is important to remark the high resolution melting analysis PCR (HRMA-PCR), the amplification refractory mutation system PCR (ARMS-PCR), the cleaved amplification polymorphism sequence-tagged sites PCR (PCR-RFLP), PCR clamp assay, the COLD-PCR, and the digital PCR (dPCR) [131],[135].

HRMA-PCR is a fast, simple and not expensive technique, particularly attractive for single nucleotide polymorphism (SNPs) detection, in which a saturating dye is added before or after the PCR but always prior to the rapid melting analysis of the PCR products, with the main drawback of the impossibility of multiplexing [136]. **ARMS-PCR** is an allele-specific amplification technique that allows the detection of any point mutation (SNP) or small deletions by using two complementary reactions, one that contains a primer for the amplification of the normal DNA sequence whilst the other reaction contains a mutant-specific primer for the amplification of the mutant DNA [137]. **PCR-FLP** is an approach in

which base pair changes, either small indels or SNPs, are measured due to their location within the recognition sequence of a restriction enzyme, resulting in the cleavage of a resistant site or the cleavage of fragments of several sizes, by endonucleases [138]. **PCR clamping** utilises the high affinity and specificity of peptide nucleic acid (PNA) probes to their complementary target nucleic acid [139]. PNA probe specifically designed for a WT sequence when finding a WT allele does not allow the generation of amplicons in combination with standard PCR primers, whereas it does when finding a mutant allele. **COLD-PCR** is a co-amplification at lower denaturation temperature PCR, often coupled to pyrosequencing, which settles the denaturation temperature in 80 ºC instead of 94 ºC in the conventional PCR, which selectively amplifies the minority alleles, regardless the mutation type or position [140]. **dPCR** [141] is a cutting edge technology that enables the absolute quantification of the target nucleic acid by creating a myriad of independent PCR-sub-reactions in the sample that contain a few or no target sequence, resulting in a binomial analysis of the events (absence (0) or presence (1) of the target). Moreover, the partitioning of the samples efficiently concentrates the target nucleic acid sequences, enabling the detection of rare mutations amongst WT sequences [142]. In fact, one of its kinds, the droplet-based PCR, allows the detection and quantification of circulating tumour DNA at very low concentrations, even though if it only represents the 0.1% of total DNA in blood [74]. All these techniques create preferentially amplicons containing the mutated variants rather than the WT ones.

Once amplicons are produced, then they have to be detected. In regards to detection methods for KRAS mutations, several technologies have been developed and compared. For instance, PNA clamp PCR and Scorpion-ARMS PCR [143], Therascreen (Qiagen) ARMS-PCR and competitive allele-specific TaqMan PCR (castPCR, Life Technologies) [144], or Scorpion-ARMS PCR, direct sequencing, pyrosequencing and multi-analyte profiling (Luminex® xMAP technology) [145], all of them performed in metastatic colorectal cancer. All three studies drove to similar conclusions: all the methods employed had a high ratio of success in determining KRAS mutations and WT sequences, with high concordance in the results obtained from each compared method. Thus, they could not establish a predetermine method for KRAS testing.

While current assays use amplify materials obtained from genomic DNA, a novel method capable of determine their mutations directly without performing the amplification step, could reduce time and avoid errors, has been developed. In this Doctoral Thesis, reagents capable of identify KRAS mutations using FACS and Chem-NAT technology have been developed.

2.1.4. Dynamic Chemistry

In spite of RT-PCR / RT-qPCR are the gold standard methods for miRNA analysis, they have several drawbacks such us (i) the high cost of the equipment and the material implicated [119], (ii) the need of a high quality and purity RNA sample which is essential for their success, (iii) the whole process is determined and limited by the first reaction efficiency, (iv) the high probability of contamination issues, and (v) in the dye-based RT-qPCR strategy, the dye will bind to any dsDNA present in the sample whereas the probe-based strategy requires optimisation and the design of a target-specific probe. On the other hand, there are other approaches which are based on just a hybridisation step between targets and capture probes, which tend to be long and increase the probability of obtaining false positives [146]. In order to overcome these problems, it has emerged a PCR-free alternative approach for nucleic acid testing that takes advantage of the dynamic chemistry, the Chem-NAT technology, which is one of the most recent and promising technologies [147],[148].

The Chem-NAT technology is based on PNAs, which were developed in 1991 by Nielsen [149] and are mimic structures of the nucleic acids but replacing the sugar-phosphate backbone for a peptide backbone. The PNA probes have a general backbone consisting of units of N-(2-aminoethyl)glycine wherein nucleobases are attached via carboxyalkyl moiety forming an amide bond [150] (Figure 6).

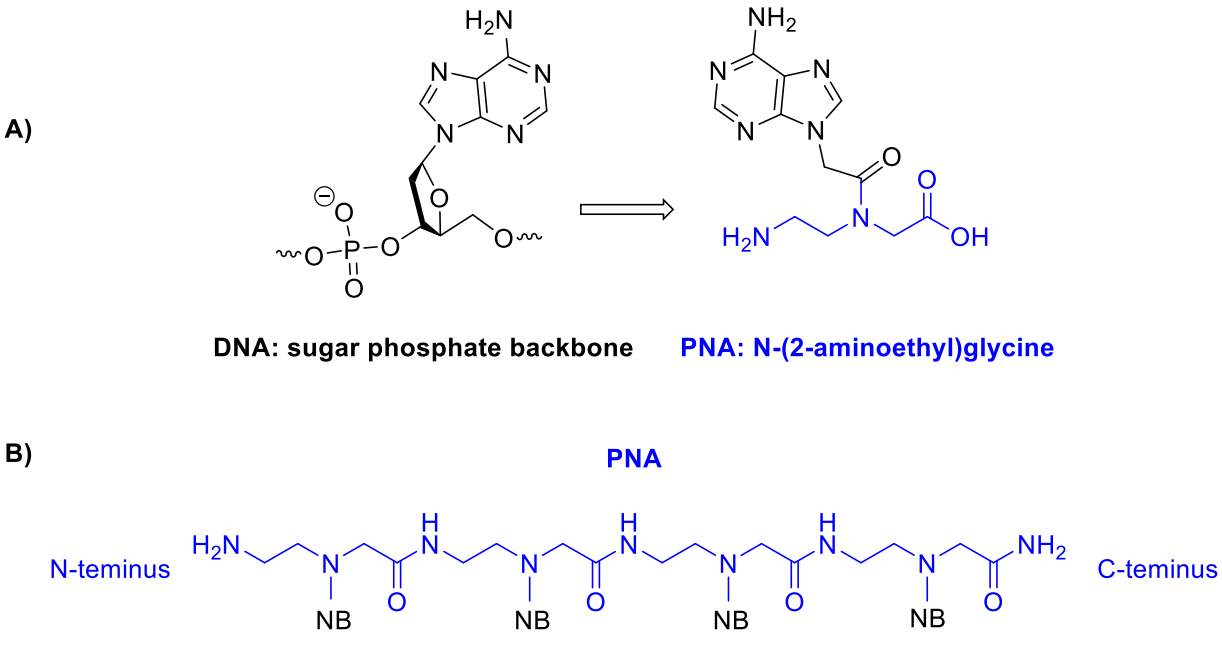

Figure 6. A) Structures of DNA and PNA: the sugar phosphate backbone is replaced by N-(2-aminoethyl)glycine and Adenine is attached to the PNA through a carboxyalkyl chain. **B)** PNA backbone general structure to which the nucleobases (NB) are covalently attached to the nitrogen of the glycine forming an amide bond.

PNA probes hybridise with the complementary target nucleic acid strand, usually in an antiparallel orientation following Watson and Crick base pairing rules, by aligning the N terminus of the PNA with the 3' terminus of the target nucleic acid (Figure 7). The peptide-based backbone confers PNA probe very interesting features, such as resistance to nucleases and proteases, higher affinity for RNA than for DNA, high stability in acid and week basic medias, and a higher binding affinity and sequence selectivity which makes the duplexes containing PNA to be more sensitive to mistmatches [151],[152]. Moreover, PNA probes have a stronger binding towards DNA and RNA, being the PNA-DNA and PNA-RNA duplexes thermally more stable than DNA-DNA or DNA-RNA duplexes. Nevertheless, as PNA probes possess an uncharged nature, they tend to aggregate due to poor water solubility, particularly when they are more than 12 mer in length and they have a high content in guanine [153]. This can be improved by introducing charges to the structure, either negative or positive charges, for instance by adding a lysine residue instead of glycine.

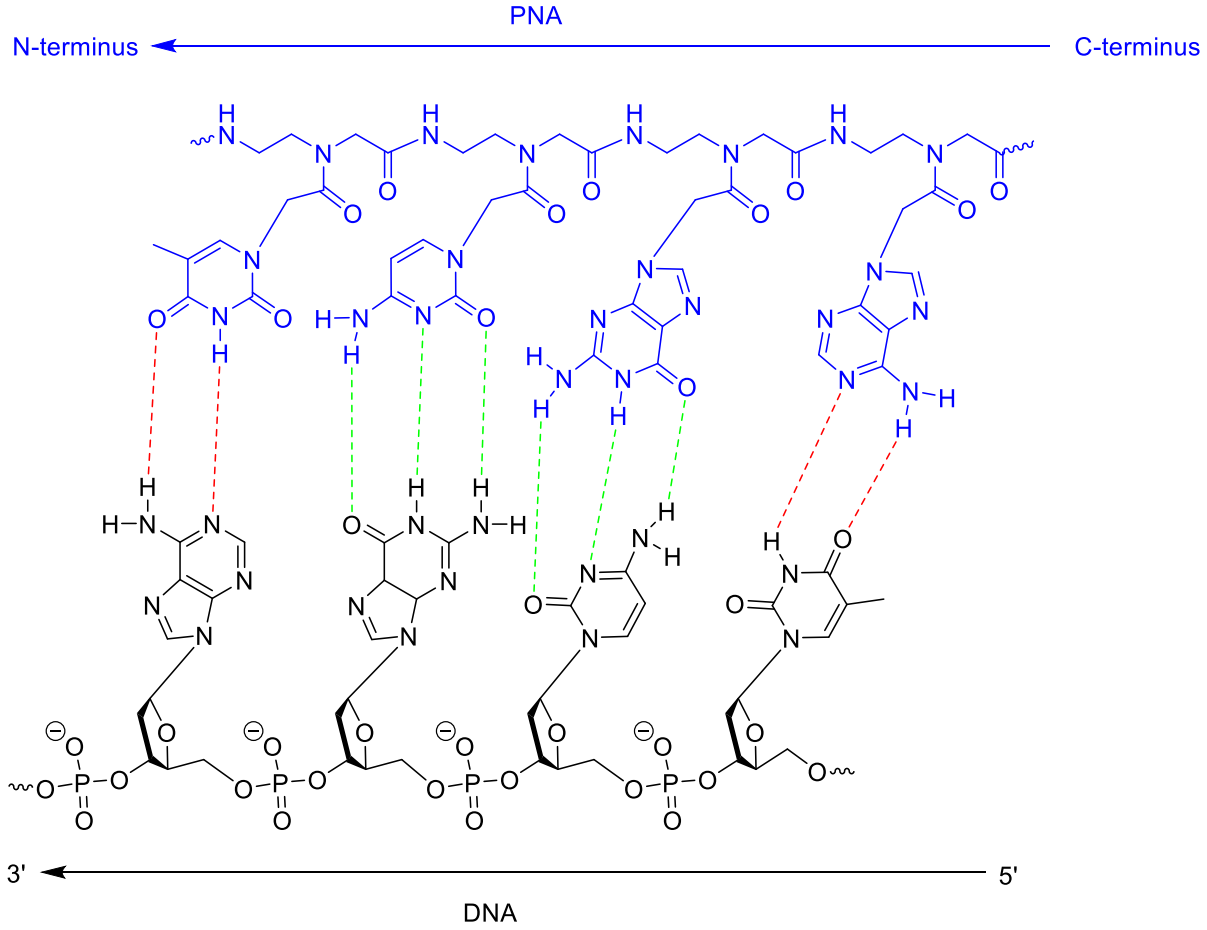

Figure 7. Hybridisation process between a PNA probe and a DNA strand: the N terminus of the PNA probes aligns with the 3' terminus of the DNA strand, and hydrogen bonds are formed between the nucleobases, 2 between adenine and thymine (red dashed lines) and 3 three between cytosine and guanine (green dashed lines).

In terms of PNA/NA interactions, longer PNA probes form more stable duplexes on the grounds of more base pairings are achieved, what means a higher number of hydrogen bonds and thus, an enthalpy gain. However, a higher PNA probe length also means less degrees of freedom and entropy loss, which is the driven force for the duplex formation. As a consequence, when designing and synthesising a PNA probe it is highly important to balance both things, to have the longest PNA probe that allows the highest stability but without losing the discrimination power for mismatches given by shorter sequences [154]. Regarding the PNA modifications, one of the most interesting is the introduction of a chiral centre at the γ position of the PNA backbone, which can induced the formation of a right or left helical motif (Figure 8). In fact, of special interest is the presence of a γ-(S)-chiral centre (from L-aminoacids) which contributes to enhance the PNA probes binding effect and sequence specificity by inducing the formation of the right-handed helical motif. Another interesting modification is the introduction of charges in substituent of the γ position of the PNA, also enhancing the PNA/NA duplex stability. In fact, PNA probes with negatively charged side chains not only do not decrease their binding effect but also increase their binding strength to RNA compared to positively charged PNA probes [155].

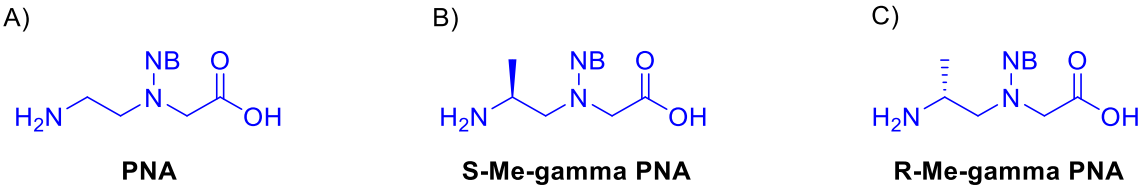

Figure 8. A) Standard unmodified PNA monomer; **B)** Introduction of a substituent (methyl) in the γ-position of the PNA monomer to afford a γ-(S)-stereocentre; **C)** Introduction of a substituent (methyl) in the γ-position of the PNA monomer to afford a γ-(R)-stereocentre.

Thus, the Chem-NAT technology harnesses Watson and Crick base pairing rules to template a dynamic reaction on a strand of abasic peptide nucleic acid (PNA) probes, which also contains gamma-modified PNA units, so called DGL probes in this Doctoral Thesis.

The DGL probes hybridise with the complementary target nucleic acid, leaving the abasic position in front of the nucleotide of the nucleic acid sequence which is under interrogation. As a consequence of the abasic position, a “chemical pocket” in DGL/NA duplex is created. Then, the target nucleic acids acts as a template, driving a reversible and thermodynamically controlled chemical reaction between the free secondary amine located on the DGL probe and the aldehyde-modified nucleobases (Smart-NB), generating an iminium intermediate, which can be reduced to a stable tertiary amine (chemical “lock up”), covalently modifying the DGL probe. As a reversible and dynamic reaction, several iminium species will be generated (one for each nucleobase employed) [156]; however, according to Watson and Crick base

pairing rules and π-stacking of nucleobases, only the most thermodynamically stable product will be generated. Hence, the Smart-NB dynamic incorporation is highly specific and selective as it removes the false positives produced by mismatches [147],[148],[157]. The final step of the Chem-NAT technology consists of the detection of the Smart-NB specifically incorporated, which can be done by mass spectroscopy [147],[148],[158], by fluorescence [61],[122],[159]–[161], or by using a colorimetric-based assay [162]. Scheme 1 shows the Chem-NAT technology.

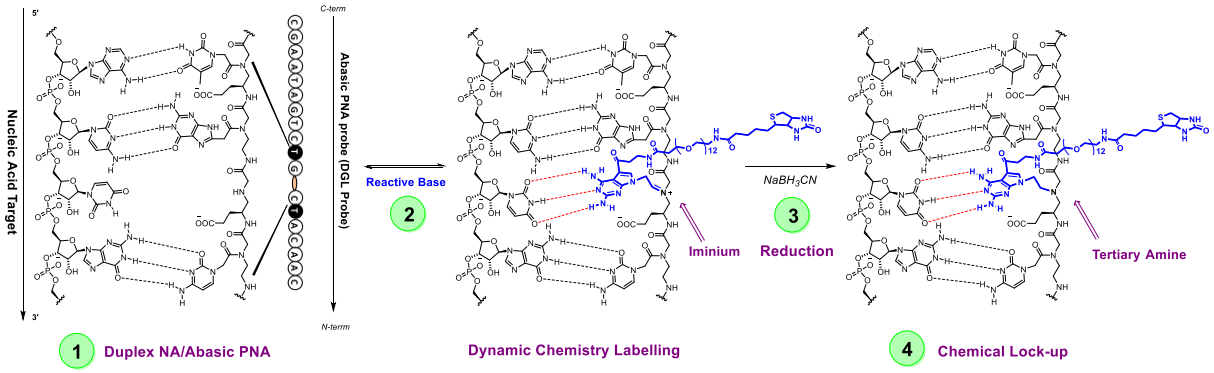

Scheme 1 General scheme of the Chem-NAT technology. Firstly, a DGL probe complementary to a target nucleic acid is designed and synthesised. **1)** The DGL probe and the complementary target nucleic acid hybridise to afford a duplex which forms a chemical pocket containing the DGL abasic position and the nucleotide located opposite to it. **2)** The complementary nucleic acid templates a reversible and thermodynamically controlled chemical reaction between the Smart-NBs and the free secondary amine of the chemical pocket. **3)** The generated iminium specie is reduced to a stable tertiary amine, covalently attaching the Smart-NB stabilised by the Watson and Crick base pairing rules and π-stacking of nucleobases to the DGL probe. **4)** Thus, the detection of the nucleotide located in front of the selectively incorporated Smart-NB is then allowed. (**To see in more detail go to Appendix 2**)

It is important to remark that several studies have shown good selectivity for the four nucleobases. Variations in base selectivity depend on the number of hydrogen bonds templating the incorporation reaction; G and C incorporate approximately five-fold more selectively than A and T. Within these subsets, purine bases are incorporated around two times more selectively than the pyrimidines (i.e. A > T, G > C); this is attributed to differences in π-stacking interactions [147],[148],[150]. Furthermore, the effect of the pH in the dynamic chemistry reaction has also been studied. The optimal pH for the iminium formation through a reductive amination reaction is around 6, which ensures a mildly acidic pH that allows not only the protonation of the aldehyde oxygen of the Smart-NB, but also to have the free secondary amine of the abasic position of the DGL probe to attack the carbonyl group in a nucleophilic attack, and then the protonation of the intermediate for water elimination [147].

Chem-NAT technology approaches to nucleic acid testing can be used for qualitative applications, determining the presence of a specific nucleic acid strand with single base resolutions and for quantitative applications, quantifying the number of molecules of a specific nucleic acid sequence. As an example of the former, the determination of single mutations, the so called SNPs, and of the later, the absolute quantification of miRNA molecules. Within qualitative applications, the Chem-NAT technology has been used to:

(i) genotype 12 cystic fibrosis patients, detecting one mutation, G551D, and one indel, ΔF508, associated to the disease, by mass spectroscopy [148];

(ii) rapidly identify and differentiate between *Trypanosoma cruzi*, *Trypanosoma brucei* and *Leishmania spp.* by mass spectroscopy through the analysis of their single nucleotide fingerprints (SNF) in a highly homologous region, combining 2 DGL probes and three Smart-NBs [158];

(iii) rapidly and easily discriminate *Leishmania major* and *Trypanosoma cruzi* by naked eye thanks to the development of a micro Spin-Tube device wherein is performed a colorimetric assay based on the discrimination of both parasite SNF markers [162].

Furthermore, Chem-NAT technology is being applied in the international consortium Liqbiopsens, whose aim is to develop a novel, reliable, affordable, and multiplexing platform for the detection of KRAS and BRAF mutations in colorectal cancer using blood liquid biopsy using acoustic sensors.

On the other hand, for quantitative applications, the Chem-NAT technology has been used to:

(i) quantify miR-122, a liver biomarker, through DCL, using the Luminex® bead-based detection platform [160];

(ii) quantify miR-122 from human serum of patients suffering from acetaminophen-derived acute induced liver injury by comprising the magnetic-beads Dynabeads® and DGL probes with the fluorescent detection platform developed by Quanterix Corporation, Simoa [61];

(iii) quantify the erythroid cell-specific miR-451a from human plasma without performing RNA extraction, by employing DGL probes attached to Dynabeads® and the conventional multi-mode microplate reader FLUOstar Omega [161];

(iv) develop a new detection platform (ODG platform) which combines Chem-NAT and a silicon photomultiplier (SiPM)-based reader for detection and quantification of circulating

miRNAs. The ODG platform was used to profile hsa-miR-21-5p from plasma of NSCLC patients [122].

During this Doctoral Thesis, the rapid detection and quantification of miR-21 directly from tumour cells without RNA extraction, by obtaining the cell lysate, through attaching DGL probes to the Dynabeads® and using fluorescence-based readout platforms, the FACS and the FLUOstar Omega, has been developed and it is described in chapter 1. Furthermore, this research has been published in Talanta journal [163].

2.2. Direct detection of miRNAs from biological samples through Dynamic Chemistry Labelling

2.2.1. miR-21 direct detection and quantification from tumour cells

2.2.1.1. Results

2.2.1.1.1. Optimisation of Magbeads-21 for direct detection of miR-21

Aiming to develop a novel assay for the direct detection and quantification of hsa-miR-21-5p of cell lines, DGL probes, which are PNA probes with an abasic position, complementary to miR-21 have been synthesised and chemically coupled to commercially available magnetic Dynabeads®. Then, Chem-NAT has been applied for the specific and covalently dynamic incorporation of Smart-Adenine through dynamic chemistry labelling (DCL). This is a thermodynamically controlled reaction templated by miR-21 strand, which is complementary hybridised to the DGL probes. Since Smart-Adenine is biotnylated, SAPE binds to the incorporated Smart-Adenine, releasing fluorescence, which is directly proportional to the amount of miR-21 presented in the samples.

In this process, three DGL probes of 17 mer complementary to the miR-21 sequence were designed and synthesised. The three DGL probes, **DGL-21-1.0**, **DGL-21-2.0**, and **DGL-21-3.0**, were designed to have their non-chiral abasic position located within the 9th and 10th position from the N terminus of their PNA sequence, and to be located in front of different nucleotides of the miR-21 sequence. Table 4 shows the DGL probes sequences, the synthetic miR-21 sequence used in the experiments (ssDNA-21) and in front of which nucleotides are the abasic positions located. According to what it is shown, **DGL-21-1.0** should incorporate a cytosine, whilst **DGL-21-2.0** and **DGL-21-3.0** should incorporate an adenine.

Table 4. ssDNA (5'→3') and DGL probes sequences (N→C). "_" (highlighted in yellow) represents the neutral abasic position. "Xglu" represents the chiral and negatively charged PNA monomers, containing a propanoic acid side chain at the gamma position. DGL probes have a miniPEG group (xx) and an amine group at their N-terminal, and a C-terminal primary amide. Highlighted in colour, the nucleotides of the ssDNA-21 sequence which are in front of the abasic positions of the DGL probes

ssDNA-21	TAG CTT ATC AGA CTG ATG TTG A		
DGL probes – Sequences – Magbeads – Bioconjugation Chemistry			
DGL-21-1.0	NH_2-xx-AAC ATCglu AGT _TG ATgluA AG-$CONH_2$	**Magbeads-21-1.0**	Amide
DGL-21-2.0	NH_2-xx-TCA ACA TgluC_ GTgluC TGA TA-$CONH_2$	**Magbeads-21.2.0**	Amide
DGL-21-3.0	NH_2-xx-ATC AGT CTgluG _TA AGCglu TA-$CONH_2$	**Magbeads-21-3.0**	Amide

These probes were aminopegylated at their N-terminal end that enabled their coupling to Dynabeads® M-270 Carboxylic acid through amide formation, to afford **Magbeads-21** (Figure 9). **DGL-21.1.0**, **DGL-21-2.0** and **DGL-21-3.0** were coupled to Dynabeads® to give rise to **Magbeads-21-1.0**, **Magbeads-21-2.0**, and **Magbeads-21-3.0**, respectively.

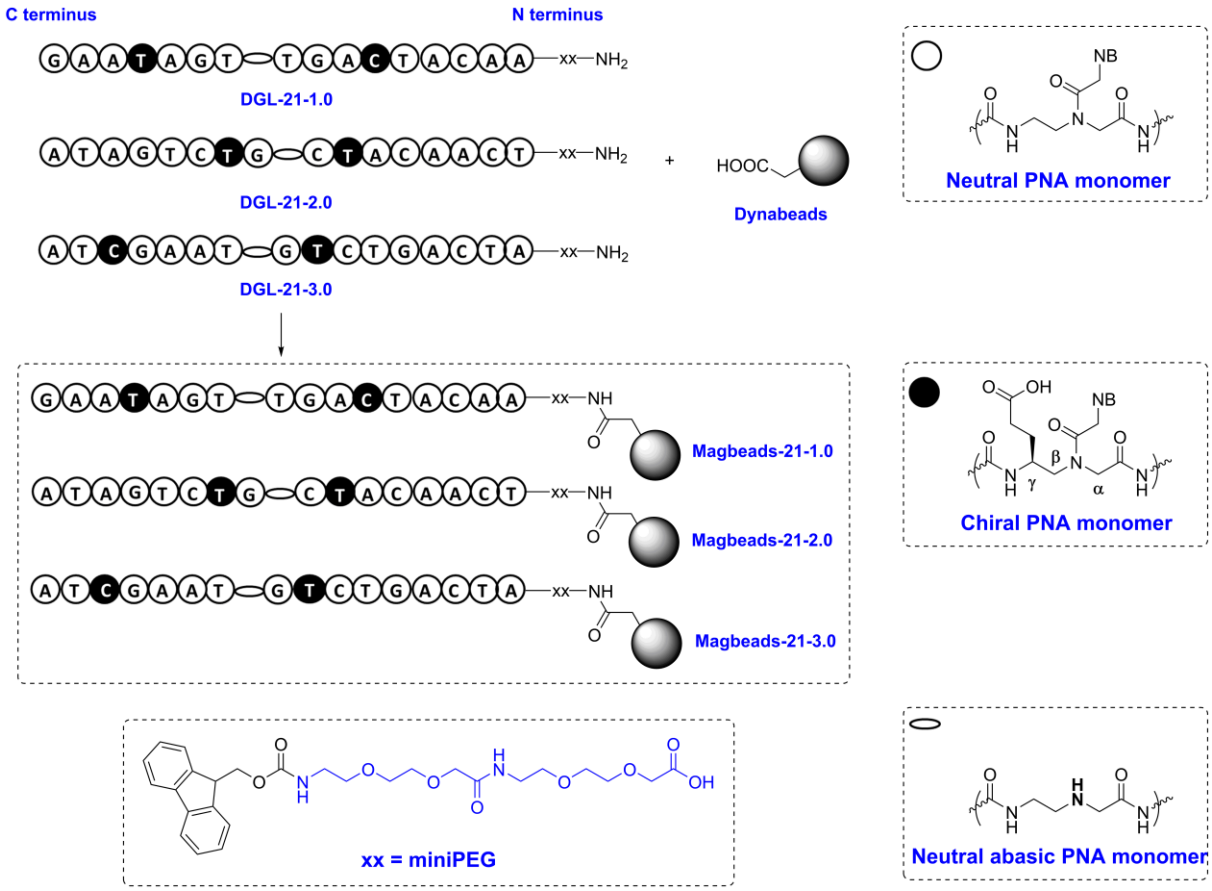

Figure 9. General scheme of **DGL-21-1.0**, **DGL-21-2.0**, and **DGL-21-3.0** coupling to Dynabeads® to afford **Magbeads-21-1.0**, **Magbeads-21-2.0**, and **Magbeads-21-3.0**.

DGL coupling to Dynabeads® was afforded by using a total of 2,100 pmol of oligonucleotides for 3 mg of Dynabeads®, being 2/3 of this 2,100 pmol for DGL probes and 1/3 for a small oligonucleotide, which enhanced the coupling efficiency. In order to measure whether DGL probes had been efficiently coupled to Dynabeads®, their concentration was determined before and after the chemical coupling by Nanodrop™ (λ= 260 nm). Absorbance analysis showed low efficiency coupling for **DGL-21-1.0** and **DGL-21-2.0**, and better for **DGL-21-3.0** (Table 5).

Table 5. Coupling efficiency of **DGL-21-1.0**, **DGL-21-2.0**, and **DGL-21-3.0** probes to Dynabeads® in order to afford **Magbeads-21-1.0**, **Magbeads-21-2.0**, and **Magbeads-21-3.0**. Loading of **Magbeads-21** was calculated taking into account the amount of DGL loaded in **Magbeads-21** and the amount of beads employed (3 mg).

Magbeads	DGL Employed	DGL Coupled	Efficiency	Loading
Magbeads-21-1.0	1,400 pmol	144.9 pmol	10.4%	48.3 pmol/mg
Magbeads-21-2.0	1,400 pmol	110.9 pmol	7.9%	47.0 pmol/mg
Magbeads-21-3.0	1,400 pmol	645.2 pmol	46.1%	215.1 pmol/mg

Nonetheless, to assess whether the DGL probes coupled to the Dynabeads® were able to hybridise complementary nucleic acid sequences, the three **Magbeads-21** types were mixed with ssDNA-21-Cy5 for 1 h at 41 ºC. Besides, **Magbeads-21** were also incubated with G2pr1-C-Cy5, a non-complementary sequence, and only with water, as negative controls. The hybridisation was measured by FACS, analysing the Cy5 fluorescence obtained in the APC channel (filter 660/20 nm), showing that the hybridisation did not take place (Figure 10).

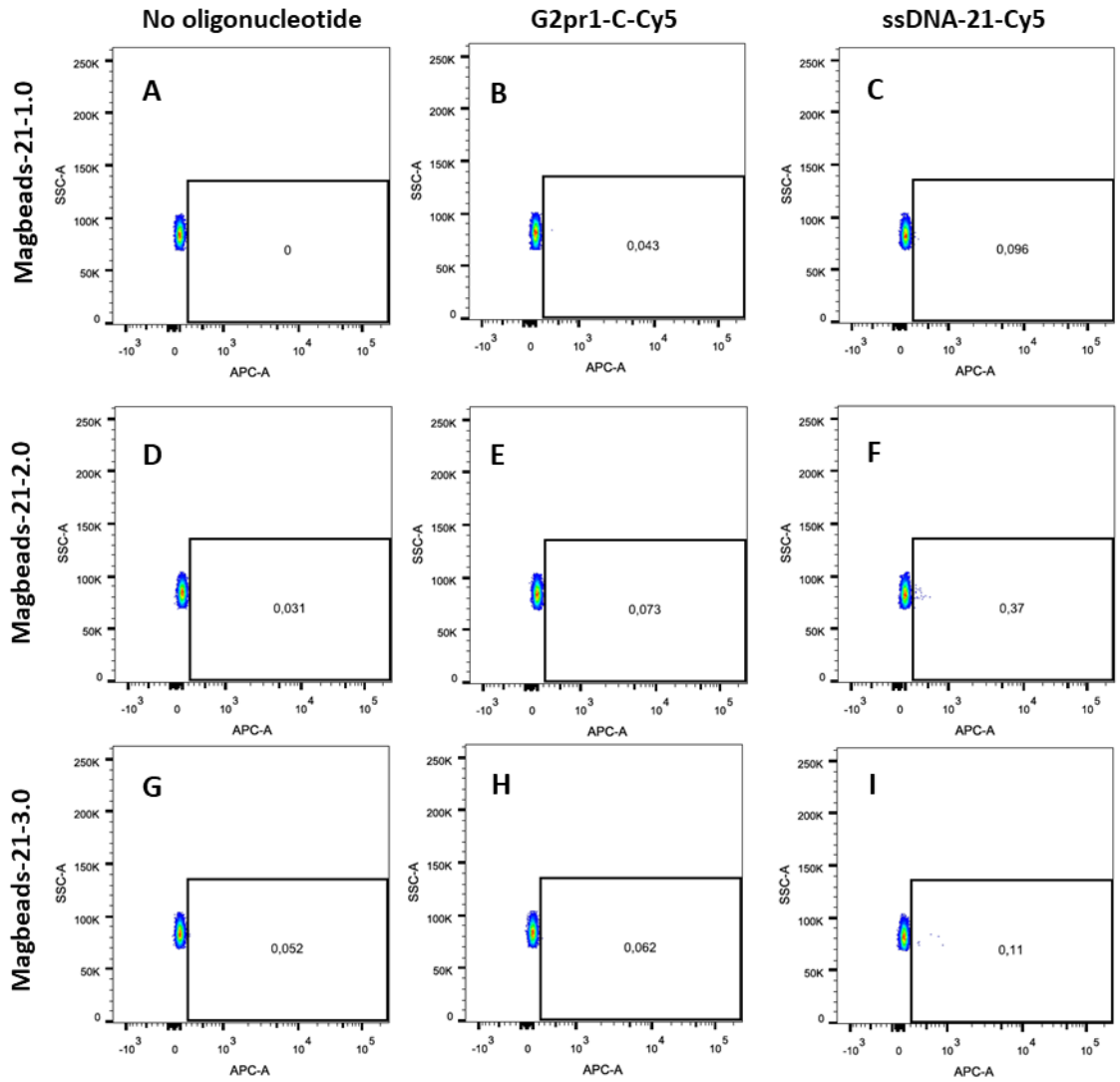

Figure 10. FACS dot plots for the **Mabeads-21-1.0 (A-C)**, **Magbeads-21-2.0 (D-F)**, and **Magbeads-21-3.0 (G-I)** fluorescence in the APC channel.

Another round of DGL probes were coupled to the Dynabeads® to afford new **Magbeads-21**. As it was previously done, the DGL probes absorbance at 260 nm before and after the coupling was measured, obtaining a considerable decrease between the two measurements for **DGL-21-1.0**, **DGL-21-2.0**, and **DGL-21-3.0** (Table 6).

Table 6. Coupling efficiency of **DGL-21-1.0**, **DGL-21-2.0**, and **DGL-21-3.0** probes to Dynabeads® in order to afford **Magbeads-21-1.0**, **Magbeads-21-2.0**, and **Magbeads-21-3.0**. Loading of **Magbeads-21** was calculated taking into account the amount of DGL loaded in **Magbeads-21** and the amount of beads employed (3 mg).

Magbeads	DGL Employed	DGL Coupled	Efficiency	Loading
Magbeads-21-1.0	1,400 pmol	730.2 pmol	52.2%	243.4 pmol/mg
Magbeads-21-2.0	1,400 pmol	794.8 pmol	56.8%	264.9 pmol/mg
Magbeads-21-3.0	1,400 pmol	1,003.6 pmol	71.7%	334.5 pmol/mg

Again, ssDNA-21-Cy5 was used to assess the **Magbeads-21** hybridisation. As control, there were also used G2pr1-C-Cy5 and only water. Thus, the three types of **Magbeads-21** (**Magbeads-21-1.0**, **Magbeads-21-2.0**, and **Magbeads-21-3.0**) were mixed, in different reaction tubes, with ssDNA-21-Cy5, with G2pr1-C-Cy5, and with water, being incubated in two different ways:

1) 41 ºC for 1 h.

2) 94 ºC for 5 min and then 41ºC for 1 h.

FACS analysis did not show fluorescence for neither both incubation methods for any of the **Magbeads-21**.

Following the negative hybridisation results, specific Smart-NB incorporation into the blank position of the DGL probe attached to the **Magbeads-21**, when the complementary target (ssDNA-21) was present, was assessed. For that, **Smart-2dA-Biotin** and **Smart-C-Cy5** were used (Figure 11).

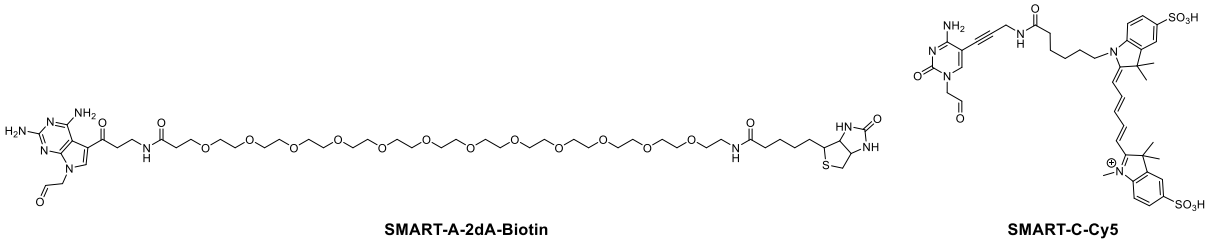

Figure 11. Smart-2dA-Biotin and **Smart-C-Cy5** chemical structures.

Therefore, as Smart-NB, for **Magbeads-21.1.0** containing the blank position in front a guanine, **Smart-C-Cy5** was used, whilst for **Magbeads-21** functionalised with **DGL-21-2.0** (**Magbeads-21.2.0**) and **DGL-21-3.0** (**Magbeads-21.3.0**), as it was located in front a

thymine, **Smart-2dA-Biotin** was used. The **Smart-2dA-Biotin** was then labelled via biotin-streptavidin recognition using SAPE. The fluorescence was measured by FACS, using the PE-channel (filter 585/42 nm) for **Smart-2dA-Biotin**-SAPE, and the APC channel for **Smart-C-Cy5** (Figure 12).

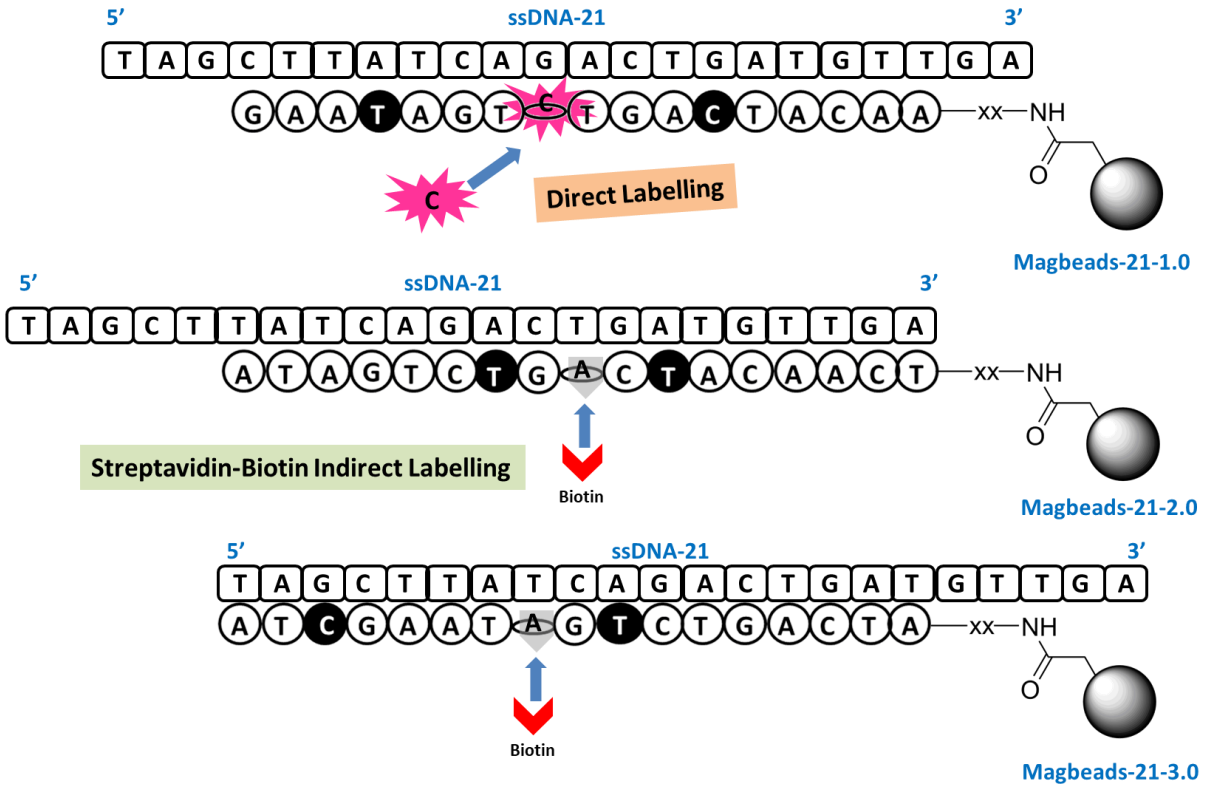

Figure 12. Scheme representing the direct and indirect fluorescence signal generation. **Smart-Cy5** is directly attached to the fluorophores whilst **Smart-2dA-Biotin** undergoes an indirect fluorescent labelling with SAPE via biotin-streptavidin recognition.

Thus, all **Magbeads-21** were mixed with ssDNA-miR-21, reducing agent $NaBH_3CN$, and their specific Smart-NB, **Smart-C-Cy5** for **Magbeads-21-1.0** and **Smart-2dA-Biotin** for **Magbeads-21-2.0** and **Magbeads-21-3.0**, in Buffer A pH 6 in individual tubes. As negative controls, **Magbeads-21** were mixed, separately, with the Smart-NB and the reducing agent, but adding water instead of the complementary target. The mixtures were then incubated at 41 ºC for 1 h, and after that, those samples containing **Magbeads-21-2.0** and **Magbeads-21-3.0**, including the controls, were incubated with SAPE. The resulting fluorescence in the APC and PE channels were analysed by FACS, showing barely fluorescent signals, although slightly higher for **Magbeads-21** functionalised with **DGL-21-2.0** and **DGL-21-3.0** (Figure 13).

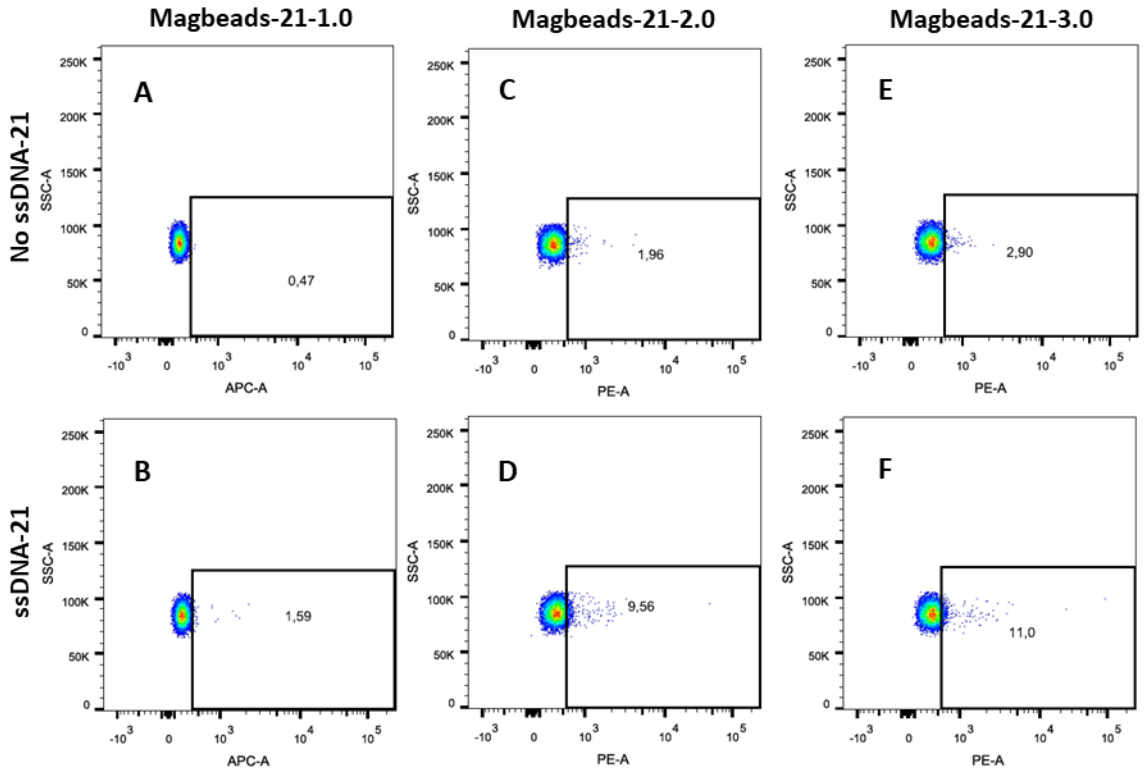

Figure 13. FACS dot plots in APC channel for the **Magbeads-21-1.0** incubated with **Smart-C-Cy5** without complementary target ssDNA-21 **(A)** and with it **(B)**; PE channel for the **Magbeads-21-2.0** incubated with **Smart-2dA-Biotin**+SAPE without ssDNA-21 **(C)** and with it **(D)**; and PE channel for the **Magbeads-21-3.0** incubated with **Smart-2dA-Biotin**+SAPE without ssDNA-21 **(E)** and with it **(F)**.

Bearing in mind all the negative results obtained with this set of DGL probes, they were tested in DestiNA Genomica SL using membranes and a colorimetric assay [162]. The membranes were spotted with avidin (two spots) as positive control, in the upper part of the membrane, with **DGL-21-1.0** in the left part, with **DGL-21-2.0** in the right part, and with **DGL-21-3.0** in the lower part. Then, **Smart-C-Biotin** (membrane 1) or **Smart-2dA-Biotin** (membrane 2) alongside ssDNA-21 and reducing agent were added to assess the specific dynamic incorporation performance. ssDNA-21-Biotin (membrane 3) was also added to check the hybridisation. Finally, a colourless streptavidin-alkaline phosphatase substrate was added, which resulted in a blue precipitate in the presence of biotin. The expected results were:

(i) **DGL-21-1.0** spot in blue in membrane 1.

(ii) **DGL-21-2.0** and **DGL-21-3.0** spots in membrane 2.

(iii) All the spots in membrane 3.

Thus, membrane assays confirmed that these set of DGL probes hardly incorporate the Smart-NB and hybridise with the complementary target either (Figure 14).

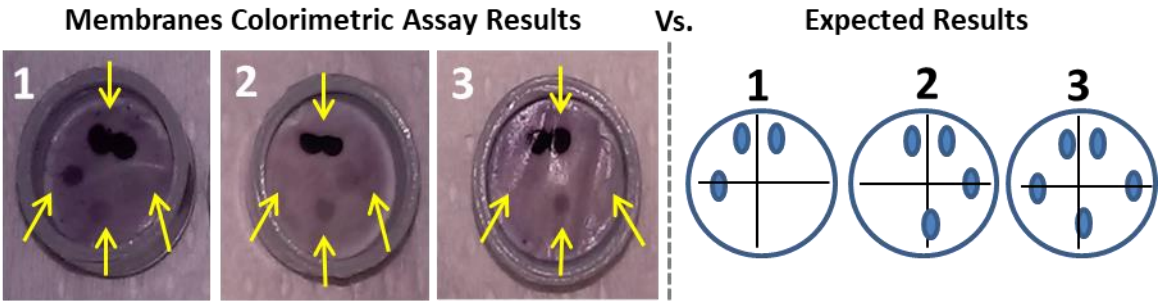

Figure 14. At the left, pictures of the membranes and at the right, schemes depicting the expected results. The yellow arrows point where are located the spots in the membranes. **1)** ssDNA-21 and **Smart-C-Biotin** were added. **2)** ssDNA-21 and **Smart-2dA-Biotin** were added. **3)** ssDNA-21-Biotin was added.

Since the first round of DGL probes did not work, two new DGL probes of 19 mer of length modified at their N-terminal with a cysteine were designed. Therefore, the new DGL probes were designed to be coupled, in this case, to Dynabeads® M-270 Amine through thiol-maleimide chemical reaction prior activation of the Dynabeads® (Figure 15). Moreover, the new DGL probes, **DGL-21-4.1** and **DGL-21-5.1**, also differed from the previous probes in that they contained a chiral blank position.

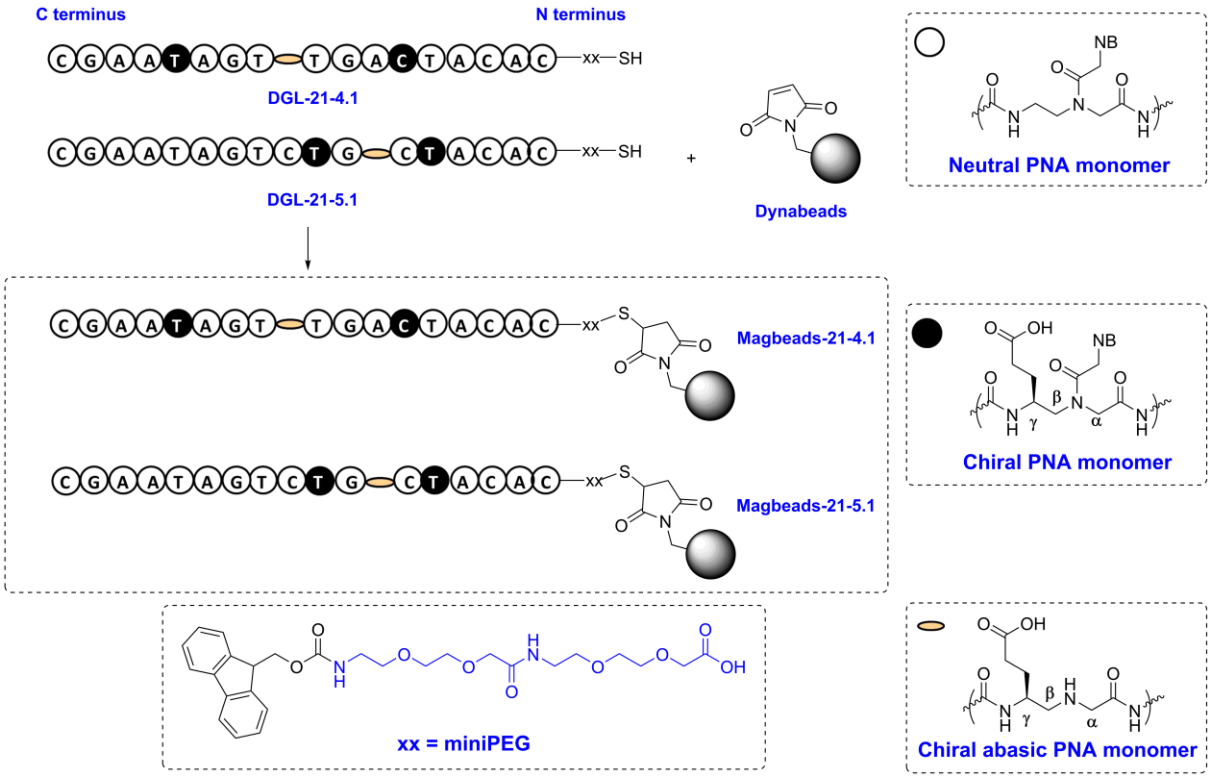

Figure 15. General scheme of **DGL-21-4.1**, and **DGL-21-5.1** coupling to Dynabeads® to afford **Magbeads-21-4.1**, and **Magbeads-21-5.1**.

Besides, the difference between **DGL-21-4.1** and **DGL-21-5.1** lied on the location of the chiral blank position, which was in the 10th and in the 7th position of the probe from the N terminus, respectively (Table 7). As a consequence, the blank position of **DGL-21-4.1** was in front of a guanine, incorporating Smart-C, while that the blank position of **DGL-21-5.1** was located in front of a thymine, incorporating Smart-A.

Table 7. ssDNA (5'→3') and DGL probes sequences (N→C). *GL* (highlighted in yellow) represents the chiral abasic position containing a propanoic acid side chain at gamma position. "Xglu" represents the chiral and negatively charged PNA monomers, containing a propanoic acid side chain at the gamma position. DGL probes have a miniPEG group (xx) and a cysteine (Cys) in their N-terminal, and a C-terminal primary amide. Highlighted in colour, the nucleotides of the ssDNA-21 sequence which are in front of the abasic positions of the DGL probes. In **red** and in **purple**, the mutated nucleobases compared with the ssDNA-miR-21 sequence.

ssDNA-21	TAG CTT ATC AGA CTG ATG TTG A		
ssDNA-miR-21-1T	TAG CTT ATC ATA CTG ATG TTG A		
ssDNA-miR-21-2G	TAG CTT ATC AGA CGG ATG TTG A		
DGL probe – Sequences – Magbeads – Bioconjugation Chemistry			
DGL-21-4.1	Cys-xx-CAC ATCglu AGT *GL*TG ATgluA AGC-$CONH_2$	**Magbeads-21-4.1**	Thioether
DGL-21-5.1	Cys-xx-CAC ATgluC *GL*GTglu CTG ATA AGC-$CONH_2$	**Magbeads-21.5.1**	Thioether

Once that it was assessed that the DGL probes had been coupled to the beads, the specific dynamic incorporation of the Smart-NBs with these two DGL probes was evaluated. For that, the **Magbeads-21-4.1** were mixed with ssDNA-21, **Smart-C-Cy5**, and the reducing agent in Buffer A, whilst the **Magbeads-21-5.1** were mixed with ssDNA-21, **Smart-2dA-Biotin**, and the reducing agent in Buffer A. Besides, as specificity controls, instead of ssDNA-21, two oligonucleotides similar to ssDNA-21 but with a mutation in the nucleobase located in front of the abasic position of the DGL probes were used (Table 7). The mixtures were then incubated for 1 h at 41 ºC. **Magbeads-21-5.1** which were incubated with **Smart-2dA-Biotin** were, following washing steps assisted by a magnet, incubated with SAPE for 1 h, at 25 ºC, for the indirect fluorescent labelling of the Smart-NB. All the samples were finally analysed by FACS, using as negative control **Magbeads-21** that did not undergo any chemical reaction.

FACS analysis showed that in **Magbeads-21-4.1** loaded with both with 175 and 350 pmol of DGL/mg of beads, ssDNA-21 templated the **Smart-C-Cy5** incorporation, as the **Magbeads-21-4.1** populations moved to the APC channel compared with the negative control (Figure 16-A-B). Nevertheless, the **Magbeads-21-4.1** containing double amount of DGL probe did not present more fluorescence, being both APC signals practically the same, as it can be observed in the histogram (Figure 16-E). Remarkably, **Magbeads-21-4.1** also

showed fluorescence in the APC channel when the oligonucleotide – ssDNA-21-1**T** – containing a wrong nucleobase (**T**) in front of the blank position was used (Figure 16-C-D). Moreover, these unexpected APC signals were the same for **Magbeads-21-4.1** containing 175 pmol of DGL/mg of bead and for **Magbeads-21-4.1** containing 350 pmol of DGL/mg of bead (Figure 16-F).

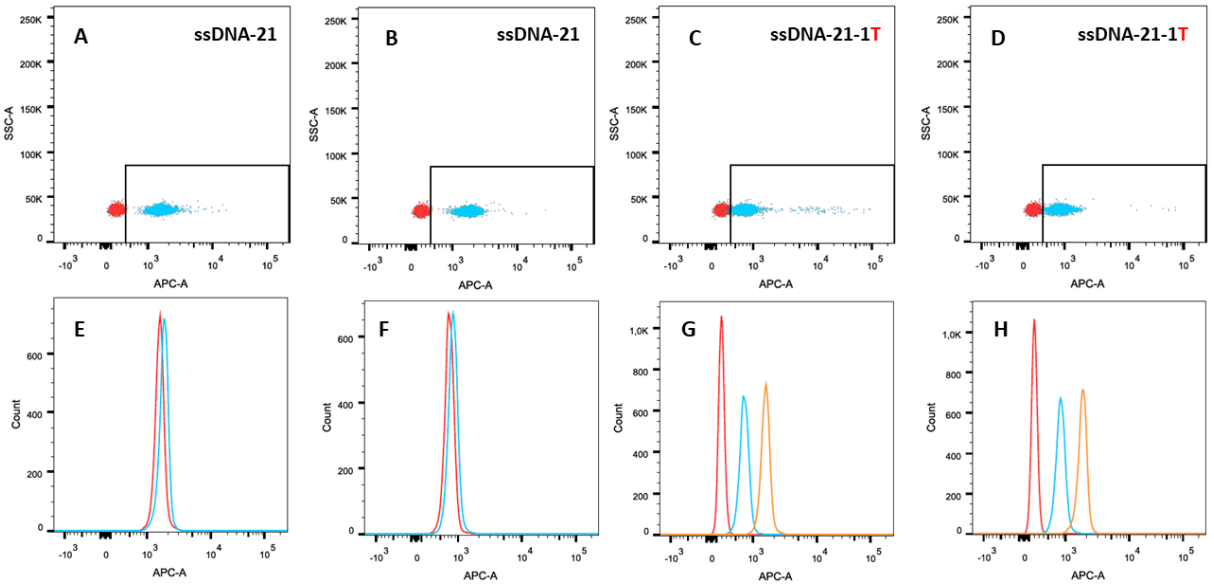

Figure 16. In plots **A** to **D**, in red, **Magbeads-21-4.1** that did not undergo any chemical reaction, used as control; in blue, the **Magbeads-21-4.1** incubated with Smart-C-Cy5 and oligonucleotides. **A)** In blue, the **Magbeads-21-4.1** loaded with 175 pmol of DGL/mg of beads incubated with ssDNA-21. **B)** In blue, the **Magbeads-21-4.1** loaded with 350 pmol of DGL/mg of beads incubated with ssDNA-21. **C)** In blue, the **Magbeads-21-4.1** loaded with 175 pmol of DGL/mg of beads incubated with ssDNA-21-1T. **D)** In blue, the **Magbeads-21-4.1** loaded with 350 pmol of DGL/mg of beads incubated with ssDNA-21-1T. **E-F)** Histogram of the APC channel for **Magbeads-21-4.1** loaded with 175 pmol (in red) and 350 pmol (in blue) of DGL/mg of beads when incubated with ssDNA-21 **(E)** or ssDNA-21-1T **(F)**. **G)** Histogram of the APC channel for **Magbeads-21-4.1** control (in red) and for **Magbeads-21-4.1** loaded with 175 pmol of DGL/mg of beads incubated with ssDNA-21-1T (in blue) or ssDNA-21 (in orange). **H)** Histogram of the APC channel for **Magbeads-21-4.1** control (in red) and for **Magbeads-21-4.1** loaded with 350 pmol of DGL/mg of beads incubated with ssDNA-21-1T (in blue) or ssDNA-21 (in orange).

Likewise, in **Magbeads-21-5.1** coupled with both 175 and 350 pmol of DGL21-5.1/mg of beads, there was, as expected, **Smart-2dA-Biotin** incorporation, being the **Magbeads-21-5.1** population clearly located in the PE-channel (Figure 17-A-B). Likewise, **Magbeads-21-5.1** populations were also located into the PE-channel when they were incubated with the oligonucleotide ssDNA-21-2**G**, containing a wrong nucleobase (**G**) in front of the blank position (Figure 17-C-D). Although **Magbeads-21-5.1** containing 350 pmol of DGL/mg of

beads and **Magbeads-21-5.1** containing 175 pmol of DGL/mg of beads showed almost the same PE fluorescence when they were incubated with ssDNA-miR-21, it was noteworthy that having more DGL probes in the **Magbeads** also produced more PE signal when incubated with the wrong oligonucleotide ssDNA-21-2**G** (Figure 17-E-F).

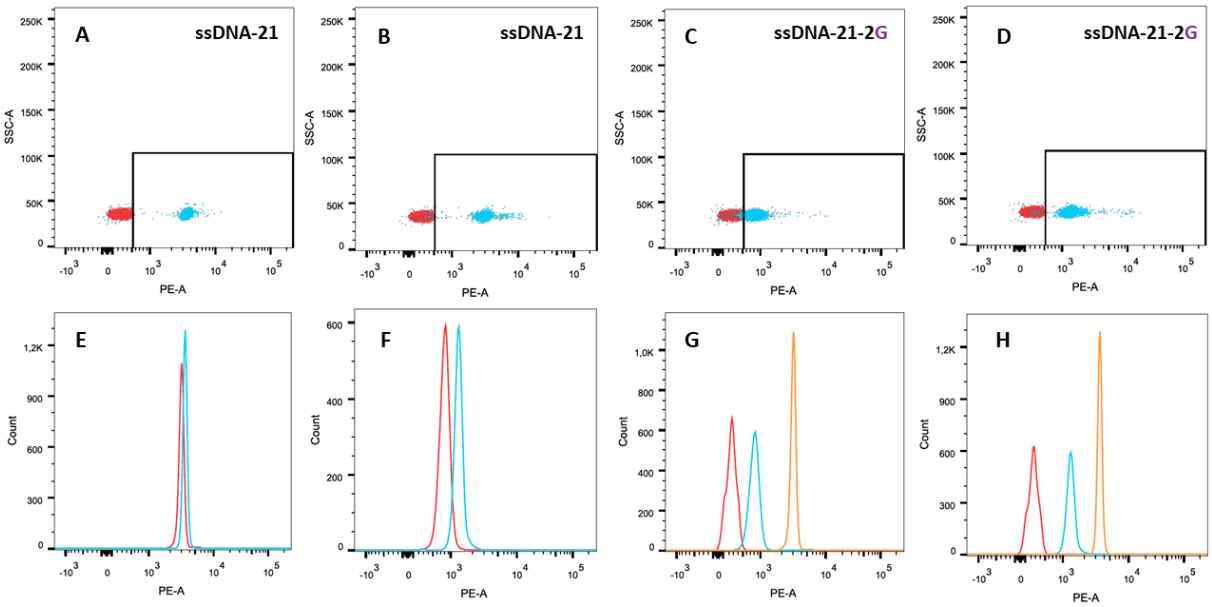

Figure 17. In plots **A** to **D**, in red, **Magbeads-21-5.1** that did not undergo any chemical reaction, used as control; in blue, the **Magbeads-21-5.1** incubated with Smart-2dA-Biotin+SAPE and oligonucleotides. **A)** In blue, the **Magbeads-21-5.1** loaded with 175 pmol of DGL/mg of beads incubated with ssDNA-21. **B)** In blue, the **Magbeads-21-5.1** loaded with 350 pmol of DGL/mg of beads incubated with ssDNA-21. **C)** In blue, the **Magbeads-21-5.1** loaded with 175 pmol of DGL/mg of beads incubated with ssDNA-21-2G. **D)** In blue, the **Magbeads-21-5.1** loaded with 350 pmol of DGL/mg of beads incubated with ssDNA-21-2G. **E-F)** Histogram of the PE channel for **Magbeads-21-5.1** loaded with 175 pmol (in red) and 350 pmol (in blue) of DGL/mg of beads when incubated with ssDNA-21 **(E)** or ssDNA-21-2G **(F). G)** Histogram of the PE channel for **Magbeads-21-5.1** control (in red) and for **Magbeads-21-5.1** loaded with 175 pmol of DGL/mg of beads incubated with ssDNA-21-2G (in blue) or ssDNA-21 (in orange). **H)** Histogram of the PE channel for **Magbeads-21-5.1** control (in red) and for **Magbeads-21-5.1** loaded with 350 pmol of DGL/mg of beads incubated with ssDNA-21-2G (in blue) or ssDNA-21 (in orange).

Regarding these results, it was decided to work with and to optimise the **Magbeads-21-5.1** rather than the **Magbeads-21-4.1**.

Firstly, whether a lower concentration of **Smart-2dA-Biotin** could help to decrease the background signal was hypothesised. Thus, to provide insights about the influence of the Smart-NB concentration, **Magbeads-21-5.1** containing 175 and 350 pmol of DGL/mg of beads were mixed with ssDNA-21, reducing agent, and **Smart-2dA-Biotin** at different concentrations, 30 µM, 15 µM, and 5 µM, in buffer A, and the mixtures were incubated for 1 h

at 41 ºC. In parallel, it was done the same experiment but using ssDNA-21-2**G** as control. After that, all the **Magbeads-21-5.1** were incubated with SAPE, measuring the PE fluorescence by FACS.

Table 8 shows mean fluorescence intensity (MFI) of PE channel obtained for all conditions studied and analysed by FACS. It is observed that despite decreasing the amount of **Smart-2dA-Biotin**, non-specific fluorescence signal with ssDNA-21-2**G** were still produced; nevertheless, these signals were less intense when lower concentrations of **Smart-2dA-Biotin** were used. Besides, non-specific fluorescent signals were higher for **Magbeads-21-5.1** containing 350 pmol of DGL/mg of beads than for those containing 175 pmol of DGL/mg of beads incubated with 30 µM and 15 µM of **Smart-2dA-Biotin**. Higher concentrations of **Smart-2dA-Biotin** were related to higher MFI values when ssDNA-21 was used. Remarkably, for **Magbeads-21-5.1** containing 350 pmol of DGL/mg of beads it was obtained that 30 µM and 15 µM of **Smart-2dA-Biotin** gave almost the same fluorescent intensity in the PE channel, and that they were much more intense than that for 5 µM. Moreover, comparing these values in **Magbeads-21-5.1** containing 175 or 350 pmol of DGL/mg of beads, it was observed that in the case of 30 µM of **Smart-2dA-Biotin** there were barely differences between both signals, suggesting SAPE saturation. Curiously, **Magbeads-21-5.1** labelled with 175 pmol of DGL/mg of beads incubated with 5 µM of **Smart-2dA-Biotin** exhibited higher MFI values than **Magbeads-21-5.1** labelled with 350 pmol of DGL/mg of beads.

Table 8. MFI values of PE channel in FACS obtained for the different conditions of **Smart-2dA-Biotin** concentration, both types of **Magbeads-21-5.1**, and both ssDNA-21 and ssDNA-21-2G.

	Magbeads-21-5.1 – 175 pmol		**Magbeads-21-5.1 – 350 pmol**	
Smart-2dA-Biotin	**ssDNA-21**	**ssDNA-21-2G**	**ssDNA-21**	**ssDNA-21-2G**
0 µM	276		280	
5 µM	1,214	431	902	512
15 µM	2,068	615	3,213	1,058
30 µM	3,279	904	3,681	1,474

After all these experiments, it was found out that the DGL probes 21-4.1 and 21-5.1 were incorrectly synthesised, missing a PNA monomer in the sequence, being 18 mer in length instead of the 19 mer designed DGL probes. As a consequence, a new DGL probe of 19 mer, **DGL-21-6.0**, similar to the DGL probe 21-5.1 but including the missing PNA monomer, was synthesised (Figure 18).

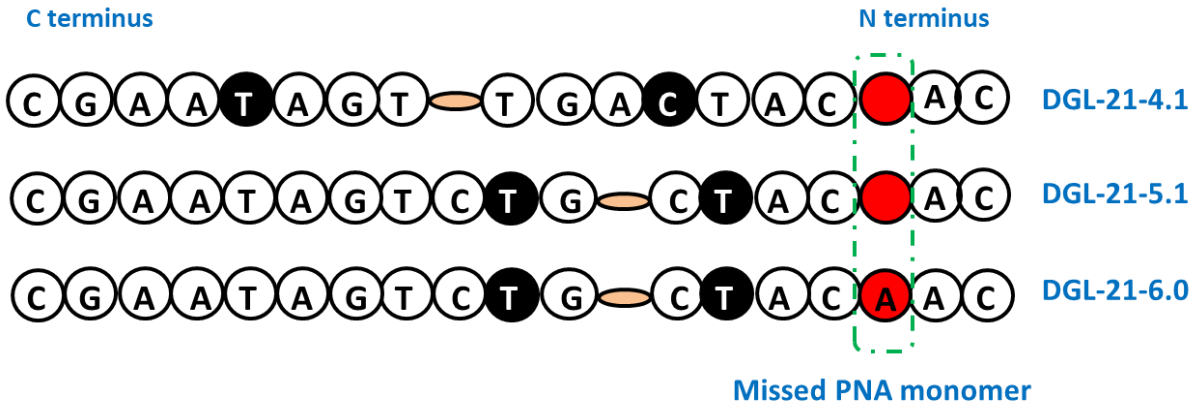

Figure 18. In red circule, the missed PNA monomer in the **DGL-21-4.1** and **DGL-21-5.1** sequences and incorporated into **DGL-21-6.0** sequence.

The new DGL probe contained the chiral blank position in the 8th position from the N terminus, which was located in front of an uracil in the miR-21 sequence (thymine in the synthetic ssDNA-21 sequence), also incorporating **Smart-2dA-Biotin** (Table 9). The DGL probe **DGL-21-6.0** was synthesised with an amine group instead of a thiol group in its N terminal, to enable labelling to Dynabeads® M-270 Carbolxylic acid via amide bond formation (Figure 19).

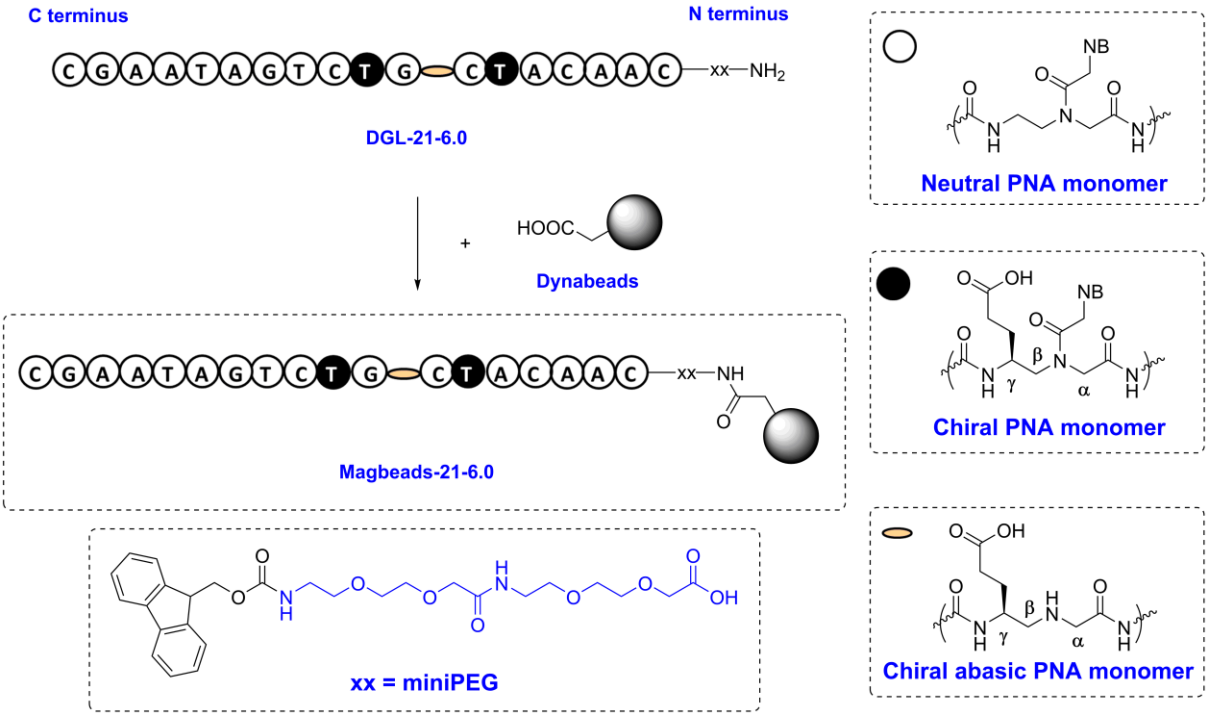

Figure 19. General scheme of **DGL-21-6.0** coupling to Dynabeads® to afford **Magbeads-21-6.0**.

Table 9. miR-21 and ssDNA (5'→3') and DGL probes sequences (N→C). *GL* (highlighted in green) represents the chiral abasic position containing a propanoic acid side chain at gamma position. "Xglu" represents the chiral and negatively charged PNA monomers, containing a propanoic acid side chain at the gamma position. DGL probes have a miniPEG group (xx) and amine in their N-terminal, and a C-terminal primary amide. Highlighted in colour, the nucleotides of the ssDNA-21 sequence which are in front of the abasic positions of the DGL probes. In **purple**, the mutated nucleobases compared with the ssDNA-miR-21 sequence.

miR-21	UAG CUU AUC AGA CUG AUG UUG A		
ssDNA-miR-21	TAG CTT ATC AGA CTG ATG TTG A		
ssDNA-miR-21-2G	TAG CTT ATC AGA CGG ATG TTG A		
DGL probe – Sequences – Magbeads – Bioconjugation Chemistry			
DGL-21-6.0	NH_2-xx-CAA CATglu C*GL*G TgluCT GAT AAG C-$CONH_2$	**Magbeads-21-6.0**	Amide

In order to determine whether the coupling of the **DGL-21-6.0** probe to the Dynabeads® had taken place, the DGL probe absorbance at 260 nm was measured before and after the chemical coupling by Nanodrop™ (Table 10).

Table 10. Coupling efficiency of **DGL-21-6.0** probe to Dynabeads® in order to afford **Magbeads-21-6.0**. Loading of **Magbeads-21-6.0** was calculated taking into account the amount of DGL loaded in **Magbeads-21-6.0** and the amount of beads employed (3 mg).

Magbeads	DGL Employed	DGL Coupled	Efficiency	Loading
Magbeads-21-6.0	1,400 pmol	938.4 pmol	67.0%	312.8 pmol/mg

Subsequently, the specific Smart-NB dynamic incorporation into the new **Magbeads-21-6.0** was assessed by FACS, as it was done before. For that, **Magbeads-21-6.0** were mixed with ssDNA-21, 5 µM **Smart-2dA-Biotin** and reducing agent in Buffer A, incubating the suspension for 1 h at 41 ºC. Afterwards, following washing steps assisted by a magnet, **Magbeads-21-6.0** were incubated with SAPE and the fluorescence was analysed by FACS. In parallel, **Magbeads-21-6.0** were mixed with ssDNA-21-2**G**, 5 µM **Smart-2dA-Biotin**, and reducing agent in Buffer A, following the same steps than before.

FACS analysis showed that **Magbeads-21-6.0** incubated with ssDNA-21-2**G** possessed negligible PE fluorescence, being the same than that of the **Magbeads-21-6.0** that did not undergo any chemical reaction. On the other hand, **Magbeads-21-6.0** incubated with ssDNA-21 were found to be PE fluorescence positive, as it could be observed in Figure 20.

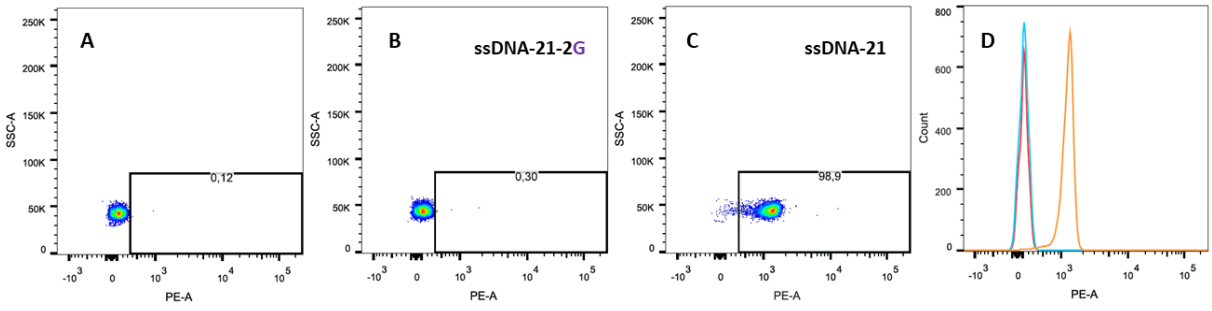

Figure 20. A) PE channel plot for **Magbeads-21-6.0** that did not undergo any chemical reaction. **B)** PE channel plot for **Magbeads-21-6.0** incubated with **Smart-2dA-Biotin** and ssDNA-21-2**G**. **C)** PE channel plot for **Magbeads-21-6.0** incubated with **Smart-2dA-Biotin** and ssDNA-21. D) In red, the **Magbeads-21-6.0** control; in blue, the **Magbeads-21-6.0** incubated with ssDNA-21-2G; and in orange, the **Magbeads-21-6.0** incubated with ssDNA-21.

According to the good results obtained for the new **DGL-21-6.0** probe, it was decided to use it for the direct detection and quantification of miR-21 from real biological samples.

To achieve this goal, firstly experiments to determine the best conditions for FACS with the **Magbeads-21-6.0** were performed. For this, 5 different concentrations of synthetic miR-21 (ssDNA-21) (15 nM, 1.5 nM, 0.15 nM, 0.015 nM, and 0 nM), obtained by serial dilutions from a stock solution, were employed. The higher concentration, 15 nM represents the concentration of ssDNA-21 generally used in these experiments. Then, the set of concentrations of synthetic miR-21 solutions were added to a mixture containing Buffer A, 5 µM **Smart-2dA-Biotin**, $NaBH_3CN$, and 2 x 10^6 **Magbeads-21-6.0**. Thus, dynamic incorporation reactions and labelling with SAPE conjugate were performed. Since PE fluorescence is directly related to the amount of complementary target, a decrease in MFI values of PE channel was expected at lower ssDNA-21 concentrations. Table 11 shows that, effectively, lower ssDNA-21 concentrations conducted to lower MFI values.

Table 11. MFI values of PE channel for increasing concentrations of ssDNA-21 using 5 µM of **Smart-dA-Biotin**. Signal-to-noise ratio was also calculated.

Smart-2dA-Biotin	ssDNA-21	MFI – PE	CV (%)	Signal-to-noise ratio
5 µM	0 nM	617	8	-
5 µM	0.015 nM	891	4	1.44
5 µM	0.15 nM	994	5	1.61
5 µM	1.5 nM	2,551	3	4.13
5 µM	15 nM	5,167	3	8.37

MFI values of PE channel suggested that the LoD of the platform for this batch of **Magbeads-21-6.0** should be a concentration of ssDNA-21 between 1.5 and 0.15 nM, since a MFI value of 413 with a signal-to-noise ratio of 1.3 is not high enough.

Moreover, taking into account that the amount of collected fluorescence is directly proportional to the amount of SAPE bound to the **Smart-2dA-Biotin**, the correlation between the amount of synthetic miR-21 presented in the samples and the fluorescence collected, by representing the data as a calibration line, could be established (Figure 21). This calibration line allowed calculating the minimum concentration of synthetic miR-21 that was possible to be detected in FACS with this batch of **Magbeads-21-6.0**. Thus, the limit of detection (LoD) was calculated as three times the standard deviation (SD) at 15% of coefficient of variation

(CV): BG+3SD's @15% CV. The LoD value was calculated to be 895 units of fluorescence. Thus, applying the line equation, the LoD for synthetic miR-21 with this batch of **Magbeads-21-6.0**, in FACS, using these conditions, was calculated to be 78.2 pM.

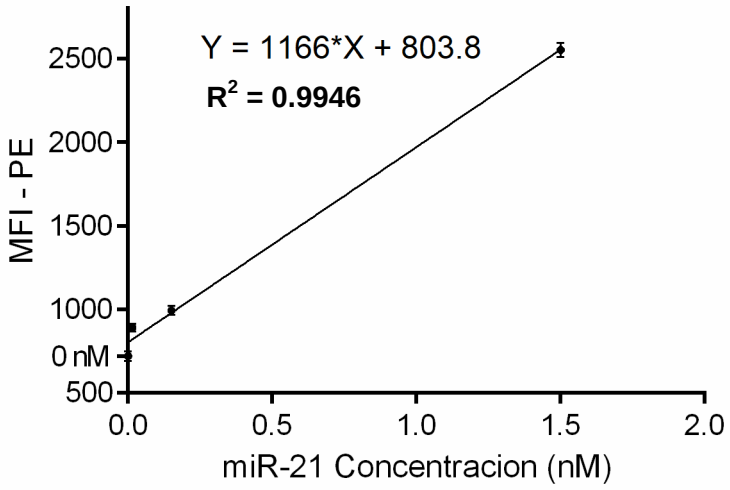

Figure 21. Calibration line for the LoD for synthetic miR-21 in FACS using 2 x 10^6 **Magbeads-21-6.0** and 5 µM **Smart-2dA-Biotin** (n=3)

2.2.1.1.2. Direct detection and quantificaton of miR-21 from cell lysates by Chem-NAT

After all these experiments using synthetic miR-21, translating the platform for the detection of miR-21 directly from biological samples was thought. Figure 22 depicts the magnetic and bead-based platform for the direct detection of miR-21 from cells through DCL [163]. For that, experiments for its optimisation were performed in close collaboration with DestiNA Genomica S.L., which resulted in a decrease of the number of **Magbeads-21-6.0** to 250,000.

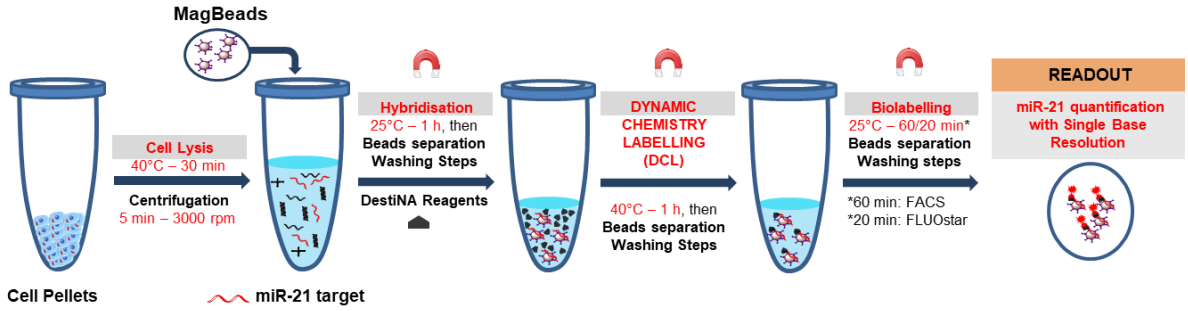

Figure 22. Direct detection of miR-21 from tumour cells using dynamic chemistry (Chem-NAT). **1)** Lysis of the cell pellets; **2)** Magnetic beads (**Magbeads-21**) functionalised with abasic PNA probes (DGL probes) are added to the supernatant and a hybridisation step takes place; then, washing are performed; **3)** biotinylated Smart-NB and reducing agent are added for the dynamic incorporation step; and washing steps are performed; **4)** Afterwards and previous to the readout step, the biotinylated Smart-NB is labelled with SAPE conjugate or Streptavidin-β-Galactosidase conjugate; and washing steps are performed; **5)** Readout by Flow Cytometry or by a Plate Reader.

Whether the amount of SAPE used to label the biotinylated **Magbeads-21-6.0**, following DCL, using **Smart-2dA-Botin**, could be modified to obtain a better fluorescence signal, was also studied. Therefore, dynamic incorporation reactions and labelling step were carried out using a range of SAPE concentrations – 20 µg/mL, 40 µg/mL, 60 µg/mL, 80 µg/mL, and 100 µg/mL, **Smart-2dA-Biotin** at 5 µM, and 15 nM of ssDNA-21. FACS analysis showed that higher concentrations of SAPE released higher MFI values in the PE channel. Signal-to-noise ratio was also calculated (Table 12).

Table 12. MFI values of PE channel and signal-to-noise ratio for increasing concentrations of SAPE and maintaining 5 µM of **Smart-dA-Biotin** and 15 nM of ssDNA-21.

Smart-2dA-Biotin	ssDNA-21	SAPE	MFI – PE	Signal-to-noise ratio
5 µM	15 nM	0 µg/mL	695	-
5 µM	15 nM	20 µg/mL	1,409	2.03
5 µM	15 nM	40 µg/mL	1,501	2.16
5 µM	15 nM	60 µg/mL	1,975	2.84
5 µM	15 nM	80 µg/mL	2,232	3.21
5 µM	15 nM	100 µg/mL	2,246	3.23

Then, aiming at detecting miR-21 directly from biological samples, two cell lines overexpressing miR-21 were selected, MDA-MB-468 (breast cancer cell line) and H1975 (lung cancer cell line), and also Peripheral Blood Mononuclear Cells (PBMCs) from healthy volunteers as control cells due to their miR-21 lack of expression. To validate such fact, RT-qPCR experiments were performed using total RNA isolated from MDA-MB-468, H1975, and PBMCs cell lines. Total RNAs were isolated from cell lysates and RT-qPCR kits from Qiagen were used to measure their Ct values, employing hsa-miR-16-5p as endogenous control. ΔCt measures the fluorescence increment between the miRNA of interest (miR-21 in this case) and the endogenous miRNA, miR-16, and it is usually expressed as $2^{-\Delta Ct}$ values, which measures the relative fold expression. Higher $2^{-\Delta Ct}$ values correspond to higher amount of miRNA in the sample. T-test analysis comparing the miR-21 expression of MDA-MB-468 and H1975 cells lines to PBMCs showed that MDA-MB-468 vs PBMCs was “very significant” (**) (p-value= 0.0058), and that H1975 vs PBMC was “extremely significant” (***) (p-value <0.0001) (Figure 23).

Samples	$2^{-\Delta Ct}$
PBMC_1	1,14231398
PBMC_2	0,69216757
PBMC_3	0,55402504
MDA-MB-468_1	4,02937199
MDA-MB-468_2	6,9963332
MDA-MB-468_3	6,59781923
H1975_1	31,1924777
H1975_2	29,1377889
H1975_3	27,9611524

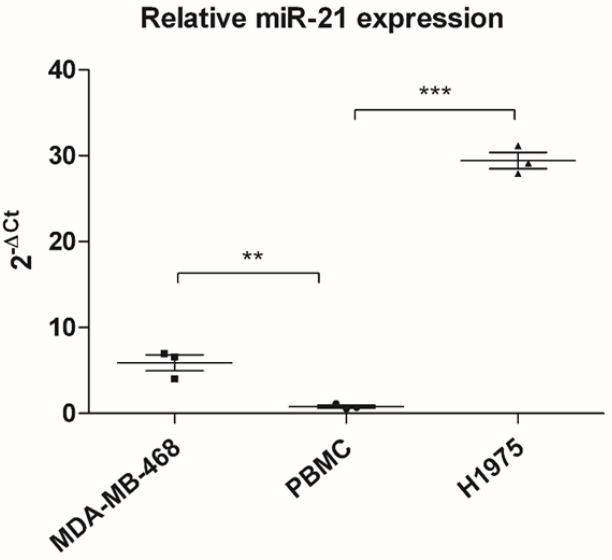

Figure 23. miR-21 RT-qPCR data analyses. At the left, the table with the $2^{-\Delta Ct}$ values for all the samples; at the right, graphic representation of the data.

After confirming the overexpression of miR21 in MDA-MB-468 and H1975 cell lines, cell pellets containing 1 x 10^6 for all cell lines, including PBMCs, were obtained. Thereupon, cells were lysated using a lysis buffer, and **Magbeads-21-6.0** were added to the supernatant, to let the miR-21 hybridise with the complementary abasic probes presented in the **Magbeads-21-6.0**. Following washing steps assisted by a magnet, **Magbeads-21-6.0** were mixed **Smart-2dA-Biotin** and reducing agent ($NaBH_3CN$) to perform DCL, which led to the covalent incorporation of the **Smart-2dA-Biotin** into the abasic position of the DGL probes, through the templating role of the complementary miR-21 strand. This means that **Magbeads-21-6.0** get biotinylated in proportion to the number of miR-21 molecules found in the sample. Finally, **Magbeads-21-6.0** fluorescent labelling step was carried out via biotin-streptavidin recognition, using SAPE conjugate.

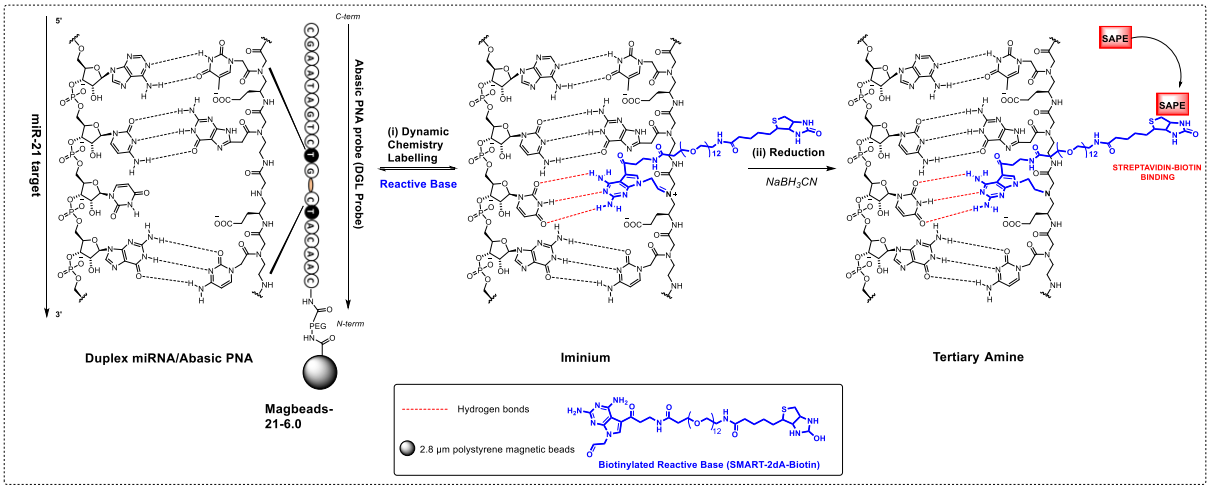

Figure 24. Schematic representation of the Chem-NAT technology developed with **Magbeads-21-6.0** for miR-21 targeting. DGL probe hybridises with miR-21 sequence, and DCL of Smart-2dA-Biotin takes place, with further SAPE conjugation for fluorescent detection. (**To see in more detail go to Appendix 3**).

Then, FACS was used to read samples. Results were analysed and represented in Figure 25 using MFI of the PE channel (585/42 nm). In order to establish the PE background signal, **Magbeads-21-6.0** that did not undergo any chemical reaction were used as control. Besides, there were also performed the dynamic incorporation reactions using **Smart-C-Biotin** instead of **Smart-2dA-Biotin** to assess the selective and specific dynamic incorporation of the Smart-NB into the abasic position of the duplex DGL-miR-21 formed onto the surface of the **Magbeads-21-6.0** as there is a natural uracile in front of the abasic position of the DGL probe. As shown in Figure 25, MFI values obtained in the PE channel for all the samples performed with **Smart-C-Biotin** (PBMC 1M + C, MDA-MB-468 1M + C, and H1975 1M + C) were basically the same than that for **Magbeads-21-6.0** control, showing the great specificity of the DCL technology. On the other hand, MFI values obtained in the PE channel when cell lysates from MDA-MB-468 and H1975 were used and the DCL assay performed with **Smart-2dA-Biotin** (MDA-MB-468 1M + 2dA and H1975 1M + 2dA) was almost the double compared with the control, being “extremely significant” (p value < 0.0001).

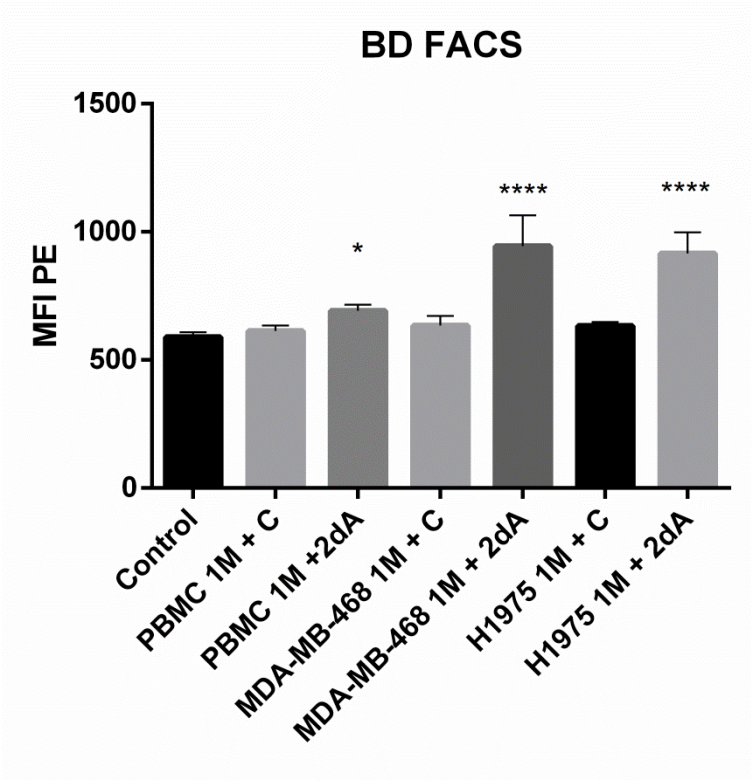

Figure 25. FACS results. MFI of PE channel (585/42 nm) for 1 million MDA-MB-468, H1975, and PBMCs, with **Smart-C-Biotin** and **Smart-2dA-Biotin**. One-Way ANOVA analysis was performed comparing the cell samples (n = 4) with **Magbeads-21-6.0** control (n=4). Errors bar correspond to ± SEM.

2.2.1.1.3. FLUOstar Omega

Bearing in mind the direct detection and quantification of miR-21 from biological samples, it was necessary to translate the bead-based diagnostic platform to another fluorescence-based readout platform with a better LoD than FACS. Therefore, and thanks to the collaboration with DestiNA Genomica S.L., it was chosen the microplate reader FLUOstar Omega, which had proven to be valid for the direct detection of miR-451 [161].

First of all, a miR-21 titration curve was performed in FLUOstar Omega through synthetic miR-21 spike-in at different concentrations (500 pM, 250 pM, 125 pM, 62.5 pM, 31.25 pM and 0 pM). For that, two solutions were prepared, one containing **Magbeads-21-6.0** and 500 pM of ssDNA-21 in lysis buffer (Mastermix A), and the other containing only **Magbeads-21-6.0** in lysis buffer (Mastermix B). Then, Mastermix A (500 pM) and Mastermix B (0 pM) were mixed in the same proportion, affording 250 pM of ssDNA-21 solution. Afterwards, a part of 250 pM solution was mixed with the same volume of Mastermix B, affording a 125 pM of ssDNA solution. Thus, by repeating these steps, serial dilution was achieved. Once the spike-in step was done, to the obtained mixtures of **Magbeads-21-6.0** and several

concentrations of synthetic miR-21, a combination of **Smart-2dA-Biotin**, $NaBH_3CN$ and Buffer A was also added, incubating the mixture to let the Smart-NB dynamic incorporation to take place. Then, biolabelling step for FLUOstar omega was performed via biotin-streptavidin recognition although differently than that for FACS. In this case, the **Magbeads-21-6.0** were incubated with Streptavidin-β-Galactosidase (SbG) instead of SAPE, which created a fluorescent solution upon enzymatic hydrolysis of Resorufin-β-D-Galactopyranoside that was recorded in the FLUOstar omega instrument (Scheme 2), calculating the slope of the linear region of the reaction time course.

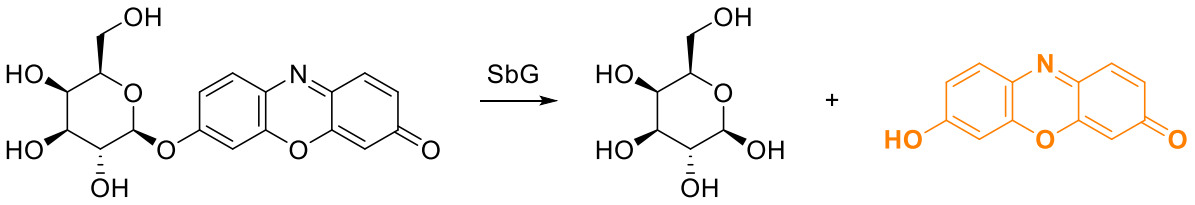

Resorufin-B-D-Galactopyranoside Galactose Resorufin

Scheme 2. Fluorogenic reaction responsible for FLUOStar Omega fluorescent readout.

Taking into account that resorufin fluorescence signals were directly proportional to the amount of SbG presented in the **Magbeads-21-6.0**, the Units of Fluorescence per Second (RFU/s) could be correlated with the amount of miR-21 (Figure 26-A). Thus, for the titration curve performed, it was calculated a LoD (BG+3SD@ 15% CV) of 35.84 ± 2.4 pM in 100 µL of hybridisation volume, corresponding to 3.58 fmol and 2.16E + 9 molecules of synthetic miR-21.

In order to determine the amount of miR-21 presented in tumour cells, the number of MDA-MB-468 and H1975 cells employed was decreased to 1 x 10^5, due to the better LoD of FLUOstar Omega than that of FACS. Therefore, 1 x10^5 cells of MDA-MB-468 and H1975 were evaluated in quadruplicate, whilst 1 x 10^6 PBMCs were evaluated in triplicate as negative controls. Afterwards, the fluorescence released in each condition was applied to the equation line obtained from the titration curve to calculate the concentration of miR-21 presented. Thus, knowing the miR-21 concentration, the hybridisation volume and the number of cells the number of molecules of miR-21 per cell, could be calculated:

$$miR21\ molecules = \frac{[(Concentration(M)) * (V) * (NA)]}{n^{o}\ of\ cells}$$

Regarding the three cell lines employed in the assay, there were found 89,834 ± 16% copies of miR-21 per cell in MDA-MB-468 cells, 104,003 ± 11% copies of miR-21 per cell in H1975 cells, and the number of molecules of miR-21 per cell in PBMCs could not be determined as the total number of calculated miR-21 molecules was below the LoD of the assay (Figure 26-B) [163].

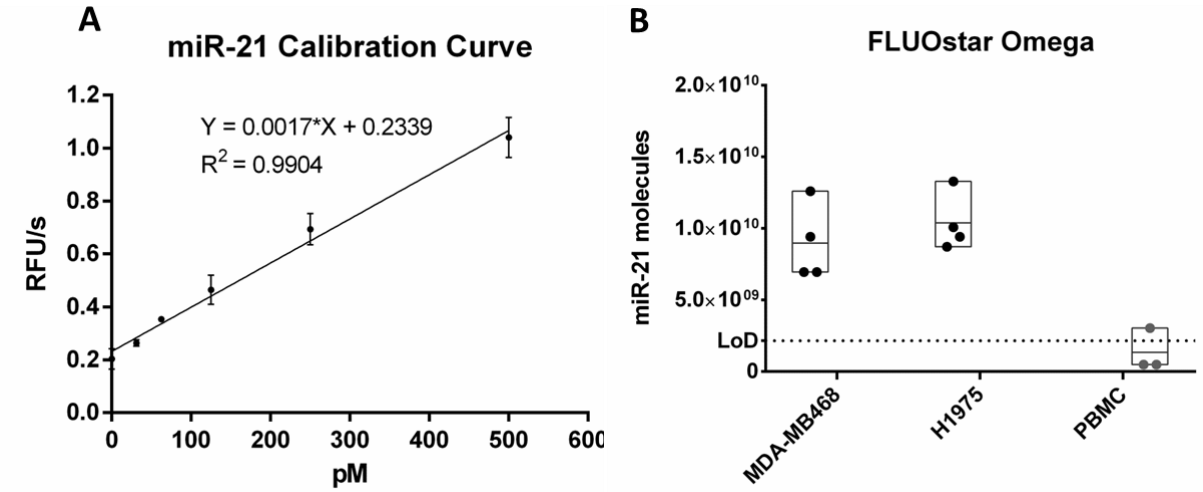

Figure 26. A) miR-21 titration curve by synthetic miR-21 spike-in. Dots represent Mean + SEM (n=3) at different synthetic miR-21 concentrations (500 pM, 250 pM, 125 pM, 62.5 pM, 31.25 pM, and 0 pM). **B)** FLUOstar omega results. In black dots, the total number of miR-21 molecules calculated for 1 x 10^5 MDA-MB-468 and H1975 tumour cells (n=4). In grey dots, the total number of miR-21 molecules calculated for 1 x 10^6 PBMCs (n=3).

2.2.2. Direct detection of miR-21 from Non-Small-Cells Lung Cancer (NSCLC) plasma

2.2.2.1. Results

Aiming to increase the bead-based platform applications in biological samples, and once the direct detection and quantification of miR-21 was carried in tumour cells, it was chosen to translate and apply the diagnostic platform to body fluids. In this case, collaborators from the Liquid Biopsies group, at the Centre Pfizer-University of Granada-Junta de Andalucia for Genomics and Oncological Research (GenYo), kindly provided plasma samples from patients with Non-Small-Cell Lung Cancer (NSCLC) in advance stages with bad prognosis.

The first proof of concept (PoC) for the direct detection and quantification of miR-21 from plasma was performed in a FACS. 100 µL of plasma were mixed with 200 µL of lysis buffer (ratio 1:2) containing 250,000 **Magbeads-21-6.0**, incubating the mixture for miR-21 hybridisation, as it was done for the cell lysate. Then, for the Smart-NB dynamic incorporation step, **Smart-2dA-Biotin** was added to some samples while **Smart-C-Biotin** was added to other samples, as negative controls. After that, biolabelling step was performed using SAPE, detecting the fluorescence by FACS. The fluorescence results shown that although MFI of PE channel for the samples with **Smart-2dA-Botin** ($\bar{x}$=636) were slightly higher than the values of the samples with **Smart-C-Biotin** ($\bar{x}$=574), which were similar to the **Magbeads-21-6.0** control (without Smart-NB, $\bar{x}$=568), the fluorescence histograms did not show any difference at all (Figure 27-A).

So, according to the strategy previously followed with the tumour cells, the plasma samples were then analysed with the FLUOstar omega. For that, as described in the FACS assay, 100 µL of NSCLC plasma were mixed with 200 µL of lysis buffer containing 250,000 **Magbeads-21-6.0**, incubating the mixture for miR-21 hybridisation. Subsequently, some samples were added **Smart-2dA-Biotin** while others were added **Smart-C-Biotin**, for the Smart-NB dynamic incorporation step. After that, the biolabelling step was performed by adding SbG to the **Magbeads-21-6.0**, which reacted with Resorufin-β-D-Galactopyranoside releasing resorufin fluorescence that was recorded in the FLUOstar omega instrument. Interestingly, there existed a noteworthy difference between the slope obtained for the samples which were added **Smart-2dA-Biotin** ($\bar{x}$=0.44) and the samples control, which were added **Smart-C-Biotin** ($\bar{x}$=0.03). Moreover, applying the miR-21 calibration curve equation previously shown (Y=0.0017*X + 0.2339), it was calculated the average concentration of miR-21 presented in the NSCLC plasma samples (n=3), 119.27 ± 7.8 pM, corresponding to

11.9 fmol and 7.18E + 9 molecules of miR-21 (Figuer 27-B). The number of molecules of miR-21 of the controls could not be obtained since they were very below the calculated LoD, giving negative values when the line equation was applied. Thus, they could not be represented in Figure 27-B.

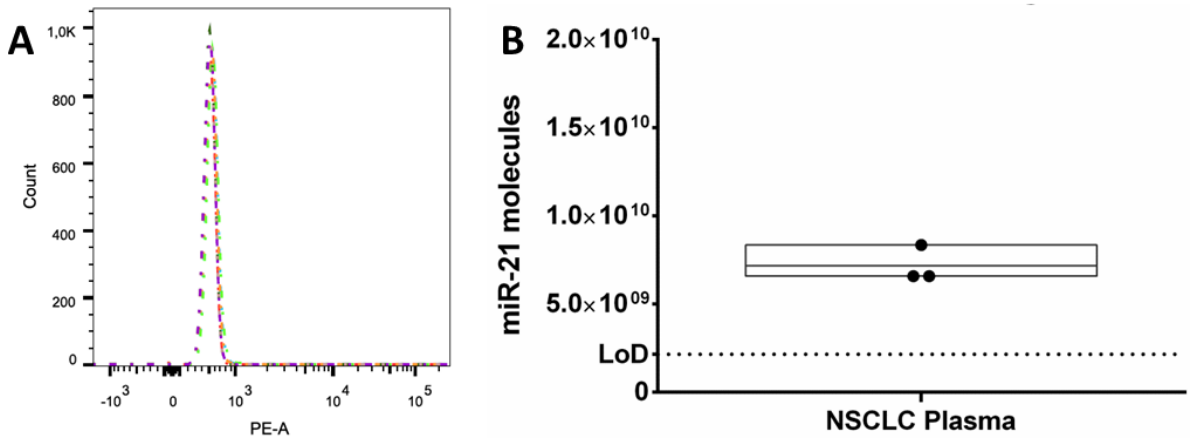

Figure 27. A) Histogram of all samples for PE channel in FACS: in red the **Magbeads-21** control; in blue, in orange, and in light green, the **Magbeads-21** + **Smart-2dA-Biotin**; in dark green, in pink, and in purple, the **Magbeads-21** + Smart-C-Biotin. **B)** Number of molecules of miR-21 in FLUOstar omega for NSCLC plasma samples (n=3) using **Magbeads-21-6.0**, **Smart-2dA-Biotin**, and SbG reagent.

2.2.3. miR-21 and miR-122 detection and discrimination in a multiplexing assay

2.2.3.1. Results

To provide insights of the translational impact of the bead-based platform in terms of multiplexing, it was assessed the capability of discriminating two miRNAs, miR-21 and miR-122, at the same time in one only sample in one run of the experiment.

To achieve such goal, there were used **Magbeads-21-6.0** and **Magbeads-122** along with **Smart-2dA-Biotin** and **Smart-C-Cy5**. **Magbeads-122** were functionalised with DGL-122, which had the abasic position located in front of a guanine, thereby incorporating a cytosine. Additionally, the **Smart-C-Cy5** dynamic incorporation efficiency had been successfully evaluated prior the multiplexing assay. Thus, miR-21 was going to be detected due to **Smart-2dA-Biotin** specific dynamic incorporation and later biotin-streptavidin recognition through SAPE conjugate, producing fluorescence in the PE channel (585/42 nm) of FACS, whilst miR-122 was going to be detected due to **Smart-C-Cy5** specific dynamic incorporation, collecting the fluorescence in the APC channel (660/20 nm) of FACS (Figure 28).

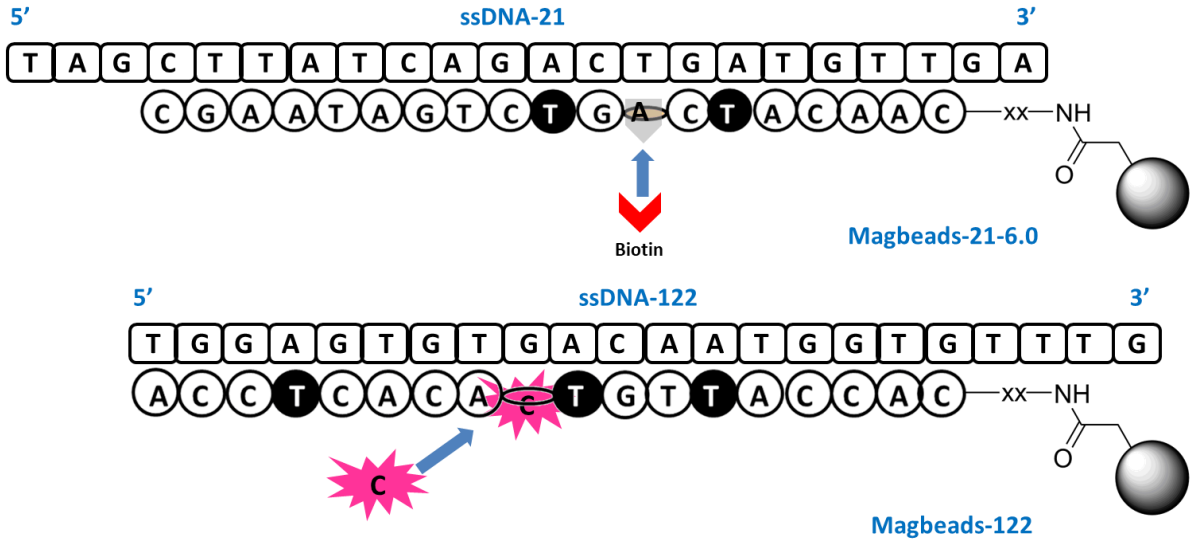

Figure 28. Schematic representation of the multiplexing miR-21 and mR-122 detection with **Magbeads-21-6.0** and **Magbeads-122**, respectively. Whereas **Smart-2dA-Biotin** is incorporated in the presence of miR-21 sequence and streptavidin-biotin binding with SAPE releases fluorescence, **Smart-C-Cy5** is incorporated in the presence of miR-122 sequence, directly emitting fluorescence.

To afford the experiment, **Magbeads-21-6.0**, **Magbeads-122**, ssDNA-21, ssDNA-122, **Smart-2dA-Biotin**, and **Smart-C-Cy5** were mixed in multiple ways, as it is shown in Table 13, to ensure the multiplexing assay and its controls (samples n=2). All the samples were

then incubated with SAPE and analysed by FACS. The real multiplexing assay consisted in mixing **Magbeads-21-6.0**, **Magbeads-122**, ssDNA-21, ssDNA-122, **Smart-2dA-Biotin**, and **Smart-C-Cy5** altogether, expecting two different signals, one of each type of miRNA.

Table 13. Multiplexing assay samples. Squares in blue, those components included in the samples: **A*)** Control: Non-DGL-functionalised Magbeads + ssDNA-21 + **Smart-2dA-Biotin**; **B*)** Control: Non-DGL-functionalised Magbeads + ssDNA-122 + **Smart-C-Cy5**; **C)** Control: **Magbeads-21-6.0** + ssDNA-21 + **Smart-C-Cy5**; **D)** Control: **Magbeads-122** + ssDNA-122 + **Smart-2dA-Biotin**; **E) Magbeads-21-6.0** + ssDNA-21 + **Smart-2dA-Biotin** + **Smart-C-Cy5**; **F) Magbeads-122** + ssDNA-122 + **Smart-2dA-Biotin** + **Smart-C-Cy5**; **G) Magbeads-21-6.0** + **Magbeads-122** + ssDNA-21 + ssDNA-122 + **Smart-2dA-Biotin** + **Smart-C-Cy5**.

SAMPLES	Magbeads-21-6.0	Magbeads-122	ssDNA-21	ssDNA-122	Smart-2dA-Biotin	Smart-C-Cy5
A*						
B*						
C						
D						
E						
F						
G						

FACS analysis showed that in the samples were the beads did not contain DGL probes, **sample A*** (Non-DGL-beads + ssDNA-21 + Smart-2-dA-Biotin) and **sample B*** (Non-DGL-beads + ssDNA-122 + **Smart-C-Cy5**), there were not events neither in the PE nor in the APC channels (Figure 29-A). Likewise, in **sample C** (**Magbeads-21-6.0** + ssDNA-21 + **Smart-C-Cy5**) and in **sample D** (**Magbeads-122** + ssDNA-122 + **Smart-2dA-Biotin**), containing the beads functionalised with DGL probes, the target nucleic acid, but a Smart-NB which is not complementary to the nucleobase found in front of the abasic DGL position (wrong Smart-NB), there were not found events in neither PE nor APC channels (Figure 29-B-C). On the other hand, in **sample E** (**Magbeads-21-6.0** + ssDNA-21 + **Smart-2dA-Biotin** + **Smart-C-Cy5**) and in **sample F** (**Magbeads-122** + ssDNA-122 + **Smart-2dA-Biotin** + **Smart-C-Cy5**), containing the DGL-functionalised beads, the target nucleic acid, and both Smart-NBs, there were found events in the channels. In **sample E**, the FACS plots showed that the **Magbeads-21-6.0** population moved to the PE channel, being clearly positive for PE

fluorescence, whilst it stood still in the APC channel (Figure 29-D). In **sample F**, on the contrary, the **Magbeads-122** displaced to the APC channel and remained in the same position in the PE channel (Figure 29-E). The fluorescence correlogram APC/PE showed that **sample E** and **sample F** possessed the inverse profile, APC-/PE+ and APC+/PE-, respectively. Therefore, in **sample G**, which represented the multiplexing assay (**Magbeads-21-6.0** + **Magbeads-122** + ssDNA-21 + ssDNA-122 + **Smart-2dA-Biotin** + **Smart-C-Cy5**), it was observed two clear populations, APC+/PE- and APC-/PE+, gathering each of them approximately 50% of all the events (Figure 29-F).

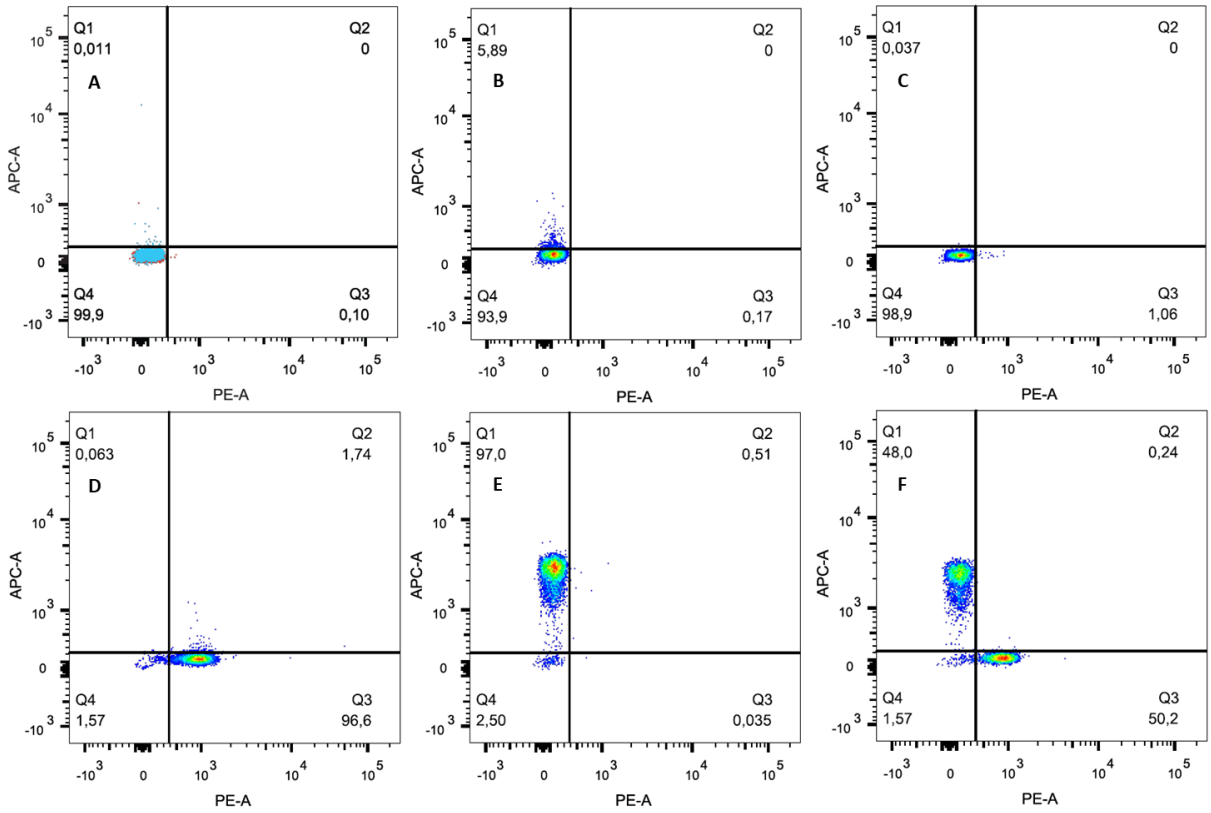

Figure 29. Correlograms for APC and PE channels. **A)** In red and in blue, bead populations for samples **control A* and B***, non-DGL-functionalised Magbeads incubated with ssDNA-21 + Smart-2dA-Biotin and ssDNA-122 + Smart-C-Cy5. **B) Sample C**, Magbeads-21-6.0 + ssDNA-21 + Smart-C-Cy5. **C) Sample D**, Magbeads-122 + ssDNA-122 + Smart-2dA-Biotin. **D) Sample E,** Magbeads-21-6.0 + ssDNA-21 + Smart-2dA-Biotin + Smart-C-Cy5. **E) Sample F**, Magbeads-122 + ssDNA-122 + Smart-C-Cy5 + Smart-2dA-Biotin. **F) Sample G**, Magbeads-21-6.0 + Magbeads-122 + ssDNA-21 + ssDNA-122 + Smart-2dA-Biotin + Smart-C-Cy5.

2.2.4. Discussion

In this first part of Chapter 1, the design and development of bead-based platforms, using standard flow cytometer and microplate plate readers, for the direct and rapid profiling and quantification of miRNAs using Chem-NAT technology has been presented. The development of the platforms was done using miR-21 as model. Due to the universality of the bead-based reagents, Dynabeads®, and the Chem-NAT reagents, these platforms can be applied to nearly any expressed miRNA with high biomarker value [61],[161]. Besides, herein the multiplexing capability was also demonstrated by detecting miR-122 and miR-21 in the same sample. All of these demonstrate their multiplexing capability and great versatility for developing novel miRNA-based assays.

The results have shown that the design of the abasic PNA probes (DGL probes) is a key element in successfully profiling miRNAs. Incorrect designs could lead to false negatives and false positive results, due to a lack of specificity and sensitivity. Probes design is not a straightforward process since there is not a well-established relationship between the abasic PNA probe features and their behaviour yet. The need to use chiral units at gamma positions of the PNA and abasic units of DGL probes and the location of the abasic positions at different probing areas makes the whole design process a challenging one. This fact was particularly difficult during the development of the miR-21 assay. The first three designed DGL probes, **DGL-21-1.0**, **DGL-21-2.0**, and **DGL-21-3.0**, were designed with a non-chiral abasic position, as it happens for DGL-122, which has been demonstrated to be a reliable DGL probe for miR-122 testing [61],[160], however, this approach did not work for miR-21 testing. Then, DGL probes designed with a chiral abasic position, **DGL-21-4.1**, **DGL-21-5.1**, and **DGL-21-6.0**, successfully incorporated the Smart-NB. It was described that longer PNA probes tend to form more stable duplexes and our results also confirmed this. In this work, the length of the DGL probes changed from 17 to 19 mer. In order to address the solubility issue of PNA probes longer than 12 mer [153], a mini-PEG unit was coupled to the N terminus and propionic acid groups, which are negatively charged at the assay pH, were incorporated at gamma positions of some DGL units.

During the development of this part of the project, **DGL-4.1** and **DGL-5.1** probes were unconsciously designed wrong, as they were containing one base less than initially intended at position 3 from the N-terminal end. This error was later found out after tests were performed. This allowed to drawing interesting conclusions. Table 8 shows that both DGL probes presented non-specific Smart-NB incorporation when incubated with a mimic miR-21 containing a nucleotide in front of the abasic position which was not complementary to the labelled Smart-NB used.

When comparing them, **DGL-21-4.1** probe, which should incorporate **Smart-C-Cy5**, showed to have a higher fluorescence signal than **DGL-21-5.1** probe, which incorporates **Smart-dA-Biotin**, when incubated whith ssDNA-21. However, **DGL-21-4.1** also presented higher non-specific signal when incubated with the non-complementary oligonucleotide. This fact could be related to two motives:

1) **DGL-21-4.1** probe incorporates a Smart-NB directly labelled with a fluorophore whilst **DGL-21-5.1** incorporates a non-fluorescent Smart-NB that create fluorescent signals via specific biotin-streptavidin binding through a two steps reaction. Thus, **DGL-21-5.1** undergoes more washing steps in the whole process than **DGL-21-4.1**, what helps to remove non-specific interactions. Moreover, previous studies undertaken for optimisation of the platform showed that directly fluorescent labelled Smart-NB tend to produce higher background.

2) In this Doctoral Thesis, instead of using adenine as Smart-A, it has been used the 2-diamino-deazapurine (**Smart-2dA**) which is an analogue. It is well known that 2,6-diaminopurine:thymine/uracil base pair proceed through three hydrogen bonds rather than the two that occurs between natural adenine and thymine/uracil, increasing their base pair stability. Besides, Brown et al. demonstrated that modified 7-deaza 2,6-diaminopurines significantly stabilize DNA duplexes [164].

Whether a higher amount of DGL probe attached to the beads would reasonably increase the performance of the base filling reaction was also assessed. Nonetheless, the results obtained in Table 8 were somehow confusing. It was observed that a higher amount of DGL probe covalently immobilised through amide bonds on beads, in general terms, neither provoked a rise in the positive fluorescence signal when incubated with ssDNA-21, nor produced an increase of the non-specific signal when incubated with the wrong oligonucleotide. There could be made two exceptions to this statement. The first one refers to **DGL-21-5.1** presenting a slightly higher non-specific signal corresponding to higher DGL amount (350 pml/mg of bead). The second one refers to **DGL-21-5.1** incubated with an increasing amount of Smart-NB, wherein it seems to be related to higher fluorescence signals for both expected positive and non-specific situations, particularly in those beads loaded with 350 pmol DGL/mg of beads. Thus, these data suggest that the performance of the specific nucleobase DCL reaction is, at some point, non-dependant on the amount of DGL probes loaded into the beads. This could be explained as an excess of DGL probes could hinder the Smart-NB specific incorporation by steric hindrance without removing the non-specific interactions that Smart-NB may be undergoing onto the surface of the beads. Therefore, it is important to balance both the amount of DGL attached to the beads and the

amount of Smart-NB employed in the assay to obtain strong positive fluorescent signal without having an excess of non-specific signal. The key is to find the correct balance that allows obtaining a low limit of detection with a dynamic range as large as possible.

After realising the design error a new DGL probe, the **DGL-21-6.0**, containing the abasic position in front of a thymine (ssDNA-21) when duplex is formed, was synthesised. This means that DCL reaction provokes the incorporation of a **Smart-dA** onto the abasic position of the DGL probe. Preliminary results showed an improved incorporation yield without non-specific incorporation if compared to the previous DGL-21 probes. Consequently, the capability of the bead-based platform for the real detection and quantification of miR-21 directly from samples was assessed. For that, two tumour cell lines overexpressing miR21, the breast cancer cells MDA-MB-468 and the lung cancer cells H1975, and a control cell line that did not express miR-21, PBMCs, were selected. The overexpression or not of miR-21 was successfully assessed by RT-qPCR. So, the implantation of the bead-based and chemistry-dependant detection platform into two fluorescent readout platforms, the FACS and the microplate reader FLUOStar Omega, was evaluated.

FACS analysis showed to be a readout platform with a limit of detection which was low enough to identify the overexpression of miR-21 from samples, as it happens with the tumour cell lines. Figure 25 shows MFI signals for the tumour cancer cells which are significantly increased in regards to the control PBMCs. Moreover, when using a **Smart-C-Biotin** as control, it is also observed that the MFI signals were equal as background levels due to uracil nucleobase of miR-21 did not template the cytosine nucleobase incorporation, as expected. Nonetheless, FACS platform has also its drawbacks since MFI values for tumour cells overexpressing miR-21 (MDA-MB-468 and H1975) are not very high in comparison with PBMCs, which do not overexpress miR-21. For that reason, FACS readout platform could be used just for qualitative assays for the direct detection of miR-21.

Hence, the bead-based platform had to move to another and more sensitive readout platform, the FLUOStar Omega. This platform allows detecting end-point kinetic-based fluorescence assay. Bearing this in mind, the number of tumour cells employed decreased from 1 x 10^6 in FACS to 100,000 cells in FLUOStar Omega, showing its higher sensitivity. Moreover, performing spike-in, a calibration curve with synthetic miR-21 was performed, allowing to determining the LoD of the platform, 35.84 ± 2.4 pM. Using this calibration curve, the FLUOStar Omega readout platform enabled the absolute quantification of miR-21. By using a simple equation, the number of molecules of miR-21 per cell was calculated [163]. Notably, even when using one million PBMCs signals below the LoD of the platform were obtained, hence undetectable as it was expected on the grounds of its lack of miR-21

expression. While the number of miR-21 per cell is not very well reported in literature, our numbers are consistent with some previous reports, being 89,834 ± 16% copies of miR-21 per cell in MDA-MB-468 cells, 104,003 ± 11% copies of miR-21 per cell in H1975 cells [165].

Lately, and aiming to moving one step forward for developing clinical diagnostics, the robustness and capability of translating the platform to another matrix, plasma, for the detection and quantification of circulating miR-21 directly from the plasma of patients with NSCLC in advance stages with bad prognosis, was also assessed. This assessment was performed with FLUOStar Omega. Data showed that the bead-based platform was able to detect and quantify miR-21 in plasma of NSCLC patients while healthy volunteers' plasma did not present detectable levels of miR-21. This platform also allowed determining that the concentration of miR-21 found in patient plasma is significantly lower than miR-21 concentrations from tumour cells. This means that this platform can be successfully applied for the direct detection and quantification of miR-21 from liquid biopsies [61],[122],[161].

In addition, the multiplexing capability of the platform for the direct identification of miRNAs was proven. In order to do so, a PoC project was designed and executed. **Magbeads-21-6.0** and **Magbeads-122** were used concomitantly, for profiling miR-21 and miR-122, respectively, using **Smart-2dA-Biotin** and **Smart-C-Cy5** as the Smart-NBs. This assay showed the high affinity of the DGL probes and the high specificity of the DCL reaction. Despite incubating the two different Magbeads with different nucleic acid targets and several Smart-NBs, there were no unspecific fluorescent signals. The only fluorescent signals came from the specific DCL reaction. Thus, the multiplexing capability of the bead-based platform is definitely demonstrated as two well defined beads populations are identified in FACS, allowing detecting two miRNAs in the same sample within the same experiment.

All in all, the bead-based platform designed for molecular assays has been successfully validated for miR-21 detection and quantification, proving its robustness across two of the most used readout platforms in any molecular biology laboratory and using different types of biological specimen samples. This, along with its multiplexing capacity, makes this platform very suitable to be translated to its clinical use. On top of that, this platform can be extended to daily basic research due to it is cost-effective and easy to use.

2.3. Single Nucleotide Polymorphism (SNP) detection through Single Base Resolution

2.3.1. Detection of KRAS mutation

2.3.1.1. Results

As initial PoC for the direct detection of genomic mutations, the design of reagents and protocols to detect the mutation G13C in the codon 13 of KRAS (GGC>**T**GC) was decided. A DGL probe (**K13SRC**) targeting a part of the KRAS sequence which included the codon 13 was designed with the abasic position located in the 11th position, from the N terminus, of the probe and in front of the position 37 of the KRAS sequence, in the codon 13, which is responsible for the G13C mutation (G>T). To afford this aim, the DGL probe aforementioned and two synthetic oligonucleotides (DNA-KRAS and DNA-G13C-KRAS) mimicking part of the exon 2 of KRAS gene containing codons 12 and 13, were used. Sequences are shown in the Table 14.

Table 14. ssDNA (5'→3') and DGL probes sequences (N→C). *GL* (highlighted in yellow) represents the chiral and negatively charged abasic position. "Xglu" represents the chiral and negatively charged PNA monomers, containing a propanoic acid side chain at the gamma position. DGL probes have a miniPEG group (xx) and an amine group at their N-terminal, and a C-terminal primary amide. Highlighted in yellow, the nucleotides involved in G13C KRAS mutation and located in front of the abasic positions of the DGL probe.

DNA-KRAS	TTG GAG CTG GTG GCG TAG GCA A		
DNA-G13C-KRAS	AGC TGG TTG CGT AGG CAA		
DGL probe – Sequence – Magbeads – Bioconjugation Chemistry			
DGL-K13SRC	NH_2-xx-TTG CCT ACGglu C*GL*A CgluCA GCT-$CONH_2$	**Magbeads-KRAS**	Amide

DGL-K13SRC contained an amine pegylated residue at the N-teminal to enable its coupling to Dynabeads® M-270 Carboxylic acid through an amide bond formation, to afford **Magbeads-KRAS**. Abasic position of **DGL-K13SRC** contains a propionic acid chain at its gamma position being the *S*-enantiomer.

To assess whether the detection of the mutation G13C in KRAS with the **Magbeads-KRAS-G13C** was able, the beads were mixed with the oligonucleotide DNA-G13C-KRAS,

model of the mutated region, the reducing agent and the **Smart-2dA-Biotin** due to the abasic position of the DGL probe was located in front of a thymine. The mixture was incubated at 41 ºC for 1 h to let the specific dynamic incorporation of the Smart-NB to take place. Afterwards, the **Magbeads-KRAS-G13C** were incubated with SAPE to label the Magbeads via biotin-streptavidin recognition. Also, **Magbeads-KRAS-G13C** were incubated with the oligonucleotide DNA-KRAS, model of the WT sequence, the reducing agent and the **Smart-C-Cy5** to allow the detection of the WT sequence of KRAS, on the grounds that the abasic position was located in front of a guanine in this case. Scheme of the mutation can be seen in Figure 30. Besides, as controls, **Magbeads-KRAS-G13C** were incubated with the reducing agent and the following:

1) The oligonucleotide DNA-miR39, as a scramble sequence, and **Smart-2dA-Biotin**.

2) The oligonucleotide DNA-miR39 and **Smart-C-Cy5**.

3) No oligonucleotide and **Smart-2dA-Biotin**.

4) No oligonucleotide and **Smart-C-Cy5**; incubating the mixtures at 41 ºC for 1 h. Then, those mixtures containing **Smart-2dA-Biotin** were incubated with SAPE conjugate.

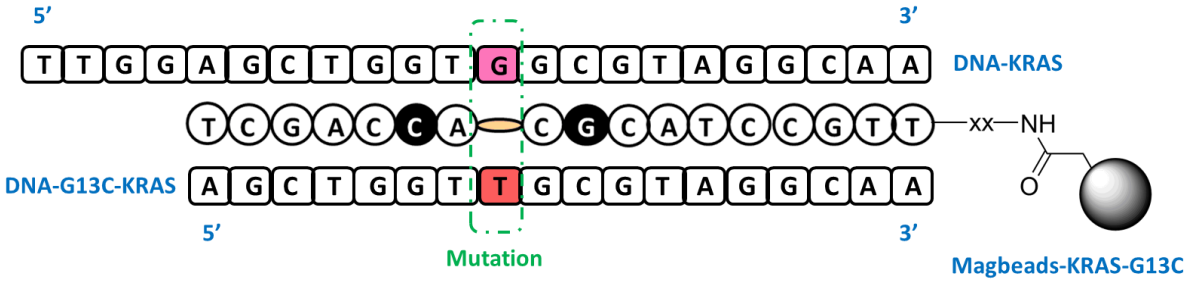

Figure 30. Representation of DNA-KRAS and DNA-G13C-KRAS hybridisation with DGL-K13SRC of **Magbeads-KRAS-G13C**. Mutation G13C is located in front of the chiral and negatively charged abasic position of the DGL probe.

Finally, the specific Smart-NB dynamic incorporation, in all the cases, was evaluated by FACS, collecting the fluorescence released by SAPE, which labels samples in which **Smart-2dA-Biotin** was used, in the PE channel (585/42 nm), and collecting the fluorescence produced by **Smart-C-Cy5** in the APC channel (660/20 nm). The FACS analysis showed that none of the controls (1-4) produced fluorescence in PE channel or APC channel. Likewise, **Magbeads-KRAS-G13C** incubated with DNA-KRAS (**G** in front of the abasic position) and **Smart-2dA-Biotin** did not present fluorescence in the PE channel, just like **Magbeads-KRAS-G13C** incubated with DNA-G13C-KRAS (**T** in front of the abasic position) and **Smart-C-Cy5** did not show fluorescence in the APC channel. On the contrary, **Magbeads-KRAS-**

G13C incubated with DNA-G13-KRAS with **Smart-2dA-Biotin** presented fluorescence in the PE channel (Figure 31-A), whilst **Magbeads-KRAS-G13C** incubated with DNA-KRAS with **Smart-C-Cy5** were positive for fluorescence in the APC channel (Figure 31-B).

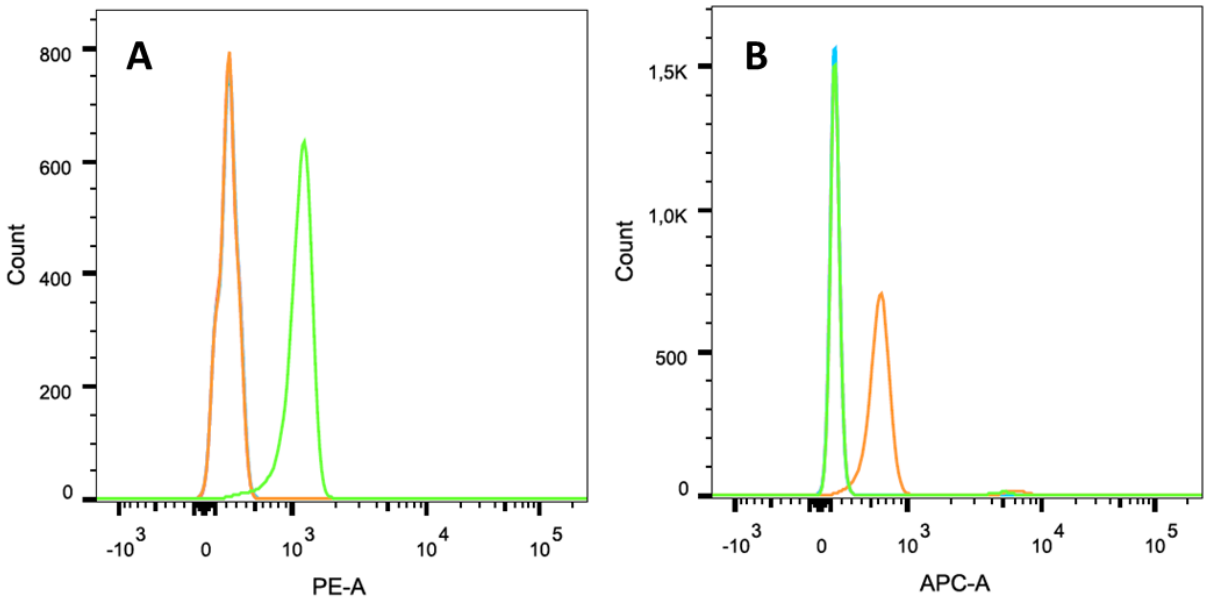

Figure 31. A) Histogram showing fluorescence in PE channel for **Magbeads-KRAS-G13C** incubated with **Smart-2dA-Biotin** and: 1) no oligonucleotide (negative control); 2) DNA-miR39 (negative control); 3) DNA-KRAS (negative control); 4) DNA-G13C-KRAS (positive condition). **B)** Histogram showing fluorescence in APC channel for **Magbeads-KRAS-G13C** incubated with **Smart-C-Cy5** and: 1) no oligonucleotide (negative control); 2) DNA-miR39 (negative control); 3) DNA-KRAS (positive condition); 4) DNA-G13C-KRAS (negative control).

To provide insights of the real capability of the platform to discriminate between WT KRAS and G13C KRAS, a multiplexing experiment using only **Magbeads-KRAS-G13C** was performed. For that, **Magbeads-KRAS-G13C** were incubated with DNA-KRAS, DNA-G13C-KRAS, **Smart-C-Cy5**, and **Smart-2dA-Biotin**, to afford different conditions, as it follows:

- Control-C: **Magbeads-KRAS-G13C** + no oligonucleotide + **Smart-C-Cy5** + Reducing agent.

- Control-A: **Magbeads-KRAS-GC13C** + no oligonucleotide + **Smart-2dA-Biotin** + Reducing agent.

- Condition-1: **Magbeads-KRAS-G13C** + DNA-KRAS + **Smart-2dA-Biotin** + **Smart-C-Cy5** + Reducing agent.

- Condition-2: **Magbeads-KRAS-G13C** + DNA-G13C-KRAS + **Smart-2dA-Biotin** + **Smart-C-Cy5** + Reducing agent.

- Condition-3: **Magbeads-KRAS-G13C** + DNA-KRAS + DNA-G13C-KRAS + **Smart-2dA-Biotin** + **Smart-C-Cy5** + Reducing agent.

All **Magbeads-KRAS-G13C** were incubated at 41 ºC for 1 h and, except for the control-C, the rest of the samples were incubated with SAPE conjugate.

FACS analysis showed that **Magbeads-KRAS-G13C** incubated without oligonucleotides but with Smart-NB and undergoing the DCL reaction, presented no fluorescence in PE or APC channels (Figure 32-A). Then, in conditions 1, in which **Magbeads-KRAS-G13C** were incubated with both Smart-NBs, **Smart-2dA-Biotin** and **Smart-C-Cy5**, and one oligonucleotide, DNA-KRAS (**G**GC), it was observed that **Magbeads-KRAS-G13C** presented fluorescence in the APC channel but not in the PE channel (Figure 32-B). On the other hand, in condition 2, in which **Magbeads-KRAS-G13C** were incubated with both Smart-NBs, **Smart-2dA-Biotin** and **Smart-C-Cy5**, and one oligonucleotide, DNA-G13C-KRAS (**T**GC), it was observed that **Magbeads-KRAS-G13C** presented fluorescence in the PE channel but not in the APC channel (Figure 32-C). At last, when **Magbeads-KRAS-G13C** were incubated with both Smart-NBs and both oligonucleotides, **Magbeads-KRAS-G13C** showed to be displaced to the APC and PE channels, showing fluorescence in both channels (Figure 32-D). Moreover, it was observed that compared to the control, nearly the 80% of the populations were APC+/PE+.

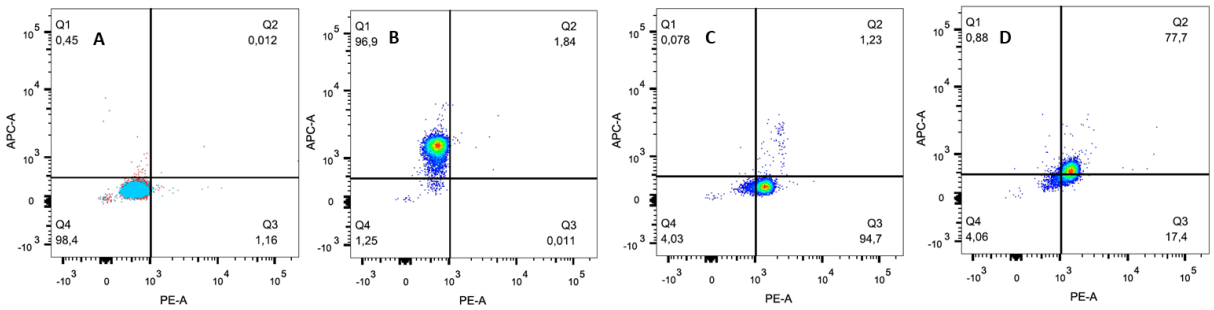

Figure 32. Correlograms for APC and PE channels. **A)** In red and in blue, **Magbeads-KRAS-G13C** for conditions Control-C and Control-A, respectively. **B) Magbeads-KRAS-G13C** for Condition-1, incubated with DNA-KRAS, **Smart-C-Cy5**, and **Smart-2dA-Biotin**. **C) Magbeads-KRAS-G13C** for Condition-2, incubated with DNA-G13C-KRAS, **Smart-C-Cy5**, and **Smart-2dA-Biotin**. **D) Magbeads-KRAS-G13C** for Condition-3, incubated with DNA-KRAS, DNA-G13C-KRAS, **Smart-C-Cy5**, and **Smart-2dA-Biotin**.

2.3.2. KRAS detection from serum samples

2.3.2.1. Results

Aiming to detect KRAS directly from biological samples without gene amplification and to apply the developed bead-based platform, serum samples from lung cancer (NSCLC) kindly provided by the Liquid Biopsies group, at the Centre Pfizer-University of Granada-Junta de Andalucia for Genomics and Oncological Research (GENyO), were selected.

As a PoC, synthetic DNA-KRAS was added, at final concentration of 15 nM, to NSCLC serum samples in order to assess its detection with the developed bead-based platform. Thus, **Magbeads-KRAS-G13C** along with **Smart-C-Cy5** and reducing agent $NaBH_3CN$ were incubated with 15 nM KRAS spiked-in NSCLC serum samples. Firstly, **Magbeads-KRAS-G13C** were incubated with the serum samples to hybridise with the DNA-KRAS for, afterwards, let the Smart-NB dynamic incorporation to take place, measuring the obtained fluorescence by FACS in the APC channel. Likewise, **Magbeads-KRAS-G13C**, **Smart-C-Cy5**, and reducing agent were incubated with non-spiked-in serum samples. Furthermore, the influence of two different concentrations of Smart-NB (10 µM and 20 µM) was also analysed.

Table 15. MFI values of APC channel of **Magbeads-KRAS-G13C** incubated with non-spiked-in (0 nM of DNA-KRAS) and spiked-in (15 nM of DNA-KRAS) NSCLC serum at several concentrations of **Smart-C-Cy5** (10 and 20 µM), for the detection of KRAS WT sequence.

Magbeads	Smart-C-Cy5	Serum DNA-KRAS	MFI – APC
Magbeads-KRAS-G13C	20 µM	(water – control)	228
Magbeads-KRAS-G13C	10 µM	0 nM	308
Magbeads-KRAS-G13C	20 µM	0 nM	343
Magbeads-KRAS-G13C	10 µM	15 nM	521
Magbeads-KRAS-G13C	20 µM	15 nM	516

Table 15 collects the FACS MFI values of the APC channel. Furthermore, FACS analysis showed that **Magbeads-KRAS-G13C** incubated with non-spiked-in NSCLC serum samples, independently of the Smart-NB concentration, seemed to have the same fluorescence than the **Magbeads-KRAS-G13C** incubated with **Smart-C-Cy5** but without the oligonucleotide DNA-KRAS (Figure 33-A-C). On the other side, it was observed that **Magbeads-KRAS-**

G13C incubated with DNA-KRAS spiked-in NSCLC serum samples were slightly displaced to the APC channel (Figure 33-D-E); nevertheless, in terms of fluorescence intensity, this small population displacement seemed to be enough to distinguish between the **Magbeads-KRAS-G13C** incubated with the spiked-in NSCLC serum samples and those **Magbeads-KRAS-G13C** that did not (Figure 3-F-J).

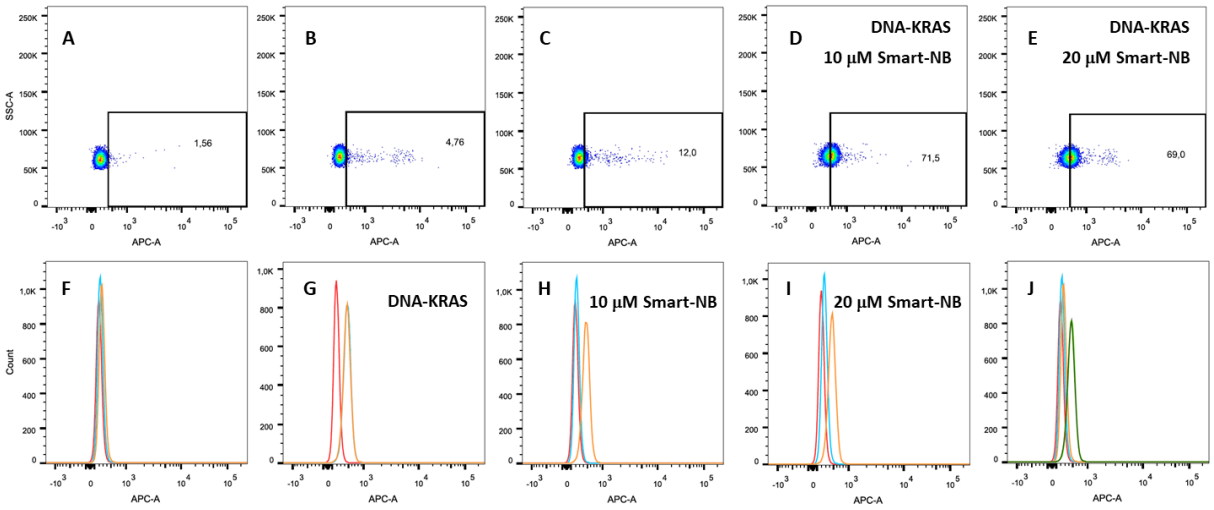

Figure 33. **A) Magbeads-KRAS-G13C** control incubated only with 20 µM of **Smart-C-Cy5** in water; **B) Magbeads-KRAS-G13C** incubated with non-spiked serum and 10 µM **Smart-Cy5**; **C) Magbeads-KRAS-G13C** incubated with non-spiked serum and 20 µM **Smart-Cy5**; **D) Magbeads-KRAS-G13C** incubated with DNA-KRAS spiked serum and 10 µM **Smart-Cy5**; and **E) Magbeads-KRAS-G13C** incubated with DNA-KRAS spiked serum and 20 µM **Smart-Cy5**. **F)** Samples in non-spiked serum: In red, **Magbeads-KRAS-G13C** control, in blue, **Magbeads-KRAS-G13C** + 10 µM **Smart-C-Cy5**, in orange, **Magbeads-KRAS-G13C** + 20 µM **Smart-C-Cy5** ; **G)** Samples in DNA-KRAS spiked serum: in red, **Magbeads-KRAS-G13C** control, in blue, **Magbeads-KRAS-G13C** + 10 µM **Smart-C-Cy5**; **Magbeads-KRAS-G13C** + 20 µM **Smart-C-Cy5**; **H)** Samples with 10 µM **Smart-C-Cy5**: In red, **Magbeads-KRAS-G13C** control, in blue, **Magbeads-KRAS-G13C** + non-spiked serum, in orange, **Magbeads-KRAS-G13C** + DNA-KRAS spiked serum; **I)** Samples with 20 µM **Smart-C-Cy5**: In red, **Magbeads-KRAS-G13C** control, in blue, **Magbeads-KRAS-G13C** + non-spiked serum, in orange, **Magbeads-KRAS-G13C** + DNA-KRAS spiked serum; and **J)** In red, **Magbeads-KRAS-G13C** control, in blue, **Magbeads-KRAS-G13C** + non-spiked serum + 10 µM **Smart-C-Cy5**, in orange, **Magbeads-KRAS-G13C** + non-spiked serum + 20 µM **Smart-C-Cy5**, in light green, **Magbeads-KRAS-G13C** + spiked serum + 10 µM **Smart-C-Cy5**, in dark green, **Magbeads-KRAS-G13C** + spiked serum + 20 µM Smart-C-Cy5.

2.3.3. Discussion

In this part of Chapter 1, Chem-NAT was applied to develop new reagents and protocols to detect SNPs rather than to quantify nucleic acid molecules as in the first part of Chapter 1. Herein, the development of a bead-based platform for the identification of single mutations was developed as the first PoC of this kind. For initial PoC, the oncogene KRAS and one of its mutations, G13C, was chosen as model to be studied due to its huge impact in cancer and companion diagnostics.

The DGL probe selected for the KRAS mutation testing was designed in order to have the abasic position in front of the position 37 of the codon 3. Whereas WT KRAS sequence contains a guanine at that position, the variant G13C presents a thymine. This means that when Chem-NAT chemistry is applied, WT variant drives the incorporation of a Smart-C while that the G13C mutation does it with Smart-2dA. To this end, it was synthesised a DGL probe of 18 mer in length to which a mini-PEG unit was attached at the N terminus to solve the solubility problems, along with the inclusion of charges across the DGL probe sequence at certain gamma positions. Besides, this DGL probe (DGL-K13SRC) contains a chiral and negatively charged abasic position. As aforementioned, it does not exist a well-established structure-activity relationship for PNAs yet, that is why in this case a chiral and negatively charged blank position was selected. In fact, this PNA structure worked for KRAS testing as it also works for miR-21 detection.

Taking into account the qualitative approach of this assay, which only aimed to detect the KRAS mutation, FACS was selected as the readout platform. The first results showed that the DGL-13SRC was able to bind to a synthetic WT KRAS sequence which successfully drove the incorporation of the **Smart-C-Cy5** into the abasic position, and also to a synthetic KRAS sequence containing the mutation (G13C) which drove the incorporation of **Smart-2dA-Biotin**, which was then fluorescently labelled with SAPE. Furthermore, when the **Magbeads-KRAS-G13C** were incubated simultaneously with both KRAS sequences and both Smart-NBs, it was possible to distinguish between the WT KRAS and the mutated KRAS sequences, as it can be clearly seen in Figure 32. However, this first set of products and protocols were not able to find WT KRAS or G13C KRAS mutated target in NSCLC plasma patients.

In summary, a PoC bead-based platform for an alternative approach to the conventional techniques for KRAS mutation testing has been developed. This platform has shown its feasibility for discriminating a punctual mutation using cost-effective and universal reagents and a basic fluorescence platform, which is commonly and widely used in most laboratories of chemical biology. This platform could also be implanted for detecting circulating KRAS

mutated sequences in liquid biopsies; nonetheless, the main limitation lies in the sensitivity of the platform for detecting mutations which are presented at a low frequency in patients. Perhaps this bead-based platform can be more easily applied to solid tumour biopsies, wherein the amount of target KRAS will not represent a problem, rather than to liquid biopsies, in which its performance remains unclear. A possible solution to overcome these drawbacks could be the combination of this Chem-NAT platform with PCR techniques, what would ensure enough material for the bead-based platform to detect the KRAS mutations without a high cost.

CHAPTER III

Chapter 3. Development of bead-based technologies for cellular assays using Flow and Mass Cytometry

3.1. Polystyrene NPs – Versatile tools

3.1.1. Polystyrene NPs

Amongst the most employed nanomaterials in biotechnology, nanotechnology and nanomedicine there are found the polymeric and biocompatible NPs of polystyrene, which can be used for a myriad of applications [166]. Amongst these applications, it is of special interest their use as diagnostic tools [167]. As a result of their small size the NPs have a very large surface area which allows them to interact with biological systems offering quite interesting possibilities [168], such as cell uptake. In this sense, polystyrene NPs are easily, rapidly, and efficiently internalised by many types of cells, including adherent cells, suspension cells, stem cells, and primary cells [169],[170].

The polystyrene NPs are an interesting choice as diagnostic tools since they present several advantages compared to other diagnostic systems:

- A wide variety of small molecules with biological relevance are easily and efficiently conjugated in a controlled manner to the NPs following established solid phase peptide synthesis (SPPS) protocols.

- Despite the small size of the NPs, it is big enough to be detected by standard microscopy techniques, what enables their individual detection, which is a fundamental point in multiplexing cell-based assays.

- Multifunctionalisation of the NPs is easily afforded by following standard solid phase peptide chemistry protocols, enhancing and broadening the possible applications.

- Selective and bioorthogonal molecular activation can be done within cells without producing toxicity.

3.1.1.1. Synthesis and characterisation

The synthesis of polystyrene particles was firstly described as a process of dispersion polymerisation in EtOH to afford uniform polystyrene particles of 1 – 10 μm size range by using styrene, azo-type initiators, polymeric stabiliser polyvinylpyrrolidone (PVP), and an anionic, non-ionic, or comonomeric co-stabiliser [171]. It was later described another process for the synthesis of amino-functionalised polystyrene NPs by emulsifier-free emulsion

polymerisation. This new method employed styrene, vinylbenzylamine hydrochloride (VBAH), 2,2'-azobis(2-methylpropionamidine) dihydrochloride (AIBN·2HCl; V50) which acts as the reaction initiator, and 2% of divynilbenzene (DVB) to afford monodispersed cross-linked amino-functionalised polystyrene NPs ranging from 200 nm to 1 µm in size (Scheme 3) [172]. This synthetic method allowed the synthesis of amino-functionalised cross-linked polystyrene NPs of a wide range of size; moreover, the cross-linked component enhanced the robustness of the NPs [173]. Besides, amino-functionalised cross-linked polystyrene NPs undergo chemical reactions that allow the labelling of several molecules such as fluorophores [173],[174], oligonucleotides [170],[175]–[178], biomolecules [169],[170],[179],[180], metals[181],[182] or drugs [183], amongst others, with a non-toxic effect to the cells [170],[173],[184].

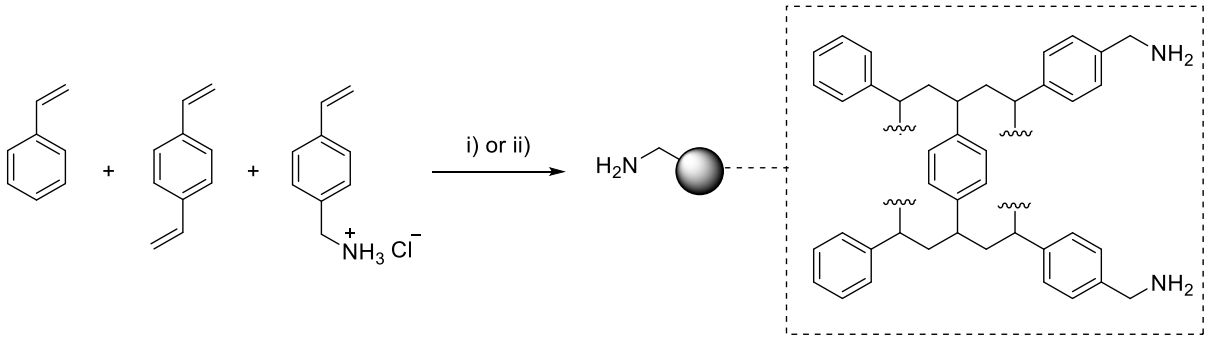

Scheme 3. Synthesis of amino-functionalised cross-linked polystyrene particles. **i)** Dispersion polymerisation: Styrene, DVB, VBAH, AIBN, PVP, in EtOH; **ii)** Emulsifier-free emulsion: Styrene, DVB, VBAH, AIBN·2HCl (V50), in H_2O.

Thereupon the synthesis and functionalisation of the amino-functionalised cross-linked polystyrene NPs, it is crucial to perform a thorough and rigorous characterisation, especially regarding the size, the stability, the surface, and the chemical composition. Although there are several techniques, not all of them are always employed. In fact, their usage will be done in accordance to the labels attached to the NPs, being sometimes used alone or in combination with others. The most commonly used techniques are shown in Figure 34.

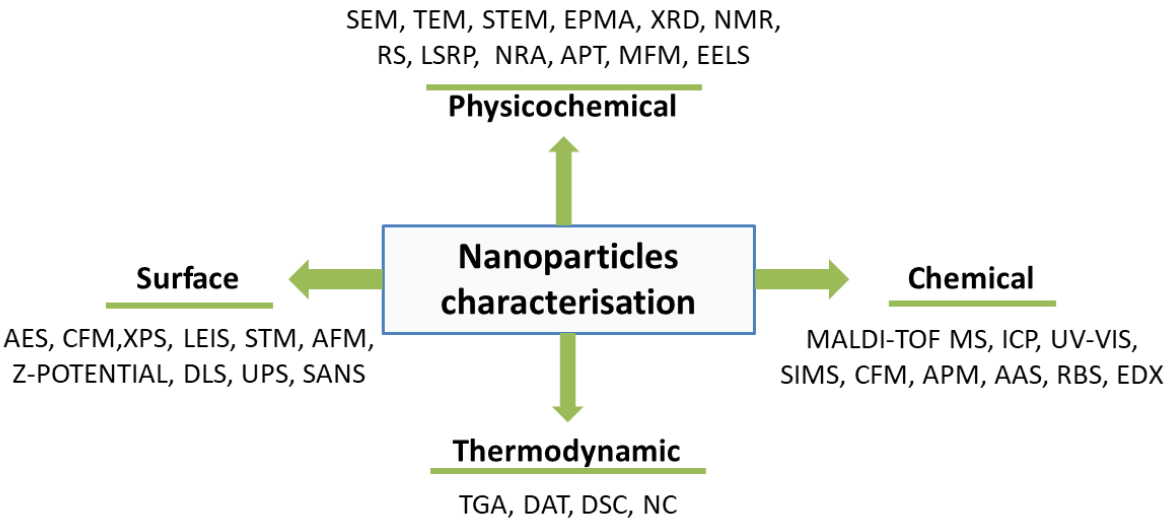

Figure 34. Some of the commonly applied techniques for the characterisation of the NPs. AAS, atomic absorption spectroscopy; AES, auger electron microscopy; AFM; atomic force microscopy; APM, atomic probe microscopy; APT, atomic probe tomography; CFM, chemical force microscopy; DLS, dynamic light scattering; DSC, differential scanning colorimeter; DTA, differential thermal analysis; EDX, energy-dispersive X-ray spectroscopy; EELS, electron energy loss spectroscopy; EPMA, electron probe microanalysis; ICP, inductively coupled plasma spectroscopy; LSRP, localised surface plasmon resonance; MFM, magnetic force microscopy; NC, nanocalorimetry; NMR, nuclear magnetic resonance; NRA, nuclear reaction analysis; RBS, Rutherford back scattering; RS, Raman spectroscopy; SANS, small-angle neutron scattering; SEM, scanning electron microscopy; STEM, scanning-transmission electron microscopy; STM, scanning tunnelling microscope; TEM, transmission electron microscopy; TGA, thermal gravimetric analysis; UPS, ultraviolet photoemission; UV-VIS, ultraviolet-visible spectrometry; XRD, x-ray diffraction; and XPS, x-ray photoelectron spectroscopy. Adapted from [185].

Regarding the most commonly used techniques for NPs characterisation, those generally employed in NanoChemBio lab should be highlighted.

3.1.1.1.1. Dynamic Light Scattering (DLS)

Also known as photon correlation spectroscopy (PCS) is based in that light scatters in all directions when a beam of light encounters a solution of particles, as a function of the size and shape of the particles. In DLS, a beam of light is incised into a solution containing particles, analysing the intensity fluctuations of the scattered light over the time as a result of the Brownian motion of the particle in solution, obtaining the diffusion coefficient (D_T) that is related to the hydrodynamic size. Thus, it is obtained the polydispersity index (PDI) as a measure of the size, which ranges from 0 (monodisperse) to 1 (polydisperse), considering values <0.1 as monodisperse systems, values within 0.1 and 0.7 as nearly monodisperse systems, and values >0.7 polydisperse systems [186].

3.1.1.1.2. Scanning Electron Microscopy (SEM)

SEM is a technique based on the scanning of the NPs surface with a focused beam of electrons, detecting the secondary electrons scattered off the surface [187], which allows observing the dispersion and agglomeration of the NPs and the surface morphology, amongst others [185],[188]. SEM can be considered a method for the absolute determination of the particle size as each particle can be individually examined. Nevertheless, SEM encounters problems with small particles due to diffraction effects, causing blurring at the edges [185].

3.1.1.1.3. Scanning Transmission Electron Microscopy (STEM)

STEM is a particular type of high resolution TEM combining both SEM and TEM, employed for the characterisation of the NPs [189]. While TEM focuses on the beam electrons transmitted by NPs, STEM also scans the surface of the NPs following a pattern, detecting scattered beam electrons and secondary electrons, like in SEM, but enhancing the spatial resolution to afford high resolution images [185]. This amelioration is achieved by employing a high-angle annular field (HAADF) detector, which also enhances contrast, especially of heavy metals conjugated to the NPs; hence the electron-dense areas appear darker [187]. Furthermore, HAADF detector allows the determination of the chemical composition of NPs as well [190].

3.1.1.1.3. Zeta potential

It measures the difference in potential between the fluid in which a particle is dispersed and the layer of fluid containing the oppositely charged ions that is associated with the particle surface. Zeta potential is, in fact, a measurement and quantification of the effective electric charge of the surface of the NPs [191]. Additionally, the Zeta potential provides information about the stability of the NPs dispersions, which are considered to be more stable at higher values, generally over 18 mV for latex polymers [192].

3.1.1.1.4. Inductively Coupled Plasma Mass Spectrometry (ICP-MS)

It is a sensitive method for the analysis and quantification of the metal ions presented in the NPs with high linear dynamic range. In ICP-MS the NPs are introduced in argon plasma which converts the material into individual positively charged ions; then, the positive ions enter into a quadrupole mass analyser where they are separated according to their ratio mass/charge (m/z), allowing the detection of the element [185].

3.1.1.1.5. Energy-Dispersive X-ray Spectroscopy (EDX)

This technique allows the characterisation of the elemental composition of the NPs by detecting the emitted X-rays from the NPs when X-rays hit the sample. This is achieved on the grounds that X-rays characteristic energy is unique to the atoms presented in the NPs [185],[193].

3.1.1.1.6. X-ray Photoelectron Spectroscopy (XPS)

In XPS, the NPs surface is bombarded with X-ray, making the electrons to absorb energy and to be expelled as photoelectrons. These emitted photoelectrons come from the inner orbitals (such as K orbitals) and have unique and characteristic energies [185]. Consequently, the elemental and chemical composition of the NPs can be identified by analysing the binding energy [194].

3.1.1.1.7. Fluorescence-Activated Cell Sorted (FACS) and Fluorescence Microscopy

Both are fluorescence based techniques that there were firstly designed for cells. These two techniques allow the characterisation and detection of fluorescently labelled NPs, either by themselves or within biological systems by exciting a fluorophore with a laser and collecting the released fluorescence [195],[196]. The election of the excitation laser and the fluorescence collecting filters depends on the fluorophores absorbance/emission spectra.

3.1.1.2. Functionalisation of amino-functionalised cross-linked NPs

The amino-functionalised cross-linked polystyrene NPs can be easily functionalised by routine solid phase chemical reactions thanks to the amino-functionalisation [173]. Because of cross-linkage with DVB, polystyrene NPs can be chemically modified in organic solvents like DMF or hydrophilic solvents like H_2O. Furthermore, NPs suspensions are also stable in PBS, MeOH, EtOH, DMSO, ACN, THF, and dioxane; however, they are unstable in Et_2O and DCM.

The chemical reactions are mostly performed by coupling an acid group to the amine group of the NPs to afford an amide bond. In order to achieve this reaction, the acid has to be firstly activated. For that, there has to be used activation reagents, which react with the acid group to generate an active specie capable of reacting with the amine group. Amongst other activation reagents, oxime carbonates have been proposed as novel reagents [197] and their combination with cabodiimides is widely used since it provides better yielding and purity by forming active esters [198]. In addition, the commercially available OxymaPure [199] shows better coupling efficiency and circumvents the security problems associated with the typically employed SPPS reagent HOBt [198],[199]. The carbodiimides frequently used

for amide form formation are DIC [200] which is employed with organic solvents, and EDC [201], also known as WSC (water soluble carbodiimide), which is used in water [202].

In order to quantify the loading of the NPs, an aminoacid with the amine group protected with Fmoc group, usually Fmoc-glycine-OH, is coupled to the NPs via acid-amine reaction. Then, the Fmoc protecting group is removed with piperidine, which allows Fmoc quantification by measuring the dibenzofulvene-piperidine adduct that is formed [203]. This measurement not only allows the quantification of the loading of the NPs but also monitoring the coupling efficiency of the upcoming reactions. Thus, as the amine group is free to react, another Fmoc protected aminoacid or spacer can be coupled to the NPs. A serie of spacers can be coupled to the NPs by following cycles of protection and deprotection reactions. Nonetheless, this has the drawback of enlarging the chain by only one site, which limits the range of spacers or molecules that can be conjugated. On top of that, the larger the chain is, the lower the loading and the lower the coupling efficiency are, reaching a point wherein performing a coupling could not be worthy. So as to overcome these problems a bi-functionalised spacer protected with orthogonal protecting groups, such as Fmoc-Lysine-Dde-OH, can be introduced. Thus, Fmoc and Dde protecting groups can be full orthogonally deprotected [204], allowing the introduction of two different molecules at different time-points, such as a fluorophore and a protein. The scheme of the amino-functionalised cross-linked NPs multi-functionalisation is shown in Scheme 4.

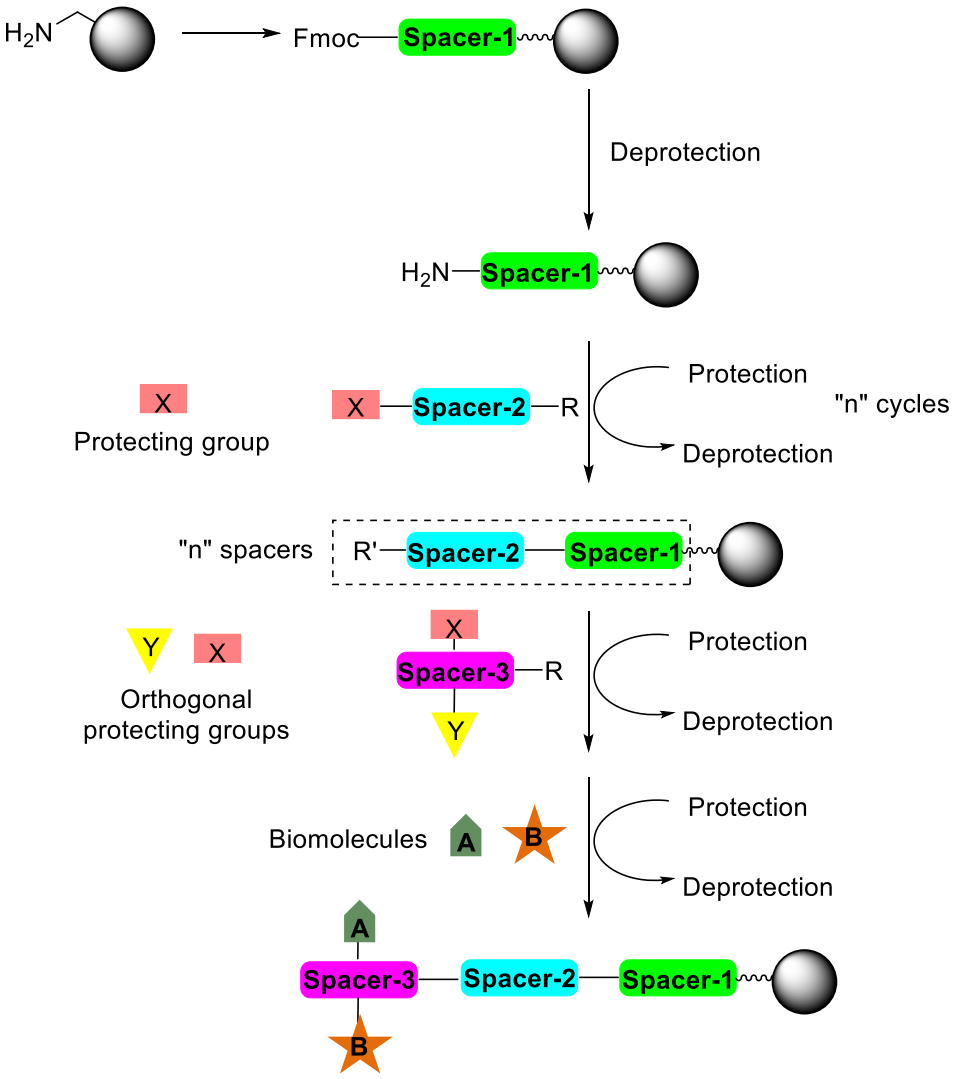

Scheme 4. Multi-functionalisation of amine-functionalised cross-linked polystyrene NPs.

3.1.1.3. Applications of amino-functionalised cross-linked NPs

As aforementioned, following this chemical strategy for the multi-functionalisation, the amino-functionalised cross-linked NPs have been successfully conjugated with several molecules, according to the desired application. Amongst them, it is important to remark:

3.1.1.3.1. Cell proliferation tracking

An efficient fluorescent-based method using fluorescently-labelled polystyrene NPs to track cell proliferation has been developed. For that, several adherent and suspension cell lines were incubated with 200 nm fluorescent polystyrene NPs for their internalisation. Then, every day since the moment of the uptaking process was completed, and for 7 days, samples of the nanofected cells were taken and the fluorescence was evaluated by flow cytometry. The fluorescence was reduced upon cell division, allowing tracking cell proliferation [205]. This novel method supposes a methodological advantage for monitoring

the proliferation in hard-to-transfect cells in long-term assays employing the well-established flow cytometry.

3.1.1.3.2. Nucleic acids delivery

The development of DNA-conjugated [176] and siRNA-conjugated NPs [170],[175],[177],[178] for the delivery of genetic material has been reported.

On the one hand, plasmid DNA was efficiently conjugated to carboxy-functionalised NPs to afford DNA-conjugated NPs which were employed for DNA delivery. These NPs allowed the successful transfection of plasmid DNA into hybridoma T cells, which are hard-to-transfect cells, leading to the expression of a biologically relevant protein involved in cell signalling processed, fused to YFP (yellow fluorescent protein) [176].

On the other hand, siRNA-conjugated NPs have been employed for several approaches such as eGFP (enhanced green fluorescent protein) protein silencing in HeLa cells without detrimental toxicity. Furthermore, these siRNA-conjugated NPs also contained a fluorophore (Cy5) which enabled tracking the NPs and enhanced the accuracy of selecting silenced cells [175]. In this sense, the silencing of GFP by siRNA-conjugated NPs was also reported, but employing a thiol-based strategy [177]. Moreover, the siRNA-conjugated NPs were also used for the efficient delivery of biological material in both undifferentiated and differentiated embryonic stem cells without harming the cells in terms of cytotoxicity or pluripotency [170].

Thanks to the easy and efficient conjugation of nucleic acid material, the non-toxicity, the proven and validated effectiveness, and the robustness, these NPs are definitely considered an excellent alternative to other delivery technologies [178].

3.1.1.3.3. Proteins carriers and protein delivery

A set of particles of different size, 200 nm, 500 nm, and 2 μm, have been efficiently functionalised with proteins for their evaluation as protein delivery systems [169],[170],[179]. The selected proteins were eGFP and β-Galactosidase. The protein-loaded particles proved to be a valid system for carrying proteins and deliverinf them in several cell lines [179], including embryonic stem cells [170] and neural stem cells [169]. Moreover, in order to check the functionality of the β-Galactosidase protein conjugated to the NPs after it has been delivered, a specific fluorogenic substrate that released a fluorescence proportional to the protein activity upon hydrolysis was used [179]. Besides, the protein-loaded NPs were also fluorescently labelled, which allowed the easy and accurate detection of the nanofected cells by flow cytometry and by fluorescence microscopy [169],[170].

3.1.1.3.4. In-cell sensing

The application of amino-functionalised cross-linked NPs as sensor has been assessed and validated in three cases:

(i) **pH sensors in living cells** through the real time measurement of intracellular pH in living cells by using fluorescent covalently loaded particles. This application has been validated with several techniques such as spectrofluorometry, fluorescence microscopy, and flow cytometry. The key point of this pH sensing application lies in the fluorescein covalent binding to the particles, eliminating leakage of the dye, which is translated into a dramatically improvement of the stability of the indicator overtime. Furthermore, this keeps the properties of the fluorescein for pH sensing, as its fluorescence intensity varies according to the pH values [206].

(ii) **Real-Time calcium sensing** by functionalising the cross-linked amino-functionalised particles with Indo-1, a molecule sensor which was sensitive to changes in cytosolic calcium concentration due its acid groups chelate the Ca^{2+} ions. A rise in intracellular Ca^{2+} ions was followed by a decrease as a result of the rapid and good sensitivity of the calcium-sensor loaded particles. Besides, it is quite remarkable that these sensor-based particles, likewise the pH-sensor particles, avoid problems related with cellular leakage, what allows performing long term studies [180].

(iii) **Apoptosis sensing**. Multifunctionalised NPs were synthesised to determine, monitor and measure apoptotic processes mediated by caspase-3/7 in living cells. These NPs carried the fluorophore Cy5 to act as a tracker, and a non-fluorescent peptide comprising a peptide substrate of caspase-3, DEVD, and a fluorogenic reporter, AFC (7-amino-4-trifluoromethylcoumarin). Thus, in an apoptotic state, the overexpressed caspases-3/7 bind to their substrate DVED, cleaving the DEVD-AFC bond and releasing fluorescence which is proportional to the amount of caspase-3/7 [207]. This sensor allows the *in situ* detection of apoptosis mediated by several caspases.

3.1.1.3.5. Proteomic analysis of drug targets

It has been lately reported the synthesis of drug-loaded NPs capable of penetrating mammalian cells and capable of binding target proteins in the intracellular environment [183]. Azide-modified tyrosine kinase inhibitor Dasatinib was successfully conjugated to alkyne-modified fluorescently labelled NPs via Click chemistry reaction [51],[208] in order to assess the ability of the drug-loaded NPs to bind to its target the SRC kinase protein. As a result, the Dasatinib-loaded NPs not only bound to the SRC kinase target protein *in cellulo*, but also

induced a reduction in SRC activity *in vitro*, indeed [183]. Therefore, this Click-chemistry based stratey can be used to prepare a set of drug-loaded NPs for proteomic approaches.

3.1.1.3.6. Multifluorescent and molecular imaging tools

The synthesis and functionalisation of fluorescently labelled NPs have been widely mentioned before; nevertheless, it is important to highlight that these NPs can be functionalised with a great variety of dyes, not only for the aforementioned applications along with other cargoes, but also for molecular imaging and fluorescence-related technologies. In this regard, the synthesis of NPs carrying fluorophores such as Dansyl [173],[174], Rhodamine B [173],[174], 5(6)-carboxyfluorescein [173],[174], Texas Red [174], Cy5 [205], carrying xanthene dyes [209], and carrying streptavidin-conjugated NPs for an indirect fluorescent labelling using biotinylated fluorescein [210], has been reported.

3.1.1.3.7. Cytosolic catalysts

The synthesis of palladium-conjugated polystyrene NPs for bioorthogonal organometallic chemistry inside living cells was reported. These palladium-conjugated NPs contained Pd^{2+} ions coordinated with the free amine groups and the aromatic rings of the polystyrene NPs, which provide an electron-rich network. The Pd^{2+} ions were then trapped by extensive crosslinking and their subsequently reduction to Pd^{0} particles. The amino-functionalised cross-linker molecule allowed coupling a fluorophore to the NPs for their easy tracking [181],[182].

Due to the presence of palladium, these NPs acted as cytosolic nanoreactors capable of giving rise to a fluorescent compound by catalysing the Suzuki-Miyaura cross-coupling reaction [211],[212], of two non-fluorescent compounds, within HeLa cells [181],[182]. Thus, intracellular bioorthogonal prodrug activation can be accomplished with these NPs, avoiding the undesired side-effects of drugs.

3.1.2. Mass Cytometry

3.1.2.1. Brief overview

After several efforts in 2007 and 2008 [213]–[216], in 2009 Scott Tanner and his group, from the University of Toronto, introduced mass cytometry, a novel and cutting edge analytical platform which allows the simultaneous detection and quantification of nearly 40, and up 52, markers within cells, with single-particle resolution [213],[217]. Mass cytometry is an adapted form of mass spectroscopy combined with flow cytometry that overcomes the main limitations of flow cytometers, related to the spectral overlapping between fluorescent signals [218], and exponentially increasing the number of markers that can be identified within a single analysis [213]. Mass cytometry consists in an inductively coupled plasma (ICP) as the ionizing source, with a time-of-flight (TOF) mass spectrometer (MS) – ICP-MS tuned to the elemental weight range of the isotopes of study [216],[219]. Therefore, isotopes of rare earth elements or other several elements, which are not usually presented in cells, are tagged to antibodies. These tagged antibodies are employed for staining the cells. Afterwards, the cells are rapidly passed through a 7,500 K argon plasma, as individual cells at a time [213],[219], which transforms the individual cell content into ions. These ions go through the MS-TOF, enabling the detection of those isotopes that fall within the CyTOF instrument mass range, thereby creating a cell-by-cell thorough information report analogous to a flow cytometry data file [219]. Nevertheless, the differences between flow cytometry and mass cytometry are quite significant. Although both platforms allow a single-cell resolution, flow cytometry speed is higher, ~25,000 cells/s, than mass cytometry, ~1,000 cells/s; on the other hand, mass cytometry offers much more sensitivity enabling the detection of ~1,500x10^7 molecules/cell whilst flow cytometry enables the detection of ~5x10^7 molecules/cell [219]. Furthermore, despite the common thinking of the high cost of mass cytometry reagents, when the commercial reagent cost of flow and mass cytometry, estimated based on the price of commercially conjugated reagents or unconjugated antibodies and commercial conjugation kits, are compared, surprise come to mind. The commercial reagent cost measured as price per probe per test is considerably cheaper in mass cytometry ($1.50-$3.00) than in flow cytometry ($2.00-$8.00) [220]. On top of that, mass cytometry requires new chemistry and detection optimisation for every new developed parameter, and approximately 70%of the cells ejected from the nebulizer do not maintain full integrity [219]. Figure 35 depicts how mass cytometry works and Figure 36 shows the elements that are susceptible to be detected by CyTOF.

Nowadays, the CyTOF instrument is exclusively commercialised by Fluidigm Corporation (FLDM-NASDAQ) after it acquired the Canadian company DVS Sciences for $207.5 million in 2014.

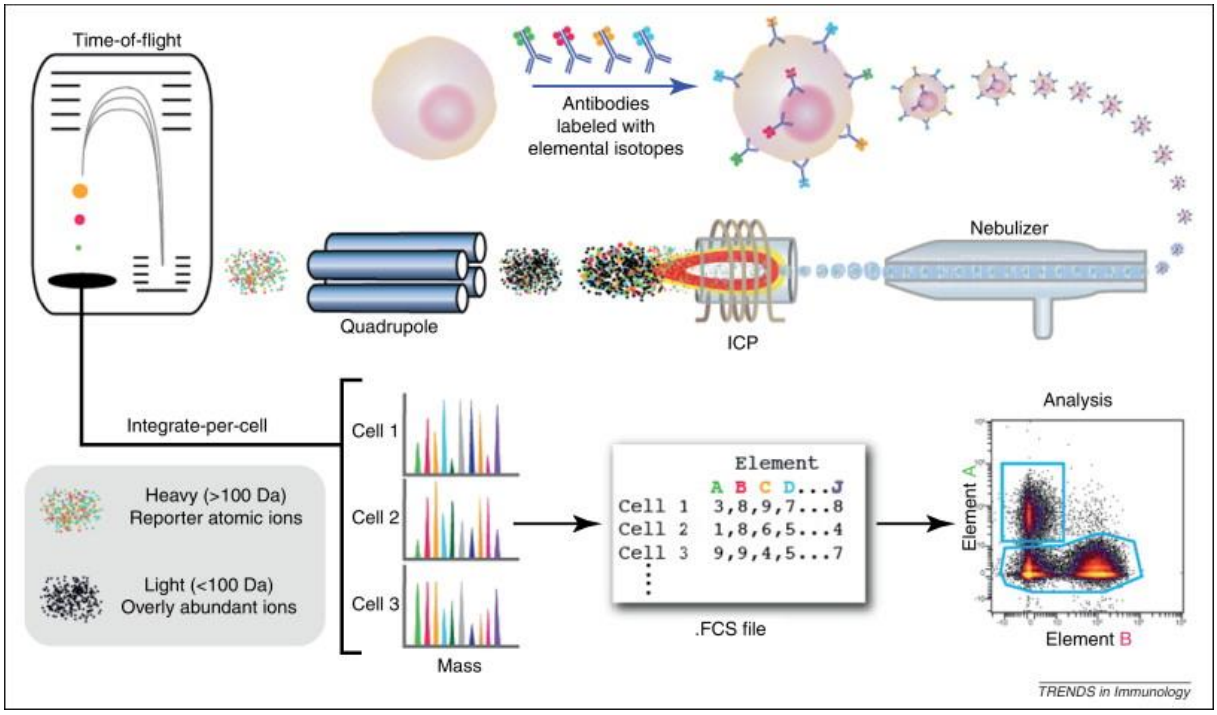

Figure 35. Scheme of mass cytometry workflow. Metal-tagged antibodies are firstly bound to cell antigens, and then the cells are passed through a nebuliser that transforms the metals in ions. These ions enter inside, being separated in the quadrupole and in the TOF, what enables the identification of the different elements. Signals corresponding to the metal tags are correlated with the presence of the respective markers within cells (Reproduced with permission from [220]).

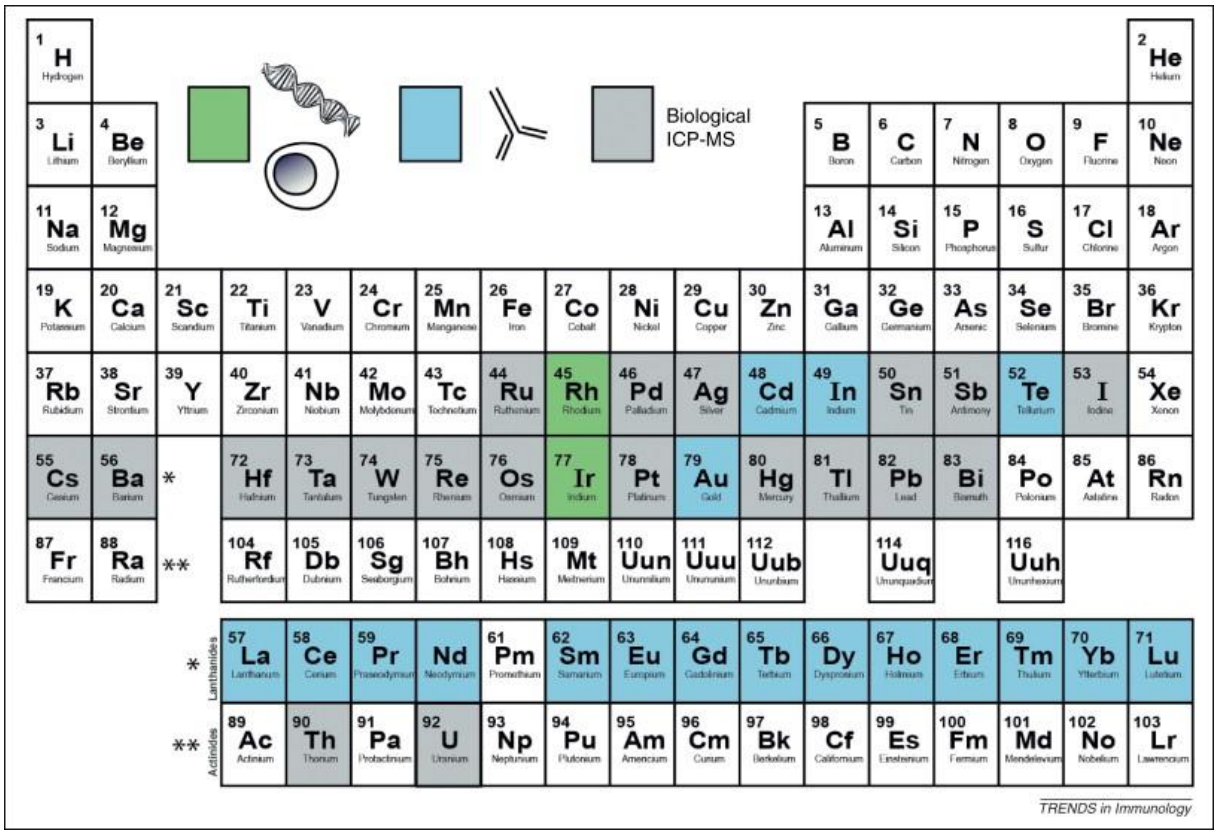

Figure 36. Periodic table of the elements. The coloured elements present at least one stable isotope having an atomic mass > 100 Da and can be used in mass cytometry (Reproduced with permission from [220]).

3.1.2.2. Mass cytometry reagents

Currently, the vast majority of the mass cytometry reagents are antibodies conjugated to metal-containing polymers. These metals are specific and stable metal isotopes of defined mass, which act as reporters. The conjugation typically takes place through chelation, which allows the polymer to contain several copies of the metal isotope, usually lanthanides. Moreover, the signal levels of the metals are correlated with the antigen expressions in the individual cell, thereby enabling quantification.

Contrarily to flow cytometry, cell events cannot be detected by light scattering. Therefore, cells are detected by using DNA intercalator iridium (Ir) or rhodium (Rh), and measuring the cell-induced ion clouds duration ("event length"), which enables to determine the DNA content and approximate size, respectively [217],[221],[222]. Besides, from the total of 24 elements capable of being detected by ICP-TOF MS, there are 14 commercially available lanthanides (from La to Lu, except Pm) [220],[223], making a total of 38 pure and stable single mass isotopes. Nevertheless, other elements have been investigated as mass tags: yttrium (Y), indium (In), iodine (I), cadmium (Cd), tellurium (Te), silver (Ag), palladium (Pd),

rhodium (Rh), iridium (Ir), platinum (Pt), ruthenium (Ru), osmium (Os), and bismuth (Bi) [223].

In the firsts mass cytometry reports, Tanner and colleagues employed lanthanide-containing polystyrene beads [213],[216]. This election was based on the lanthanides low natural abundance, the large number of resolvable isotopes (54), and their similar chemistry [224],[225]. Later, metal-containing polystyrene beads were employed for the calibration of the instrument, finding that polystyrene beads ranging from 0.8 to 3 μm were suitable for standard mass cytometry [224]. Two groups of reagents were developed for mass cytometry: on the one hand, the non-polymer-based reagent and, on the other hand, the polymer-based reagents. In both cases coordinative ligands such as bifunctionalised maleimido-mono-amide-DOTA compound (mDOTA) or polymeric pentetic acid (DOTA) are employed to chelate the metals [223].

As non-polymer-based reagents, mass-tag reagents for multiplexing assays have been developed. These reagents consists of a lanthanide isotope ion loaded inside the chelator ligand that contains a reactive tag to covalently bind the target (Figure 37-A) [226]. On the other hand, the synthesis of metal-chelating polymers (MCP) easily attached to antibodies for their application in mass cytometry has also been reported [216],[227]. These polymers were functionalised with diethylene triamine pentaacetic acid (DTPA) or 1,4,7,10-tetraazacyclododecane-1,4,7,10-tetraacetic acid (DOTA) chelating groups, which allowed the chelation of an average of 35 trivalent metal lanthanide ions (Gd^{3+}) per polymer [217],[227]. Afterwards, the number of metal isotopes linked to antibodies was increased up to approximately 50 [228],[229]. The polymer is functionalised with maleimide groups to enable the antibodies attachment via Michael addition of a thiol group in the hinge region [230], which is previously generated by the mild reduction of a disulphide bond (Figure 37-B) [216],[227],[229].

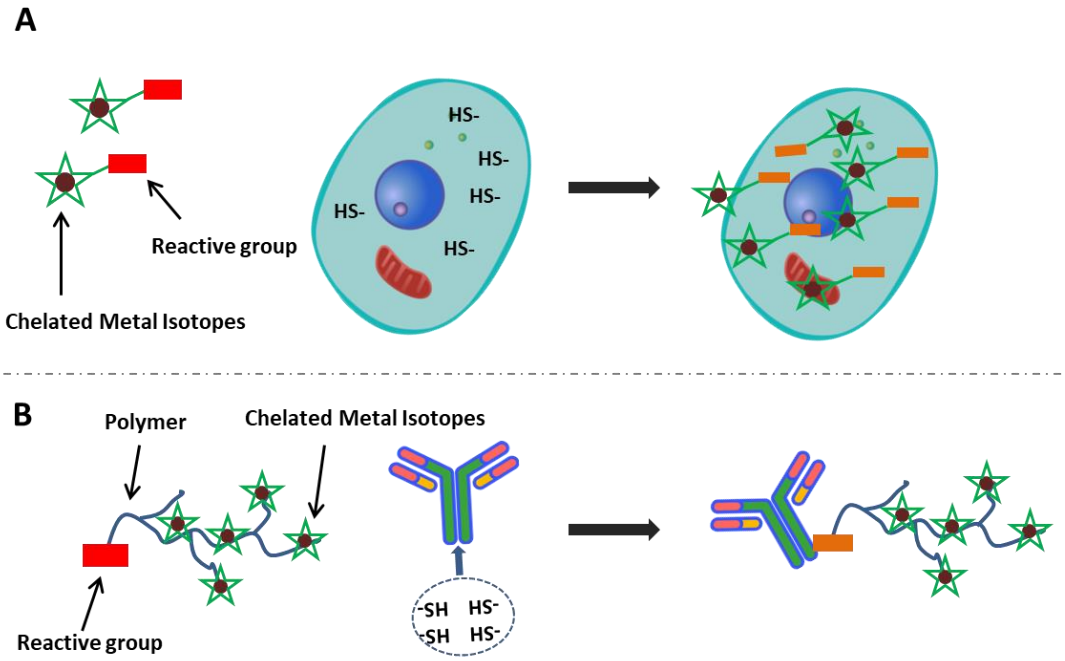

Figure 37. A) Non-polymer based strategy mass-tag reagents; **B)** Polymer-based mass-tag reagents.

Following the non-polymer-based strategy, the synthesis of palladium-based reagents has been described [231],[232]. Six palladium stable isotopes with masses 102, 104, 105, 106, 108, and 110 u, which fall below the 139 – 176 u mass range of the lanthanides and within the range suitable for mass cytometry [217], were functionalised with the bifunctionalised molecule isothiocyano-benzyl-EDTA to afford palladium chelates capable of covalently tagging cells through amine groups [232]. Interestingly, the development of not even non-polymeric-based mass cytometer reagents but also non-chelation-based reagents has been reported over the last few years [233]–[238]. These reagents are probes containing the metal as a part of their chemical structure and can be used alone or tagged to antibodies. These are the platinum-based reagent cis-dichlorodiamine-platinum(II) (cisplatin) which can be used alone as a probe [234] or tagged to antibodies [235],[236], the palladium-based reagent dichloro-(ethylenediamine) palladium(II) (DCED-Pd) [235], and tellurium-based reagents [233],[237],[238].

On the contrary, following the polymer-based strategy, fluorescent poly(N-alkylacrilamide) polymers carrying DTPA for metal chelation and orthogonal maleimide group for the covalent tagging of antibodies has been reported [216],[227]–[229],[239]. Recently, the development of biotinylated lanthanide NPs ($NaHoF_4$) containing 15,000 Ho atoms per probe, and capable of tagging streptavidin in a microgel via biotin-streptavidin binding, has been reported [240]. Furthermore, it was reported that these $NaHoF_4$ NPs coated with a maleimide-modified pegylated silica shell enabled antibody tagging through thiol-maleidimide strategy [241].

A recently published article in 2018 gathers the aforementioned different methods for metal-isotope tagging to monoclonal antibodies for high-dimensional mass cytometry [223].

3.1.2.3. Mass cytometry applications

Although it took many years to develop CyTOF, the quick development of mass-tag reagents has enabled to analyse the multiparametric attribute of the analytical platform through vast multiparametric and high-dimensional single-cell applications covering a wide range of fields. Most of the single-cell mass cytometry studies have been focused on the immune system, although they are not exclusive. Many other studies have been focused in basic research, therapeutics, pharmaceutical development, elemental biodistribution, pathogens, solid tumours, leukaemia, or stem cells, amongst others [217],[223]. The single-cell mass cytometry studies have been developed with several main purposes: (i) immune and phenotype profiling and quantification, (ii) intracellular signalling pathways identification, (iii) cellular integrity and functionality determination, and (iv) high-throughput barcoding [223].

Regarding the immune system studies, in the firsts reports “single-cell” mass cytometry was applied to perform a deep proteomic study in which the signalling responses in specific immune cell subsets within the hematopoietic continuum was assessed [219],[242]. Mass cytometry was applied to stimulated CD8+ T cells, obtaining about 200 distinguishable subtypes of cytokines, revealing a very complex network [217],[243]. Single-cell mass cytometry has enabled the study of cell signalling during naive T-cell expansion. This has led to the development of a method for inducing T-cell activation and differentiation towards T-stem cell memory-like phenotype, tracing the cell fate across division states and time [244]. Furthermore, a mass cytometry workflow for standardised, systems-level biomarker discovery in immunotherapy trials has been very recently reported [245]. Besides, single-cell mass cytometry has also been applied for systemic lupus erythematosus [246].

As aforementioned, not all the studies have been focused on the immune system. Single-cell mass cytometry enabled the identification of early reprogramming regulators, thus deconvoluting the first steps that lead to pluripotency acquisition of adult cells [247]. Moreover, leukaemias and solid tumours have also been within the range of study by mass cytometry. In this sense, mapping healthy and cancerous bone marrow samples to compare leukaemia diagnosis and relapse samples, and the identification of a rare leukaemia population reminiscent of minimal residual disease have been successfully achieved [248]. Likewise, the B cell precursor acute lymphoblastic leukaemia single-cell-based study at diagnosis enabled its developmental classification. In addition, developmentally dependent cell signalling states associated with relapse were revealed [249]. Regarding solid tumours, single-cell mass cytometry allowed a thorough single-cell phenotypic characterisation of

high-grade serous ovarian cancer (HGSOC). Thus, cell subsets that co-occurred across tumours with potentially critical roles in metastasis and relapse were profiled [250]. In addition, research has been focused on the development of biocompatible toolkits for mass cytometry for activity-based profiling of single cells, such as the identification of hypoxic cells [233].

Cell cycling phase analysis is fundamental to obtain a complete biological evaluation [217]. Hence, Behbehani et al. reported a panel of metal-chelated antibodies to provide a comprehensive analysis of the cell cycle progression. This panel included a combination of antibodies against cyclins, phosphorylated retinoblastoma (Rb), phosphorylated histone H3, and Ki67 to identify cells in phases G0, G1, G2, and M, of the cycle. Furthermore, 5-iodo-2-deoxyuridine (IdU) was also employed [251]. Iodo-deoxyuridine has been widely used for cell cycle analysis since it incorporates into newly synthesised DNA. Due to the presence of iodine, which has an atomic mass of 127, its incorporation is detected by mass cytometry, enabling the clear and direct detection of S-phase cells and increasing the resolution between the G1 and G2 phases [217].

In cell viability analysis by mass cytometry, Cisplatin is the most employed reagent due to its covalent binding to compromised cells, forming extremely stable DNA-platinum adducts, enabling the identification of viable cells [234]. Given that platinum (Pt) has six stable isotopes with three dominants (194, 195, and 196) well separated from the lanthanides, it is an excellent reagent for cellular viability measurements by mass cytometry [217]. Besides, studies have demonstrated not only the potential of platinum but also of palladium for cellular viability assays [252]. In this regard, a palladium-based reagent (DCED-palladium) that covalently binds to death cells, showing a better performance than cisplatin, has also been reported [235].

Regarding high throughput barcoding, several mass-tag reagents have been reported [226],[232],[235],[238]. The first mass-tag barcoding reagent consisted of a combination of 7 lanthanide isotopes (La139, Pr141, Nd146, Tb159, Ho165, Tm169, and Lu175) to generate 128 combinations, allowing the characterisation of PBMC signalling dynamics and cell-to-cell communication [226]. Curiously, 18,816 phosphorylation levels from each multiplexed sample were quantified in this experiment. Interestingly, a method in which 120 codes with 10 different metal isotopes for the analysis of T-cell has been described [253],[254]. Nonetheless, using lanthanides for high throughput barcoding could compromise the number of channels in CyTOF, decreasing the multiparametric capacity of the platform. Hence, a novel palladium-based barcoding reagent, consisting in 6 stable palladium isotopes that can be combined following a 6-choose-3 scheme, affording 20 individual barcodes, following

doublet-filtering barcoding was reported [232]. This 6-choose-3 scheme (n-choose-k) refers to a mixture of 6 barcodes (number of palladium channels), selecting 3 channels/plots to be analysed. The combination will give rise to one definite barcode (Figure 38). Besides, following the aforementioned scheme allows combining barcoding reagents at desire. In fact, following this scheme, a combination of four palladium isotopes and two indium isotopes labelled to anti-CD45 were employed for barcoding PBMCs [236]. Recently, a monoisotopic cisplatin-based barcoding without requiring cell permeabilisation has been developed [255]. Similarly, an antibody-conjugated platinum-based reagent targeting both the beta-2-microglobulin of the MHC class I complex and the sodium-potassium ATPase-subunit (CD298) which are broadly expressed in the cell surface, has been published. In addition, the platinum-based reagent can also be also applied to other elements such as indium to barcode up to 20 samples following the 6-choose-3 scheme [235]. Likewise, the development of tellurium-based reagents for live and fixed cell barcoding by employing the tellurium probes TeMal has been reported. These probes combine four tellurium isotopes, 124, 126, 128, and 130, and could eventually afford 35 barcodes [238]. Besides, ratiometric-based barcoding with 3 metal isotopes and 4 ratio intensities to afford 16 barcodes has also been described [256].

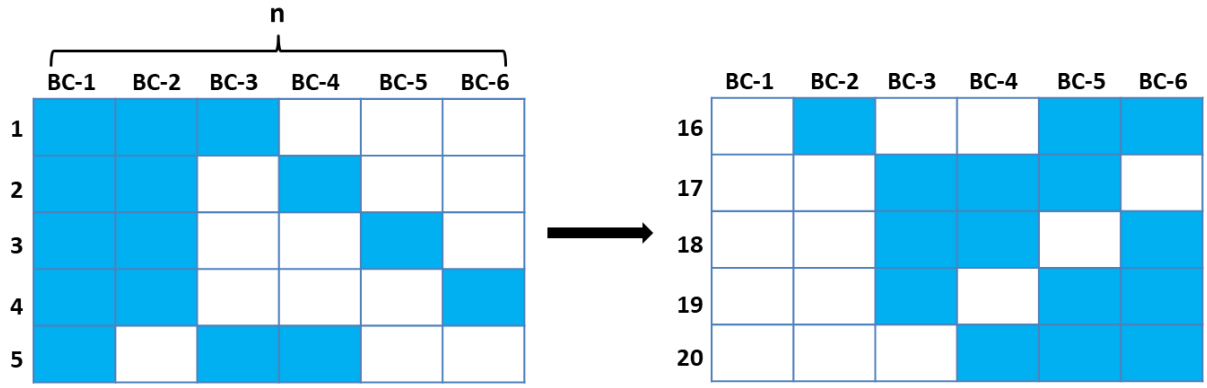

Figure 38. Depiction of the doublet-filtering barcode n-choose-k wherein “n” is the number of possible barcodes (BC-6), defined by the number of channels in CyTOF, and “k” is the number of plots/channels selected for each condition (in blue). The total number of possible combinations determines 20 final barcodes (Adapted from [232]).

3.2. Metallofluorescent NPs

The development of metallofluorescent NPs, carrying simultaneously a fluorophore and a metal, acting as multimodal probes for cellular applications has been successfully accomplished. These multimodal NPs were designed to be reagents with application in several approaches: 1) Fluorescence, such as flow cytometry, fluorescent microscopy, molecular imaging, and fluorescence-lifetime imaging (FLIM); 2) Bioorthogonal catalysts since different metals can be conjugated, such as palladium, copper or nickel; and 3) Mass-based platforms, such as mass cytometry, that allows the detection of multiple elements and their pure isotopes.

Thus, the synthesis and development of the metallofluorescent NPs with multimodal applications is hereby described in chapter 3. This research has been published in ACS Omega journal [257].

3.2.1. Results

Firstly, amino-functionalised cross-linked polystyrene NPs were synthesised following NanoChemBio group established protocols. For that, dispersion polymerisation and modified emulsifier-free emulsion polymerisation methods were employed.

On one hand, as dispersion-polymerisation method, a mixture of EtOH:H_2O (86:14) was mixed with styrene, DVB, poly(N-vinylpyrrolidone) (PVP) of 29,000 g/mol of molecular weight (stabiliser), VBAH (**3**), and AIBN (radical initiator), under argon atmosphere. The mixture was stirred under argon atmosphere at 68 ºC for 4 h. Then, NPs suspension was cooled for 30 min prior washing with MeOH and water through centrifugation-dispersion cycles, affording monodispersed and amino-functionalised cross-linked polystyrene NPs. A 92% of yield was obtained. On the other hand, modified emulsifier-free emulsion polymerisation method, VBAH (**3**) and $MgSO_4$, which acted as stabiliser, were added to previously purged water, under argon atmosphere. The mixture was stirred at 80 ºC for 30 min, and then, radical initiator 2,2'-Azobis(2-methylpropionamidine) dihydrochloride (V_{50}) was added. This led to an emulsion formation, which was stirred at 80 ºC for 4 h, under argon atmosphere. Thereupon, amino-functionalised cross-linked polystyrene NPs were washed with MeOH and water through centrifugation-dispersion cycles, in order to purify them. Both synthesis were performed in a 90 mL reactor (Figure 39)

Figure 39. 90 mL reactor for the synthesis of amino-functionalised cross-linked polystyrene NPs.

In order to develop metallofluorescent NPs, a set of polystyrene NPs with different sizes and labelled molecules has been synthesised. A summary of these NPs is shown in Table 16, including the abbreviation, the size, and the main conjugated molecules. All the particles have been synthesised following established SPPS protocols [181] and successfully characterised.

Table 16. Design of the different particles prepared and used in this Doctoral Thesis. All the NPs were covalently bound to their cargo through amide bonds. PEG = 1-amino-4,7,10-trioxa-13-tridecanamine succinamyl.

PARTICLE	SIZE (nm)	SPACER	DYE	ADDITIONAL
NH_2-PEG-NP	500	PEG	-	-
NH_2-Gly-NP	500	Glycine	-	-
Cy5-NP	500	PEG	Sulfo-Cy5	-
Fmoc-Lys(Cy5)-NP	500-900	PEG / Lysine	Sulfo-Cy5	-
Strp-Lys(Cy5)-NP	1200	PEG / Lysine	Sulfo-Cy5	Streptavidin
A647-NP	500	PEG	ATTO 647N	-
Fmoc-Lys(A647)-NP	900-2500-5000	PEG / Lysine	ATTO 647N	-
Pd(II)-Cy5-NP	500	PEG	Sulfo-Cy5	Pd^{2+}
Cu(I)-Cy5-NP	500	PEG	Sulfo-Cy5	Cu^{2+}
Ni(II)-Cy5-NP	500	PEG	Sulfo- Cy5	Ni^{2+}
Pd(0)-Cy5-NP	500	PEG	Sulfo-Cy5	Pd^{0}

In terms of functionalisation, the NPs can be divided in three main groups: (i) non-fluorescent NPs, (ii) fluorescent NPs, and (iii) metallofluorescent NPs (Figure 40).

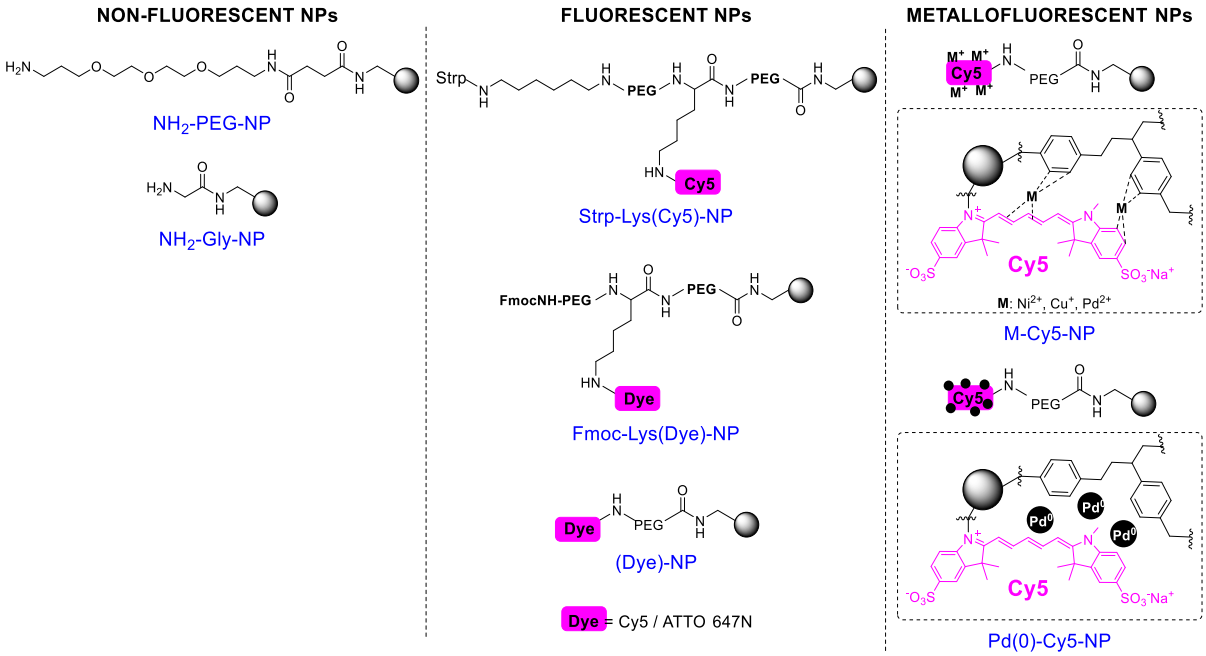

Figure 40. Chemical structure of the synthesised NPs shown in Table 16.

A set of non-fluorescent or naked NPs of different sizes, 500 nm, 900 nm, and 1200 nm, were synthesised. In order to determine the size of the non-fluorescent NPs, DLS and SEM analysis were performed. DLS analysis showed narrow populations, confirming that the synthesis of amino-functionalised cross-linked polystyrene NPs was accomplished (Figure 41).

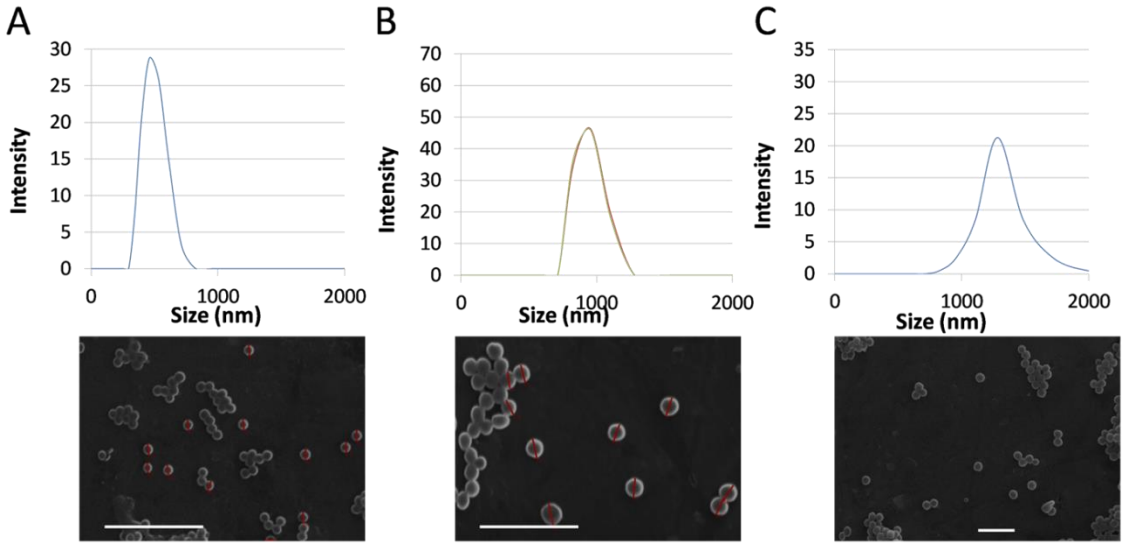

Figure 41. DLS (top) and SEM (bottom) characterization of 500 nm (**A**), 900 nm (**B**), and 1,200 nm (**C**) amino-functionalised cross-linked polystyrene NPs. The SEM analysis of, at least, 10 different particles resulted in the following average particle diameter: 490 ± 70 nm (**A**); 910 ± 110 nm (**B**); and 1,220 ± 130 nm (**C**). Scale bars in SEM images represent 5 μm.

NH_2-PEG-NP and **NH_2-Gly-NP** were prepared to be used as controls due to their non-fluorescent nature. For that, amino-functionalised cross-linked NPs were incubated with Fmoc-PEG-OH or Fmoc-Gly-OH, for **NH_2-PEG-NP** and **NH_2-Gly-NP** respectively, along with OxymaPure and DIC, in DMF, for 2 h at 60 ºC. Then, Fmoc protecting group was removed using a solution of 20% piperidine in DMF (Scheme 5).

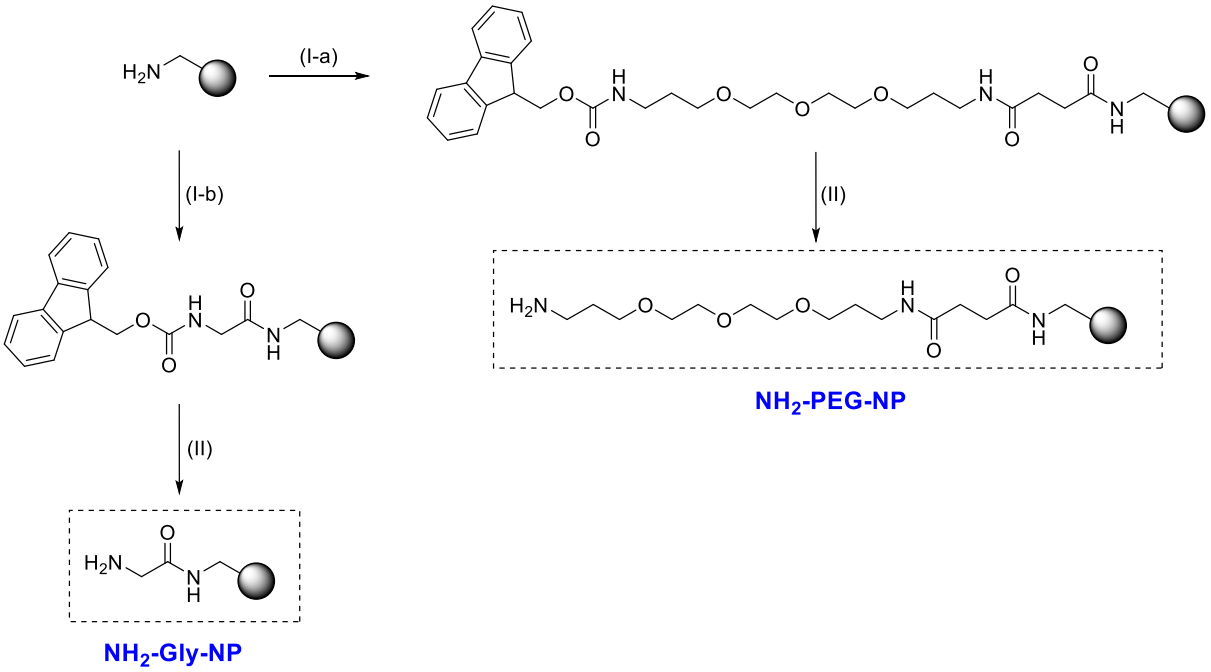

Scheme 5. Synthesis of **NH_2-PEG-NP** and **NH_2-Gly-NP**. **(Ia)** Fmoc-PEG-OH and **(Ib)** Fmoc-Gly-OH conjugation to naked amino-functionalised cross-linked polystyrene NPs. **(II)** Fmoc group removal.

NH_2-PEG-NP and **NH_2-Gly-NP** analysis by flow cytometry showed that they did exhibit no fluorescence (Figure 42-A). Contrarily to the metallofluorescent NPs, they did not contain any molecule suitable for being characterised with other techniques, such as XPS, CyTOF or EDX, which allow detecting the presence of a metal (Figure 42-B-C).

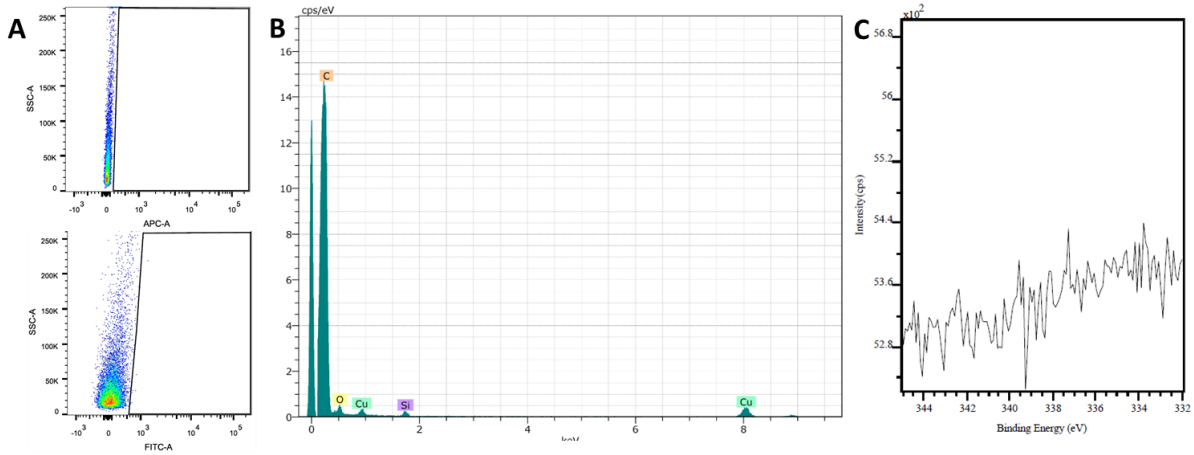

Figure 42. Representative plots of NH_2-PEG-NPs and NH_2-Gly-NP for APC and FITC channels in FACS **(A)**, in EDX analysis **(B)**, and in XPS analysis **(C)**.

In order to obtain fluorescent NPs capable of being used as fluorescence and imaging probes, **Cy5-NP** were synthesised by Cy5 dye ($\lambda_{Ex/Em}$= 649/666 nm) conjugation to NH_2-PEG-NP. For that NH_2-PEG-NP were firstly synthesised, and then sulfo-Cy5 NHS ester and

DIPEA were added to the NPs, mixing the suspension for 14 h at RT in darkness (Scheme 6).

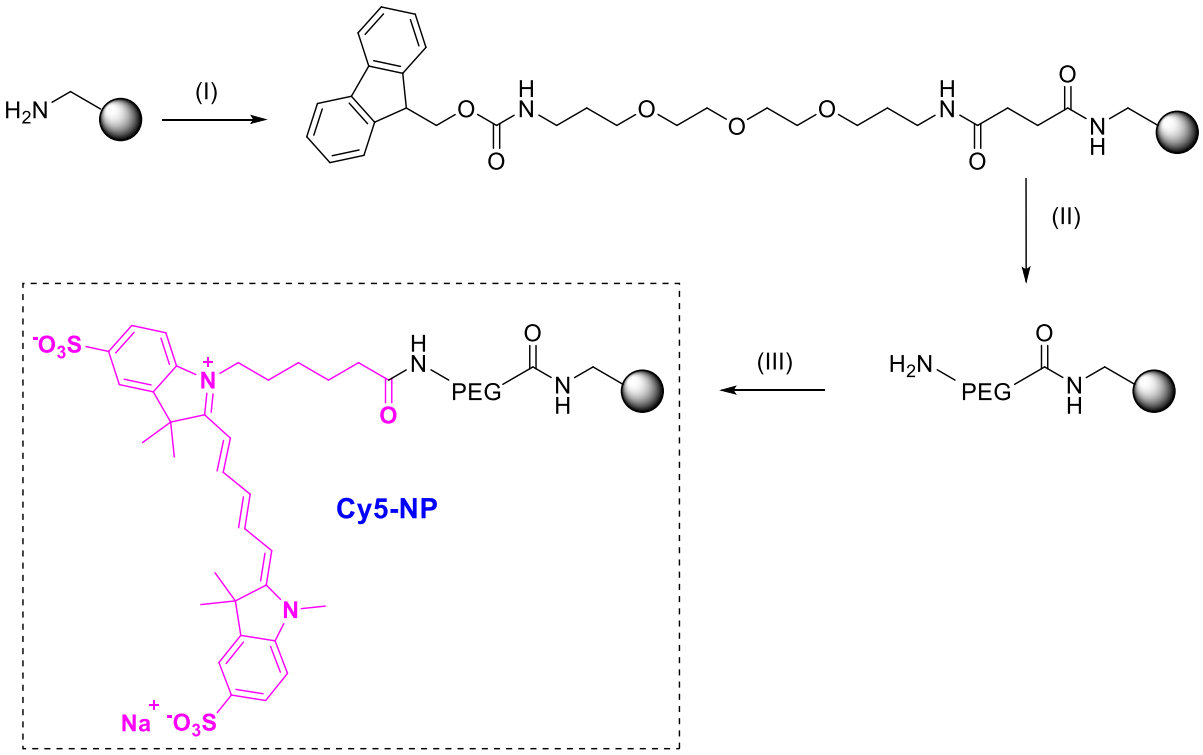

Scheme 6. Synthesis of **Cy5-NP**. **(I)** Fmoc-PEG-OH conjugation to naked amino-functionalised cross-linked polystyrene NPs; **(II)** Fmoc group removal; and **(III)** Cy5 conjugation.

The efficient fluorophore labelling was assessed by flow cytometry using a FACSCanto II instrument with a red laser at λ= 633 nm as excitation source, recording the emitted fluorescence with a 660/20 nm filter. Besides, aiming to multifunctionalise the NPs with other fluorophores such as fluorescein ($\lambda_{Ex/Em}$= 490/525 nm), emitting in the green range of the spectrum, the **Cy5-NPs** were also analysed with a blue laser at λ= 488 nm, and the emitted fluorescence was recorded with a 530/30 nm filter. Surprisingly, an unexpected fluorescent signal in the green part of the spectrum along with the typical red fluorescent signal was reported (Figure 43-A-B). Trying to determine whether the unexpected signal was the result of a scientific phenomenon or an inherent problem associated to the FACSCanto II instrument, the **Cy5-NPs** were also analysed using a confocal microscope LSM 710 Axio Observer, collecting the green channel with a 480/40-nm excitation bandpass filter, a 505 nm dichroic mirror and a 527/30 nm emission bandpass filter, whereas the red channel was obtained using a 620/60 nm bandpass filter for the excitation, a 660 nm dichroic mirror, and a 700/75nm bandpass emission filter. Similarly, it was observed that the **Cy5-NPs** showed fluorescence in both channel (Figure 43-C-D).

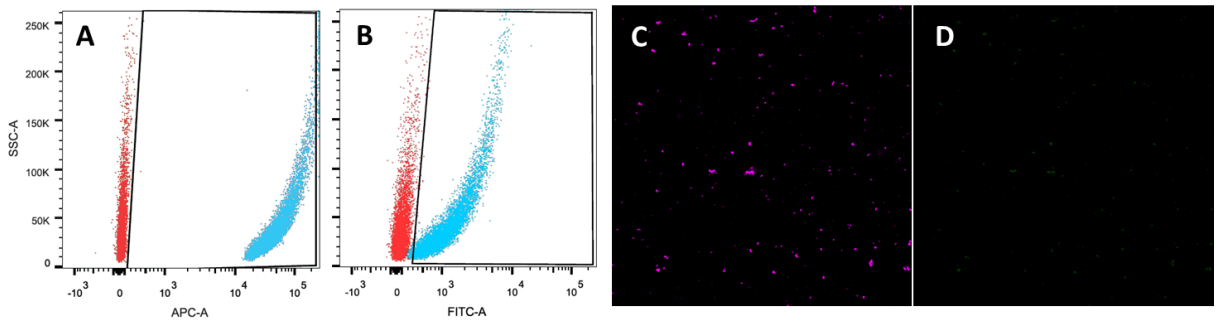

Figure 43. FACS dot plots for APC channel **(A)** and FITC channel **(B)**, containing in red, NH_2-PEG-NPs and in blue, Cy5-NPs. **C-D)** Confocal images of Cy5-NPs in the red channel (magenta) and in the green channel (green), respectively.

Firstly, organic dye aggregation accounting for this unexpected green fluorescence was hypothesised. Cyanine dyes form H- [258] and J- aggregates [259], especially J-aggregates [260], which modify their vibrational states and thus, cause changes in their spectroscopic and fluorescent properties [261]. Furthermore, H- and J- aggregates of cyanine dyes have been reported in DNA [262], in NPs, and in other structures. As a result, the possible implications of H- and J- aggregates in the unexpected green fluorescent signal were investigated.

Consequently, diverse strategies were followed in order to get a deeper insight on this phenomenon. Amongst these strategies, the influence of the NPs size, the influence of spacers, the influence of additional functionalisations, or even the influence of the fluorophore concentration were studied. To expand additional conjugations to the NPs, a modified lysine spacer was included into the chemical structure, which enabled the synthesis of bivalent NPs. Thus, this lysine spacer allowed the conjugation of spacers through the Nα amino group, and the conjugation of dyes through its Nε amino group.This led to the synthesis of several **Fmoc-Lys(Cy5)-NP** and **Strep-Lys(Cy5)-NP** of 500 nm, 900 nm, and 1200 nm in size. The synthesis of both NPs was accomplished from NH_2-PEG-NP employing the orthogonal spacer Fmoc-Lys-(DDe)-OH which was conjugated using OxymePure and DIC strategy for 2 h at 60 ºC. The full orthogonal protected groups Fmoc and Dde enabled the conjugation of the NPs by two different arms. Therefore, Fmoc protecting group was firstly removed with a solution of 20% priperidine in DMF, and Fmoc-Lys-OH spacer was conjugated via OxymaPure/DIC to enlarge the chain. Afterwards, Dde protecting group was removed with a mixture of hydroxylamine hydrochloride and imidazole in a mixture NMP/DMF [204], enabling the conjugation of Cy5 dye using sulfo-Cy5 NHS ester and DIPEA for 14 h, at RT, in darkness. This gave rise to **Fmoc-Lys(Cy5)-NP**. Then, Fmoc protecting group was removed and the NPs were suspended in a solution of 25% glutaraldehyde in water, and mixed for 14 h at RT, to conjugate glutaraldehyde. At last, the NPs were

suspended in a solution of streptavidin in PBS (pH 7.4) and mixed for 14 h at RT, when the reaction was stopped by adding a solution of 40 mM ethanolamine in 1% BSA in PBS as a quenching solution. This quenching solution was employed for 2 h at RT to afford, after washings in PBS, **Strep-Lys(Cy5)-NP** (Scheme 7)

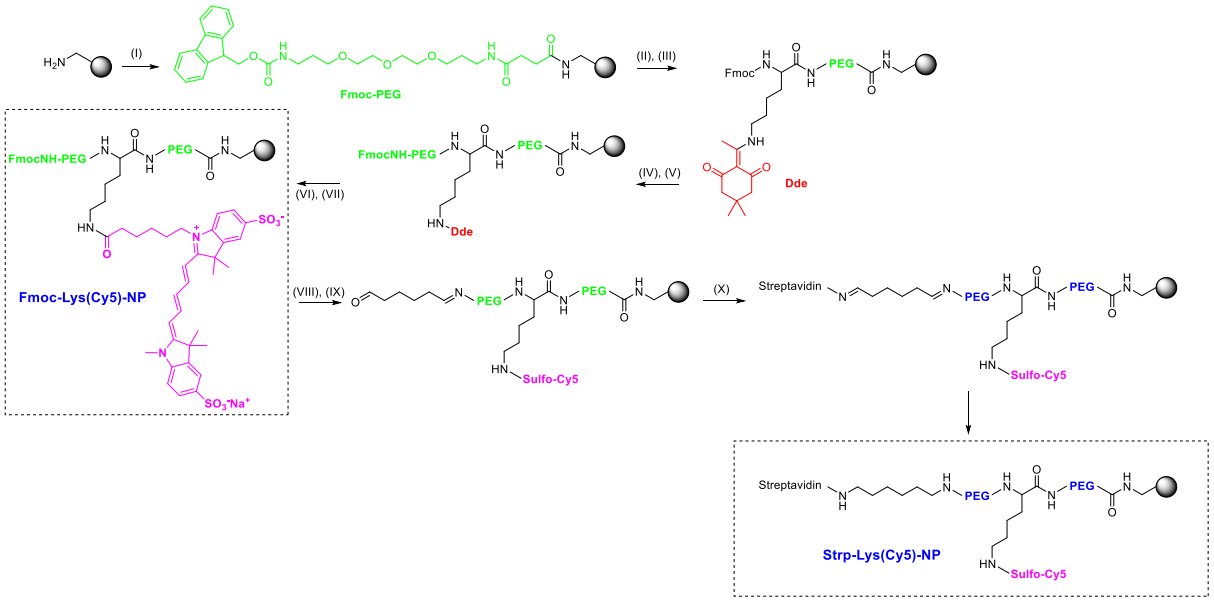

Scheme 7. Synthesis of **Fmoc-Lys(Cy5)-NP** and **Strp-Lys(Cy5)-NP**. **(I)** Fmoc-PEG-OH conjugation to naked amino-functionalised cross-linked polystyrene NPs; **(II)** Fmoc group removal; **(III)** Fmoc-Lys-Dde-OH conjugation; **(IV,V)** Fmoc group removal and subsequent Fmoc-PEG-OH conjugation; and **(VI,VII)** Dde group removal and Cy5 conjugation, affording Fmoc-Lys(Cy5)-NP. **(VIII,IX)** Fmoc group removal and glutaraldehyde conjugation; and **(X)** Streptavidin conjugation to afford Strp-Lys(Cy5)-NP.

To provide insights of the phenomenom, a collaboration with the Department of Physical Chemistry at the Faculty of Pharmacy of the University of Granada was established, allowing the analysis of the Cy5 labelled NPs by dual FLIM with spectrographic capabilities, using a 470 nm pulsed excitation and recording the fluorescence emission in two detection channels: green (I_G, with a 520/35 nm bandpass filter) and red (I_R, with a 685/75 nm bandpass filter) (Figure 44). FLIM helped to study what happens to the dye fluorescence-lifetime and its dual band emission according to the milieu.

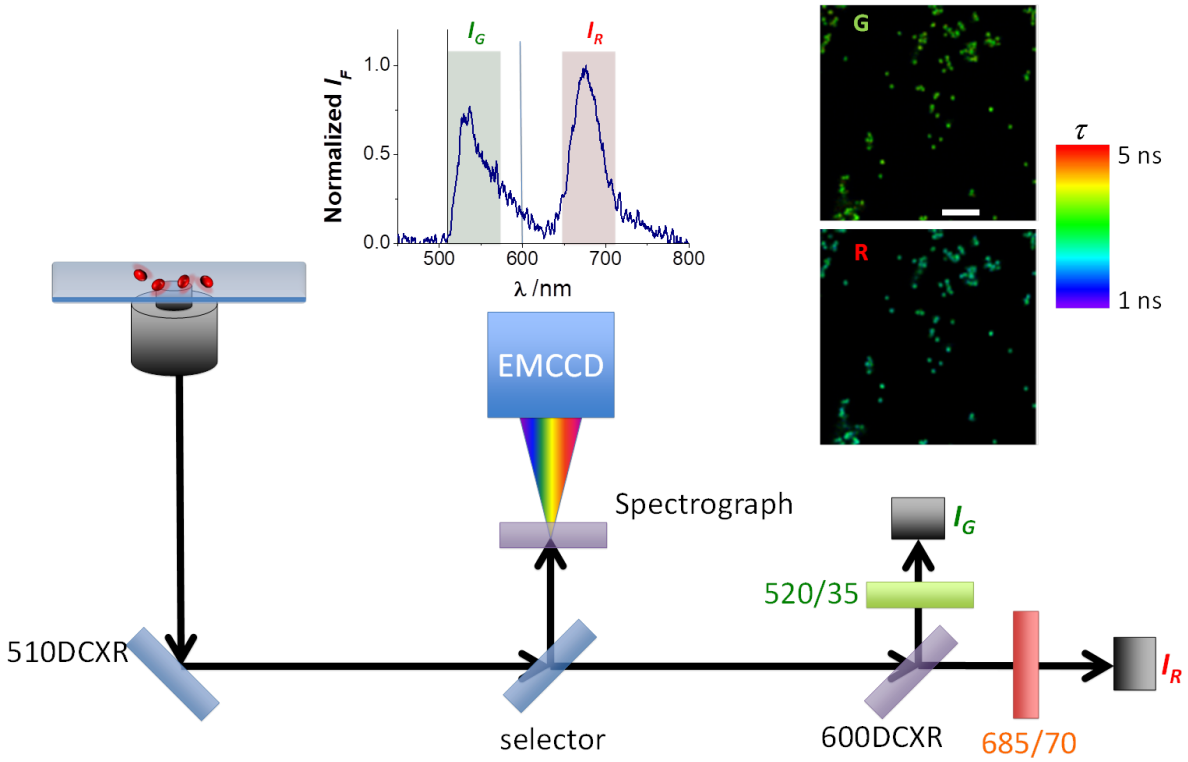

Figure 44. Scheme of the instrumentation for FLIM and fluorescence spectroscopy employed. A representative spectrum of a particle containing dual-band emission is shown to highlight the bandpass filters used to define the green (I_G) and red (I_R) channels. The scale bar in the image represents 5 μm.

FLIM images of **Cy5-NP** of 500 nm in size (**Cy5-NP$_{500}$**) clearly showed fluorescent emission from the NPs in both the green and red channels when excited at 470 nm (Figure 45-A), obtaining that the ratio of fluorescence intensities between the green and the red channels (I_G/I_R) was 0.5 ± 0.1, although some **Cy5-NP$_{500}$** exhibited high green fluorescence (Figure 45-B). Moreover, the emission spectrum obtained from a set of different Cy5-conjugated NPs, which included **Cy5-NP$_{500}$**, **Fmoc-Lys(Cy5)-NP** (500 nm and 900 nm), **Strep-Lys(Cy5)-NP** (1200 nm), showed dual-band behaviour with two maxima, once centred at approximately 670 nm (characteristic of free Cy5) and a second band centred at approximately at 530 nm (green spectra) (Figure 45-C). As aforementioned, **Cy5-NP$_{500}$** were analysed by FACS, and when plotting the recorded events in a fluorescence correlogram, it was also showed that the green and red channels events were proportionally correlated (Figure 45-D).

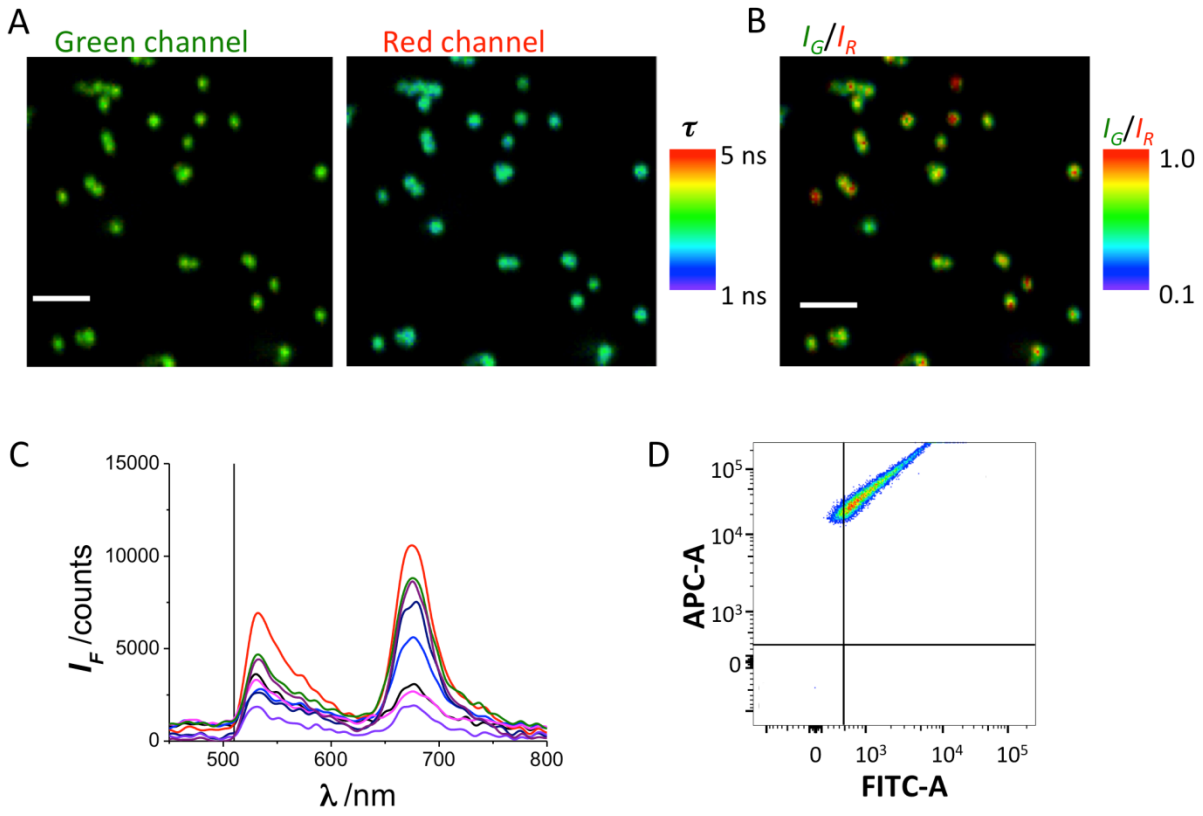

Figure 45. A) Dual-colour FLIM images of **Cy5-NP$_{500}$** in the green and red emission channels. The pseudo-colour scale indicates the average fluorescence lifetime of the emission in each pixel. The scale bar represents 2.5 µm. **B)** I_G/I_R ratio image of the images shown in A). The pseudo-colour scale indicates the I_G/I_R value in each pixel. **C)** Fluorescence emission spectrum of different NPs in the image. **D)** FACS correlogram of detected fluorescence in the red (APC-A) and green (FITC-A) channels of Cy5-NP$_{500}$.

When analysing the data obtained from FLIM for more complexes and larger Cy5-conjugated NPs, **Fmoc-Lys(Cy5)-NP$_{500}$**, **Fmoc-Lys(Cy5)-NP$_{900}$**, **Strep-Lys(Cy5)-NP$_{1200}$**, it was also observed that these particles exhibited dual-band green/red emission behaviour, thereby confirming that this effect was nothing inherent to the spacers but to the NPs themselves (Figure 46).

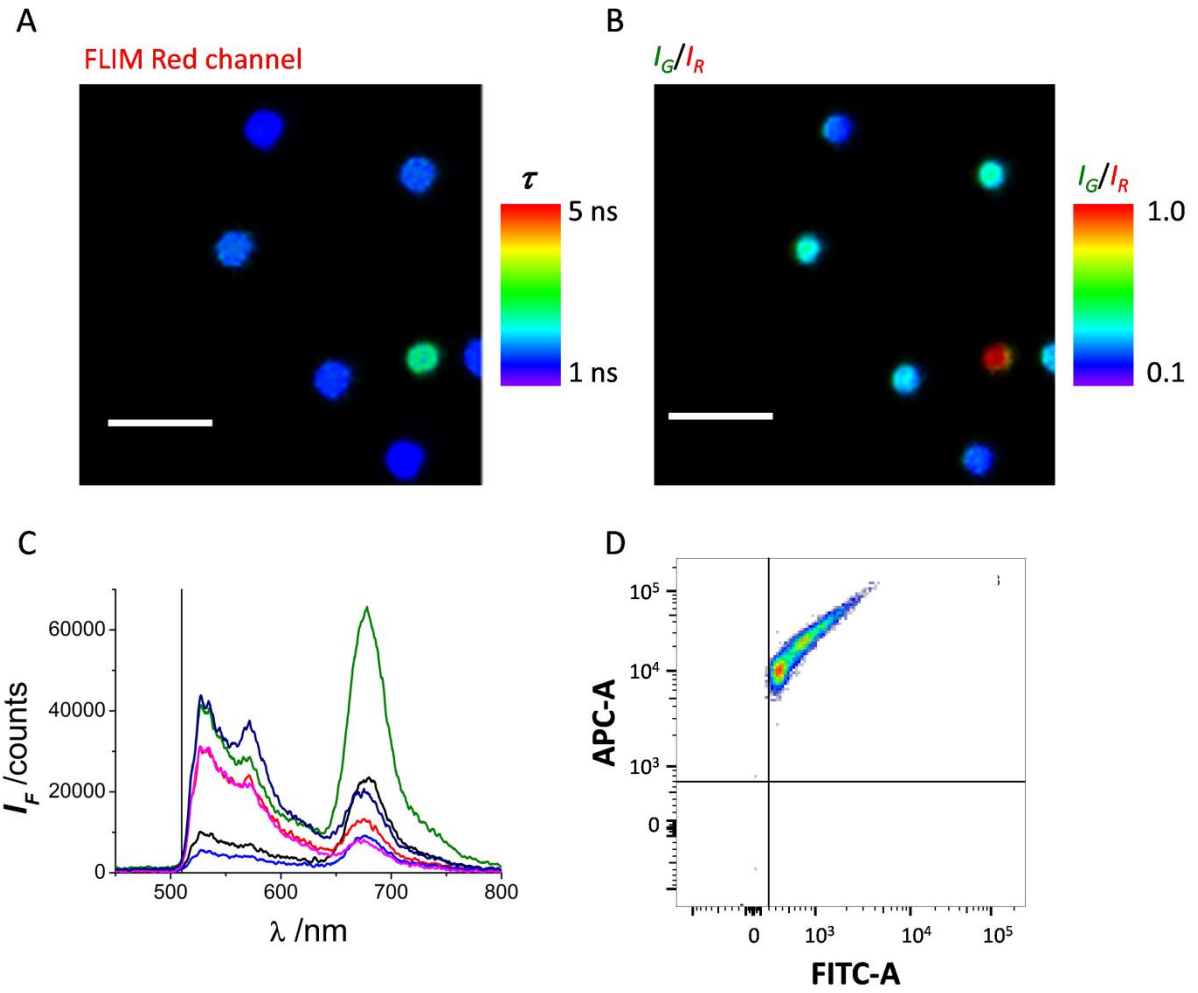

Figure 46. A) Dual-colour FLIM image of **Strp-Lys(Cy5)-NP$_{1200}$** particles in the red emission channel. The pseudo-colour scale indicates the average fluorescence lifetime of the emission in each pixel. The scale bar represents 2.5 µm. **B)** Corresponding I_G/I_R ratio image, with the pseudo-colour scale indicating the I_G/I_R value in each pixel. **C)** Fluorescence emission spectrum of different particles in the image. **D)** FACS correlogram of detected fluorescence in the red (APC-A) and green (FITC-A) channels of Strp-Lys(Cy5)-NP$_{1200}$ particles.

Since the apparition of dye aggregates is directly related to high amounts of dye, the effect that a diminution of the amount of loaded Cy5 in the NPs could provoke was assessed by flow cytometry and dual-channel fluorescence confocal microscopy. Thus, a set of of 4 different **Cy5-NP$_{500}$** carrying different loadings of Cy5, 130 µM, 13 µM, 1.3 µM, and 0.13 µM, were synthesised. Theoretically, this should provoke a progressive removal of the unexpected green emission; hence, the ratio of intensity between the green and the red fluorescence (I_G/I_R) should decrease. Nonetheless and surprisingly, it was found the other way round. FACS experiments showed that despite decreasing the Cy5 concentration provoked the **Cy5-NP$_{500}$** to diminish both the red (APC) and green (FITC) fluorescence

(Figure 47-A), the ratio between green and red emission (I_G/I_R) increased with lower Cy5 concentrations (Figure 47-B).

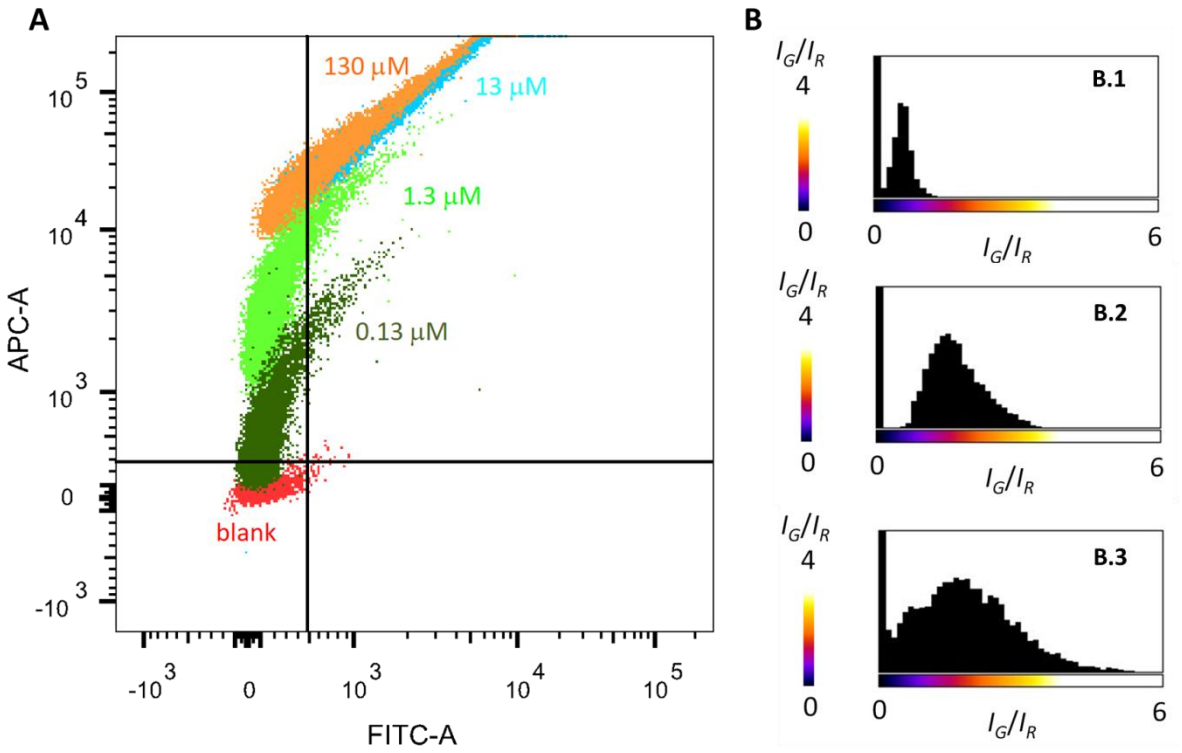

Figure 47. A) FACS results of **Cy5-NPs** carrying different loadings of Cy5, from 0.13 µM to 130 µM. PEGylated-NPs were used as blank. **B)** The I_G/I_R histogram of Cy5-NPs carrying 130 µM of Cy5 (**B.1**), 13 µM (**B.2**), and 1.3 µM (**B.3**), surpassing an automatic set threshold.

These results were incongruous with the hypothesis of H- and J- aggregates, produced by Cy5 aggretation, being responsible for the unexpected green fluorescence emission, so that this theory had to be discarded. Instead, the possibility of an intermolecular interaction between the Cy5 moiety and the NP components came to mind. Thusly, the cyanine conjugated system could be interacting with polystyrene aromatic groups through π-π stacking interaction, causing a Förster resonance energy transfer (FRET) effect [263]. As a result, the occuring π-π stacking interaction could be acting as a donor, emitting green fluorescence that was being absorbed by the free Cy5 dyes that acted as acceptors, releasing red fluorescence. As a consequence of this effect, the green fluorescence emitted by the donor was being quenched, but as the amount of dye was decreased, there were less free Cy5 molecules without undergoing interaction; hence, the quenching effect was weaker, increasing the green fluorescence emission (Figure 48) [257].

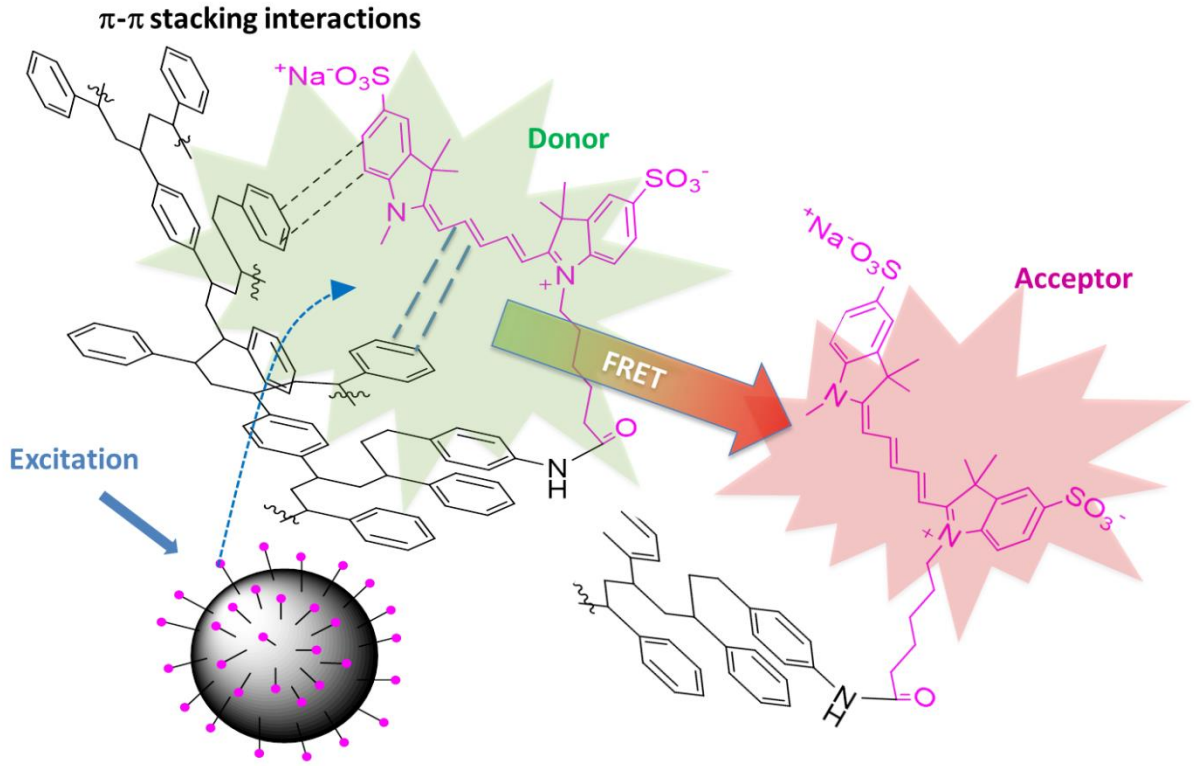

Figure 48. Representative scheme of the FRET phenomenon. When Cy5-NPs are excited by a source, π-π interactions between the aromatic rings of polystyrene and Cy5 absorb the energy and release green fluorescence, acting as a donor. The green fluorescence is transferred to Cy5 molecules which are not interacting with polystyrene, acting as acceptor and releasing fluorescence in the red part of the spectra.

To provide insights about this energy transfer phenomenon, the fluorescence-lifetime (τ) of Cy5 in the different NPs was studied. It was observed that the τ values of the Cy5 conjugated to the NPs were different from that of the dye in solution (1.0 ns) [264]. Remarkably, Cy5 conjugated to 500 nm size NPs, **Cy5-NP$_{500}$**, showed to double the τ values of Cy5 in solution, 2.3 ns, whilst larger particles, **Fmoc-Lys(Cy5)-NP$_{900}$** and **Strep-Lys(Cy5)-NP$_{1200}$**, showed τ values slightly higher than that of Cy5 in solution, 1.4 ns and 1.2 ns respectively. This enhancement in the fluorescent lifetime correlated with the appearance of the green fluorescence emission, likewise, its reduction, as it happened with larger particles, was also correlated to a decay of the green fluorescence emission. Additionally to the NPs size, the spacers had also an influence in the Cy5 lifetime, as it was observed that **Cy5-NP$_{500}$** exhibited a longer Cy5 τ value than those obtained for the NPs (**Fmoc-Lys(Cy5)-NP$_{900}$** and **Strep-Lys(Cy5)-NP$_{1200}$**) carrying lysine as spacer. Because of lysine spacer is longer than

PEG, the results suggested that smaller spacers increase the dye lifetime, as well as smaller nanoparticle sizes do (Figure 49). These fluorescence lifetime values seemed to confirm that the energy transfer phenomenomen, FRET, would be inducing an increase in the fluorescence lifetime of the Cy5 acceptor dye since the fluorescence decay of the acceptor would be a convolution of its natural decay law with that of the donor [265].

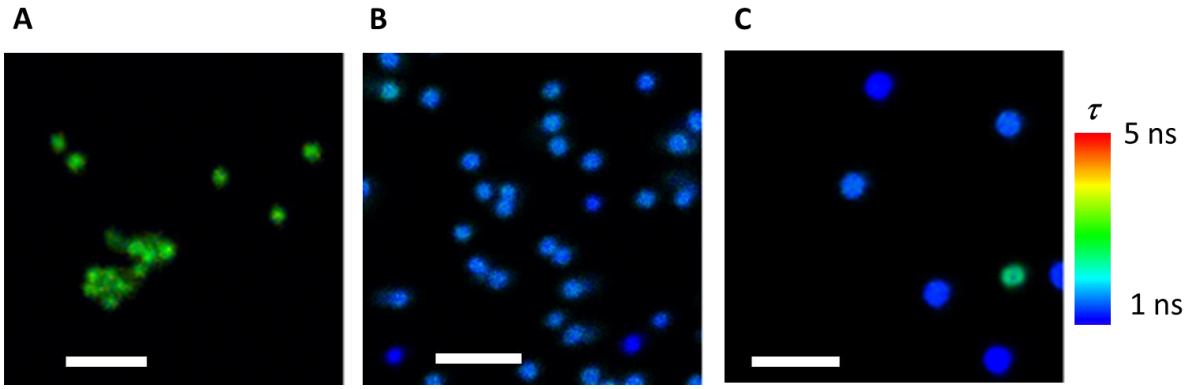

Figure 49. FLIM images in the red emission channel of Cy5-conjugated NPs. The pseudo-colour scale indicates the average fluorescence lifetime in each pixel. The scale bars represent 2.5 µm. **A)** Cy5-NP_{500}; **B)** Fmoc-Lys(Cy5)-NP_{900}; and **C)** Strep-Lys(Cy5)-NP_{1200}.

Therefore, so as to determine whether this phenomenon was inherent to Cy5, the influence of another fluorophore, ATTO 647N (λ_{ex}= 647 nm and λ_{em}= 661 nm) was assessed. ATTO 647N is spectrally equivalent to Cy5 but has a different chemical structure, as Cy5 is a carbocyanine dye, whereas ATTO 647N is a carbopyronin dye, fact that hinders the H- and J- aggregates formation [266]. Therefore, a set ATTO 647N labelled NPs structurally similar to those Cy5 labelled NPs were synthesised. To achieve **A647-NP**, NPs were previously conjugated with PEG spacer by using Fmoc-PEG-OH with OxymaPure/DIC and the subsequent removal of Fmoc protecting group with a solution of 20% piperidine in DMF. Afterwards, ATTO 647N NHS ester was added, in darkness, to the NPs along with DIPEA to afford **A647-NP** (Scheme 8).

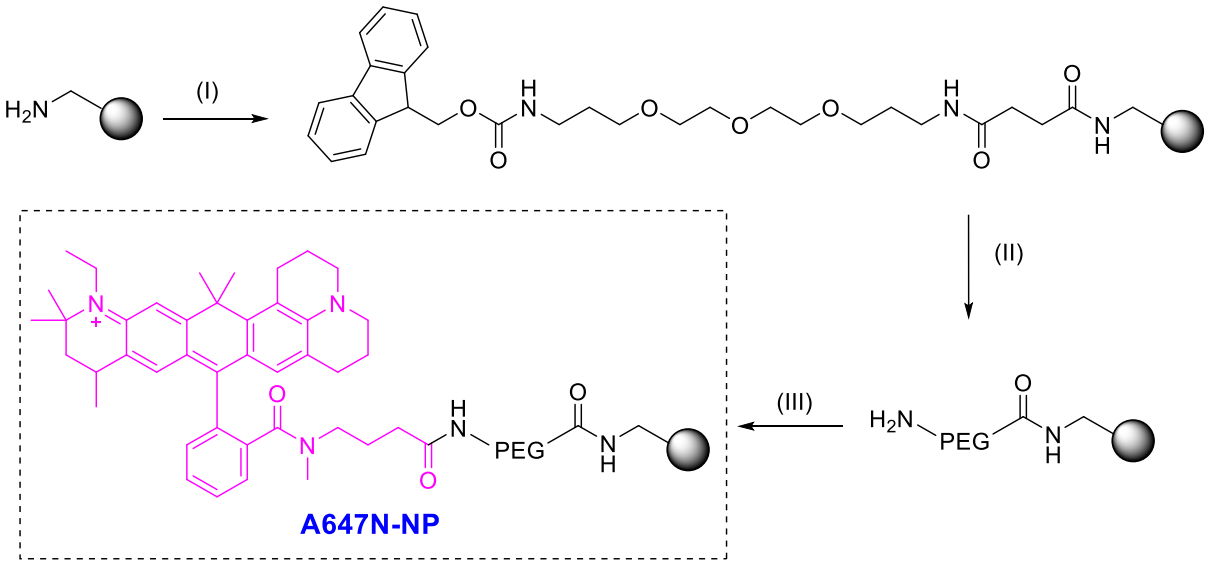

Scheme 8. Synthesis of **A647-NP**. **I)** Fmoc-PEG-OH conjugation to naked amino-functionalised cross-linked polystyrene NPs; **(II)** Fmoc group removal; and **(III)** ATTO 647N conjugation.

Likewise, a set of multifunctionalised ATTO 647N labelled NPs, **Fmoc-Lys(A647)-NPs**, of several sizes, 500 nm and larger particles of 2,500 nm and 5,000 nm, were also synthesised. To afford **Fmoc-Lys(A647)-NP$_{500}$** there were used homemade NPs whereas to afford **Fmoc-Lys(A647)-NP$_{2500}$** and **Fmoc-Lys(A647)-NP$_{5000}$** commercially available amino-functionalised cross-linked polystyrene NPs, were used. So, to accomplished the synthesis of the aforementioned particles, NH_2-PEG-NPs were functionalised with full orthogonal Fmoc-Lys-Dde(OH) to enable the dual conjugation, using OxymaPure/DIC. Thus, Fmoc protecting group was removed using a solution of 20% of piperidine in DMF to allow the further conjugation of Fmoc-PEG-OH via OxymaPure/DIC conjugation chemistry. Subsequently, Dde protecting group was removed by employing the mixture hydroxylamine hydrochloride and imidazole in NMP and DMF, enabling the conjugation of ATTO 647N as NHS ester form when it is incubated with the NPs and DIPEA for 14 h, at RT, in darkness (Scheme 9)

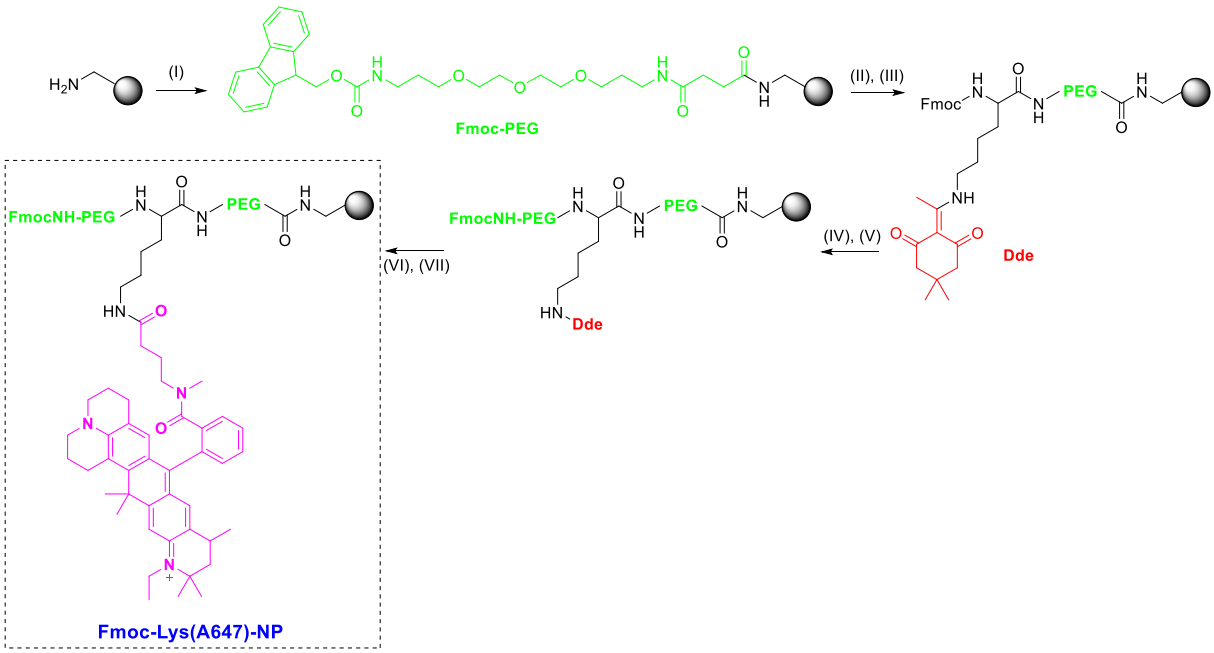

Scheme 9. Synthesis of **Fmoc-Lys(A647)-NP**. **(I)** Fmoc-PEG-OH conjugation to naked amino-functionalised cross-linked polystyrene NPs; **(II), (III)** Fmoc group removal and Fmoc-Lys(Dde)-OH conjugation; **(IV,V)** Fmoc group deprotection and Fmoc-PEG-OH conjugation; and **(VI,VII)** Dde group selective removal and ATTO 647N conjugation.

The entire set of ATTO 647N conjugated particles showed typical red fluorescent emission but negligible green fluorescence emission (Figure 50-A). Furthermore, the set of **A647N-NPs** exhibited I_G/I_R ratio values generally below 0.1 when studied by dual-channel FLIM and FACS (Figure 50-B), confirming that unexpected green fluorescence was not being produced.

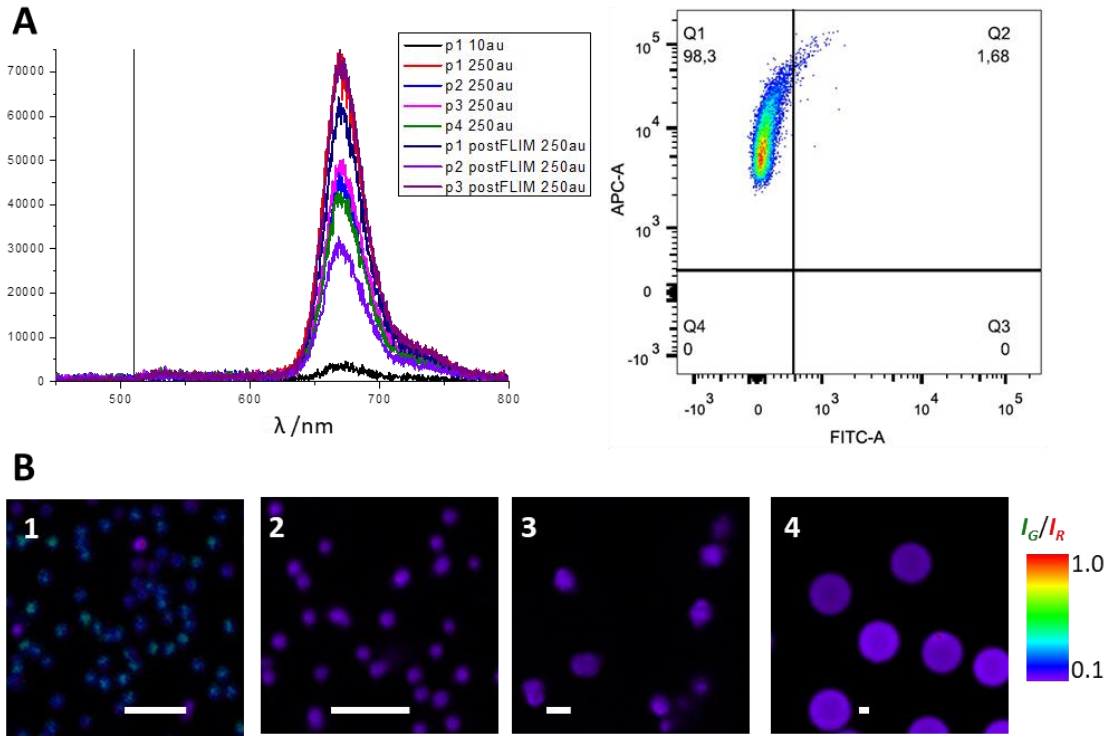

Figure 50. A) At the left, fluorescence emission spectra of different particles containing **ATTO 647N** as the fluorophore, exclusively showing emission in the red channel and negligible emission on the green channel. At the right, FACS correlogram of detected fluorescence in the red (APC-A) and green (FITC-A) channels of A647-NPs. **B)** I_G/I_R ratio images of A647-loaded particles: A647-NP_{500} (**1**), Fmoc-Lys(A647)-NP_{900} (**2**), Fmoc-Lys(A647)-NP_{2500} (**3**), and Fmoc-Lys(A647)-NP_{5000} (**4**). The pseudo-colour scale indicates the I_G/I_R value in each pixel. The scale bar represents 2.5 µm.

Additionally, FLIM studies were performed over ATTO 647N conjugated particles to analyse what was happening to ATTO 647 fluorescence-lifetime. In theory, as ATTO 647N would not induce π-π stacking interaction and FRET process, the fluorescence lifetime values should not be higher than that for ATTO 647N in solution, which is 3.5 ns. The average τ value obtained for the ATTO 647N conjugated to particles were as expected, as in **A647-NP_{500}** its value was 1.3 ns, whereas in larger and multifunctionalised partices, the ATTO 647N lifetime increased up to the τ value in solution, being 1.8 ns in **Fmoc-Lys(A647)-NP_{900}**, 2.8 ns in **Fmoc-Lys(A647)-NP_{1200}** and 3.7 ns in **Fmoc-Lys(A647)-NP_{5000}** (Figure 51). As expected, the trend behaviour observed for ATTO 647N was the inverse to the trend observed for Cy5, this is that ATTO 647N shortens its lifetime when either short spacers are used or it is conjugated to smaller particles. Therefore, these results supported the energy transfer theory.

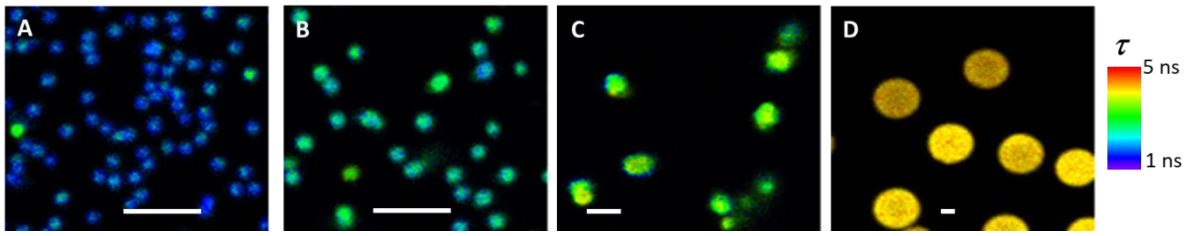

Figure 51. FLIM images in the red emission channel of **A647-loaded particles**. The pseudo-colour scale indicates the average fluorescence lifetime in each pixel. The scale bars represent 2.5 µm. **A)** A647-NP_{500}, **B)** Fmoc-Lys(A647)-NP_{900}, **C)** Fmoc-Lys(A647)-NP_{2500}, and **D)** Fmoc-Lys(A647)-NP_{5000}.

Nonetheless, in order to totally corroborate the FRET process taking place over Cy5 labelled NPs, the influence of ATTO 647N concentration over the NPs was also assessed. In this sense, a set of **A647-NP_{500}** differing in the ATTO 647N loading, ranging from 130 µM to 0.13 µM, were synthesised, as it was done with **Cy5-NP_{500}**. As expected, regarding the previous results obtained for ATTO 647N conjugated particles, there was no green emission but red emission in FACS, being the number of events exhibiting green fluorescence always lower than 10%, similar to the blank NPs, and negligible compared with the number of events exhibited by Cy5 conjugated particles (Figure 52).

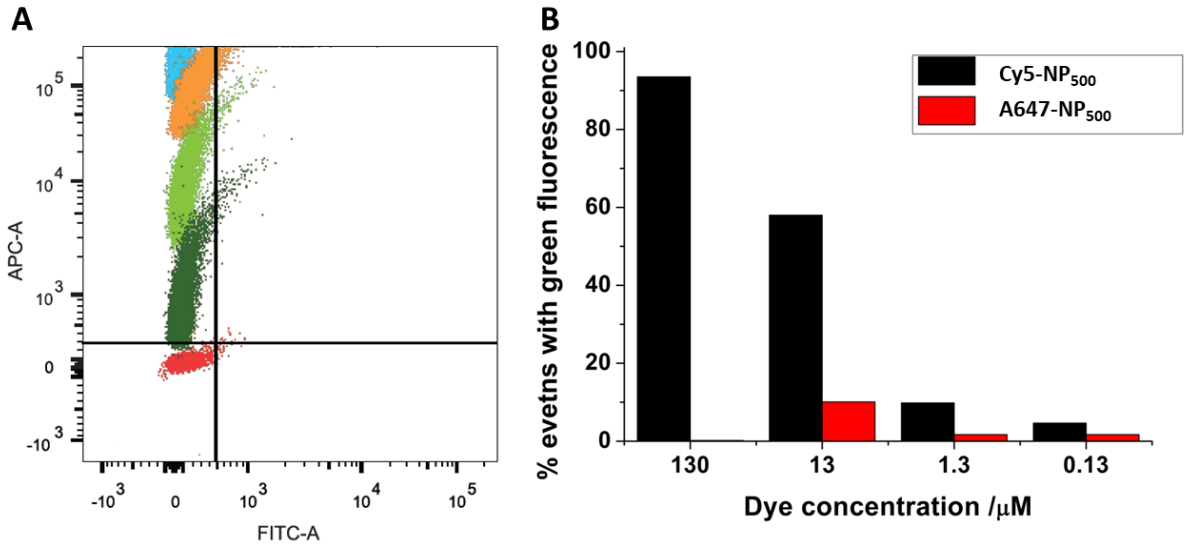

Figure 52. A) FACS results of **A647-NP_{500}** particles carrying different loadings of A647 in the conjugation reaction: in blue 130 µM, in orange, 13 µM, in olive green, 1.3 µM, in dark green, 0.13 µM, and in red, the blank NPs. **B)** Percentage of events showing green events (FITC-A channel) in FACS experiments of Cy5-NP_{500} and A647-NP_{500} particles with different loadings of the dye in the conjugation reaction.

Since the dual green-red emission in Cy5 labelled NPs represented a major problem to our intentions, it was decided to seek solutions and remove the unexpected green emission. To overcome this drawback, the use of metals capable of interacting with the electron-rich network created by the stacking interactions between the polymethine groups of the Cy5 fluorophore and the polystyrene aromatic rings, bears to mind. Thus, regarding the demonstrated capability of palladium to coordinate with free amino groups and aromatic rings of polymer networks, quenching green dyes as a result [267],[268], three different metals, palladium (Pd), copper (Cu) and nickel (Ni) were employed. The conjugation of these metals to Cy5 labelled NPs gave rise to metallofluorescent NPs. For that, **Cy5-NP** were incubated with a 10 mM solution of $Pd(OAc)_2$, CuBr, or $NiCl_2$, in DMF for 14 h, at RT, in darkness, to afford **Pd(II)-Cy5-NP**, **Cu(I)-Cy5-NP**, and **Ni(II)-Cy5-NP**, respectively (Scheme 10).

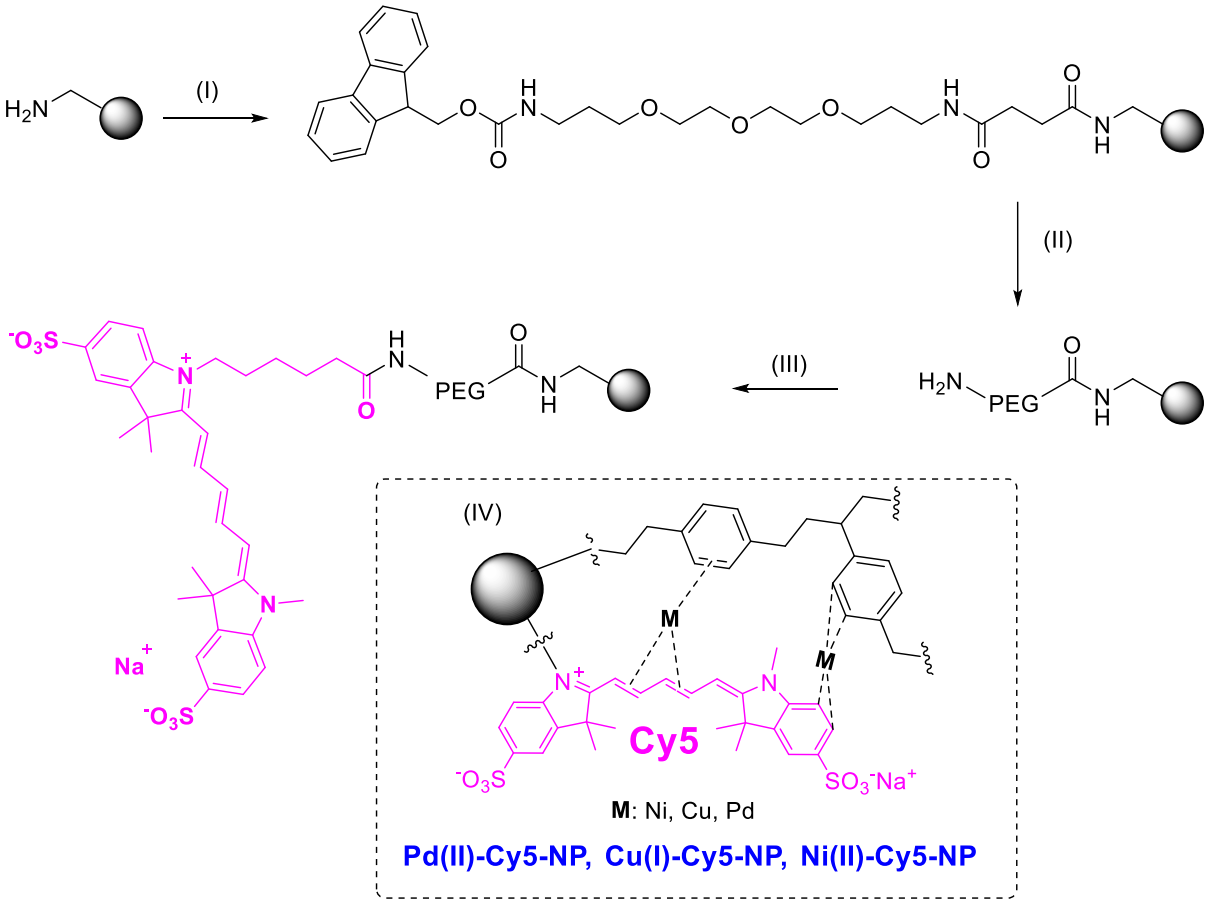

Scheme 10. Synthesis of **metallofluorescent NPs**. **(I)** Fmoc-PEG-OH conjugation to naked amino-functionalised cross-linked polystyrene NPs; **(II)** Fmoc group removal; **(III)** Cy5 conjugation; and **(IV)** Solutions of $Pd(OAc)_2$, CuBr, and $NiCl_2$ to afford Pd(II)-Cy5-NP, Cu(I)-Cy5-NP, and Ni(II)-Cy5-NP, respectively.

Remarkably, the presence of the metal ions in the metallofluorescent NPs produced the disappearance of the unexpected green fluorescence with only inducing a dim quenching effect of the inherent Cy5 red fluorescence signal, when analysed by FACS. Notably, palladium was the metal exhibiting better green fluorescence quenching though nothing considerable (Figure 53).

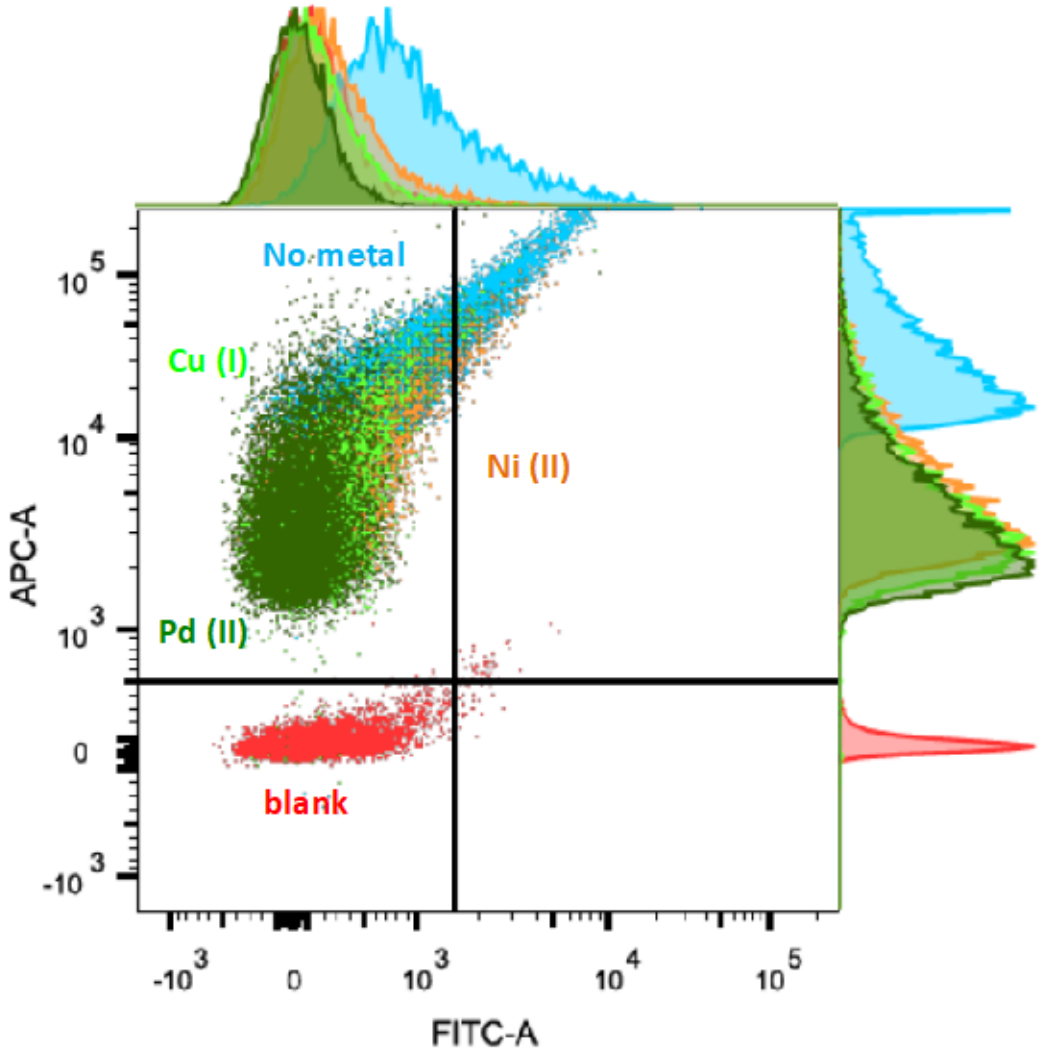

Figure 53. FACS correlogram of **metallofluorescent NPs** in the red (APC-A) and green (FITC-A) emission channels. The correlogram shows results from NH_2-PEG-NP (blank, red), Cy5-NPs (no metal, cyan), Pd(II)-Cy5-NP (dark green), Cu(I)-Cy5-NP (light green), and Ni(II)-Cy5-NP (orange). The fluorescence of Cy5 in all the metal-carrying NPs was partially quenched. Moreover, the presence of Cu, Ni, and Pd ions in the NPs caused the disappearance of the green emission.

As aforementioned in the introduction of this chapter, the potential biotechnological applications of metallofluorescent NPs carrying Pd as the metal are enormous [181],[182]; hence, these NPs were selected to keep working with. However, palladium as its ion form

Pd(II) has been reported to be cytotoxic since its coordination chemistry is very similar to that of Pt(II) [269]. Thus, to minimise the possible effects that **Pd(II)-Cy5-NP** could generate, an *in situ* reduction of the Pd(II) ions to Pd(0) via hydrazine treatment in MeOH was employed to obtain **Pd(0)-Cy5-NP** [181],[182]. As a result of this reduction, Pd(0) precipates forming tiny NPs that are entrapped whithin the surface of the NPs due to the π electron-rich network created by Cy5 and polystyrene (Scheme 11).

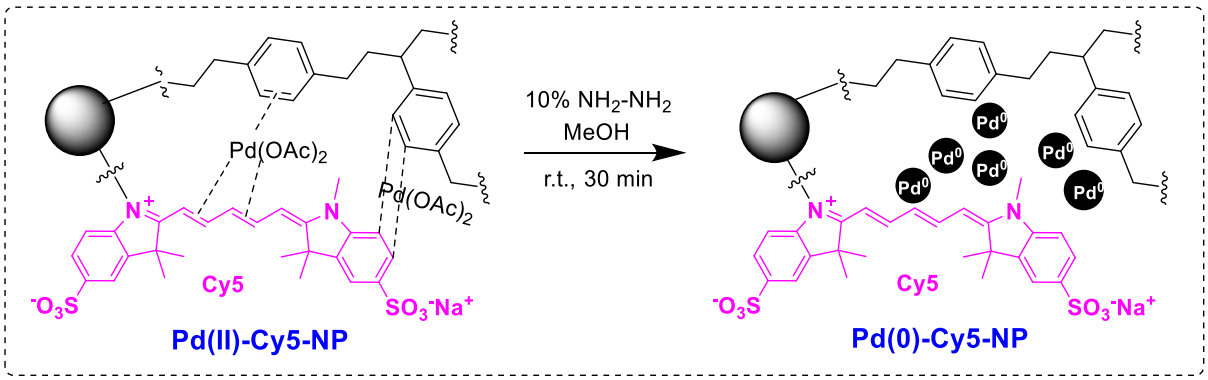

Scheme 11. Synthesis of **Pd(0)-Cy5-NP** from Pd(II)-Cy5-NP by reducing Pd(II) to Pd(0).

In order to prove the effective reduction of Pd(II) to Pd(0) within the NPs, a test assessing the catalytic activity of the **Pd(0)-Cy5-NP** was done. Since Pd(0) is capable of catalysing the removal of allyloxycarbonyl protecting groups [182], a fluorogenic version of this reaction wherein the non-fluorescent bis-allyloxylcarbonyl rhodamine was transformed into fluorescent rhodamine 110 upon protecting groups removal, was performed (Scheme 12). Figure 54-G shows that neither **Cy5-Pd** nor **Pd(II)-Cy5-NP** induced the fluorogenic reaction, whilst **Pd(0)-Cy5-NP** and old Pd(0) microspheres, used as control, could effectively catalyse the fluorogenic reaction.

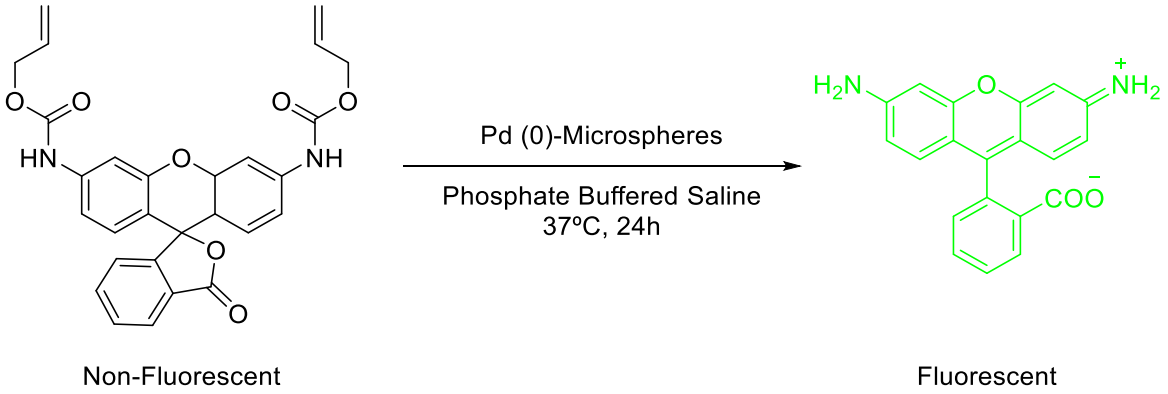

Scheme 12. Fluorogenic reaction produced by Pd(0) deprotection of bis-allyloxylcarbonyl groups.

Thereupon and once the presence of Pd(0) in **Pd(0)-Cy5-NP** was demonstrated, a in-depth characterisation of both **Pd(II)-Cy5-NP** and **Pd(0)-Cy5-NP** was perfomed. As it is observed in Figure 54-A and Figure 54-D, XPS analysis clearly showed the presence of palladium in **Pd(II)-Cy5-NP** and **Pd(0)-Cy5-NP**, respectively. In Figure 54-A for **Pd(II)-Cy5-NP**, two main peaks were observed with binding energies of, approximately 336 eV and 342 eV, corresponding to $Pd3d_{5/2}$ and $Pd3d_{3/2}$, respectively, as usual for Pd^{2+} [270]. In Figure 54-D, for **Pd(0)-Cy5-NP** is observed that along with the Pd^{2+} peaks it appears two extra peaks shifted to lower binding energies, corresponding to Pd^0 [271]. Furthermore, FACS analysis confirmed that ionic palladium (Pd^{2+}) reduction to palladium particle (Pd^0) did not affect the green fluorescence quenching and neither the red fluorescence, which was maintained (Figure 54-H). EDX analysis of **Pd(II)-Cy5-NP** and **Pd(0)-Cy5-NP** clearly showed the presence of palladium in the metallofluorescent NPs as both peaks have a binding energy of, approximately, 2.9 keV (Figures 54-B and 54-E). Besides, the EDX-HRTEM maps shown in Figure 54-C and Figure 54-F for **Pd(II)-Cy5-NP** and **Pd(0)-Cy5-NP**, respectively, confirmed that palladium was located over the metallofluorescent NPs.

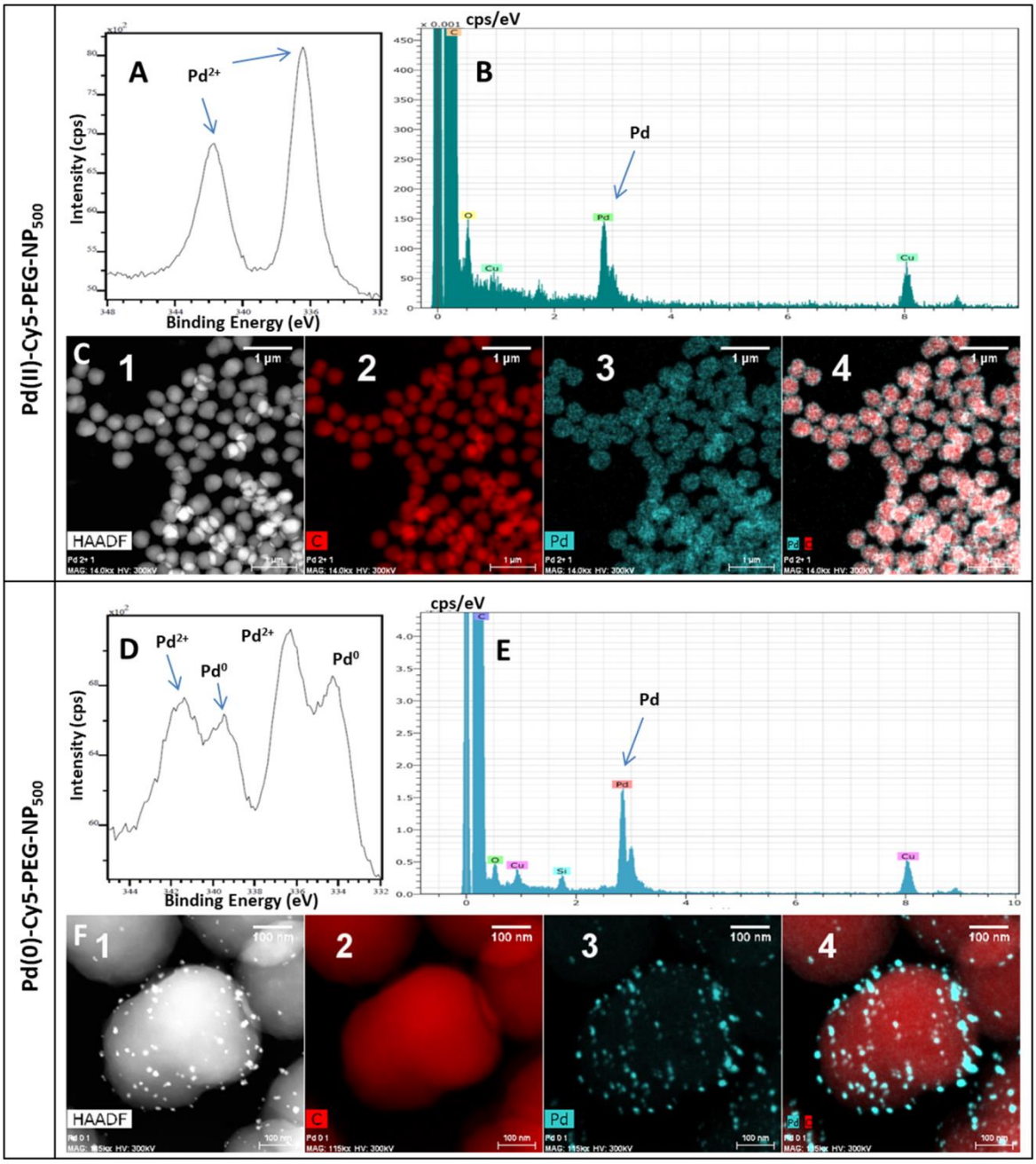
Pd(II)-Cy5-PEG-NP500
A
Pd2+
Intensity (cps)
Binding Energy (eV)
B
cps/eV
Pd
C
1
2
3
4
1 µm
HAADF
Pd(0)-Cy5-PEG-NP500
D
Pd2+
Pd0
E
F
100 nm

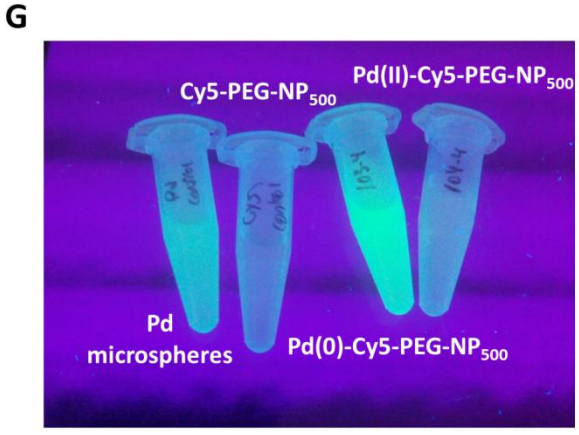
G
Cy5-PEG-NP500
Pd(II)-Cy5-PEG-NP500
Pd microspheres
Pd(0)-Cy5-PEG-NP500

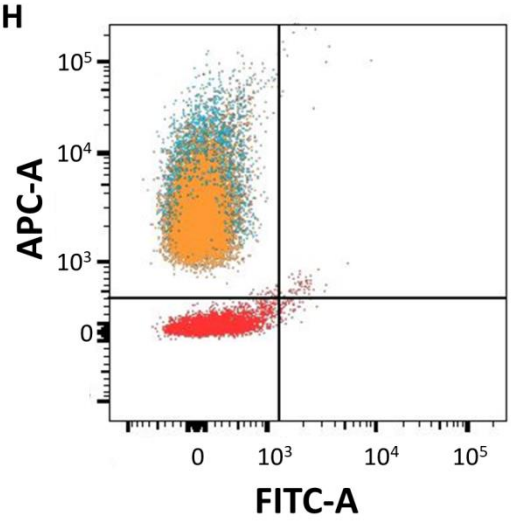
H
APC-A
FITC-A

Figure 54. A-C) XPS and EDX-HRTEM analysis of Pd(II)-Cy5-NP NPs. **D-F)** XPS and EDX-HRTEM analyses of Pd(0)-Cy5-NP NPs. **A and D)** XPS high-resolution spectra for Pd. **B and E)** EDX analyses showing the presence of Pd in Pd(II)-Cy5-NP and Pd(0)-Cy5-NP. **C and F)** EDX-HRTEM composite: high-angle annular dark field (HAADF) (**1**), carbon (**2**), palladium (**3**) and the stacked image palladium-carbon (**4**). **G)** Evidence of the Pd(0)-catalytic activity of Pd(0)-Cy5-NP, represented as Pd(0)-Cy5-PEG-NP_{500} in the figure, from the fluorogenic reaction consisting of the removal of allyloxycarbonyl groups. The fluorogenic emission is compared with a control using Pd microspheres as a catalyst. Cy5-NPs (Cy5-PEG-NP_{500} in the figure) and Pd(II)-Cy5-NP (Pd(II)-Cy5-PEG-NP_{500} in the figure) are not capable of catalysing the reaction. **H)** FACS counting of Pd(II)-Cy5-NP (cyan), Pd(0)-Cy5-NP (orange), and blank control, NH_2-PEG-NP (red) NPs.

In addition, HRTEM analysis, in STEM mode, for **Cy5-NP**, **Pd(II)-Cy5-NP**, and **Pd(0)-Cy5-NP** was performed (Figures 55, 56, and 57). X-ray diffraction analysis was also performed in order to determine the amorphous or crystalline nature of the black particles observed. As a matter of fact, when the Fast Fourier Transform (FFT) was applied to the data obtained for the palladium particles of **Pd(II)-Cy5-NP** and **Pd(0)-Cy5-NP**, following the next equation $FFT\ (\text{Å}) = 1/(\frac{\emptyset\ (nm)}{2}) * 10$, it was obtained that the Pd particles X-ray diffraction data were 2.20 Å and 2.26 Å in **Pd(II)-Cy5-NP** and **Pd(0)-Cy5-NP**, respectively, whereas the reported diffraction data for Pd is 2.24 Å [272],[273].

Figure 55-A shows the HRTEM image of **Cy5-NP** wherein an almost spheric shape is observed. In Figure 55-B a zoom to the edge of **Cy5-NP** is presented, observing the absence of any abnormal particle. This was checked by performing X-ray diffraction in that particular section, confirming the amorphous nature of the **Cy5-NP** since no diffraction pattern was obtained (Figure 55-C)

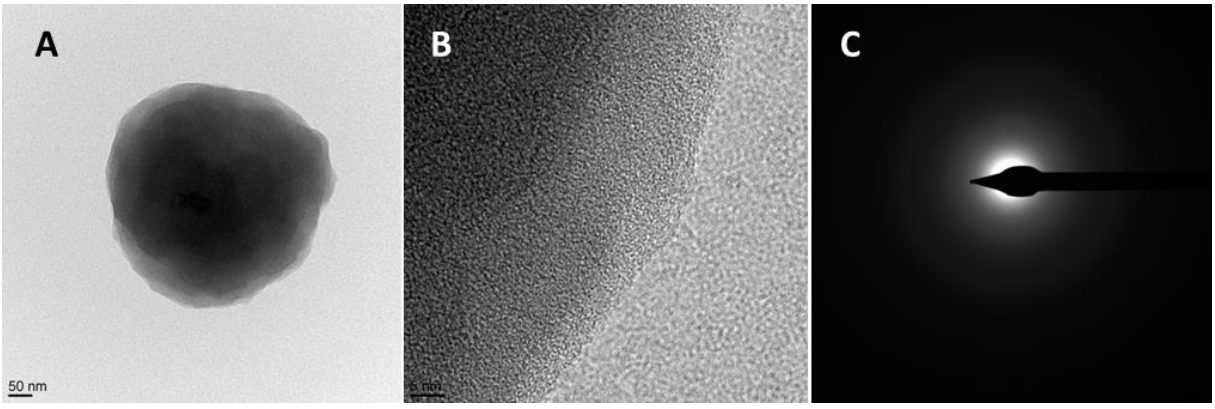

Figure 55. A) High resolution transmission electron microscopy (HRTEM) of NH_2-PEG-NP (nanoparticles control) in STEM mode. Scale bar represents 50 m. **B)** Edge of the NP surface. Scale bar represents 5 nm. **C)** X-ray diffraction (XRD) of NH_2-PEG-NP, showing that it is an amorphous structure.

On the other hand, in HRTEM images of **Pd(II)-Cy5-NP** is clearly observed the presence of palladium as black dots over the NPs (Figure 56-A-B). At this time, a tiny black dots or particles are seen at the edge of the **Pd(II)-Cy5-NP** (Figure 56-C), which exhibit a diffraction pattern when X-ray diffraction was performed, giving a distance of 9.071 nm (Figure 56-D-E).

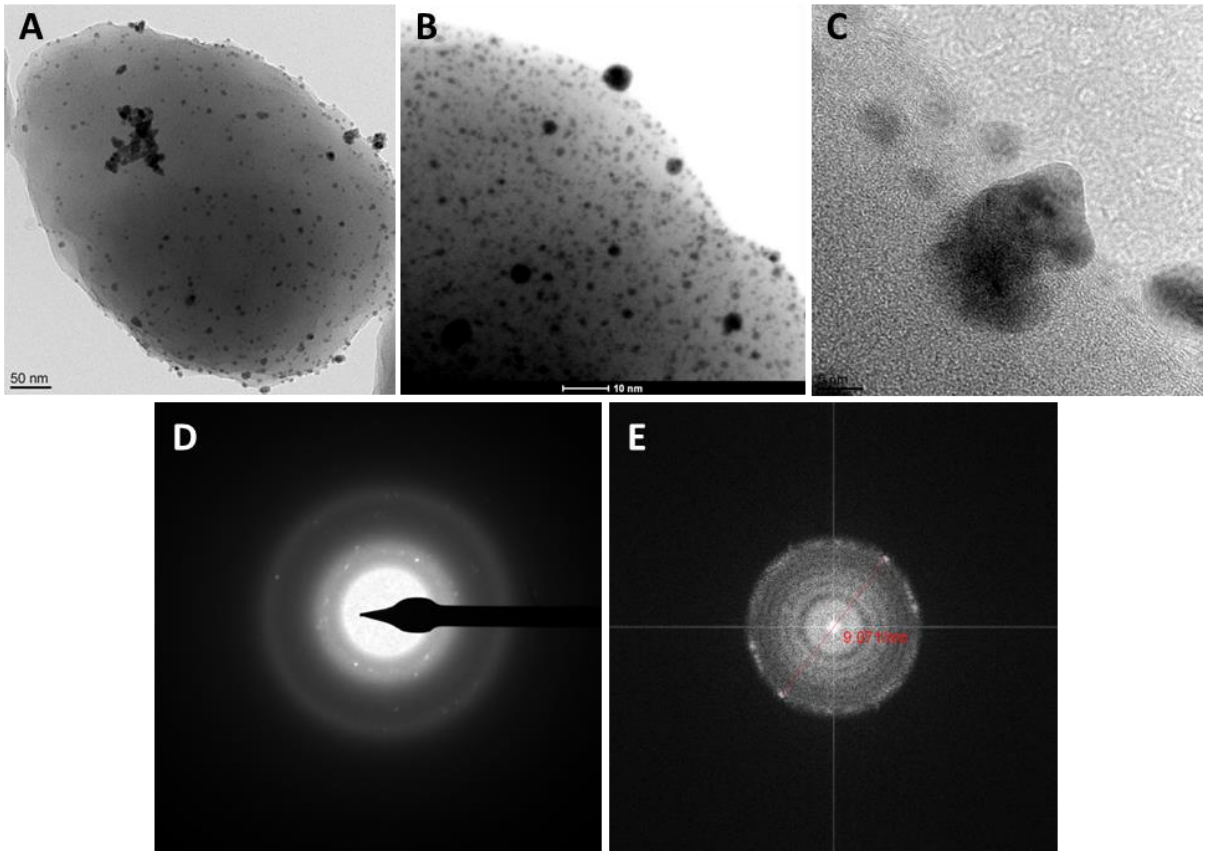

Figure 56. A-C) HRTEM of Pd(II)-Cy5-NP in STEM mode. Scale bar represents 50 nm in A and B, and 5 nm in C. **C)** Palladium particle at the surface of the NP. **D-E)** XRD of the palladium particles of C, exhibiting crystalline structure.

Likewise, HRTEM analysis was performed to **Pd(0)-Cy5-NP**. Similarly than in **Pd(II)-Cy5-NP**, black dots corresponding to palladium are observed over the NPs; however these dots are bigger than in **Pd(II)-Cy5-NP**, as they are particles of palladium (Pd^0). Besides, small dots are barely observed (Figure 57-A-B). X-ray diffraction was performed over a particle located at the edge of the **Pd(0)-Cy5-NP** (Figure 57-C), obtaining a diffraction pattern of an average distance value of 8.861 nm (Figure 57-D-E).

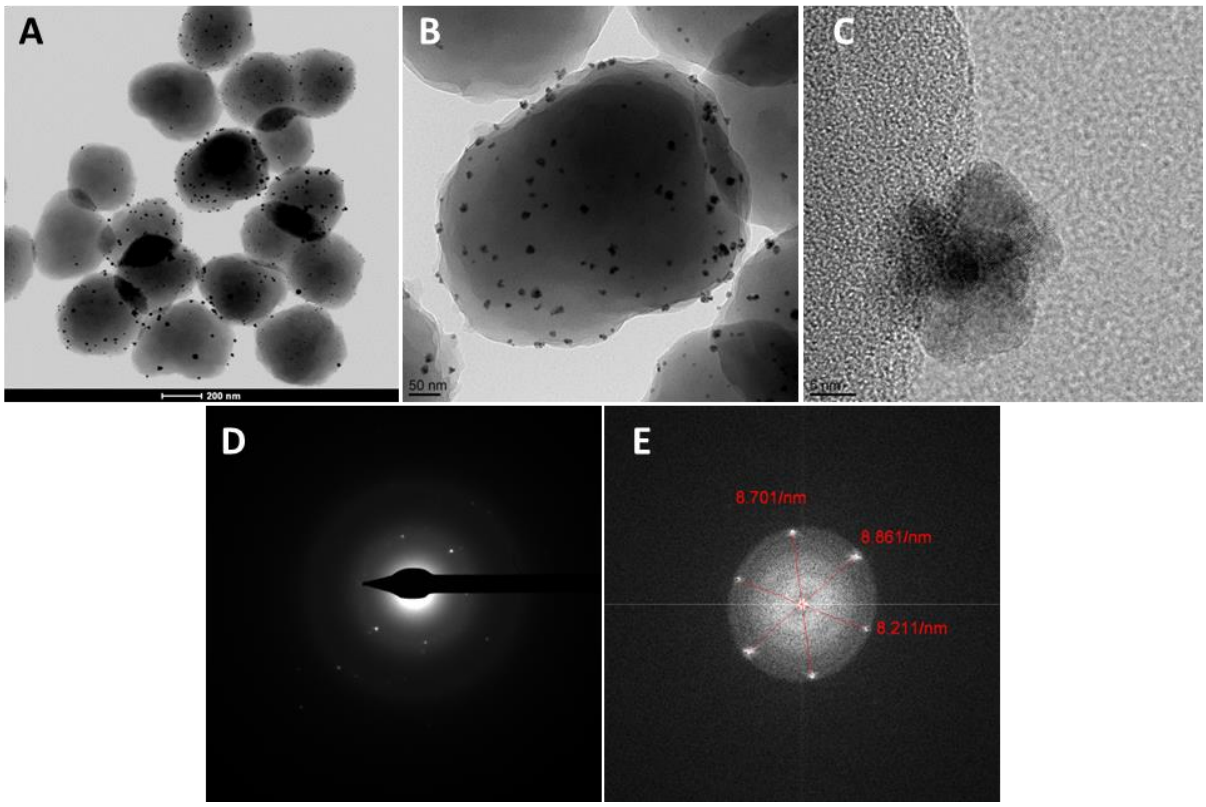

Figure 57. A-C) HRTEM of Pd(0)-Cy5-NP in STEM mode. Scale bar represents 200 nm in A, 50 nm in B, and 5 nm in C. **C)** Palladium particle at the surface of the NP. **D-E)** XRD of the palladium particles of C, exhibiting crystalline structure

To provide further insights into the role of the polymethine chain in the interactions responsible for the emergence of green fluorescence from the red-emitting dye Cy5, it was studied whether the interruption of the electronic conjugation of the system could somehow affect the fluorescent properties of the NPs. To this end, due to the capability of gold ions Au(III) to catalyse addition reactions to alkenes [274], the effect of gold over the Cy5 fluorophore was assessed. For that, firstly, $HAuCl_4 \cdot 3H_2O$ was added to an aqueous solution of the dye, producing an instant colour loss, from blue to transparent, meaning the utter disappearance of the typical Cy5 absorption spectrum (Figure 58-A). Secondly, a solution of 1 mg/mL of $HAuCl_4 \cdot 3H_2O$ was added to **Cy5-NP**, and after being washed, the NPs were analysed by XPS, showing traces of gold, and by FACS, where it was noted that the typical

Cy5 red fluorescence had disappeared whilst the unexpected green fluorescence remained stable, compared with the untreated **Cy5-NP** (Figure 58-B).

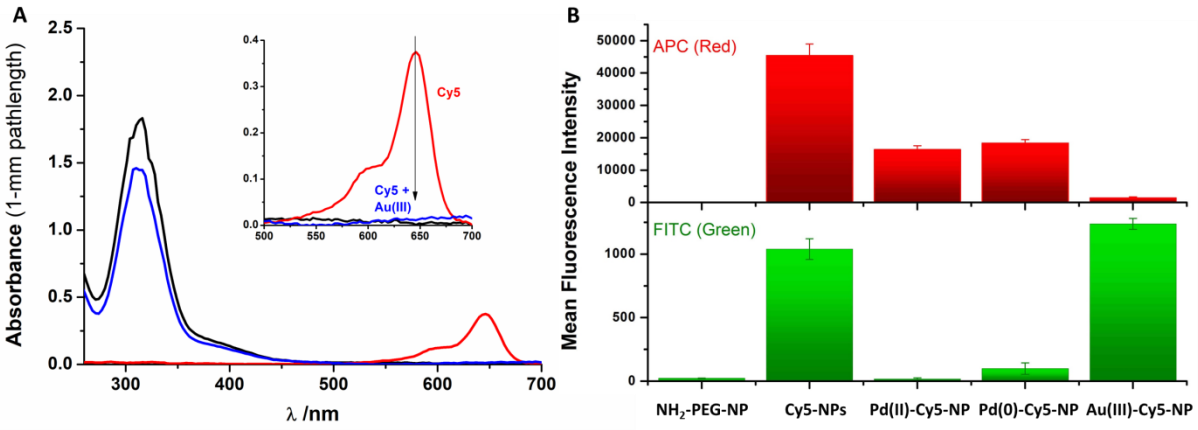

Figure 58. **A)** Absorption spectra of Cy5 in aqueous solution (red line) and after treatment with $HAuCl_4 \cdot 3H_2O$ (blue line). The absorption spectra of $HAuCl_4 \cdot 3H_2O$ in solution is also shown as a control (black line). **B)** APC (red) and FITC (green) channels MFI from FACS experiments of, from left to right, NH_2-PEG-NP, Cy5-NPs, Pd(II)-Cy5-NP, Pd(0)-Cy5-NP, and Cy5 conjugated NPs incubated with $HAuCl_4 \cdot 3H_2O$ [Au(III)-Cy5-NP].

These results demonstrated that gold was indeed catalysing addition reactions to alkenes, thereby breaking the polymethine chain conjugation, resulting in a complete loss of the red fluorescence emission but keeping the green fluorescence emission. This fact confirms and supports the idea of the π-π interactions being responsible of the green emission. On the one hand, palladium coordinates with the polymethine chain of Cy5 and the aromatic rings of polystyrene. Thus, palladium avoids the FRET process and quenches the green fluorescence emission while allowing the Cy5 red fluorescence emission (Figure 59-A). On the other hand, gold catalyses addition reactions to the Cy5 polymethine chain, thereby breaking and disrupting the conjugation effect responsible for the Cy5 typical red fluorescence whilst the π-π interactions between the two aromatic rings of the Cy5 molecule and the aromatic rings of polystyrene still occurs, hence producing green fluorescence (Figure 59-B) [257].

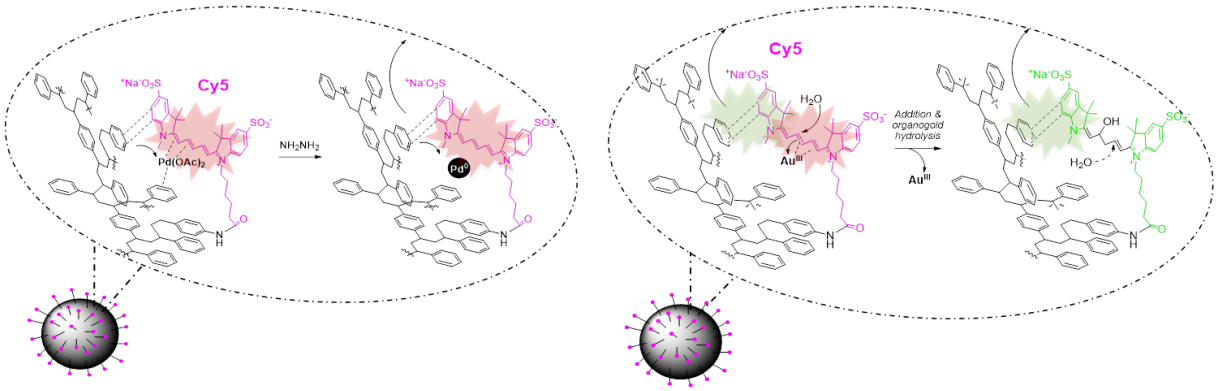

Figure 59. General scheme of palladium and gold interactions in the FRET phenomenon. **A)** Palladium avoids π-π interaction, thereby impeding FRET. As a result, green fluorescence is removed and red fluorescence is maintained. **B)** Gold catalyses addition reactions to the polymethine chain of Cy5, hence disrupting the Cy5 conjugation effect responsible for the red fluorescence. As a result, green fluorescence is maintained and red fluorescence is removed.

3.2.2. Discussion

In this first part of chapter 2 it has been presented the synthesis, in-depth characterisation and multimodal applications of novel metallofluorescent NPs. These metallofluorescent NPs carry simultaneously a fluorophore, Cy5, and a metal, preferably palladium, thereby allowing their employment as probes for fluorescence microscopy, fluorescence-lifetime imaging, flow cytometry, catalysits and mass cytometry [257].

The applications of these metallofluorescent NPs acting as multimodal probes have been shown to be broad and promising. As a matter of fact, the application of these NPs as cellular imaging probes and flow cytometry probes, has already been proven; thus, these are not exciting applications on the ground of the great number of publications reporting the use of polystyrene NPs in this regard [173],[174],[205],[209]. On the other hand, the use of metallofluorescent NPs as sensing probes for FLIM to determine changes in cellular environments, such as pH o protein expressions, is quite interesting. Furthermore, the fact that fluorescence lifetime of Cy5 and ATTO 647N, loaded in the NPs varies depending on the size of the NPs and their functionalisation enables the production of multiple unique probes. The employment of multiple probes within a sample would allow performing multiplexing, which has shown to be an useful approach in FLIM [275].

The inclusion of metals wihithin polystyrene NPs structure seems not to be innovative due to the synthesis of palladium-conjugated polystyrene NPs [181] have been previously reported. These NPs have been capable of acting as cytosolic catalysts [181],[182] which has open the possibility to drug-*in situ* actions within cells [276]. However, the previous reported NPs and the one described in this Doctoral Thesis differs in the manner in which the metal is coupled to the NPs. In this Doctoral Thesis, the fluorophore is added prior than the metal, avoiding further chemical manipulation, whereas the other NPs firstly incorporate palladium, and then extensive crosslinking to trap the coordinated palladium is performed, for, at last, keep conjugating molecules through more chemical reactions. Therefore, the method reported in this Doctoral Thesis is easier, quicker, and more efficient than the previous reported [181]. Furthermore, this method is not limited only to palladium conjugation but expanded to other metal such as copper and nickel. This enlarges the cytosolic catalyst reactions that can be performed with the metallofluorescent NPs, such as the clean and widely used in the biological field “Click reaction”. Click reaction has been successfully achieved with copper-trapped resins [277]. Nevertheless these resins have the principal drawback of their size which totally impedes their cellular uptake. In addition, since palladium also allows the metallofluorescent NPs to be identified by mass cytometry, their use as mass cytometry probes remains clear.

Overall, the metallofluorescent NPs have been shown to be valid reagents for multiple applications on the grounds of their dual-functionalisation fluorophore-metal. Of special interest is their promising application in the breakthrough technology mass cytometry. The fact of being easily and efficiently internalised by the cells opens up the applications of the metallofluorescent NPs as mass-tag reagents for single-cell mass cytometry.

3.3. Live cell barcoding using metallofluorescent NPs

3.3.1. Metallofluescent NPs as mass-tag barcodes PoC

3.3.1.1. Results

Given the previous reports of the versatility of fluorescently-labelled cross-linked polystyrene particles for bead-based analysis [173],[174],[205] and polystyrene particles carrying metals for *in-cellulo* chemical applications [181],[182],[277], the potential applications of these metallofluorescent NPs within cells has been assessed. In spite of previous experiments reporting that polystyrene NPs, even carrying metals, are non-toxic for the cells [182], the toxicity that these metallofluorescent NPs could provoke in mammalian cell lines was firstly evaluated. For that, the colorimetric MTT assay was performed in order to determine the cell viability. Breast cancer cell line MDA-MB-231 was incubated with a range of NPs up to 20,000 NPs/cell, for 6 days, measuring the cell viability after that. In this experiment the toxicity of control NPs (**NH_2-PEG-NP**), Cy5 conjugated NPs (**Cy5-NPs**), and Cy5 conjugated NPs carrying metals (**Ni(II)-Cy5-NP**, **Cu(I)-Cy5-NP**, **Pd(II)-Cy5-NP**, and **Pd(0)-Cy5-NP**) was evaluated. This experiment showed that the viability of cells nanofected with metallofluorescent NPs was very similar to that of cells nanofected with control NPs (**NH_2-PEG-NP**), even at higher NPs concentration per cell (Figure 60-A). Additionally, the efficient uptake of these metallofluorescent NPs by FACS analysis through incubation of cells with a range of NPs per cell (0, 125, 250, 1,000, and 2,000) for 8 h, and analysing their red fluorescence emission (Figure 60-B) was also evaluated. As it is shown, the percentage of cells containing metallofluorescent NPs increased according to the number of NPs employed during the nanofections, meaning that the more number of NPs resulted in a higher nanofection percentage. Remarkably, the multiplicity of nanofection 50 (MNF50) values [278] – the number of NPs needed to have the 50% of the cell population nanofected – of the metallofluorescent NPs were in the same order of magnitude as that of the **Cy5-NPs**. This fact allowed the use of metallofluorescent NPs as multi-modal probes for live cell-based assays.

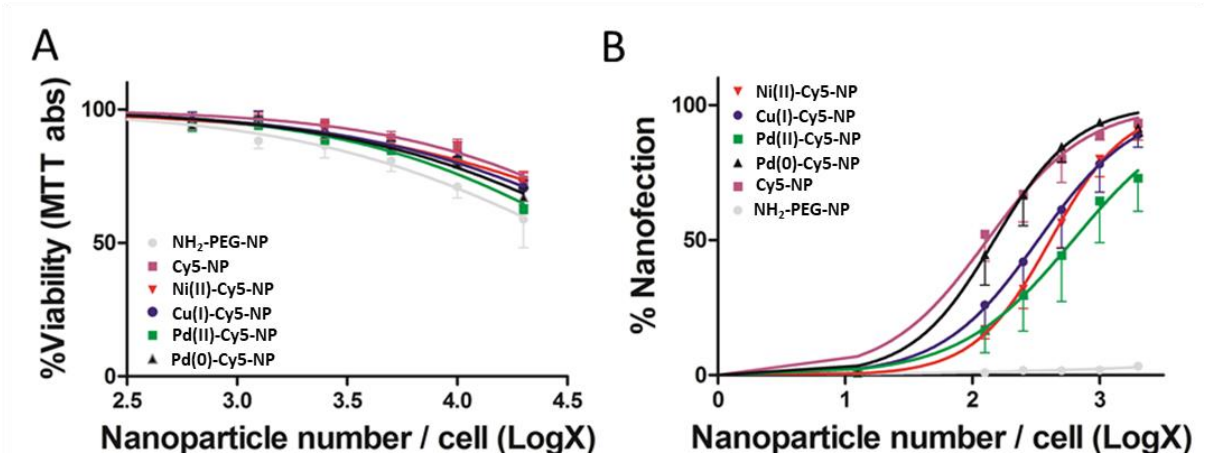

Figure 60. A) Cellular viability (MTT assay) of MDA-MB-231 cells nanofected for 6 days with metallofluorescent NPs expressed as a percentage of the control non-nanofected cells. Data are reported as the mean ± SEM. **B)** Analysis of metallofluorescent NP cellular uptake by MDA-MB-231 cells at different ratios per cell measured using FACS. Data are reported as the mean ± SEM.

Besides, the effective nanofection of metallofluorescent NPs was also assessed by confocal microscopy, showing that the NPs were inside the cells indeed. Likewise, confocal microscopy showed what was previously verified, that the unexpected green fluorescence band that appeared in **Cy5-NPs** had been effectively removed by adding palladium to the NPs. In Figure 61 it is seen that the green fluorescence band disappeared in **Pd(0)-Cy5-NP** and that the slight red quenching observed by FACS also took place in confocal microscopy; however the red fluorescence signal was clear enough to use the metallofluorescent NPs as probes for location and colocalisation studies.

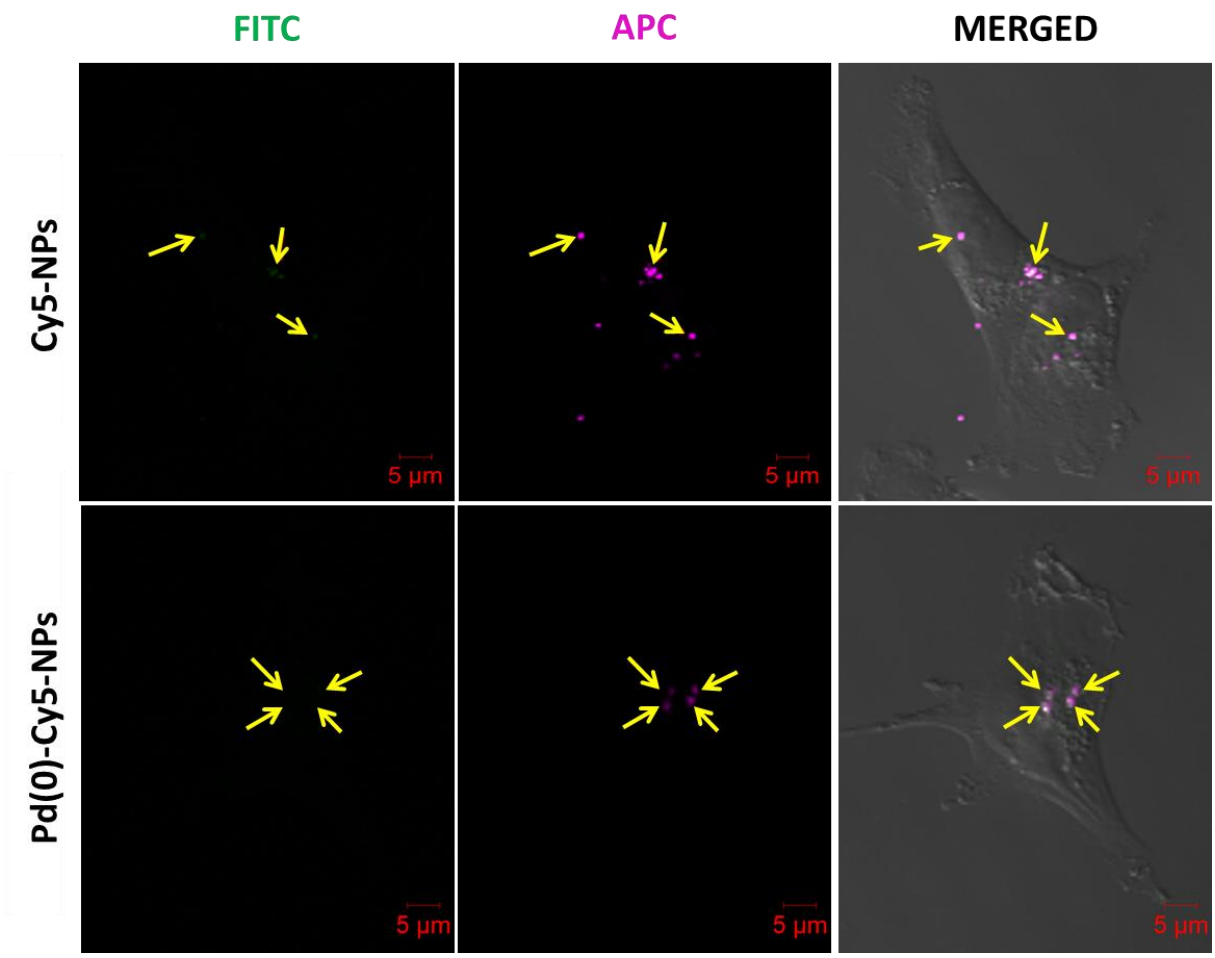

Figure 61. Confocal microscopy image of a representative nanofected cell in a ratio of 3,000 Cy5-NP/cell (upper row) and 3,000 Pd(0)-Cy5-NP/cell (lower row) through the different channels (FITC, APC and merged with the transmission image). Arrows point to single NPs in the cell cytoplasm.

At last, in order to evaluate and confirm whether the metallofluorescent NPs transported the metals into cells, there were performed several experiments for the *in situ* detection of palladium by CyTOF. For that, **Pd(0)-Cy5-NP** were incubated at different concentrations (0, 50, 100, 250, 500, and 1,000 NPs/cell) for 8 h with MDA-MB-231 cells, assessing the presence of palladium. To ensure that the palladium signal exclusively came from **Pd(0)-Cy5-NP** located inside the cells, the DNA marker iridium (Ir) was used to identify the cells. Thus, only recorded events showing both Ir (cell nuclei maker) and Pd (present in NPs) could be considered as positive nanofected cells. As expected, a higher number of NPs per cell gave a higher nanofection percentage (Figure 62-A). Surprisingly, when the percentages of nanofection obtained by FACS and CyTOF were compared, no differences between both values were reported (Figure 62-B).

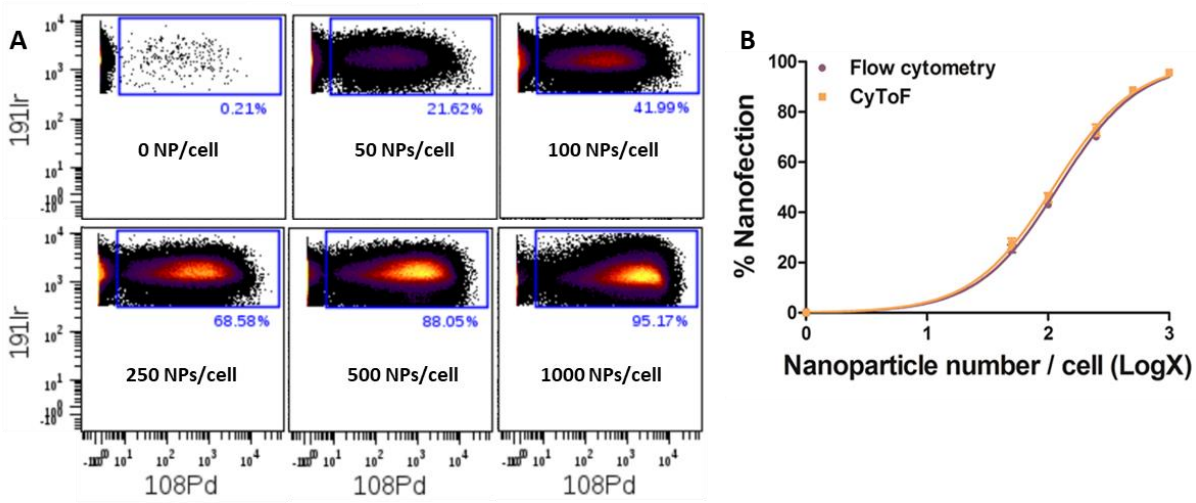

Figure 62. A) Analysis of Pd(0)-Cy5-NP uptake at different ratios of number of NP/cell by CyTOF using Cytobank Software. **B)** Comparison of Pd(0)-Cy5-NP uptake curves in the same cells using FACS and CyToF. Data are reported as the mean ± SEM.

Regarding the results obtained and seeking expansion of the metallofluorescent NPs applications in the field of cell barcoding and cell-based multiplexing assays, the research was focused on their development for CyTOF analysis. Therefore, as in CyTOF is possible to distinguish between the different palladium isotope channels, there were synthesised two novel metallofluorescent NPs containing specific Pd isotopes rather than a mixture of them, as it happened with **Pd(0)-Cy5-NP** and **Pd(II)-Cy5-NP** when $Pd(OAc)_2$ was used. Consequently, **^{106}Pd-Cy5-NP** and **^{110}Pd-Cy5-NP**, containing the isotopes ^{106}Pd and ^{110}Pd respectively, were synthesised. For that, a solution of $^{106}Pd(NO_3)_2$ or $^{110}Pd(NO_3)_2$ in water was added to Cy5-NP of 500 nm in size, mixing the suspension for 14 h, at RT, in darkness; subsequently, ionic palladium was reduced to palladium particles with a solution of 55% hydrazine in MeOH, giving rise to **^{106}Pd-Cy5-NP** and **^{110}Pd-Cy5-NP**, respectively (Scheme 13).

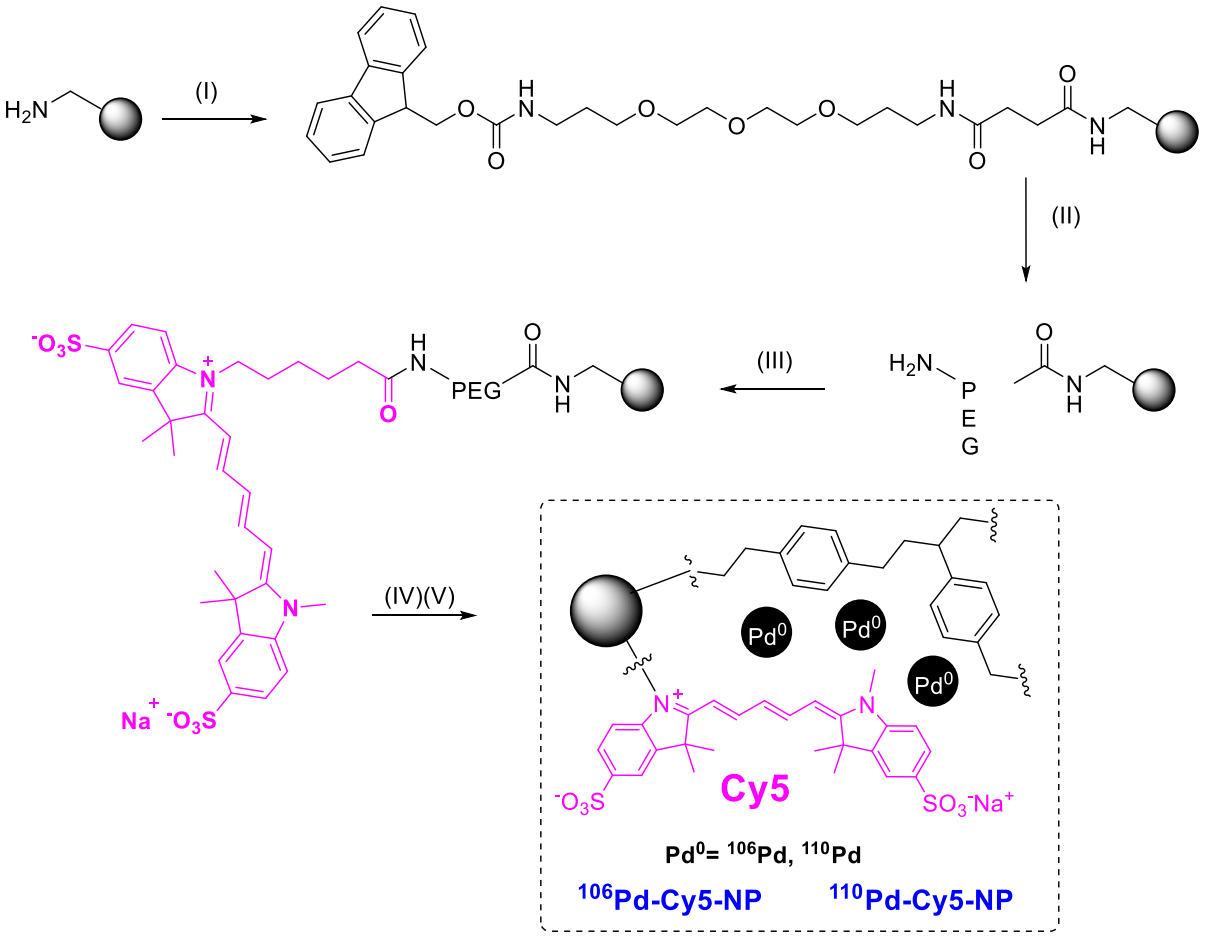

Scheme 13. Synthesis of **^{106}Pd(0)-Cy5-NP** and **^{110}Pd(0)-Cy5-NP**. **(I)** Fmoc-PEG-OH is conjugated to naked amino-functionalised cross-linked polystyrene NPs; **(II)** Fmoc group removal; **(III)** Cy5-conjugation; and **(IV,V)** isotopically pure isotopes ^{106}Pd and ^{110}Pd are added to Cy5-NP, and subsequently reduced, to afford ^{106}Pd(0)-Cy5-NP and ^{110}Pd(0)-Cy5-NP, respectively.

The effective incorporation of the Pd isotopes was verified by CyTOF, analysing both metallofluorescent NPs, **^{106}Pd-Cy5-NP** and **^{110}Pd-Cy5-NP**, and comparing the signals obtained for ^{106}Pd and ^{110}Pd channels with those obtained for **Cy5-NPs**, which are used as NPs control. Both **^{106}Pd-Cy5-NP** and **^{110}Pd-Cy5-NP** were analysed directly after being synthesised, having palladium as ions Pd(II), and after the *in situ* reduction of Pd(II) to Pd(0), showing in both cases a clear signal in the expected Pd channels ^{106}Pd or ^{110}Pd, and residual signals in the other Pd channels (Figure 63-A-C/E-G). Moreover, to ensure whether these Pd isotopes conjugated NPs could still be used as multimodal probes, they were also analysed by FACS, showing that the Cy5 red fluorescent emission remained intact. (Figure 63-D/H).

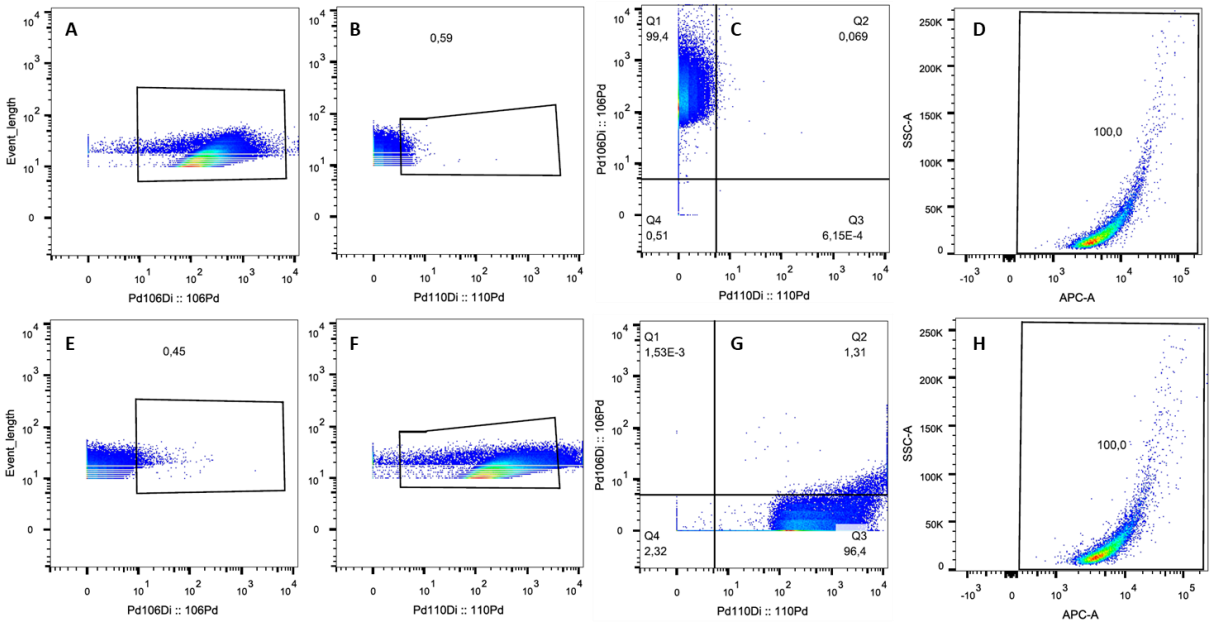

Figure 63. Plots **A-D** correspond to **^{106}Pd-Cy5-NP**, while that plots **E-H** correspond to **^{110}Pd-Cy5-NP**. ^{106}Pd isotope signals are shown in plots A and E, whilst ^{110}Pd isotope signals are shown in plots B and F. Plots C and G show the 2D plot of ^{106}Pd/^{110}Pd channels. Plots D and H show the red fluorescence of the NPs in FACS, collected in the APC channel.

Bearing this in mind and thinking of using **^{106}Pd-Cy5-NP** and **^{110}Pd-Cy5-NP** for cell barcoding and for cell-based assays, their toxicity in cells was also assessed. As described above, different concentrations of NPs per cell of these novel metallofluorescent NPs were incubated with MDA-MB-231 for 6 days, evaluating the toxicity then. To this end, it was started with 40,000 NPs/cell and the concentration was decreased following serial dilutions down to 156.25 NPs/cell. The viability of both NPs was also compared with "naked" NPs (**NH_2-PEG-NP**) and Pd-conjugated NPs with $Pd(OAc)_2$ (**Pd(0)-Cy5-NP**), which resulted to be non-toxic for the cells. As expected, the results showed that **^{106}Pd-Cy5-NP** and **^{110}Pd-Cy5-NP** did not affect the viability of the cells compared with both controls, which was only scarcely decreased when a ratio of 40,000 NPs/cell was used (Figure 64-A). Nevertheless, 40,000 NPs/cell is a ratio far higher than the ratios commonly used for nanofecting cells, fact that confirms that they can be used for live cell assays.

Moreover and thinking of the cell-based assays, to determine the optimal ratio of NPs per cells to be used, the MNF50 of both **^{106}Pd-Cy5-NP** and **^{110}Pd-Cy5-NP** in MDA-MB-231 cells was evaluated by FACS and CyTOF. For the MNF50 in FACS, a range from 50 to 10,000 NPs/cell was used to nanofect the cells for 3 h, resulting in a very rapid uptake. Regarding this, the same time setting was translated for the MNF50 in CyTOF, but using only 50, 250, 500, 1,000, and 2,000 NPs/cell according to the MNF50 obtained for FACS and due to the high sensitivity of CyTOF. Therefore, the **^{106}Pd-Cy5-NP** and **^{110}Pd-Cy5-NP** uptake resulted in

a gradual rise, obtaining MNF50 values of 500 NPs/cell and 473 NPs/cell for **^{106}Pd-Cy5-NP** and **^{110}Pd-Cy5-NP**, respectively, which were a reasonable ratio of number of NPs per cell (Figure 64-B).

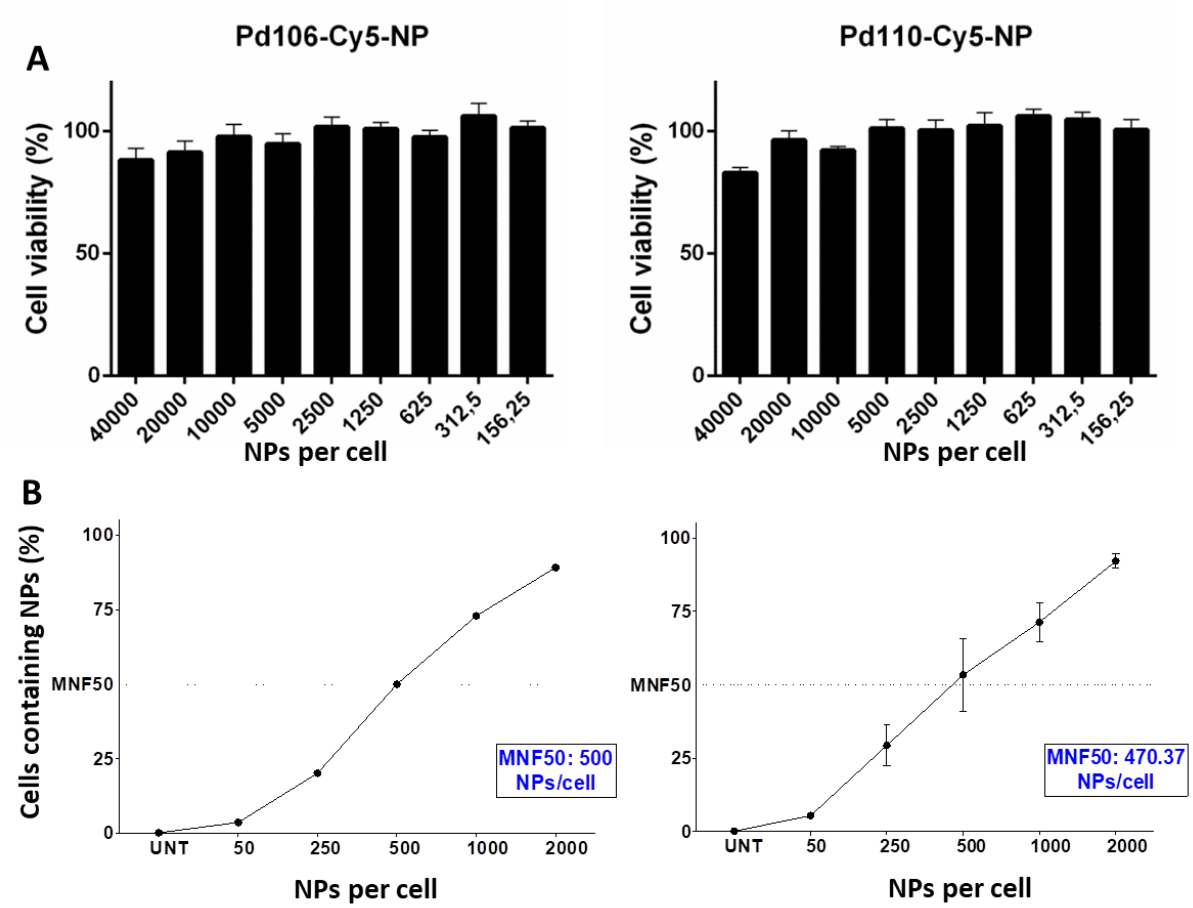

Figure 64. **A)** Cell viability bar plots of MDA-MB-231 incubated with ^{106}Pd-Cy5-NPs and ^{106}Pd-Cy5-NPs. **B)** MFN50 analysis of MDA-MB-231 incubated with ^{106}Pd-Cy5-NPs and ^{106}Pd-Cy5-NPs.

As the viability and MNF50 experiments showed both that **^{106}Pd-Cy5-NP** and **^{110}Pd-Cy5-NP** were non-toxic for the cells and that they can be easily uptaken by cells, the consideration of using these metallofluorescent NPs for live cell barcoding remained clear. Nevertheless, whether the palladium signals of the metallofluorescent NPs will continue to be detectable after a long time and whether a mixture of independently barcoded cells could be detected by CyTOF, came to mind. Regarding both questions, there were designed experiments to clarify them.

In order to evaluate whether the palladium signal would be detectable, it was considered to evaluate the nanofected cells after 5 days of incubation with the NPs. Besides, to ensure a complete nanofection of the cells, the experiment was performed using the ratios 1,000, 2,000, and 4,000 NPs/cell. Moreover, as both **^{106}Pd-Cy5-NP** and **^{110}Pd-Cy5-NP** showed a

similar value of MNF50, it was decided to do the experiment using only **^{110}Pd-Cy5-NP**. To afford it, MDA-MB-231 cells were seeded in 6-wellplate and stabilised for 18 h. The next day, suspensions of **^{110}Pd-Cy5-NP** in medium, containing 1,000, 2,000, and 4,000 NPs/cell were added to the cells, incubating them for 5 days. After the first day, cells were harvested and half of them were subcultivated again in another plate whilst the other half were fixed, stained with Ir marker, and analysed by CyTOF. The medium of the subcultivated cells was changed as it is established for MDA-MB-231 cells in the American type culture collection (ATCC). Besides, in order to avoid false signals coming from **^{110}Pd-Cy5-NP** adhered to the wells, several washings with PBS prior to adding the medium were performed. CyTOF analysis showed that, even after 5 days of incubation, the events showing double positive signals for ^{191}Ir and ^{106}Pd were above the 40% (Figure 65), what it was considered to be good enough for long term cell assays.

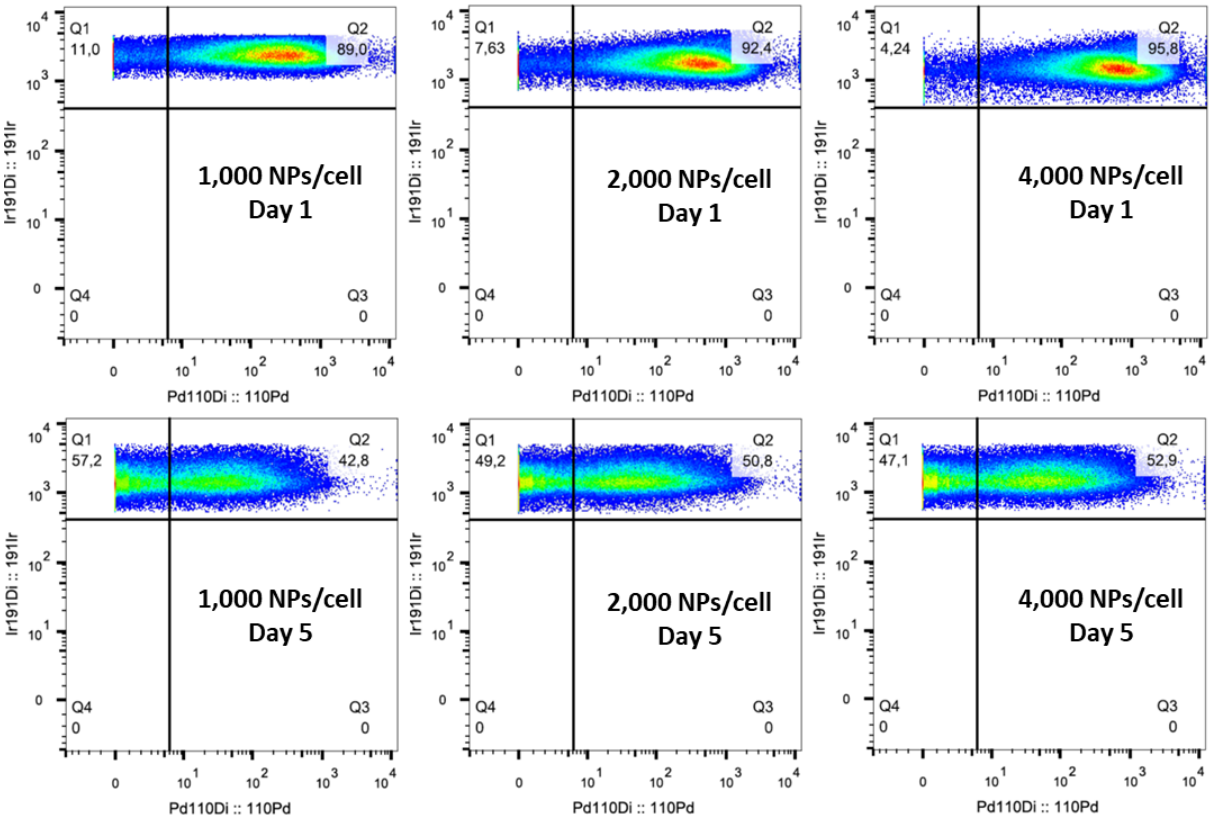

Figure 65. CyTOF plots of the ^{191}Ir and ^{110}Pd channels for ^{110}Pd-Cy5-NP after 5 days of nanofection at a ratio of 1,000 NPs/cell (left column), 2,000 NPs/cell (middle column), and 4,000 NPs/cell (right column).

Therefore, the feasibility of the Pd-conjugated NPs as codes for live cell barcoding was tested. A PoC experiment consisting of nanofecting MDA-MB-231 cells with two different codes and mixing them in different proportions, for a final analysis by CyTOF, was performed. So, two sets of MDA-MB-231 cells were seeded in 6-well plate and nanofected

independently with either **^{106}Pd-Cy5-NP** or **^{110}Pd-Cy5-NP**, at a ratio of 2,000 NPs/cell for 3 h. Then, the barcoded cells, one with **^{106}Pd** (BC-1) and the others with **^{110}Pd** (BC-2), were mixed following the next proportions: BC-1 100% – 0% BC-2, BC-1 75% – 25% BC-2, BC-1 50% – 50% BC-2, BC-1 25% – 75% BC-2, and BC-1 0% – 100% BC-2 (Figure 66). Afterwards, all the mixtures were analysed by CyTOF, assessing whether the corresponding Pd isotopes, ^{106}Pd and ^{110}Pd, signals of each sample were equivalent to the ratio of barcoded cell mixture.

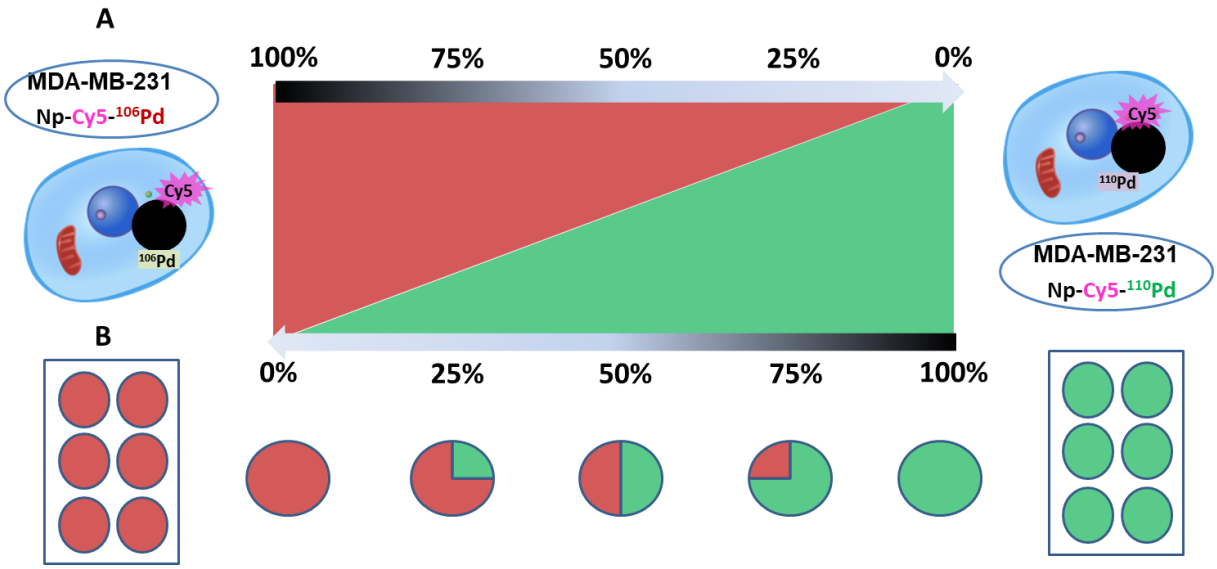

Figure 66. Depiction of the PoC experiment. **A)** Two sets of MDA-MB-231 cells nanofected with either ^{106}Pd-Cy5-NP or ^{110}Pd-Cy5-NP and a gradient of how they are mixed, showing the percentages. **B)** Representation of how the nanofected cells are mixed from the wells to the Flow Cytometer tubes according to the ratio of mixtures.

Considering that the maximum Pd signals that can be obtained for each isotope corresponded to those for the non-mixed barcoded cells, BC-1 100% – 0% BC-2 and BC-1 0% – 100% BC-2 (^{106}Pd and ^{110}Pd respectively), the relative signal for each cell mixture was calculated (Table 17). As a matter of fact, none of the Pd isotopes reached 100% of cell uptake; nonetheless, both signals were considered the maximum possible for this experiment. To afford the relative signals, the signal obtained for each isotope in each cell mixture was divided by the maximum signal obtained for them; subsequently, the calculated percentages of relative signals were compared with the theoretical ones, defined by the cell mixtures BC-1 75% – 25% BC-2, BC-1 50% – 50% BC-2, and BC-1 25% – 75% BC-2. The data represented in Table 17 showed that in all the cases, the percentages of the relative signals for both Pd isotopes were very similar to the mixture ratio of the barcoded cells. Likewise, it is observed that ^{110}Pd signals for each cell mixture were scarcely higher than ^{106}Pd signals for the correspondent percentages. In fact, 25% of BC-2 MDA-MB-231 cells

showed 22.6% of ^{110}Pd signals whereas 25% of BC-1 MDA-MB-231 cells showed 19.4% of ^{106}Pd; 50% of BC-2 MDA-MB-231 cells showed 41.5% of ^{110}Pd signals whereas 50% of BC-1 MDA-MB-231 cells showed 39.5% of ^{106}Pd; and, 75% of BC-2 MDA-MB-231 cells showed 68.7% of ^{110}Pd signals whereas 75% of BC-1 MDA-MB-231 cells showed 64.1% of ^{106}Pd. However, it is also to note that when the cells barcoded with only one isotope were compared, the signal for ^{110}Pd (BC-2) was higher than the signal for ^{106}Pd (BC-1), 87.3% and 84.7% respectively.

Table 17. Table showing the results obtained after the CyTOF run and FlowJo analysis. From left to right: BC-1 / BC-2 Mix column shows the percentages of mixture of barcoded cells; % BC-1 (^{106}Pd) column shows the average signals for ^{106}Pd channel in each sample (n=4); % BC-2 (^{110}Pd) column shows the average signals for ^{110}Pd channel in each sample (n=4); Relative % ^{106}Pd column shows the signal for ^{106}Pd channel after being normalised; Relative % ^{110}Pd column shows the signal for ^{110}Pd channel after being normalised.

BC-1 / BC-2 Mix	% BC-1 (^{106}Pd)	% BC-2 (^{110}Pd)	Relative % ^{106}Pd	Relative % ^{110}Pd
100% - 0%	84.7 ± 5%	0	100	0
75% - 25%	64.1 ± 3%	22.6 ± 6%	75.7	25.9
50% - 50%	39.5 ± 5%	41.5 ± 6%	46.6	47.5
25% - 75%	19.4 ± 6%	68.7 ± 4%	22.9	78.7
0% - 100%	0	87.3 ± 2%	0	100

The results showed that these Pd-isotopes conjugated NPs were suitable for barcoding live cells and that the barcoded cells can be identified after CyTOF analysis when they are in a mixture.

3.3.2. Metallofluorescent NPs for barcoding of ovarian cancer cells

3.3.2.1. Results

Based on these previous results, a short project in Professor Nolan's lab, at Stanford University, for barcoding ovarian cancer cells and their identification by CyTOF was developed in close collaboration with Fantl's group. In this project, three ovarian cancer cell lines, OVCAR-4, Kuramochi and TYK-nu, were selected along with a set of specific ovarian cancer cell panel of antibodies. Most of the labelled antibodies were kindly provided by Fantl's group but others were conjugated following the Maxpar® Antibody Labelling Kit protocol from Fluidigm [223].

Table 18. Pd-isotopes-conjugated metallofluorescent NPs barcodes (BC-1, BC-2, and BC-3) containing Pd isotopes ^{106}Pd and/or ^{110}Pd.

Barcodes	**^{106}Pd**	**^{110}Pd**
BC-1		
BC-2		
BC-3		

In this experiment, the ovarian cancer cell lines TYK-nu, Kuramochi and OVCAR-4 were chosen to be barcoded with **^{106}Pd-Cy5-NP** (BC-1), **^{110}Pd-Cy5-NP** (BC-2), and **$^{106\text{-}110}$Pd-Cy5-NP** (BC-3), respectively. **$^{106\text{-}110}$Pd-Cy5-NP** (BC-3) was afforded by mixing **^{106}Pd-Cy5-NP** (BC-1) and **^{110}Pd-Cy5-NP** (BC-2) in the same proportion (Table 18). Settings of a ratio of 2,000 NPs/cell and 3 h of incubation were selected to afford cells nanofection without permeabilisation. Simultaneously, as control, a set of TYK-nu cells were not chosen to be barcoded, thus, **Cy5-NPs** that contained no palladium, were also nanofected using the same settings.

Cell viability was measured using trypan blue and a TC10™ Automated Cell Counter (Bio-Rad), after NPs incubation. Cell viability of nanofected cells gave average values (n=3) of 95% for BC-1 TYK-nu (**^{106}Pd-Cy5-NP**), 80% for BC-2 Kuramochi (**^{110}Pd-Cy5-NP**), 90% for BC-3 OVCAR-4 (**$^{106\text{-}110}$Pd-Cy5-NP**), and 96% for TYK-nu control (**Cy5-NPs**). These viability values demonstrated that the NPs used for barcoding were non-toxic for the cells at a ratio of 2,000 NPs/cell. From our experience, the modest viability decrease observed in nanofected Kuramochi cells is totally normal due to inherent peculiarities of this cell line, which grows slowly and it is of difficult handling.

In order to determine the conditions to establish NPs nanofection, samples of barcoded cells were run on CyTOF. Therefore, quantification of ^{106}Pd and ^{110}Pd presented in cells as a result of the barcoding with metallofluorescent NPs was performed and compared after the analysis by Cytobank. Before running in CyTOF and to allow absolute quantification within single cells, cisplatin treatment (^{195}Pt channel) to select viable cells was performed [279]. The gating strategy employed for this experiment was similar to the previously used, but including an extra gate for selecting live cells. Thus, the hierarchical gating strategy was firstly ^{191}Ir/^{193}Ir to select the cells, then ^{191}Ir/Event length to select the singlets, afterwards ^{191}Ir/^{195}Pt to select the viable cells (low Pt signal), and at last ^{106}Pd/^{110}Pd since they were the isotopes used for the barcoding.

Average percentages of positive events in ^{106}Pd and ^{110}Pd channels for barcoded cells showed negligible signals for cells control nanofected with **Cy5-NPs**, whilst BC-1 (**^{106}Pd-Cy5-NP**) TYK-nu cells showed approximately 70% of events in ^{106}Pd channel, BC-2 (**^{110}Pd-Cy5-NP**) Kuramochi showed approximately 65% of events in ^{110}Pd channel, and BC-3 (**$^{106\text{-}110}$Pd-Cy5-NP**) OVCAR-4 showed nearly 62% of events in the double ^{106}Pd/^{110}Pd quadrant (Figure 67-A). Strikingly, any barcoding (BC-1, BC-2, and BC-3) showed no spill over signal between ^{106}Pd and ^{110}Pd channels (Figure 67-B). Nevertheless, the plots also showed that for BC-1 TYK-nu and BC-2 Kuramochi there were almost 30% of double negative ^{106}Pd/^{110}Pd evens, whereas for BC-3 OVCAR-4 the double negative ^{106}Pd/^{110}Pd events represented nearly the 20% of the total events. This suggested that the conditions employed for the cells nanofection, 2,000 NPs/cell and 3 h of incubation, were inefficient, therefore, increasing the nanofection time to 6 h to maximise the nanofection efficiency was decided.

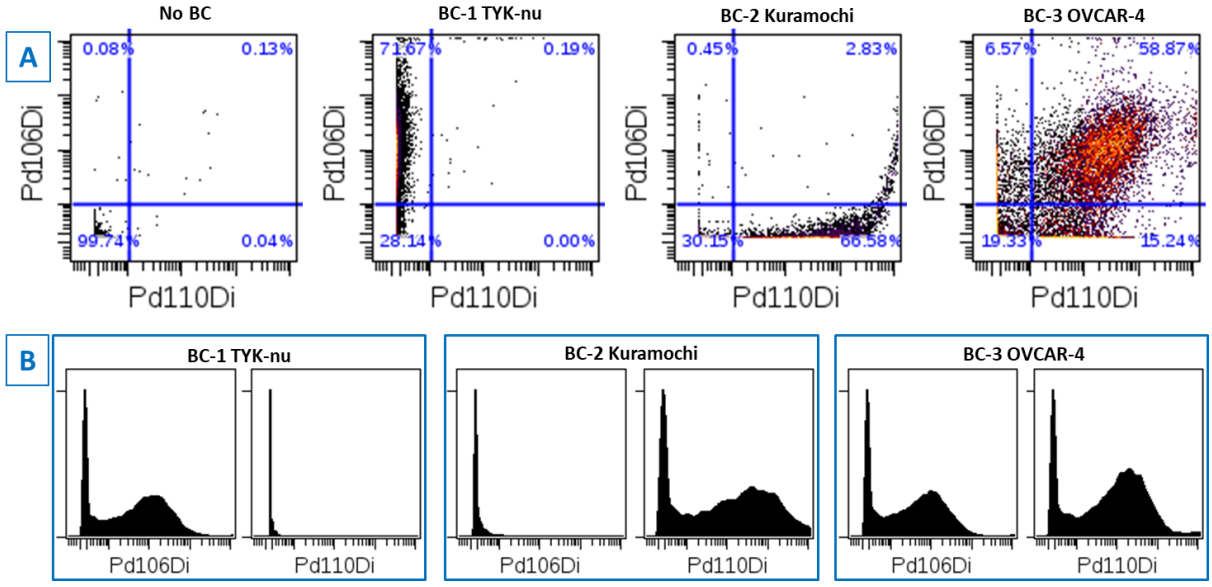

Figure 67. Representative $^{106}Pd/^{110}Pd$ 2D plots and histograms of the samples. **A)** From left to right, plots for non-barcoded cells (control), BC-1 TYK-nu (^{106}Pd), BC-2 Kuramochi (^{110}Pd), and BC-3 OVCAR-4 ($^{106\text{-}110}Pd$). **B)** Histograms of ^{106}Pd and ^{110}Pd channels for BC-1 TYK-nu, BC-2 Kuramochi, and BC-3 OVCAR-4 samples.

Looking at these results, a tool for multiparametric barcoding of ovarian cancer cell lines with specific metallofluorescent NPs acting as barcodes, without the need of permeabilisation, has been developed. In order to validate whether multiplexing barcoding nanoplatform could be combined with antibodies (Ab) to afford a more complete barcoding, a new assay came to mind (Figure 68). The potential concerns of this multiparametric combination were addressed when designing the multiparametric barcoding assay.

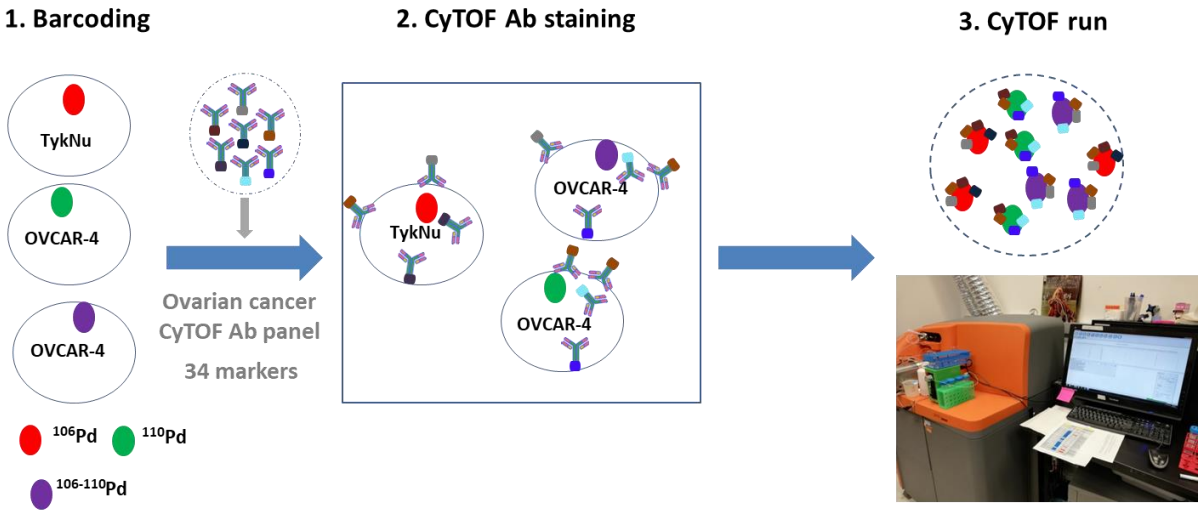

Figure 68. Live cell barcoding assay. **1)** The ovarian cancer cell lines are lively barcoded using three types of metallofluorescent NPs; **2)** Lanthanides labelled Ab are added to the barcoded cells; and **3)** The barcoded and stained cells are loaded into the CyTOF to run the experiment.

The multiplexed barcoding of ovarian cancer cell lines was done with specific barcodes of metallofluorescent NPs. For that, three different codes (**^{106}Pd-Cy5-NP**, **^{110}Pd-Cy5-NP**, and **$^{106\text{-}110}$Pd-Cy5-NP**) were employed. To determine whether metallofluorescent NPs barcoding could have an impact on cellular protein expression, a critical control was the barcoding of the same ovarian cancer line with two different barcodes. Thus, TYK-nu cells were barcoded with **^{106}Pd-Cy5-NP** (BC-1), while two sets of OVCAR-4 cells were barcoded with **^{110}Pd-Cy5-NP** (BC-2) and **$^{106\text{-}110}$Pd-Cy5-NP** (BC-3), as it is shown in Figure 68. Barcoded cells were then processed for CyTOF through a viability stain [234] as well as with an ovarian cancer Ab panel. This panel included a set of 13 Ab against intracellular markers (Table 19), and a set of 21 intracellular Ab (Table 20), for a total of 33 CyTOF ovarian Ab. cPARP Ab was included amongst the intracellular Ab panel to analyse the influence of metallofluorescent NPs on apoptosis generation.

Table 19. Panel of surface antibodies, the symbols and the mass of the corresponding elements to which the antibodies are labelled with.

ANTIBODY	ELEMENT	SYMBOL	MASS
CD73	Praseodymium	Pr	141
CD61	Neodymium	Nd	142
CA125	Neodymium	Nd	143
CD90	Neodymium	Nd	144
CD151	Neodymium	Nd	145
CD49f	Europium	Eu	153
CD133	Gadolinium	Gd	155
CD10	Gadolinium	Gd	156
E-cadherin	Gadolinium	Gd	158
Endoglin	Dysprosium	Dy	163
CD24	Dysprosium	Dy	164
CD13	Erbium	Er	168
Mesothelin	Ytterbium	Yb	173

Table 20. Panel of intracellular antibodies, the symbols and the mass of the corresponding elements to which the antibodies are labelled with.

ANTIBODY	ELEMENT	SYMBOL	MASS
Vimentin	Indium	In	115
pATM	Neodymium	Nd	146
pH2AX	Samarium	Sm	147
CyclinB1	Neodymium	Nd	148
pNFkB	Samarium	Sm	149
pBcl2	Neodymium	Nd	150
pERK	Europium	Eu	151
Ki67	Samarium	Sm	152
pSTAT3	Samarium	Sm	154
SNAIL	Gadolinium	Gd	157
pAkt	Terbium	Tb	159
Sox2	Gadolinium	Gd	160
cMyc	Dysprosium	Dy	161
pSTAT5	Dysprosium	Dy	162
pRb	Holmium	Ho	165
PAX8	Erbium	Er	167
Non-p-β-catenin	Erbium	Er	170
cPARP	Ytterbium	Yb	171
pS6	Ytterbium	Yb	172
Total p53	Lutetium	Lu	175
pHH3	Ytterbium	Yb	176

To afford multiparametric barcoding of ovarian cancer cells and CyTOF Ab staining, four 6-well plates were used, using 8 wells for TYK-nu and 16 wells for OVCAR-4, seeding 1.5 x 10^6 cells/well. The cells were stabilised for 18 h and then the NPs **^{106}Pd-Cy5-NPs** were added to TYK-nu, and **^{110}Pd-Cy5-NPs** and **$^{106\text{-}110}$Pd-Cy5-NPs** were added to the two sets of OVCAR-4, at a ratio of 1,500 NPs/cell, incubating them for 6 h to achieve duplicates of **BC-1 TYK-nu**, **BC-2 OVCAR-4**, and **BC-3 OVCAR-4** cells. Barcoded cells viability was measured using trypan blue a TC10™ Automated Cell Counter (Bio-Rad). Cell viability analyses showed that 93% of BC-1 TYK-nu, 88% of BC-2 OVCAR-4, and 90% of BC-3 OVCAR-4 were viable cells. Subsequently, barcoded cells were fixed, transferred to 1.2 mL cluster tubes and kept at 4 ºC in the fridge upon continuing. Then, the pools of barcoded cells were generated by mixing one tube of **BC-1 TYK-nu**, with one tube of **BC-2 OVCAR-4**, and with one tube of **BC-3 OVCAR-4**. In total, 4 tubes containing a pool of barcoded cells (two samples and their duplicates) were generated. Subsequently, the samples were divided in two groups, one group to be stained with surface Ab and the other group to be stained with both surface and intracellular markers (Figure 69). Therefore, all the samples were stained at the same time with surface Ab. After that, on the one hand, the samples that were meant to be stained only with surface Ab were washed and kept at 4 ºC in the fridge. On the other hand, the rest of the samples were applied a permeabilisation step with MeOH for 10 min in ice, prior to be stained with intracellular Ab, affording surface and intracellular Ab staining.. At last all the barcoded and CyTOF Ab samples were incubated with DNA intercalator (Ir), PBS and PFA for 14 h at 4 ºC, washing them thoroughly before loading them in CyTOF.

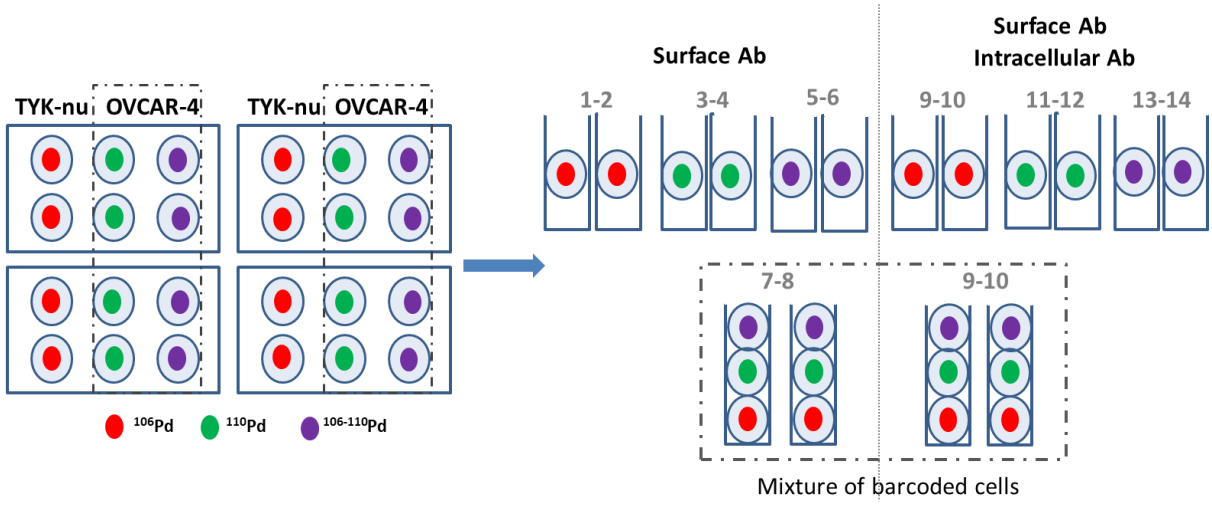

Figure 69. Depiction of how cells are barcoded and tubes are mixed in live cell barcoding prior to specific Ab staining. Cells are specifically barcoded (in duplicate) with NPs, then, each well containing barcoded cells is transferred to individual tubes (upper row) or mixed with two more wells containing the other two barcoded cells (lower row), to afford a pool of barcoded cells. Afterwards, cells are

stained with surface Ab or a mixture of surface and intracellular Ab. In grey, number of the samples included in Table 21.

Table 21 shows a summary of barcoded samples, including the metallofluorescent NP barcode and the CyTOF ovarian Ab panel staining.

Table 21. There were in total 16 samples but only 8 different types (n=2). Barcoded cells column shows the cells included in the samples. It is to be remarked that samples 7-8 and 15-16 contained a mixture of all barcoded cells: **BC-1 TYK-nu**, **BC-2 OVCAR-4**, and **BC-3 OVCAR-4**. Pd isotopes column shows the expected palladium isotope signal in CyTOF according to the NPs used to barcode the cells. Ab (S/Ic) column shows whether the Ab employed were surface Ab (S) or intracellular Ab (Ic).

SAMPLES	BARCODED CELLS	Pd ISOTOPES	Ab (S/Ic)
1 – 2	BC-1 TYK-nu	^{106}Pd	S
3 – 4	BC-2 OVCAR-4	^{110}Pd	S
5 – 6	BC-3 OVCAR-4	$^{106\text{-}110}$Pd	S
7 – 8	ALL OF THEM	^{106}Pd, ^{110}Pd, $^{106\text{-}110}$Pd	S
9 – 10	BC-1 TYK-nu	^{106}Pd	S + Ic
11 – 12	BC-2 OVCAR-4	^{110}Pd	S + Ic
13 – 14	BC-3 OVCAR-4	$^{106\text{-}110}$Pd	S + Ic
15 – 16	ALL OF THEM	^{106}Pd, ^{110}Pd, $^{106\text{-}110}$Pd	S + Ic

Sample data obtained by CyTOF was analysed with Community Cytobank® software (www.cytobank.org). Barcoded cells were hierarchically gated to obtain 2D plots: **^{191}Ir(+)/^{193}Ir(+)** to select cells; **^{191}Ir(+)/Event length** to select single cells and avoid doublets, which are two or more cells observed as a single cell [232]; **^{191}Ir(+)/^{195}Pt(-)** to select viable cells and **^{191}Ir(+)/^{171}Yb(-)** since cPARP enable the identification of "walking dead cells"; thereby selecting double negative Pt/cPARP cells for barcoding analysis (Figure 70). Barcoding analysis was completed with **^{106}Pd/^{110}Pd** 2D plots to identify specific metallofluorescent NPs.

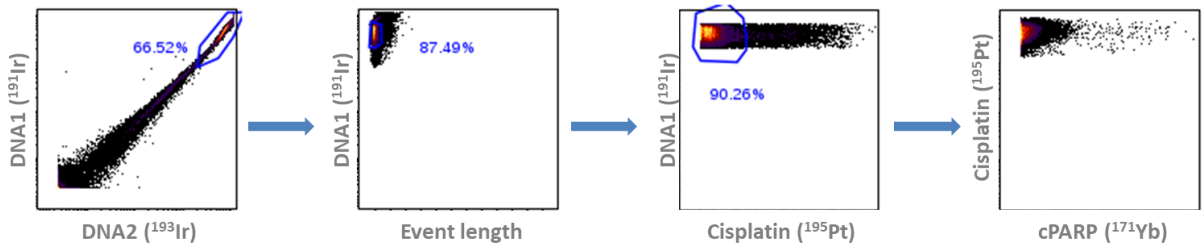

Figure 70. 2D plots of the hierarchical gating strategy employed to select viable single-cells [Pt(-)/cPARP(-)] for Pd barcoding analysis.

In order to determine whether cells could be correctly identified by the metallofluorescent NPs barcoding with our analysis, histograms of ^{106}Pd and ^{110}Pd channels across ^{191}Ir and ^{193}Ir channels were generated. It could be clearly observed that the NPs (Pd channels) were indeed inside the cells (Ir channel as DNA intercalator). Whereas samples 1, 2, 9, and 10 (BC-1 TYK-nu – **^{106}Pd-Cy5-NPs**) exhibited ^{106}Pd signal and negligible ^{110}Pd signal, samples 3, 4, 11, and 12, (BC-2 OVCAR-4 – **^{110}Pd-Cy5-NPs**) exhibited ^{110}Pd signals and negligible ^{106}Pd signal, and samples 5, 6, 13, and 14 (BC-3 OVCAR-4 – **$^{106\text{-}110}$Pd-Cy5-NPs**) and samples 7, 8, 15, and 16 (mixture of barcoded cells) exhibited signals for both ^{106}Pd and ^{110}Pd channels (Figure 71).

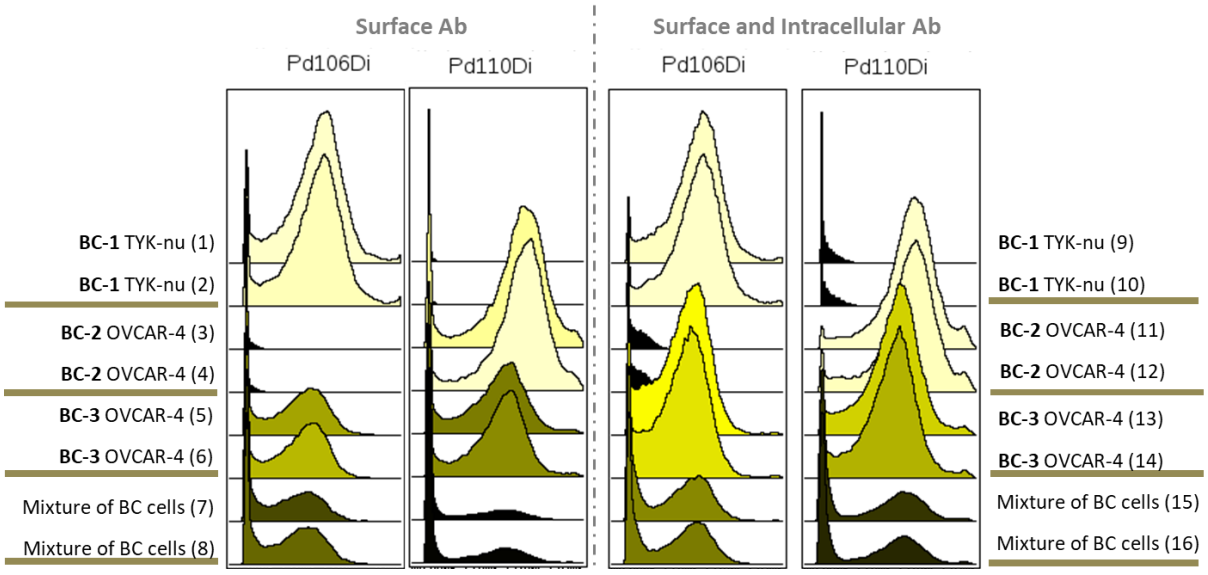

Figure 71. Overlay histograms of ^{106}Pd and ^{110}Pd channels over the samples.

The next variable to investigate was whether the intracellular metallofluorescent NPs barcode could induce some kind of interference across all Pd channels, since a more complex metallofluorescent NPs barcoding is under investigation. New metallofluorescent NPs carrying a combination of palladium isotopes covering all the Pd channels (102, 104, 105, 106, 108, and 110) are being developed to enhance the utility of the NPs barcoding.

Thus, understanding the possible spill over between the Pd channels in CyTOF is of great importance to develop a more complete barcoding tool. Histograms of all Pd channels across the barcoded cells were generated as a result (Figure 72). Those samples stained only with surface Ab (1-8) were clean and did not exhibited signals in other Pd channels. On the hand, those samples stained with both surface and intracellular Ab (9-14), except for the mixture of barcoded cells, exhibited a tiny spill over Pd channels. These signals were barely important and did not comprise the barcoding analysis. Nevertheless, we are confident that we can further eliminate these signals.

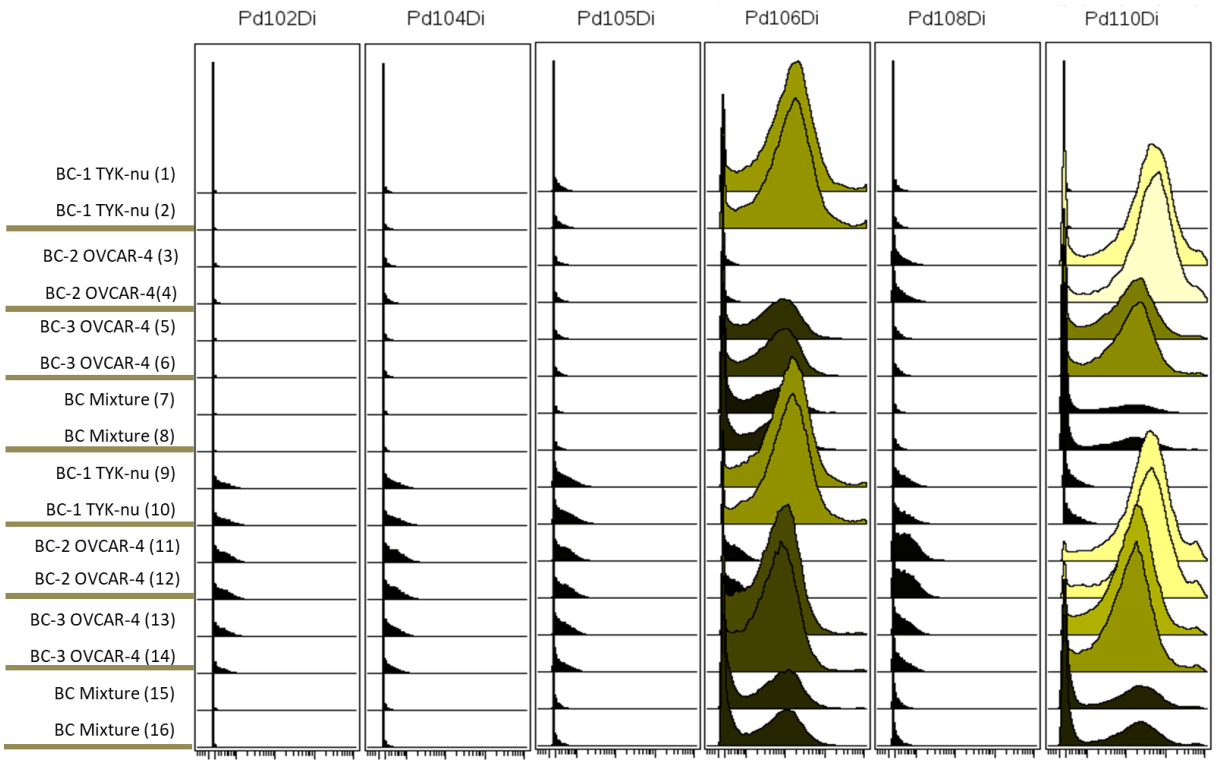

Figure 72. Overlay histograms of ^{102}Pd, ^{104}Pd, ^{105}Pd, ^{106}Pd, ^{108}Pd and ^{110}Pd channels over the samples.

To determine the barcoding profile of each sample, the plots obtained for ^{106}Pd/^{110}Pd channels were assessed. In this context, barcoded cells with the same code but differing in the kind of the markers were compared. Firstly, samples 1-2, which are **BC-1** TYK-nu cells (**^{106}Pd-Cy5-NP**) and stained with surface Ab (Figure 73-A) were compared with samples 9-10, which are **BC-1** TYK-nu cells (**^{106}Pd-Cy5-NP**) and stained with both surface and intracellular Ab (Figure 72-B). In both cases the main population was located in the ^{106}Pd(+)/^{110}Pd(-) quadrant, presenting similar average frequency values: 86.1% and 83.6%, respectively.

Secondly, in both **BC-2** OVCAR-4 (**^{110}Pd-Cy5-NP**) cells stained with surface Ab, samples 3-4 (Figure 73-C), and stained with both surface and intracellular Ab, samples 11-12 (Figure 73-D), the cell population was located in the ^{106}Pd(-)/^{110}Pd(+) quadrant, as expected. Likewise, the average frequency values of the events presented in the quadrant, and corresponding to the ^{110}Pd channel, were very alike, 86.9% in samples 3-4 and 86.5% in samples 11-12. Both samples presented negligible signal in the ^{106}Pd channel. These results, as previously mentioned, confirmed the suitable use of **^{110}Pd-Cy5-NP** as barcodes

Thirdly, both samples 5-6 (Figure 73-D) and 13-14 (Figure 73-F), **BC-3** OVCAR-4 (**$^{106-110}$Pd-Cy5-NP**) stained with surface Ab (5-6) or with both surface and intracellular Ab (13-14), showed a main population located in the ^{106}Pd(+)/^{110}Pd(+) quadrant, since these NPs contain both palladium isotopes. Nevertheless, the percentage of nanofected cells is relatively smaller compared with the previous barcodes. On top of that, events showing only ^{110}Pd signal are above 10%, suggesting a slightly higher amount of NPs containing ^{110}Pd than NPs containing ^{106}Pd in the mixture **$^{106-110}$Pd-Cy5-NP**. Nevertheless, the amount of cells showing positive signal for both Pd isotopes are enough higher than the rest, allowing to considering the **$^{106-110}$Pd-Cy5-NP** valid for barcoding cells.

Lastly, the mixtures of cells containing the aforementioned three barcodes were studied. Whereas samples 7-8 were stained only with surface Ab (Figure 73-G), samples 15-16, were stained with both surface and intracellular Ab (Figure 73-H). As expected, three different populations were observed in the plots, one in the ^{106}Pd(+)/^{110}Pd(-) quadrant and associated to **BC-1** TYK-nu cells (**^{106}Pd-Cy5-NP**), another in the ^{106}Pd(-)/^{110}Pd(+) quadrant and corresponding to **BC-2** OVCAR-4 cells (**^{110}Pd-Cy5-NP**), and the third located in the ^{106}Pd(+)/^{110}Pd(+) quadrant and corresponding to **BC-3** OVCAR-4 cells (**$^{106-110}$Pd-Cy5-NP**). Furthermore, the three barcoded cells were presented with a similar frequency within mixture of barcoded cell. Thus, the three different barcodes were successfully identified within the barcoded cells mixtures.

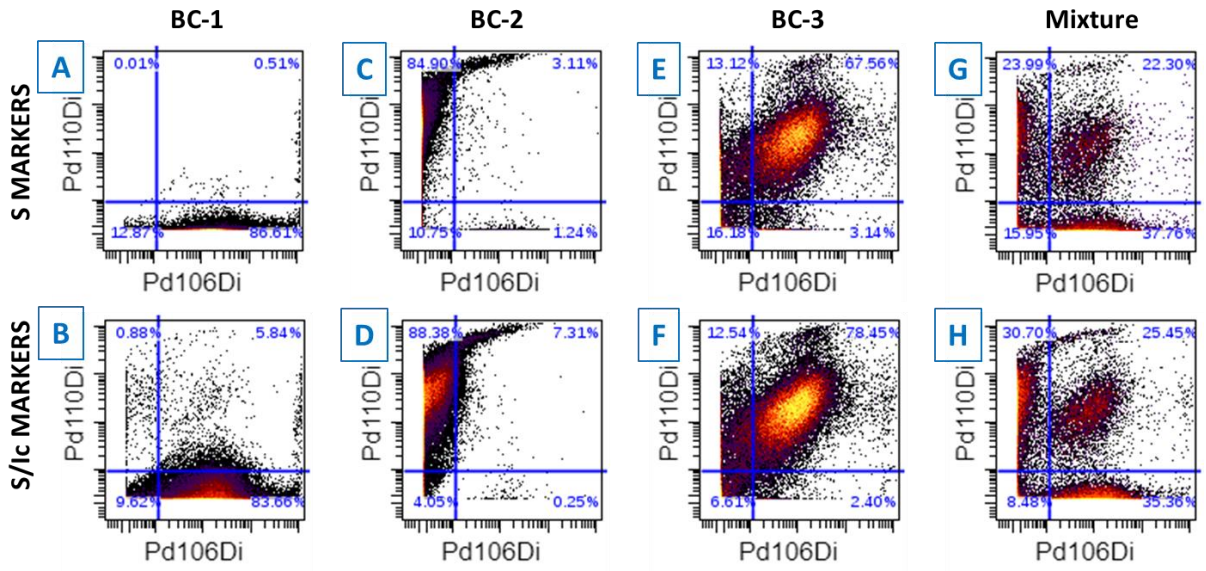

Figure 73. Representative 2D plots for ^{106}Pd and ^{110}Pd channels in samples stained with surface Ab (top row) and stained with surface and intracellular Ab (bottom row). **A-B** are representative 2D plots for BC-1 TYK-nu cells, **C-D** are representative 2D plots for BC-2 OVCAR-4 cells, **E-F** are representative 2D plots for BC-3 OVCAR-4 cells, and **G-H** are representative 2D plots for the mixture of barcoded cells including BC-1, BC-2, and BC-3 cells.

Albeit barcoded cells stained with intracellular Ab showed brighter intensity Pd signals, the frequency of barcoded cells was not affected by the NPs barcoding. These data demonstrated the successful metallofluorescent NPs utility for barcoding ovarian cancer cells. Thus, this NPs based barcoding is going to have extensive applications for barcoding many types of cells.

After proving that the identification of the different codes (NPs), employed for barcoding the cells, amongst cell mixtures of barcoded cells had been successfully achieved, the antigens expression profile of the cell populations was studied. For that, heatmap plots of the viable cells populations for ^{106}Pd(+)/^{110}Pd(-),^{106}Pd(-)/^{110}Pd(+), and ^{106}Pd(+)/^{110}Pd(+) quadrants were created. As it is shown in Figure 74 each barcoded cell line possessed a specific and unique profile of antigens expression that enabled their identification.

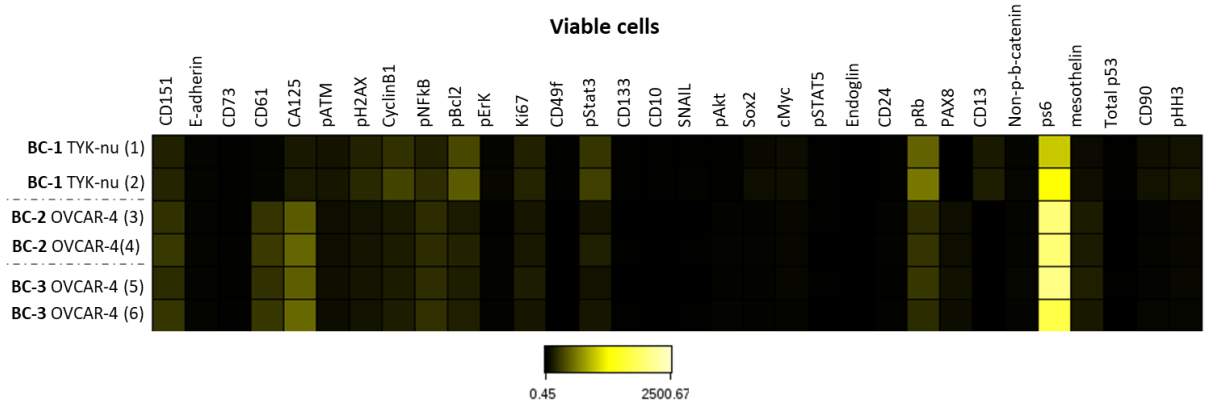

Figure 74. Heatmap of the proteins expression in barcoded cells (duplicates 1-2, 3-4, 5-6). Proteins expression is calculated as raw mean counts.

Subsequently, the heatmap plot profile obtained for the viable cells population in the samples was compared to the heatmap plot profile obtained for the aforementioned quadrants in the mixture of barcoded cells. In the case of BC-1 TYK-nu samples, the antigens profile expression showed in Figure 74 was compared with the antigen profile expression obtained for the cell population located in the ^{106}Pd(+)/^{110}Pd(-) quadrant amongst the mixture of barcoded cells. As it is seen, the patterns are similar (Figure 75).

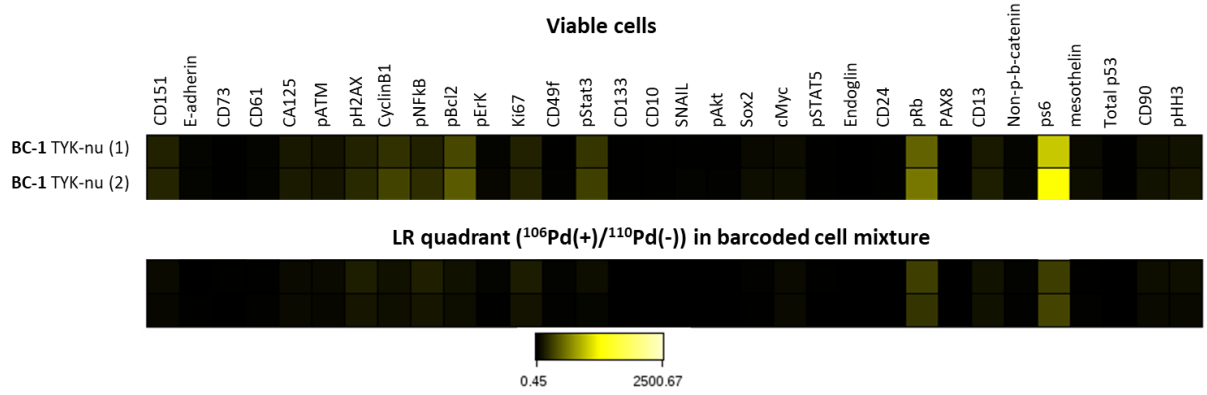

Figure 75. Comparison of the profile of proteins expression between BC-1 TYK-nu cells (upper heatmap) and the BC-1 cells located in the lower-right (LR) quadrant in the mixture of cells (lower heatmap). Proteins expression is calculated as raw mean counts.

Likewise, the specific antigen profile expression of BC-2 OVCAR-4 samples, shown in Figure 7, was compared to the antigens profile expression of the cell population located in the ^{106}Pd(-)/^{110}Pd(+) quadrant amongst the mixture of cells. Both patterns are also very alike (Figure 76).

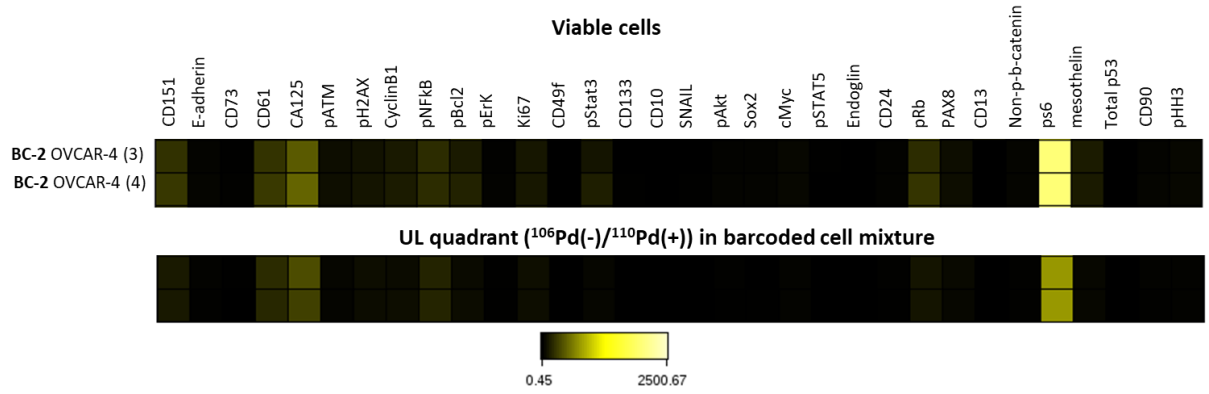

Figure 76. Comparison of the profile of proteins expression between BC-2 OVCAR-4 cells (upper heatmap) and the BC-2 cells located in the upper-left (UL) quadrant in the mixture of cells (lower heatmap). Proteins expression is calculated as raw mean counts.

Similarly, the specific antigens profile expression of BC-3 OVCAR-4 samples, shown in Figure 74 was compared with the antigens expression profile of the cell population located in the $^{106}Pd(+)/^{110}Pd(+)$ quadrant amongst the mixture of cells. Like in the previous cases, both patterns are similar (Figure 77).

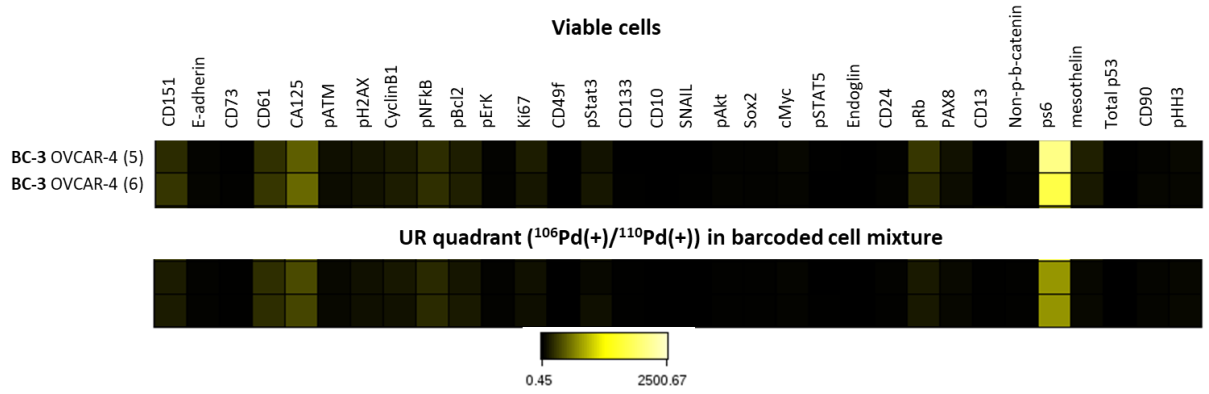

Figure 77. Comparison of the profile of proteins expression between BC-3 OVCAR-4 cells (upper heatmap) and the BC-3 cells located in the upper-right (UR) quadrant in the mixture of cells (lower heatmap). Proteins expression is calculated as raw mean counts.

In addition, to determine whether the NPs would be inducing aberrant proteins expression, the antigens expression profiles of BC-2 OVCAR-4 and BC-3 OVCAR-4 were compared (Figure 78). It is clearly seen that both patterns are the same, hence, the metallofluorescent NPs were not affecting the cells in terms of proteins expression.

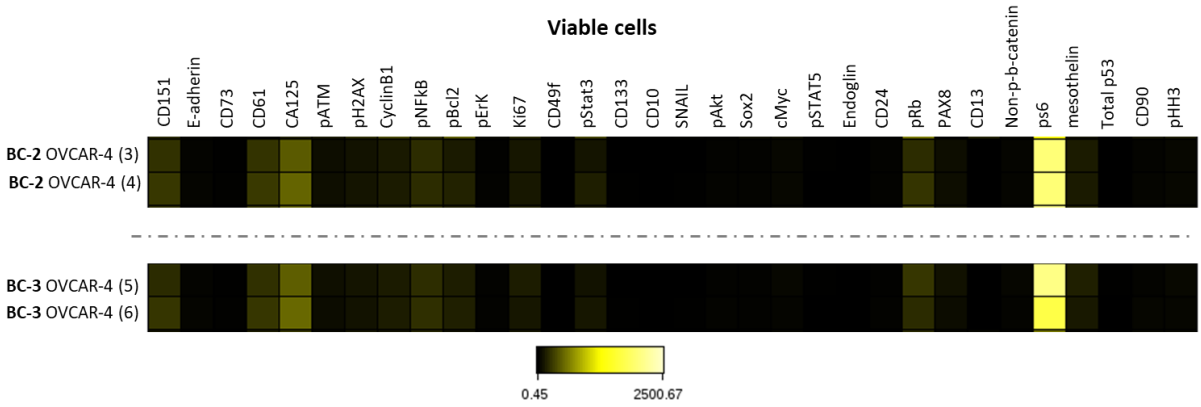

Figure 78. Comparison of the proteins expression between BC-2 OVCAR-4 and BC-3 OVCAR-4. Proteins expression is calculated as raw mean counts.

3.3.3. Discussion

In the first part of chapter 2 it has been described the synthesis, characterisation, and multimodal applications of metallofluorescent NPs, while that in the second part of the chapter 2 it has been presented the development of two isotopically pure palladium-conjugated metallofluorescent NPs and their promising applications as dual fluorescence and mass-tag reagents for live cell barcoding in fluorescence and mass cytometry.

Metallofluorescent NPs have been shown to be non-toxic for the cells and to exhibit a dual fluorescence/mass behaviour [280]. This dual behaviour could enable the specific and unique combination of Cy5 and isotopically pure palladium in metallofluorescent NPs, which exhibit fluorescence and mass signals, acting as fingerprints. This could enable their use as specific barcoding reagents. Thus, seeking to provide insights of the real understanding of metallofluorescent NPs as live cell barcoding reagents, palladium-isotope conjugated metallofluorescent NPs carrying the palladium isotopes ^{106}Pd and ^{110}Pd were synthesised.

The conjugation of the pure isotopes to the NPs did not affect the purity or stability of the isotopes. The change of $Pd(OAc)_2$ compound employed in the general metallofluorescent NPs synthesis for the nitrate salt, $Pd(NO_3)_2$, used for the palladium-isotope-conjugated metallofluorescent NPs synthesis, did not produced toxicity either. Furthermore, these palladium-isotope-conjugated metallofluorescent NPs can also be considered non-toxic for cells. These features mean three things: (i) the metallofluorescent NPs and their components are stable to degradation by enzymes or vesicles [206], (ii) the metallofluorescent NPs are suitable for long term flow and mass cytometry experiments, and (iii) the metallofluorescent NPs are suitable for live cell experiments.

In this sense, the PoC was successfully achieved since a mixture of two differently barcoded cells in several proportions was afforded. Therefore, moving to a complex live cell barcoding was inevitable. The live cell barcoding experiment has shown that, on the one hand, metallofluorescent nanoparticle-barcodes are a robust barcoding platform as cell leakage is not produced when permeabilisation step is performed. On the other hand, individually barcoded cells with specific metallofluorescent nanoparticle-barcodes can be easily identified by mass cytometry. Besides, metallofluorescent NPs barcoding neither induces cell death or apoptosis nor affects frequency of cells. These facts suggest that metallofluorescent nanoparticle-barcodes are suitable reagents for mass barcoding since they are non-toxic, specific, unique, and sensitive.

Although several barcoding reagents have been reported [232],[235],[238], as far as it is concerned, the metallofluorescent nanoparticle-barcoding is the only based on polystyrene NPs and with dual fluorescent and mass cytometry applications. The palladium-based cell barcoding [232] has its limitations in that cells have to be fixed to perform the barcoding whilst the metallofluorescent nanoparticle-based barcoding is entirely biocompatible. To circumvent this limitation, an antibody-conjugated platinum-based reagent for live cell barcoding [235] which seems to be interesting due to the targets are ubiquitously expressed cell markers, was reported. Nonetheless, this reagent might be sensitive to cell mutations, cell signals or stimuli which would inhibit the reagent targets expression. A tellurium-based reagent [238] shows to be very promising, affording potentially 35 barcodes; however, this reagent presents some leaching that could lead to some toxicity, apart from the impurities of the tellurium isotopes that could hinder the barcoding analysis.

Despite only two palladium isotopes have been employed, the metallofluorescent NPs can include not only all palladium isotopes but also other elements, as long as they are able to be coordinated within the π electron-rich network, to afford a wide variety of metallofluorescent NPs for barcoding. In fact this has been previously reported [281], however it has only been done for a combination of 6 isotopes. On the contrary, the development of metallofluorescent NPs containing palladium isotopes of different intensities to afford a ratiometric barcoding seems to be far since metallofluorescent NPs do not show homogeneity in the palladium amount.

The main advantage of the metallofluorescent nanoparticle-based barcoding is their dual fluorescence/mass behaviour, allowing them to act as transition reagents between both cytometries. Furthermore, they also allow co-culturing barcoded cells and keep working with them regarding their permanency within cells. Besides, the metallofluorescent nanoparticle-barcoded can be applied as fluorescent [205] and/or mass cell tracers.

In summary, the non-toxic effect and the dual behaviour of the metallofluorescent NPs make them suitable, interesting and promising reagents for live cell barcoding. In fact, the metallofluorescent nanoparticle-barcodes could be used alone or in combination with other mass-tag reagents for cell barcoding. Nevertheless, more experiments should be performed to enhance and optimise the metallofluorescent nanoparticle-based live cell barcoding.

CHAPTER IV

Chapter 4. Conclusions/Conclusiones

4.1. Conclusions chapter 1

1. The development of a direct, rapid, easy, cost-effective, robust, versatile and fluorescent DGL probe bead-based platform for the detection and quantification of nucleic acids, especially miR-21, using dynamic chemistry, without the need of amplification, has been successfully accomplished.

2. The DGL probe bead-based platform allows single miRNA direct detection and quantification, and SNPs detection for mutation testing, through dynamic chemistry labelling since the base-filling reaction using Smart-NB has proved to be effective.

3. The DGL probe bead-based platform is a multiplexing platform allowing the specific and unique profiling of several nucleic acids within the same sample. In fact, on one hand, miR-21 and miR-122, and on the other hand, WT KRAS and G13C-KRAS, have been specifically profiled.

4. The DGL probe bead-based platform has shown to be universal as it can be applied for testing both miRNA and DNA utilising common and user-friendly reagents with the daily basic laboratory instruments.

5. The DGL probe bead-based platform is a robust analytical platform as it can detect and quantify miRNA, and detect DNA mutations from several sources such as cells and plasma, utilising several fluorescence-based detection platforms such as flow cytometry and microplate reader. Hence, it can be integrated to other more sensitive detection platforms.

6. Chem-NAT reagents, DGL probes and Smart-NB, have been successfully translated to beads, to flow cytometry, to microplate reader, to cells and to plasma, thereby, demonstrating the robustness and high translatability of these reagents.

7. Flow cytometry has shown to be a preliminary detection platform for direct detection of miRNA from cells when using the bead-based platform, whilst microplate reader FLUOStar Omega has shown to be a more sensitive detection platform that enable quantification through an easy end-point kinetic assay.

8. KRAS mutation testing has been successfully achieved using only a DGL probe in less than one hour and half, using cost-effective reagents and a basic fluorescent detection platform, suggesting being a good method for quick testing of the most frequent KRAS mutations.

4.2. Conclusiones capítulo 1

1. Se ha llevado a cabo el desarrollo de una plataforma directa, rápida, sencilla, barata, robusta y versátil, basada en partículas y sondas DGL fluorescentes, para la detección y cuantificación de ácidos nucleicos, especialmente miR-21, mediante química y sin necesidad de amplificación.

2. La plataforma basada en partículas y sondas DGL permite la detección directa y la cuantificación de miRNAs, así como la detección de SNPs para mutaciones, a través del marcaje con química dinámica, ya que la reacción de incorporación dinámica de Smart-NB es efectiva.

3. La plataforma basada en partículas y sondas DGL es una plataforma multipléxica que permite identificar específicamente varios ácidos nucleicos en una misma muestra. De hecho, miR-21, miR122, KRAS Silvestre y la mutación G13C han sido identificadas.

4. La plataforma basada en partículas y sondas DGL ha probado ser universal ya que puede ser aplicada para detectar tanto miRNA como DNA utilizando instrumentos y reactivos de laboratorio cotidianos.

5. La plataforma basada en partículas y sondas DGL es una plataforma analítica robusta que permite detectar y cuantificar miRNA y DNA a partir de varios tipos de muestras como células o plasma utilizando plataformas fluorescentes como la citometría de flujo o lectores de placa. Así pues, la plataforma analítica puede ser integrada en otras plataformas de detección más sensibles

6. Los reactivos Chem-NAT, las sondas DGL y las Smart-NB han sido trasladadas satisfactoriamente a partículas, a citometría de flujo, a lectores de placa, a células y a plasma, demostrando la robustez de estos reactivos.

7. La citometría de flujo se ha demostrado como una plataforma de detección preliminar para la detección directa de miRNA, a partir de células, mediante el uso de la plataforma basada en partículas. Por otra parte, el lector de placas FLUOstar Omega ha demostrado ser una plataforma de detección más sensible que permite la cuantificación a través de un sencillo ensayo cinético a tiempo final.

8. Se ha conseguido identificar satisfactoriamente una mutación de KRAS, utilizando una única sonda DGL, en menos de una hora y media, mediante el uso de reactivos baratos y una plataforma de detección básica, lo que sugiere que se trata de un buen método para la detección de mutaciones frecuentes de KRAS.

4.3. Conclusions chapter 2

1. The successful synthesis and characterisation of metallofluorescent polystyrene nanoparticles carrying simultaneously a fluorophore and a metal, with multimodal applications: fluorescence microscopy, flow cytometry, fluorescence life-time imaging microscopy, catalysis, and mass cytometry, has been demonstrated.

2. Metal and fluorophore conjugation to the polystyrene nanoparticles have been performed in an easier and quicker methodology compared to previous reported methods.

3. The metallofluorescent nanoparticles have proved to be non-toxic for any of the cells in which they have been used. In addition, they neither induce apoptosis to cells nor aberrant protein expression, and they did not affect the frequency of cells.

4. The metallofluorescent nanoparticles could be used as cytosolic catalysts since they are easily internalised by cells, enabling to perform multiple metal catalysed chemical reactions for *in situ* drug synthesis.

5. The metallofluorescent nanoparticles behave as dual fluorescence and mass probes since they can be detected by both flow and mass cytometry. In fact, palladium-isotope-conjugated nanoparticles have been able to successfully barcode different type of cells.

6. Palladium-isotope-conjugated nanoparticles are easily internalised by cell and maintain their specific and unique palladium isotope signal across the time. Thus, they have showed their utility as mass-tag reagents for live cell barcoding by mass cytometry.

7. Palladium-isotope-conjugated nanoparticles do not react with cell proteins or any cell component, what enables not only their use as mass-tag reagents for live cell barcoding, but also as cell tracers in combination with other mass-tag reagents, to study live cells functional mechanisms.

8. Palladium-isotope-conjugated nanoparticles could be also functionalised with specific antibodies to afford triple functionalised probes for proteomic studies.

4.4. Conclusiones capítulo 2

1. Se ha demostrado la síntesis y caracterización de nanopartículas de poliestireno metalofluorescentes que contienen simultáneamente un fluoróforo y un metal, con aplicaciones multimodales como microscopía de fluorescencia, microscopía de imagen de tiempo de vida media de fluorescencia, catálisis y citometría de masas.

2. La conjugación del fluoróforo y el metal a las nanopartículas de poliestireno se ha llevado a cabo de una manera sencilla y rápida, en comparación con métodos previamente descritos.

3. Las nanopartículas metalofluorescentes han demostrado no ser tóxicas para las células. Además, no inducen apoptosis ni expresión aberrante de proteínas, ni afectan a la frecuencia de las células.

4. Las nanopartículas metalofluorescentes podrían ser utilizadas como catalizadores citosólicos ya que son fácilmente internalizadas por células, permitiendo llevar a cabo múltiples reacciones químicas para la síntesis *in situ* de fármacos.

5. Las nanopartículas metalofluorescentes se comportan como sondas duales para fluorescencia y masas, pudiendo ser detectadas por citometría de flujo y de masas. De hecho, las nanopartículas conjugadas con isótopos puros de paladio han permitido codificar diferentes tipos de células.

6. Las nanopartículas conjugadas con isótopos puros de paladio son fácilmente internalizadas por las células y mantienen una señal específica con el tiempo. Así pues, pueden ser útiles reactivos basados en masas para la codificación de células vivas mediante citometría de masas.

7. Las nanopartículas conjugadas con isótopos puros de paladio no reaccionan con proteínas ni con componentes celulares, lo que permite que sean utilizadas como reactivos basados en masas para la codificación de células vivas, así como para estudiar los mecanismos funcionales de células vivas.

8. Las nanopartículas conjugadas con isótopos puros de paladio podrían ser funcionalizadas con anticuerpos específicos para conseguir sondas triplemente funcionalizadas para estudios de proteómica.

CHAPTER V

Chapter 5. Experimental

5.1. General

All mimic RNA sequences were purchased from Integrated DNA Technologies (IDT) as ssDNA.

Abasic PNA probes (DGL probes) and SMART-Nucleobases were synthesised at DestiNA Genomica S.L. (Granada, Spain) following standard SPPS protocols.

All chemicals were purchased from Sigma Aldrich and used as received or stored as indicated. Streptavidin-R-phycoerithrin conjugate (SAPE 1 mg/mL) and microspheres Dynabeads® M-270 Carboxylic Acid were purchased from Thermo Fisher Scientific. Buffers PBS-Tween® 0.1%, lysis buffer (property of DestiNA Genomica S.L.) and Buffer A (2X SSC and 0.1% SDS buffer (pH 6)) are homemade.

miRNeasy Mini Kit was purchased from Qiagen (Cat No.: 217004); TaqMan™ Advanced miRNA cDNA Synthesis Kit (Cat. Nº: A28007) and TaqMan™ Universal PCR Master Mix (Cat. No.: 4304437) were both purchased from Thermofisher Scientific.

Dulbecco's modified Eagle's medium (DMEM), Gibco™ Medium M199, RPMI 1640 medium, L-Glutamine 200 mM (100X), Penicilin/Streptomycin solution (P/S), Tryple and Trypsin-EDTA 0.05% were purchased from Gibco (Thermo Fisher Scientific). Sodium Pyruvate was purchased from Sigma Aldrich. Eagle Minimum Essential Medium (EMEM) was purchased from Sigma Aldrich and American Type Culture Collection (ATCC). Fetal Bovine Serum (FBS) was purchased from Omega Scientific and Thermo Fisher Scientific.

5.1.1. Instrumentation

DGL probes were synthesised on an Automated Peptide Synthesiser (Intavis Bioanalytical Instruments MultiPrep CF Synthesiser, property of DestiNA Genomica S.L.) and analysed by HPLC (Agilent 1260 infinity). DGL probes concentrations were determined using a Thermo Fisher NanoDrop 1000 spectrophotometer. For hybridisation and dynamic chemistry incorporation reactions, a thermoshaker (Biometra TS1 ThermoShaker), a magnet rack (MagnaRackTM) and a 96-black well plates (Nunc™ MicroWell™) were used. PCR analyses were performed on a 7900 Fast Real-Time PCR System (Applied Biosystems).

Fluorescent experiments were performed on a Flow Cytometer BD FACSCanto II ™ (BD Biosciences), on a FLUOstar Omega microplate reader (BMG Labtech), on a Zeiss LSM 710 confocal laser scanning microscope (Zeiss group) and on a GloMax®-Multi Detection System

(Promega). Fluorescent experimental data were analysed using FlowJo V10 and Zeiss ZEN 2010 software. Fluorescence lifetime images were obtained using a MicroTime 200 microscope system (PicoQuant GmbH).

Polystyrene NPs were synthesised in a 90 mL glass reactor. The Zeta potential and DLS of the polystyrene NPs population were measured using a Zetasizer Nano ZS ZEN 3500. All the conjugations were performed on a themoshaker (Biometra TS1 ThermoShaker and Eppendorf Thermomixer®). The metallofluorescent NPs were characterised by a) Mass Cytometry, using a CyTOF®2 and a Helios updated to CyTOF®2 Mass Cytometer (DVS Sciences, Fluidigm); b) XPS, using a Kratos Axis Ultra-DLD X-ray photoelectron spectrometer; c) HRTEM and EDX using an ultra-high-resolution FEI Titan G2 microscope with an XFEG Field Emission Gun and a FEI microanalysis system for EDX; and d) Field Emission Scanning Electron Microscopy (FESEM), using a Zeiss SUPRA40VP with STEM and EDX.

^{1}H and ^{13}C NMR spectra were performed on a Varian Inova Unity 300 MHz, Varian Direct Drive 400 MHz and Varian Direct Drive 500 MHz at 298 K. Chemical shifts (δ) are calculated according to the corresponding deuterated solvents and are shown in ppm. The ^{1}H-NMR multiplicities are indicated as follows: s (singlet), d (doublet), t (triplet), q (quartet), dd (double doublet), m (multiplet), br (broad). The coupling constant (J) is indicated in Hz. The proton numbers for a resonance is indicated as nH, and it is based on spectral integration values.

The low resolution mass spectrometry (MS) analysis were done on an HPLC-MS Agilent Technologies 1200 (6110 Quadrupole LC / MS) with a mass detector LRMS ESI, while that the high resolution mass spectrometry (HRMS) analysis were performed on a HR Mass Spectrometer LCT-TOF Premier XE (Micromass Technology).

The cell lines have been grown in a CO_2 incubator with IR sensor NUAIRE NU-4750E US Autoflow and in a CO_2 incubator HERAcell 150i (Thermo Scientific), whilst the cell culture experiments have been conducted in a laminar flow hood, biosafety type 2A, TELSTAR Bio II A and in a laminar flow hood class II, biosafety type 2A, Baker SterilGARD®. Cell Viabilities were measured using a GloMax®-Multi Detection System (Promega) and a TC10™ Automated Cell Counter (Bio-Rad).

5.1.2. Synthesis of DGL probes by Solid-Phase Chemistry

DGL probes were synthesised on an Intavis Bioanalytical Instruments MultiPrep CF Synthesiser (at DestiNA Genomica S.L) following standard SPPS protocols by repeated rounds of coupling of activated amino-protected PNA monomers and deprotection of the terminal amino group. Scheme 14 depicts the steps involved in the DGL probes synthesis.

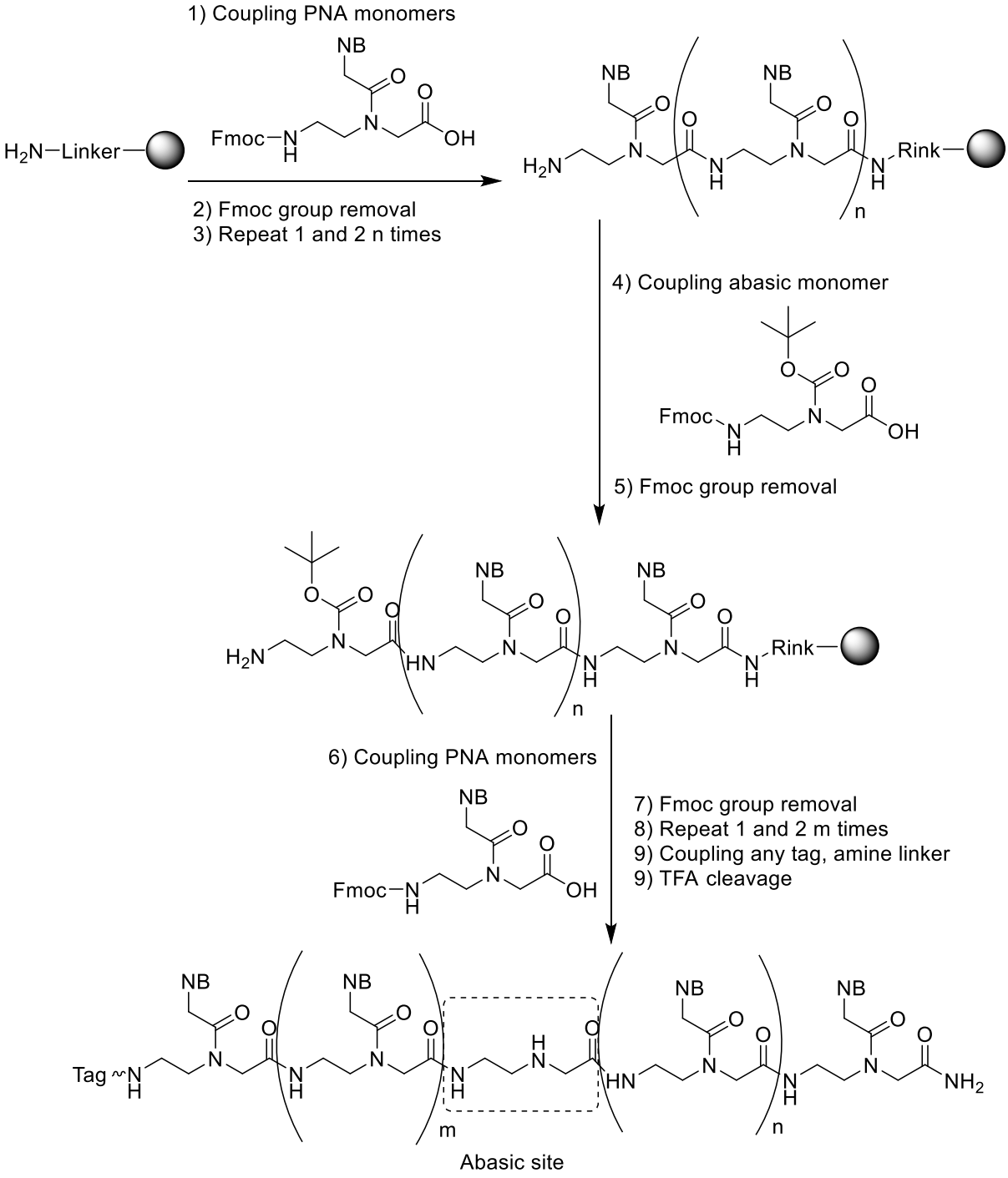

Scheme 14. General steps for DGL probes synthesis by solid-phase chemistry. DGL probes are synthesised from the C- to the N-terminal. Firstly, the first PNA monomer is coupled to the resin, then Fmoc group is removed and the following monomers, according to the DGL probe sequence, are coupled. The abasic PNA monomer is introduced across the synthesis. The last coupling step corresponds to the introduction of any tag to the DGL probe, such as a dye or an amino-mini-PEG-linker. Once the DGL probe is synthesised, an acidic mixture, mainly TFA, is added, which not only cleaves the probe from the resin but also removes the acid-labile protecting groups from the monomers, such as Boc, Bhoc and ^{t}Bu.

The chemical reactions were performed on Tentagel resin (loading 0.24 mmol/g) (Polymer Labs, UK) using Fmoc/Bhoc and Fmoc/Bhoc/^{t}Bu protected PNA monomers, along with both neutral and negatively charged abasic PNA monomers (Figures 78 and 79). All the monomers were synthesised and provided by DestiNA Genomica S.L.. The use of neutral and negatively charged abasic PNA monomers allowed to insert the neutral abasic position ("_") and the chiral and negatively charged abasic position (*GL*), respectively. In order to let the DGL probes to be used on solid surfaces, like magnetic beads, a mini-PEG linker ("x") and a nucleophilic group, such as amino (-NH_2) or thiol (-SH) were introduced at the end of them (Figures 80 and 81).

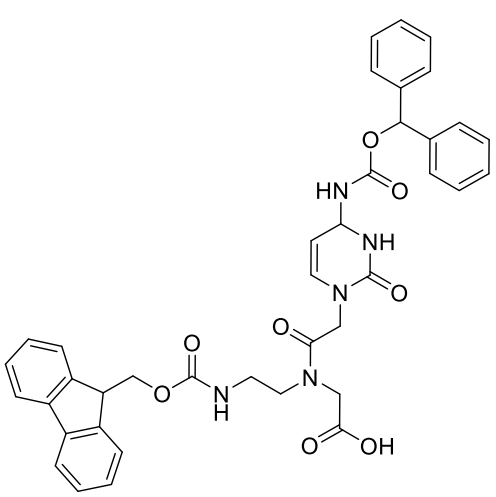

C= Cytosine PNA-COOH

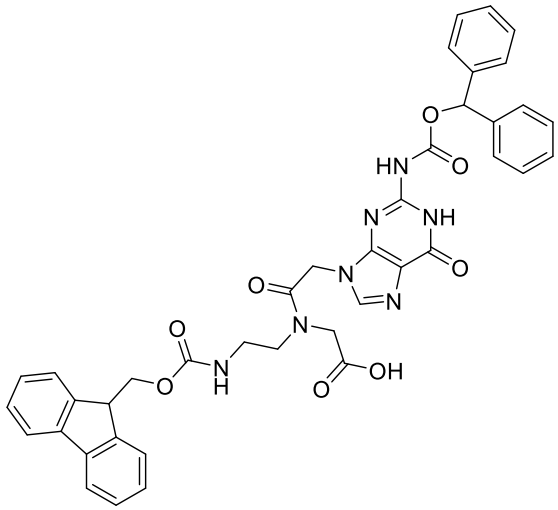

G= Guanine PNA-COOH

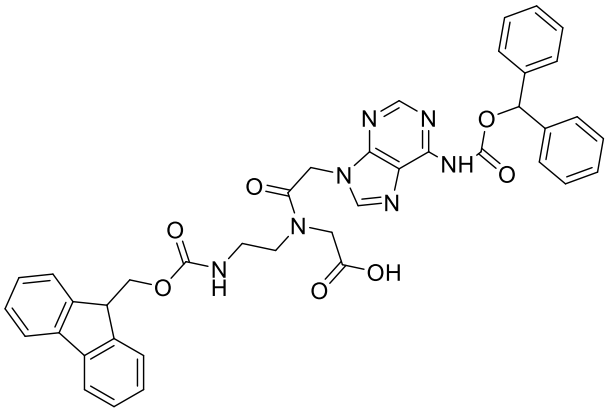

A=Adenine PNA-COOH

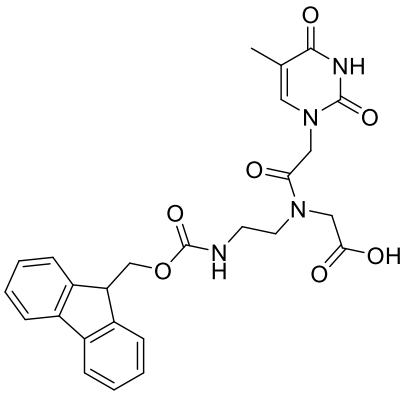

T=Thymine PNA-COOH

Figure 79. Neutral PNA monomers for DGL probes. All the monomers are N-Fmoc protected to allow the synthesis on solid phase. Additionally, to avoid secondary reactions, adenine-cytosine-guanine -NH_2 group can be protected with a second orthogonal protecting group, such as Bhoc, as shown in the figure.

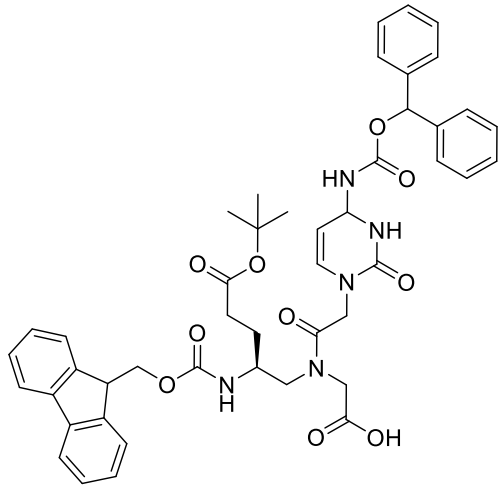

Cglu= Cytosine gamma-modified PNA-COOH

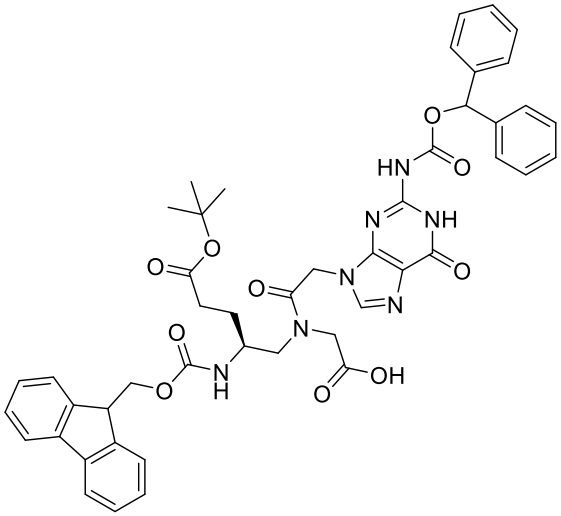

Gglu= Guanine gamma-modified PNA-COOH

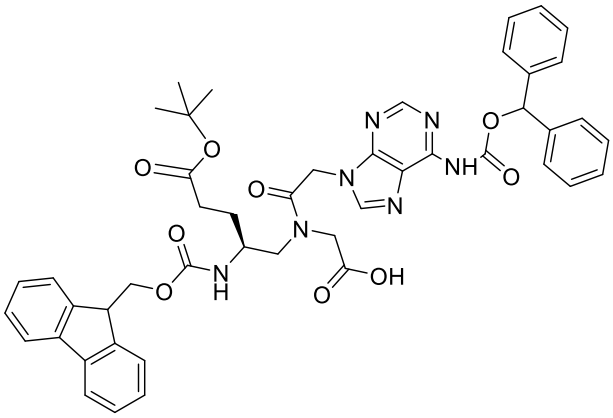

Aglu= Adenine gamma-modified PNA-COOH

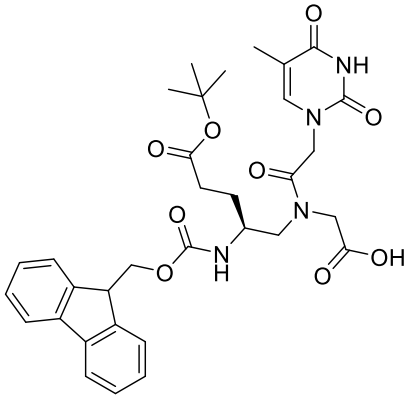

Tglu= Thymine gamma-modified PNA-COOH

Figure 80. Chiral and negatively charged PNA monomers for DGL probes. The monomers are N-Fmoc protected to allow the synthesis on solid phase. Moreover, to make the monomers chiral and negatively charged, a ^{t}Bu protected propionic acid group is introduced at γ-position. Additionally, to avoid secondary reactions, adenine-cytosine-guanine -NH_2 group can be protected with a second orthogonal protecting group, such as Bhoc, as shown in the figure.

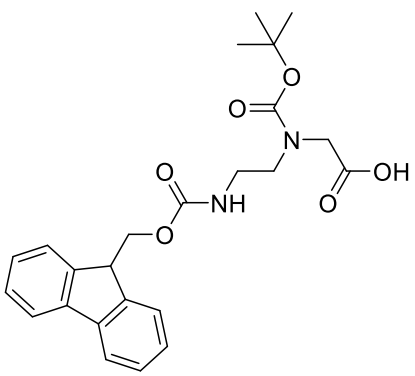

"_"= Neutral abasic PNA monomer

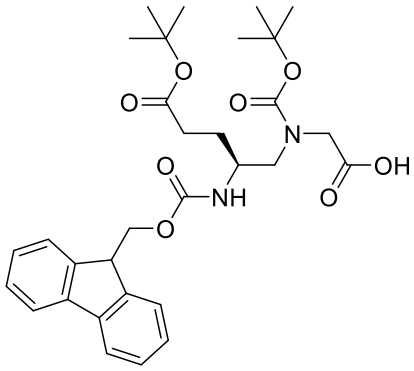

GL= Chiral and negatively charged abasic PNA monomer

Figure 81. Abasic PNA monomers to introduce the abasic position in the DGL probes. The amine groups are protected to control the synthesis: the N-terminal amine is Fmoc protected and the amine group of the glycine is Boc protected. The chiral and negatively charged monomer also carries a ^{t}Bu protected propionic acid at γ-position.

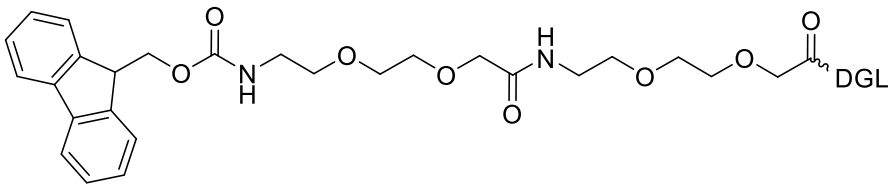

xx= amino-mini-PEG linker

Figure 82. Amino-mini-PEG linker. This spacer is generally coupled to all the DGL probes to provide the free amine N-terminal group that allows its immobilisation on any surface.

For the solid-phase couplings, 4 equivalents of protected PNA monomers, DIC and OxymaPure, previously solubilised in NMP, were used. The reagents were added to the resin and left at room temperature, for 20 min. Then, the resin was washed with DMF and fresh coupling reagents were added for another round of coupling. After the second coupling, a capping step, using a solution of 5% Luteidin and 5% of acetic anhydride in DMF, was performed. Subsequently, three washing steps of 5, 5 and 8 min, respectively, with a 20% solution of piperidine in DMF, were carried out to achieve Fmoc deprotection. Then, N-Fmoc protected PEG units (purchased from Sigma-Aldrich Inc.) were added to incorporate amino-mini-PEG linker to the DGL probes. Finally, cleavage of DGL probes, with concomitant Bhoc and Boc deprotection, were carried out using a mixture of TFA:TIS:H_2O (92.5:5:2.5 v/v) for 2 h. The resulting cleavage mixtures were precipitated by addition of cold Et_2O (-20 ºC). The precipitated DGL probes were collected by centrifugation and washed again with cold Et_2O for, afterwards, being solubilised in 1 mL of deionized H_2O. At last, the DGL probes crudes were analysed and purified by High Performance Liquid Chromatography (HPLC).

5.1.3. HPLC

All the reagents provided by DestiNA Genomica S.L. were analysed by HPLC, using an Agilent 1260 infinity coupled to a PL-ELS 1000 (Polymer Lab) equipped with UV detector at 220, 254, 260, 282 and 495 nm. Analytical HPLC analyses were performed with and Agilent Poroshell 120® EC-C18, 2.7 µm, 50 x 4.6 mm column. Detection was done by UV absorbance at 260 nm. As eluents, there were used: (A) H_2O + 0.1% TFA and (B) ACN + 0.1% TFA, at a flow rate of 1 mL/min and filtered prior to injection. The HPLC method used was: 5% to 25% B over 8 min, 25% to 95% B over 4 min and 95% B over 4 min.

Preparative HPLC runs were performed with an Agilent Eclipse XDB-C18, 5 µm, 250 x 9.4 mm column. HPLC grade eluents A and B were employed, at a flow rate of 2.5 mL/min and filtered prior to injection of a volume containing up to 10 mg of compound. The following method was applied: 5% to 17.5% B over 10 min, 17.5% to 20% B over 6 min, 20% to 95% over 4 min and 95% B over 4 min.

5.1.4. Cell Culture

Six types of cell lines have been used in this Doctoral Thesis: MDA-MB-231 (breast cancer cell line), MDA-MB-468 (breast cancer cell line), H1975 (lung cancer cell line), TYK-nu (ovarian cancer cell line), Kuramochi (ovarian cancer cell line) and OVCAR-4 (ovarian cancer cell line). The ovarian cancer cell lines (TYK-nu, Kuramochi and OVCAR-4) have been kindly provided by Garry Nolan's group at Stanford University (during my 3 months stay at the group).

All the cell lines have been grown in a CO_2 incubator with IR sensor NUAIRE NU-4750E US Autoflow. Moreover, TYK-nu, Kuramochi and OVCAR-4 have also been grown in a CO_2 incubator HERAcell 150i (Thermo Scientific) during the experiments conducted at Stanford University.

MDA-MB-231 and MDA-MB-468 cells were maintained in Dulbecco's Modified Eagle Medium (DMEM) supplemented with 10% FBS, 5% P/S, 5% L-Glutamine 100X, 5% sodium pyruvate and 5% HEPES homemade solution. H1975 cells were maintained in RPMI 1640 medium supplemented with 10% FBS, 5% P/S, 5% L-Glutamine 100X, 5% sodium pyruvate and 5% HEPES homemade solution. TYK-nu cells were maintained in EMEM supplemented with 10% FBS and 5% P/S. Kuramochi cells were maintained in RPMI 1640 medium supplemented with 10% FBS, 5% P/S and 5% L-Glutamine 100X. OVCAR-4 cells were maintained in M199 supplemented with 5% FBS and 5% P/S. All cell lines were grown to 75-80% confluence before subculturing them.

Besides, Peripheral Blood Mononuclear Cells (PBMCs) were obtained from 10 mL of venous blood samples that were collected from healthy volunteers in EDTA tubes (BD, Franklin Lakes, NJ, USA), isolating them by density gradient centrifugation (for 45 min at 7,000 RFC without brake) using Histopaque-119 (Sigma Aldrich, UK). PBMCs were then washed with PBS 1X, counted in a Bright-Line™ Hemacytometer (Sigma-Aldrich, UK).

5.1.4.1. Cell Pelleting

Cell pellets from MDA-MB-468 and H1975 cancer cell lines were obtained. For that, cells were grown to 75-80% confluence in a T75 flask. Then, the medium was removed, the cells were washed with PBS and they were trypsinised with Trypsin-EDTA 0.05% for 10 min; after that, they were neutralised with the correspondent medium, and they were counted. According to the number of cells required, specific volumes were transferred to 15 mL Falcon tubes and they were centrifuged for 5 min at 1,100 rpm. The supernatants were removed and the cell pellets were suspended in 1mL of cold PBS and transferred to 1.5 mL eppendorf tubes. Thereafter, the eppendorf tubes were centrifuged for 5 min at 1,100 rpm, subsequently, the supernatants were removed and the cell pellets were suspended in cold PBS and centrifuged again. At last, the supernatants were removed and the cell pellets were stored at -80 °C.

PBMCs were pelleted in serial concentrations, in PBS 1X, by centrifugation for 10 min at 350 RCF, and they were stored at -80 °C.

5.1.4.2. Cellular lysis

110 µL of a lysis buffer [161] are added to the cell pellets and the tubes are stirred at 1,200 rpm, for 1 h at 40 °C. Then, the tubes are centrifuged at 3,000 rpm for 5 min, transferring 100 µL to new 1.5 mL eppendorf tubes.

5.1.5. Monomers washing

Prior to use, the monomers divinylbenzene (DVB) and styrene (Figure 82) are washed to clear any presence of 4-tert-butylcatechol inhibitor from them. Styrene (50 mL) and DVB (25 mL) are washed with a 25% NaOH solution (2 x 100 mL firstly, and 2 x 50 mL then) and with miliQ H2O (2 x 100 mL firstly and 2 x 50 mL after that). The monomers are then dried over $MgSO_4$, filtered off and stored at 4 ºC until they are used for the synthesis of amino-functionalised cross-linked polystyrene NPs, following NanoChemBio group established protocols.

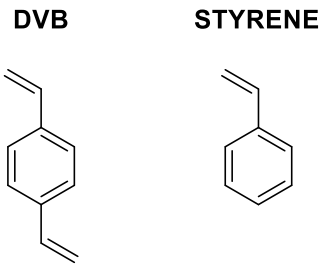

Figure 83. Monomers employed in the amino-functionalised cross-linked polystyrene NPs synthesis.

5.1.6. Kaiser Test (Ninhydrin test)

To assess whether the chemical couplings performed over polystyrene NPs have been completed, the Kaiser test [282], a very sensitive test for primary amines commonly utilised in SPPS chemistry, was carried out.

Firstly, the reagents are prepared as follows:

Reagent A

- Solution 1: Phenol (reagent grade) (40 g) is dissolved in EtOH (10 mL) using a heat source, and it is stirred over a MB-3 resin mixed with Amberlite (4 g) for 45 min. Then, the mixture is filtered.

- Solution 2: KCN (65 mg) is dissolved in H_2O (100 mL). Then, 3 mL of this solution is diluted with 97 mL of pyridine and it is stirred over a MB-3 resin mixed with Amberlite (4 g) for 45 min at RT. Subsequently, the mixture is filtered and mixed with solution 1 to obtain Reagent A.

Reagent B

- Ninhydrin (2.5 g) is dissolved in EtOH (50 mL).

To perform the Kaiser test, 6 µL of the NPs are transferred from the coupling reaction to 0.5 mL centrifuge tubes, and then the NPs are washed in MeOH and dried. Subsequently, 3 µL of Reagent A and 2 µL of Reagent B are added to the tube, dispersing the NPs in the mixture by sonication. At last, the suspension is heated up to 100 ºC for 3 min, resulting in blue or yellow colour, indicating the presence of primary amines (incomplete coupling – positive result) or the absence of them (complete coupling – negative result), respectively.

5.2. Experimental part of chapter 2

5.2.1. DGL probes

Table 22 shows the DGL probes sequences used throughout the chapter 2. They were synthesised and characterised by HPLC and MALDI-TOF, by DestiNA Genomica S.L.

Table 22. DGL probes sequences. DGL probes are written from the N-terminal to the C-terminal end. "_" (highlighted in yellow) represents the neutral abasic position. *GL* (highlighted in yellow) represents the chiral blank site, containing a propanoic acid side chain at the gamma position. "Xglu" represents the chiral and negatively charged PNA monomers, containing a propanoic acid side chain at the gamma position. All of them have a miniPEG group (xx) and a C-terminal primary amide. The third column "Smart-NB" shows the Smart-NB that is incorporated into the chemical pocket when the DGL probe hybridises with the corresponding target.

DGL probe	Sequence N→C (NH_2----CONH)	Smart-NB
DGL-K13SRC	xx-TTG CCT ACGglu C*GL*A CgluCA GCT	C (wt) / A (m)
DGL-21-1.0	xx-AAC ATCglu AGT _TG ATgluA AG	C
DGL-21-2.0	xx-TCA ACA TgluC_ GTgluC TGA TA	A
DGL-21-3.0	xx-ATC AGT CTgluG _TA AGCglu TA	A
DGL-21-4.1	Cys-xx-CAC ATCglu AGT *GL*TG ATgluA AGC	C
DGL-21-5.1	Cys-xx-CAC ATgluC *GL*GTglu CTG ATA AGC	A
DGL-21-6.0	xx-CAA CATglu C*GL*G TgluCT GAT AAG C	A
DGL-122	xx-CAC CATglu TGTglu _AC ACTglu CCA	C

5.2.2. DNA oligonucleotides

DNA oligonucleotides complementary to the DGL probes were purchased from Integrated DNA Technologies (IDT) and Microsynth as ssDNA. Table 23 show their sequences and whether they represent wild type (WT) or mutated species.

Table 23. DNA oligonucleotides sequences. ssDNA oligonucleotide sequences written from the 5'-end to the 3'-end. In colour and bold, the nucleotides mutated in the ssDNA sequences for miR-21. Underlined, in bold and highlighted in green, the nucleobase under interrogation and located in front of the blank position of the DGL probes (to be noted that for DNA-miR21, **DGL-21-6.0** is considered, and that DNA-miR39 and DNA-G2pr1-C-Cy5 are negative controls).

Reference	Sequence (5'→3')	WT / Mutation
DNA-KRAS	TTG GAG CTG GT**G** GCG TAG GCA A	WT
DNA-G13C-KRAS	AGC TGG T**T**G CGT AGG CAA	MUTATION
DNA-miR39	TCA CCG GGT GTA AAT CAG CTT G	-
ssDNA-21	TAG CTT ATC AGA C**T**G ATG TTG A	WT
DNA-G2pr1-C-Cy5	AGC ACG TGG GAG GGC GAT CG	-
DNA-miR21_1T	TAG CTT ATC A**T**A C**T**G ATG TTG A	MUTATION
DNA-miR21_2G	TAG CTT ATC A**G**A C**G**G ATG TTG A	MUTATION
DNA-miR122	TGG AGT GT**G** ACA ATG GTG TTT G	WT

5.2.3. SMART-Nucleobases

The SMART-Nucleobases that have been used in this Doctoral Thesis have been synthesised and kindly provided by DestiNA Genomica S.L.

The Smart-NBs are analogues to Cytosine (Smart-C) and to Adenine (Smart-2dA), and they are chemically modified with fluorophores or biomolecules (Table 24 and Figure 83)

Table 24. SMART-NBs classified according to their chemical modification

FLUOROPHORE	BIOMOLECULES
Smart-C-Cy5	Smart-C-Biotin
-	Smart-2dA-Biotin

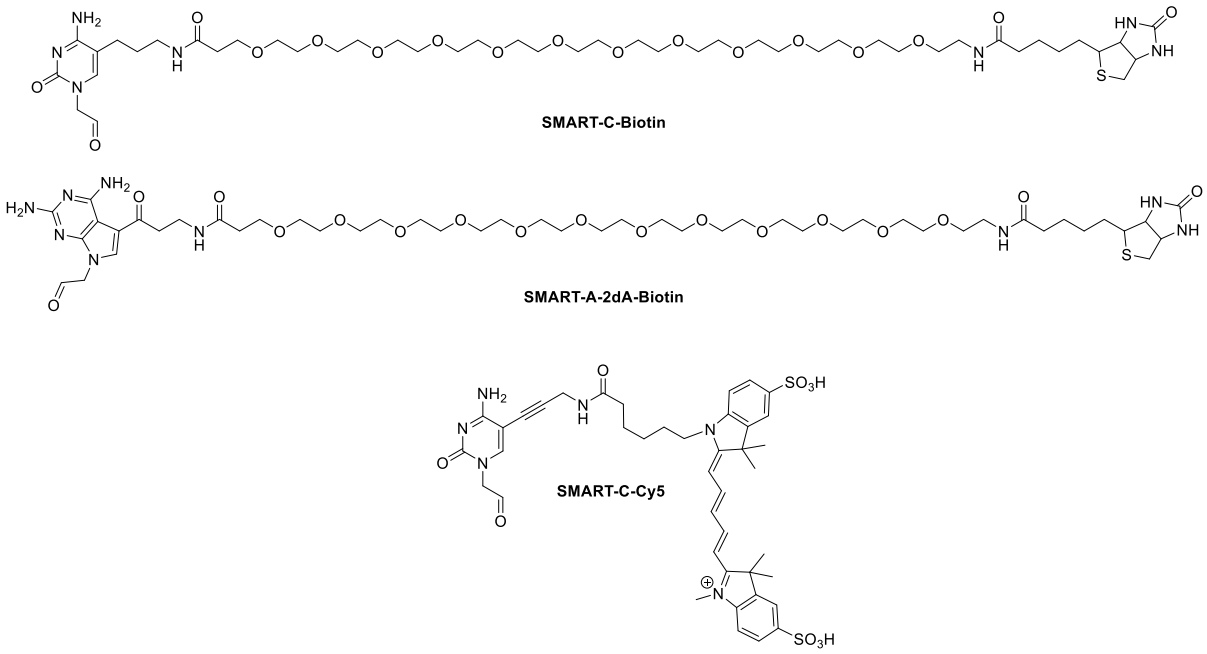

Figure 84. Smart-Cytosine-Rex-PEG12-Biotin (Smart-C-Biotin), Smart-2-diaminopurine-Deaza-Keton-PEG12-Biotin (Smart-2dA-Biotin), and Smart-Cytosine-Cyanine-5 (Smart-C-Cy5).

5.2.4. General method for DGL probes coupling to Dynabeads®

5.2.4.1. Dynabeads® M-270 Carboxylic Acid

Magbeads-122 and **Magbeads-KRAS** were provided by DestiNA Genomica S.L.., whereas **Magbeads-21-1.0**, **Magbeads-21-2.0**, and **Magbeads-21-3.0** were synthesised. For that, amine DGL probes (**DGL-21-1.0**, **DGL-21-2.0**, **DGL-21-3.0**, **DGL-21-6.0**, **DGL-122**, and **DGL-K13SRC**) employed in Chapter 2 were coupled to commercial Dynabeads® M-270 Carboxylic Acid (2 x 10^9 beads/mL and a loading of 30 mg/mL), whereas and through the following procedure:

1. First, the Dynabeads® are thoroughly resuspend in the commercial tube, then 100 µL are transferred to a new tube and centrifuged for 10 s at 10,000 rpm, prior applying a magnet for 1 min and removing the supernatant.

2. Then, 100 µL of a 0.01 M NaOH solution are added, incubating the beads for 10 min, at RT, at 1,200 rpm. After that, the beads are centrifuged and supernatant is removed, as previously described. This step is done twice.

3. Then, 100 µL of MiliQ H_2O are added, incubating the beads for 10 min, at RT, at 1,200 rpm. After that, the beads are centrifuged and supernatant is removed, as previously described. This step is done three times.

4. Afterwards, 150 µL of a freshly made EDC solution (EDC 50 mg/mL in cold, and freshly made 50 mM MES pH 5 + 0.1% Tween®-20) are added to the beads, incubating for 30 min at RT, at 1,000 rpm. Then the beads are centrifuged and the supernatant is removed, as previously described.

5. Subsequently, 100 µL of a cold, and freshly made, 50 mM MES pH 5 + PBS 0.1% Tween®-20 solution are added to the beads, and shaken well, prior to centrifuging the beads and removing the supernatant, as previously described. This step is done twice.

6. After that, 100 µL of a solution containing 700 pmol of DGL probe/mg of beads in 0.125 M $NaHCO_3$ (pH approximately 10) in 0.1% Tween®-20, are added to the beads. The suspension is incubated for 3 h at RT, at 1,000 rpm. Then, the beads are centrifuged and the supernatant is removed as previously described.

7. Afterwards, the beads are washed by adding 100 µL of a freshly made 50 mM MES pH 5 + 0.1% Tween®-20 solution. Subsequently, 100 µL of a 50 mM ethanolamine in PBS pH 8 + 0.1% Tween®-20 are added to the beads. The suspension is incubated for 1 h, at RT, at

1,000 rpm. Thereafter, the beads are centrifuged and the supernatant is removed as previously described.

8. Thereupon, the **Magbeads** are washed three times with 100 µL of a PBS-0.1% Tween®-20 + 10% PEG10K solution and eventually suspended in a final volume of 100 µL, being stored at 4 ºC.

5.2.4.2. Dynabeads® M-270 Amine

Thiol DGL probes (**DGL-21-4.1** and **DGL-21-5.1**) employed in Chapter 2 were coupled to commercial Dynabeads® M-270 Carboxylic Acid (2 x 10^9 beads/mL and a loading of 30 mg/mL) through the following procedure:

1. First, the Dynabeads® are thoroughly resuspend in the commercial tube, then 400 µL are transferred to a new tube and centrifuged for 10 s at 10,000 rpm, prior to applying a magnet for 1 min and removing the supernatant.

2. Then, 400 µL of DMF are added, vortexing well and centrifuging for 10 s at 10,000 rpm, prior to applying a magnet for 1 min and removing the supernatant. This step is done three times.

3. After that, 400 µL of a 0.5 M DIPEA solution in DMF is added, incubating the mixture for 5 min at RT, at 1,000 rpm. Then the beads are centrifuged and the supernatant is removed, as previously described.

4. Repeat the step 2.

5. Subsequently, 400 µL of a 0.2 M N-Maleoyl-β-Alanine, 0.2 M DIC, and 0.2 M OxymaPure solution in DMF is added to the beads, leaving it to react for 2 h, at RT, at 1,000 rpm. After that time, the beads are centrifuged and the supernatant is removed, as previously described.

6. Thereupon, the beads are washed five times by adding 400 µL of DMF, as described in step 2.

7. Afterwards, Kaiser-test is performed by transferring 5 µL of the beads to a PCR tube and adding 100 µL of EtOH. The suspension is mixed well prior centrifuging and removing the supernatant as previously described. Then 15 µL of Reagent A and 15 µL of Reagent B are added, mixing well. Subsequently, the suspension is incubated for 5 min at 100 ºC, after which the beads are centrifuged, the magnet is applied for 1 min, and the supernatant is collected and transferred to another PCR tube in order to determine the colour.

8. If the supernatant is not yellowish, 400 µL of a 0.5 M Ac_2O and 0.5 M DIPEA solution in DMF is added to the beads, leaving it to react for, at least 30 min and a maximum of 60 min, at RT, at 1,000 rpm. Subsequently, the beads are centrifuged and the supernatant is removed as previously described. Repeat steps 6. and 7.

9. The beads are finally suspended in 400 µL of DMF and stored at -20 ºC until the DGLs are coupled.

10. To afford **Magbeads**, 100 µL of the beads are taken from the freezer, centrifuging and removing the supernatant as previously described.

11. Then, 100 µL of a PBS-0.1% Tween®-20 solution is added to the beads, mixing well, centrifuging and removing the supernatant as previously described. This step is done three times.

12. Afterwards, 100 µL of a solution containing 175 pmol or 350 pmol of DGL probe/mg of beads are added to the beads. The suspension is incubated for 5 h, at RT, at 1,000 rpm.

13. After that, 100 µL of a PBS-0.1% Tween®-20 solution are added to the beads, mixing well, centrifuging and removing the supernatant as previously described.

14. Subsequently, 100 µL of a 2 mM mercaptoethanol solution in PBS are added to the beads, incubating for 1 h, at RT, at 1,000 rpm. After that, the beads are centrifuged and supernatant is removed as previously described.

15. Thereupon, the **Magbeads** are washed three times with 100 µL of a PBS-0.1% Tween®-20 + 10% PEG10K solution and eventually suspended in a final volume of 100 µL, being stored at 4 ºC.

5.2.5. General methods for Nucleic Acids detection through Dynamic Chemistry

5.2.5.1. miR-21 and miR-122 detection

5.2.5.1.1. FACS

When analysing cell lysates, the 100 µL volumes are incubated with 250,000 **Magbeads** at 1,200 rpm, for 1h at RT (hybridisation volume). Then, the tubes are centrifuged for 10 s at 6,000 rpm and placed on a magnet for 10 s, removing the supernatants. Subsequently, 200 µL of Buffer A are added to the tubes and the **Magbeads** are suspended, as a washing step. After that, the **Magbeads** are centrifuged for 10 s at 6,000 rpm and placed on a magnet and the supernatants are removed. This washing step is done three times.

Thereupon, dried **Magbeads** are suspended in a mixture containing the correspondent Smart-NB and the reducing agent $NaBH_3CN$ (always 1 mM), in Buffer A, to reach a final 50 µL volume. If the samples to be analysed are synthetic ssDNA, then, the first incubation step of the samples with **Magbeads** is not performed. In this case, the **Magbeads** are suspended in a mixture containing the ssDNA oligonucleotide at a desired concentration, the Smart-NB and the reducing agent $NaBH_3CN$, in Buffer A, to reach a final 50 µL volume. In both cases, Smart-NB dynamic incorporation takes place when the mixture is stirred at 1,200 rpm for 1h at 41 °C. Subsequently, 150 µL of PBS-Tween®20 0.1% are added to each tube and the washing steps, described above, are performed three times, but using PBS-Tween®20 0.1% instead of Buffer A.

When the Smart-NB is fluorescently labelled (**Smart-C-Cy5**), then, the **Magbeads** are suspended in 200 µL of PBS-Tween®20 0.1%, transferred to cytometry tubes and ready to be read by FACS. On the other hand, if the Smart-NB is biotinylated (**Smart-C-Biotin** and **Smart-2dA-Biotin**), the dried **Magbeads** are suspended in 100 µL of PBS-Tween®20 0.1%, and 20 µL of a 60 µg/mL SAPE conjugate solution in PBS-Tween®20 0.1%, are added. The mixture is stirred at 1,200 rpm, for 1 h at RT in darkness. Afterwards, the **Magbeads** are washed as described above and finally suspended in 200 µL of Buffer A and transferred to cytometry tubes.

At last, the **Magbeads** are loaded into a FACSCanto II using 488 nm and 633 nm lasers as excitation sources, and reading the fluorescence obtained with 585/42 nm (PE channel) and 660/20 nm (APC channel) filters.

5.2.5.1.2. FLUOstar Omega Plate reader

The 100 µL of cell lysate are incubated with 250,000 **Magbeads** at 1,200 rpm, for 1 h at RT (hybridisation volume). Then, the tubes are centrifuged for 10 s at 6,000 rpm and placed on a magnet for 10 s, removing the supernatants. Subsequently, 200 µL of Buffer A are added to the tubes and the **Magbeads** are suspended, as a washing step. After that, the **Magbeads** are centrifuged for 10 s at 6,000 rpm and placed on a magnet and the supernatants are removed. This washing step is done three times. Thereupon, the dried **Magbeads** are suspended in a mixture containing the corresponding Smart-NB and the reducing agent $NaBH_3CN$, in Buffer A, to reach a final 50 µL volume. Smart-NB dynamic incorporation takes place when the mixture is stirred at 1,200 rpm for 1 h at 41 °C. Subsequently, 150 µL of PBS-Tween®20 0.1% are added to each tube and the washing steps, described above, are performed three times, but using PBS-Tween®20 0.1% instead of Buffer A.

Afterwards, the dried **Magbeads** are suspended in 100 µL of SbG, and the mixture is stirred at 1,200 rpm, for 20 min at RT. Subsequently, the **Magbeads** are washed as described above and they are suspended in 200 µL of PBS-Tween®20 0.1% and transferred to a black 96 well plate, which is placed on a magnet for 1 min, removing the supernatants then. Finally, 200 µL of substrate Resorufin-β-D-Galactopyranoside are added to each well and mixed with the **Magbeads**, letting a 10 min fluorescent reaction described elsewhere [161] to take place inside the FLUOstar Omega instrument, equipped with 544 ± 10 nm excitation and 590 ± 10 nm emission filters.

5.2.5.2. KRAS detection

5.2.5.2.1. FACS for synthetic KRAS

The **Magbeads-KRAS** are suspended in a mixture containing the ssDNA oligonucleotide at a desired concentration, the Smart-NB and the reducing agent $NaBH_3CN$, in Buffer A, to reach a final 50 µL volume. In both cases, Smart-NB dynamic incorporation takes place when the mixture is stirred at 1,200 rpm for 1 h at 41 °C. Subsequently, 150 µL of PBS-Tween®20 0.1% are added to each tube and the washing steps, described above, are performed three times, but using PBS-Tween®20 0.1% instead of Buffer A.

When the Smart-NB is fluorescently labelled (**Smart-C-Cy5**), then, the **Magbeads-KRAS** are suspended in 200 µL of PBS-Tween®20 0.1%, transferred to cytometry tubes and ready to be read by FACS. On the other hand, if the Smart-NB is biotinylated (**Smart-2dA-Biotin**), the dried **Magbeads-KRAS** are suspended in 100 µL of PBS-Tween®20 0.1%, and 20 µL of a 60 µg/mL SAPE solution in PBS-Tween®20 0.1%, are added. The mixture is stirred at

1,200 rpm, for 1 h at RT in darkness. Afterwards, the **Magbeads-KRAS** are washed as described above and finally suspended in 200 µL of Buffer A and transferred to cytometry tubes.

At last, the **Magbeads** are loaded into a FACSCanto II, using a 488 nm and a 633 nm lasers as excitation sources, and reading the fluorescence obtained with 585/42 nm (PE channel) and 660/20 nm (APC channel) filters.

5.2.5.2.2. FACS for serum samples

100 µL of serum are mixed with 400 µL of lysis buffer, being mixed for a few seconds prior to adding DNA-KRAS to reach a final concentration of 15 nM and 250,000 **Magbeads-KRAS**. Then, the mixture is incubated at 94 ºC for 30 s and, immediately after, at 25 ºC for 1 h at 1,200 rpm. Thereupon, the **Magbeads-KRAS** are centrifuged for 10 s at 6,000 rpm and placed on a magnet for 10 s, removing the supernatant. Subsequently, 200 µL of Buffer A are added, mixing the beads and centrifuging for 10 s at 6,000 rpm prior placing them on a magnet for 10 s, removing the supernatants. This washing step is repeated three times.

Afterwards, dried **Magbeads-KRAS** are suspended in 22.5 µL of Buffer A solution containing **Smart-C-Cy5**. Then, the mixture is incubated at 94 ºC for 5 min at 1,200 rpm, after what the mixture is let to chill upon reaching 41 ºC, without stirring. Then, 2.5 µL of reducing agent $NaBH_3CN$ are added to reach a final volume of 25 µL, letting the Smart-NB dynamic incorporation to take place when the mixture is stirred at 1,200 rpm for 1h at 41 °C Subsequently, 150 µL of PBS-Tween®20 0.1% are added to each tube and the washing steps, described above, are performed three times, but using PBS-Tween®20 0.1% instead of Buffer A.

At last, the **Magbeads-KRAS** are loaded into a FACSCanto II, using a 633 nm laser as excitation source, and reading the fluorescence obtained with 660/20 nm (APC channel) filter.

5.2.6. RT-qPCR

Total RNA, including microRNAs, was isolated using the “miRNeasy Mini Kit” (Qiagen) according to manufacturer’s protocol. For that, one million H1975 and MDA-MB-468 cells, as well as one million human lymphocytes, were pelleted for the extraction. Then, 700 µL of Qiazol Reagent were added to the pellets, mixed and incubated for 1 min at RT; afterwards 140 µL of chloroform were added and the mixtures were incubated for 3 min at RT. Then, the mixtures were centrifuged at 12,000*g* for 15 min at 4 ºC. The upper aqueous phases were transferred into new tubes. After that, absolute EtOH were added to the new tubes, mixed a

transferred to the RNeasy Mini spin columns, being centrifuged at 10,000*g* for 15 s at RT. Keeping the same centrifugation conditions, the columns were washed with RWT and RPE buffers from the miRNeasy kit, followed by drying and elution in 50 µL of RNase-free water. The tubes containing the extracted RNA were stored at -80 ºC until the analysis with RT-qPCR.

Total miRNA recovered was reverse transcribed to cDNA using the TaqMan™ Advanced miRNA cDNA Synthesis Kit (Life Technologies). The kit consists in four stages through modification of miRNAs from total RNA: poly(A) addition, adaptor ligation, reverse transcription and amplification to an uniform increase of the amount of cDNA for all miRNAs. All the volumes of reagents and temperatures have been used according to the manufacturer's protocol.

Quantitative real time PCR was performed using the Universal PCR Master Mix kit (Life Technologies). First, it was made a dilution 1:10 of cDNA in RNase free-water to afford a range of 1-100 ng of cDNA. Then, the PCR mixture was prepared by adding 10 µL of master mix containing 1 µL of the specific probe hsa-miR-21-5p (applied biosystem) and 9 µL of cDNA in RNase free water. A technical quadruplicate was performed for each sample.

In order to take into account the variability in the initial concentration, the quality of the total miRNA and the conversion efficiency of the reverse transcription reaction, an endogenous control was used: hsa-miR-16-5p (applied biosystem), a miRNA that has been described as a suitable endogenous control for expression analysis of miRNAs [283],[284].

Quantitative PCR analysis was performed on a 7900 Fast Real-Time PCR System (Applied Biosystems), with an initial activation step of 95 ºC for 15 min followed by 40 cycles of 2-step cycling (denaturation: 15 s at 95 ºC and Annealing/Extension: 1 min at 60 ºC). Threshold cycle (Ct) values of miR-21, obtained in qRT-PCR, were normalized to miR-16 by using the -2ΔCt method. Finally, T-test analyses were performed using GraphPad Prism Software to compare the relative miR-21 expression from each cell line to the lymphocytes.

5.2.7. miR-21 Spike-in

A calibration curve was done in FLUOstar Omega using spike-in solutions of synthetic miR-21 (500 pM, 250 pM, 125 pM, 62.5 pM, 31.25 pM and 0 pM). For that, two master mix solutions were prepared:

a) Master mix solution A, containing 500 pM of synthetic mimic miR-21 in lysis buffer and 250,000 **Magbeads-21-6.0**.

b) Master mix solution B, containing 250,000 **Magbeads-21-6.0** in lysis buffer.

The spiked solution were made by serial dilutions, mixing Master mix A and Master mix B, as follows: from Master mix A, half of the volume is taken and mixed with Master mix B (same volume), then, half of the volume is transferred to a new tube to afford solution 2 (250 pM). The other half of the volume is mixed again with the same amount of volume of Master mix B, subsequently, half of the volume is transferred to a new tube to afford solution 3 (125 pM). The remaining volume is mixed again with the same volume of Master Mix B, repeating the same operation described above, to afford solution 4 (62.5 pM) and solution 5 (31.25 pM). Thus, and using Master mix B as the 0 pM solution, these solutions cover the concentration range aforementioned. Afterwards, 100 µL of these solutions are used for the hybridisation step which took place at 1,200 rpm, for 1 h at RT. Then, washing steps, dynamic incorporation step, labelling step and relative fluorescence measurement by FLUOstar Omega were performed.

5.2.8. Determination of the number of miRNA per cell

To calculate the number of miR-21 molecules per cell, it is firstly extrapolated the miR-21 concentration from the calibration curve equation, using the RFU/s obtained for each sample. Then, the next formula is applied:

$$miR21\ molecules = \frac{[(Concentration(M)) * (V) * (NA)]}{n^{o}\ of\ cells}$$

- *V = Volume of hybridisation (1e-4 L)*
- *NA = Avogadro's number (6.022 x 1e23)*

5.3. Experimental part of chapter 3

5.3.1. Chemicals

5.3.1.1. Synthesis of 4-Vinylbenzylphtalimide

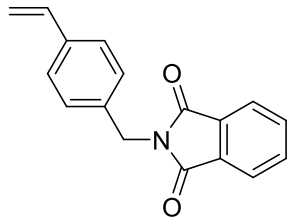

1

Potassium Phtalimide (18.5 g, 100 mmol) is dissolved in DMF (50 mL); then N-p-vinylbenzyl chloride (14.1 mL, 100 mmol) is added, resulting in an orange solution. The mixture is stirred for 18 h, at RT, and a consequent colour change to pale yellow is noted. The reaction mixture is then poured into a 1.7 M NaOH solution (1 L), producing a white precipitate that is isolated by vaccum filtration prior to re-solubilisation in EtOAc (300 mL), forming an opaque off-white solution. Subsequently, the solvent is removed and recrystallized in MeOH (200 mL). The recrystallization step is repeated twice prior filtration to afford ***compound 1*** (21 g, 79.55 mmol, 80% yield).

Rf: 0.45, Hexane/ EtOAc (3:1).

HPLC (S50D, λ=220 nm): purity 97.6%, retention time: 4.07 min.

^{1}H NMR (400 MHz, $CDCl_3$) δ 7.84 (dd, J = 5.4, 3.1 Hz, 2H), 7.70 (dd, J = 5.5, 3.0 Hz, 2H), 7.40 (d, J = 8.2 Hz, 2H), 7.35 (d, J = 8.3 Hz, 2H), 6.67 (dd, J = 17.6, 10.9 Hz, 1H), 5.71 (dd, J = 17.6, 1.0 Hz, 1H), 5.22 (dd, J = 10.9, 0.9 Hz, 1H), 4.83 (s, 2H).

^{13}C NMR (100 MHz, $CDCl_3$) δ 168.15, 137.37, 136.47, 136.00, 134.12, 132.29, 129.00, 126.63, 123.48, 114.28, 41.50.

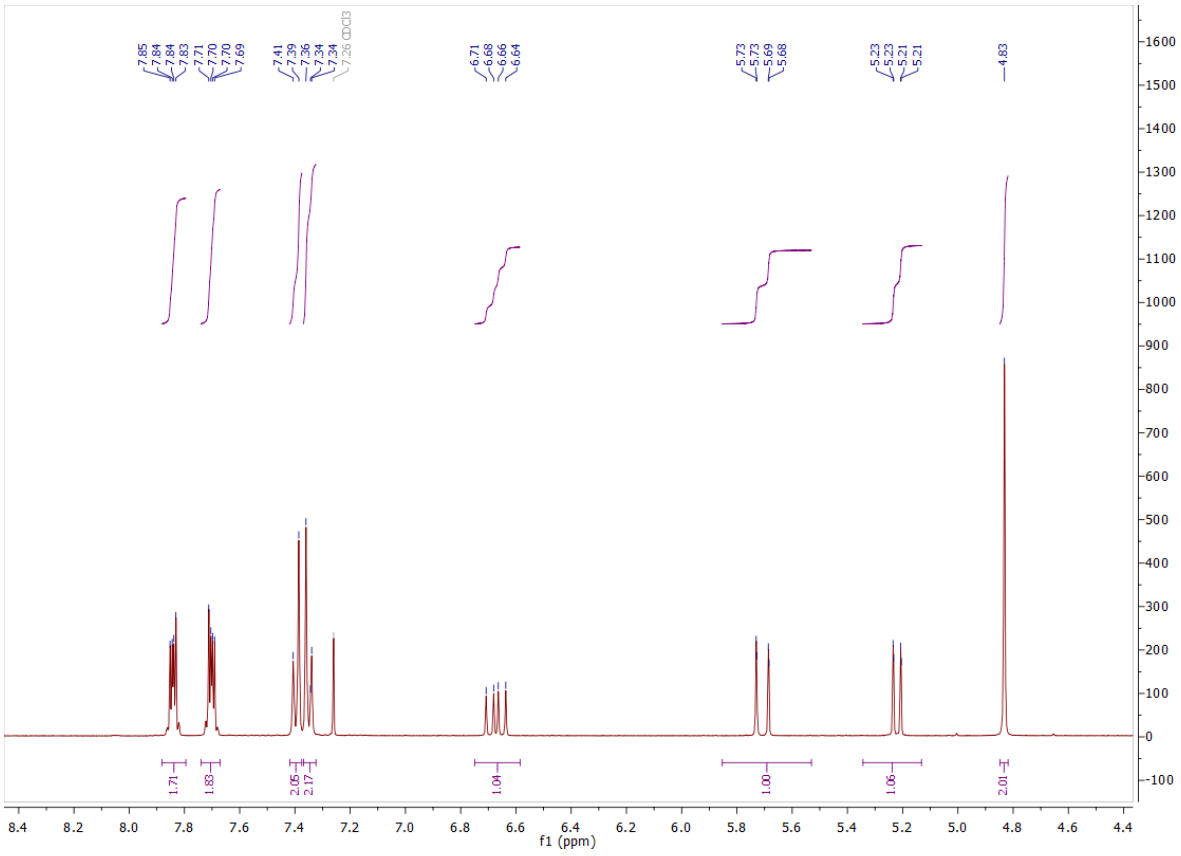
7.85
7.84
7.84
7.83
7.71
7.70
7.70
7.69
7.41
7.39
7.36
7.34
7.34
7.26 CDCl3
6.71
6.68
6.66
6.64
5.73
5.73
5.69
5.68
5.23
5.23
5.21
5.21
4.83
1.71
1.83
2.05
2.17
1.04
1.00
1.06
2.01
f1 (ppm)

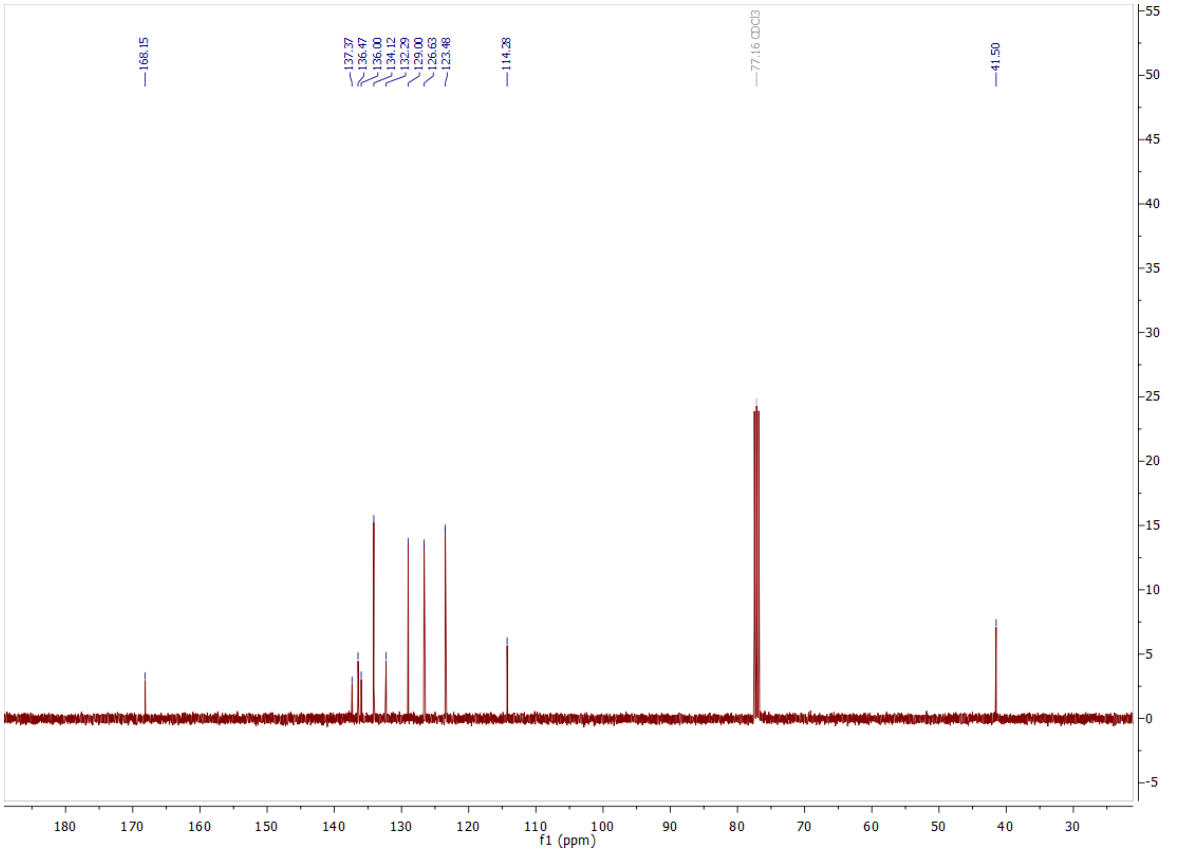
168.15
137.37
136.47
136.00
134.12
132.29
129.00
126.63
123.48
114.28
77.16 CDCl3
41.50
f1 (ppm)

5.3.1.2. Synthesis of Vinylbenzylamine

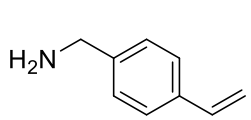

2

Compound 1 (8 g, 30 mmol) is suspended in Ar purged EtOH (50 mL) and heated to reflux under Ar until dissolution. After stirring it for 30 min, Ar purged hydrazine hydrate (55% w/v) (3 mL, 60 mmol) is added via a self-equilibrating dropping funnel, resulting in a colour change to bright yellow. After 5 min, a gelatinous off-white precipitate appears. Upon a reaction time of 3 h, the white gelatinous by-product is removed by filtration and the filtrate is concentrated. Afterwards, the crude product is treated with 1.5 M KOH solution (75 mL), subsequently, the aqueous mixture is extracted with Et_2O (2 x 100 mL). The organic fractions are combined, washed with 2% K_2CO_3 solution (3 x 100 ml), dried over $MgSO_4$ and concentrated under vaccum to afford the colourless oil ***compound 2*** (2.83 g, 21.24 mmol, 70% yield).

HPLC (S50D, λ=220 nm): purity 100%, retention time: 2.30 min.

^{1}H NMR (400 MHz, Methanol-d_4) δ 7.55 (d, *J* = 8.2 Hz, 2H), 7.47 (d, *J* = 8.3 Hz, 2H), 6.79 (dd, *J* = 17.7, 10.9 Hz, 1H), 5.87 (dd, *J* = 17.7, 0.9 Hz, 1H), 5.32 (dd, *J* = 10.9, 0.9 Hz, 1H), 4.14 (s, 2H).

^{13}C NMR (100 MHz, CD_3OD) δ 139.93, 137.33, 133.76, 130.30, 127.89, 115.34, 44.07.

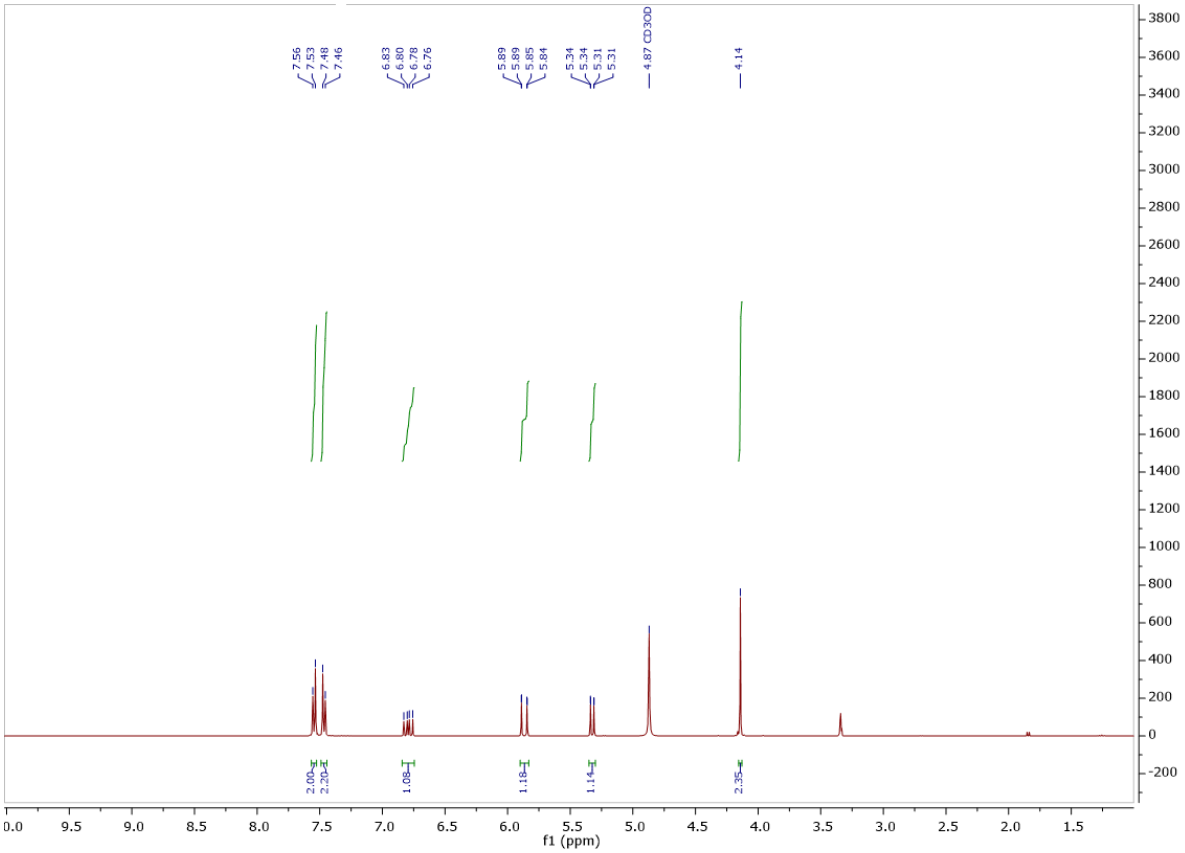

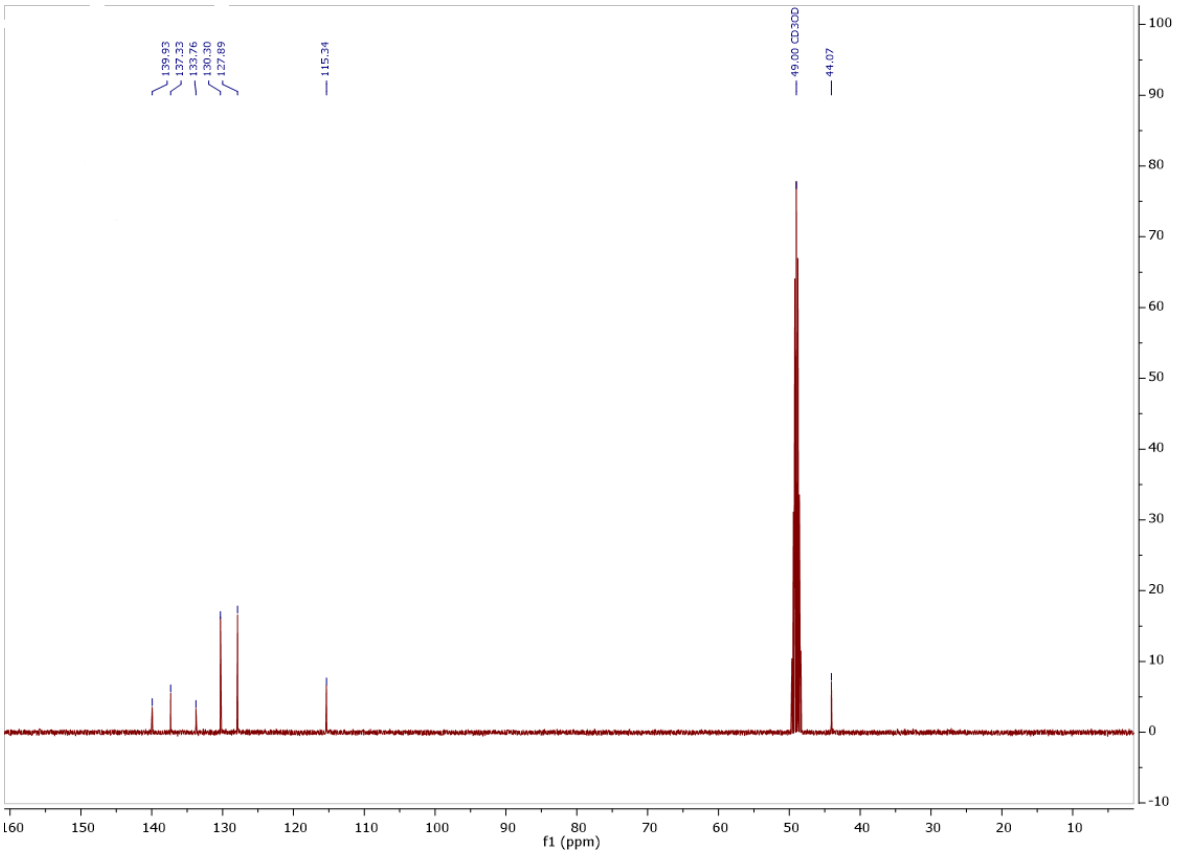

5.3.1.3. Synthesis of Vinylbenzylamine hydrochloride

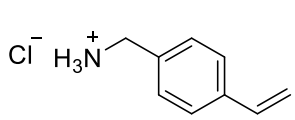

3

Compound 2 (1.5 g, 11.26 mmol) is dissolved in MeOH (6 mL) and chilled to 0 ºC, then isopropanol (6 mL, HCl 6 mL) is added drop wise for 1.5 h. A white precipitate is obtained by filtration and dried under vacuum to afford, as a white solid, the ***compound 3*** (1.56 g, 9.2 mmol, 82% yield).

5.3.1.4. Synthesis of Fmoc-4,7,10-trioxa-1,13-tridecanediamine succinic acid

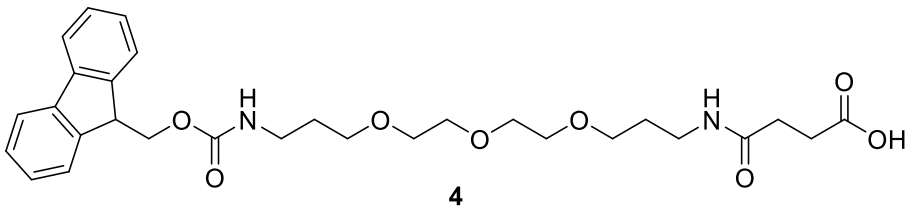

4

Succinic anhydride (1 g, 10 mmol) is dissolved in ACN (25 mL) and added drop wise, under strong stirring, to a solution of 4,7,10-trioxa-1,13-tridecanediamine (19 mL, 10 mmol) in ACN (50 mL). The mixture is stirred for 3 h; at RT, then, the liquid phase is decanted and discarded once the waxy product is settled. The waxy product is dissolved by the addition of a mixture ACN:H_2O (1:1) (100 mL) and the solution is chilled to 0 ºC prior to drop wise addition of a solution of Fmoc N-hydroxysuccinimide ester (4.38 g, 13 mmol) in ACN (25 mL)

under vigorous stirring, during which time the pH is kept between 8 and 9 by addition of DIPEA. After 12 h of reaction at room temperature, the solvents are removed under vaccum and the residue is dissolved in a 5% $NaHCO_3$ solution (100 mL) and washed with EtOAc (3 x 50 mL). After that, the aqueous phase is acidified to pH 2 with 37% HCl and extracted with EtOAc (3 x 50 mL), then the organic phases are combined , washed with brine, dried over $MgSO_4$ and concentrated under vacuum to afford the yellowish sticky product ***compound 4*** (4.215 g, 7.78 mmol, 78% yield).

HPLC (S50D, λ=220 nm): purity 100%, retention time 8.4 min.

m/z (ES+) 565.5 (100%) [M+Na]+

^{1}H NMR (400 MHz, CD3OD) δ 7.78 (d, *J* = 7.5 Hz, 2H), 7.63 (d, *J* = 7.5 Hz, 2H), 7.38 (t, *J* = 7.4 Hz, 2H), 7.30 (t, *J* = 7.4 Hz, 3H), 5.48 (s, 2H), 4.36 (d, *J* = 6.7 Hz, 2H), 4.18 (t, *J* = 6.7 Hz, 1H), 3.63 – 3.44 (m, 12H), 3.23 (t, *J* = 6.8 Hz, 2H), 3.18 (t, *J* = 6.7 Hz, 2H), 2.58 (t, *J* = 7.1 Hz, 2H), 2.44 (t, *J* = 6.9 Hz, 2H), 1.77 – 1.68 (m, 4H).

^{13}C NMR (100 MHz, CD3OD) δ 176.12, 174.37, 158.78, 145.34, 142.60, 128.74, 128.11, 126.11, 120.92, 71.48, 71.18, 71.16, 69.83, 69.70, 67.44, 54.78, 39.09, 37.83, 31.64, 30.74, 30.33, 30.31, 26.26.

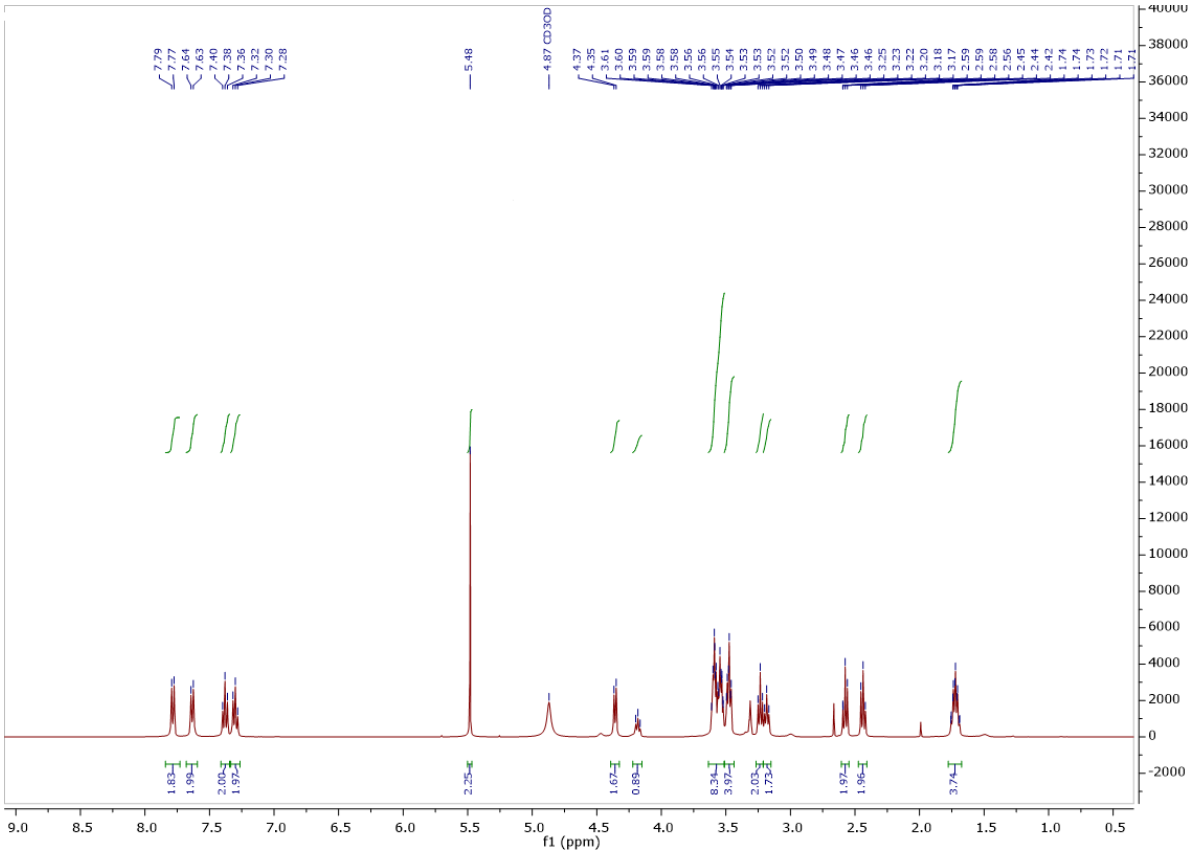

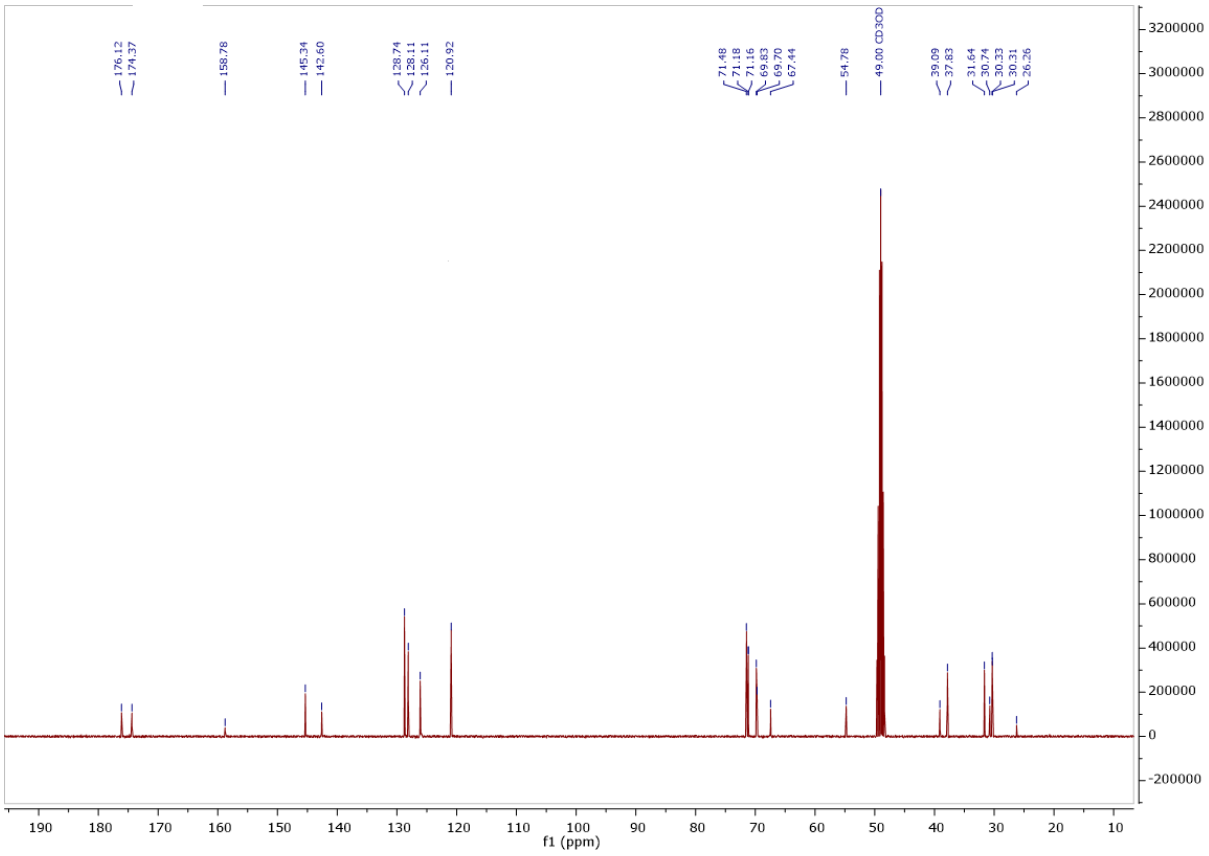

5.3.1.5. Synthesis of Dde-OH

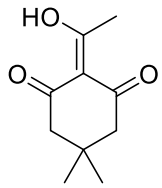

5

DCC (14.68 g, 71.3 mmol) is added to a solution of dimedone (10 g, 71.3 mmol) and DMAP (0.87 g, 7.13 mmol) in DMF (125 mL). Subsequently, acetic acid (8.3 mL, 142 mmol) is added to the solution and it is let to stir for 36 h at RT. Upon completion of the reaction, the mixture is filtered to remove the by-product DCU, then the organic phase is poured over H_2O (200 mL) and extracted with Et_2O (3 x 100 mL). The organic phase is dried over $MgSO_4$ and concentrated under vacuum to afford the final ***compound 5*** as an orange oil (9.745 g, 53.5 mmol, 75% yield).

Rf: 0.55, Hexane:EtOAc (1:2)

HPLC (SODNEW, λ=254): purity 98%, retention time: 3.321 min

m/z (ES+) 183.0 (100%) [M+H]+

^{1}H NMR (300 MHz, $CDCl_3$) δ 2.61 (s, 3H), 2.55 (s, 2H), 2.37 (s, 2H), 1.09 (s, 6H).

^{13}C NMR (75 MHz, $CDCl_3$) δ 202.64, 198.10, 195.41, 112.63, 52.73, 47.16, 30.87, 28.74, 28.43.

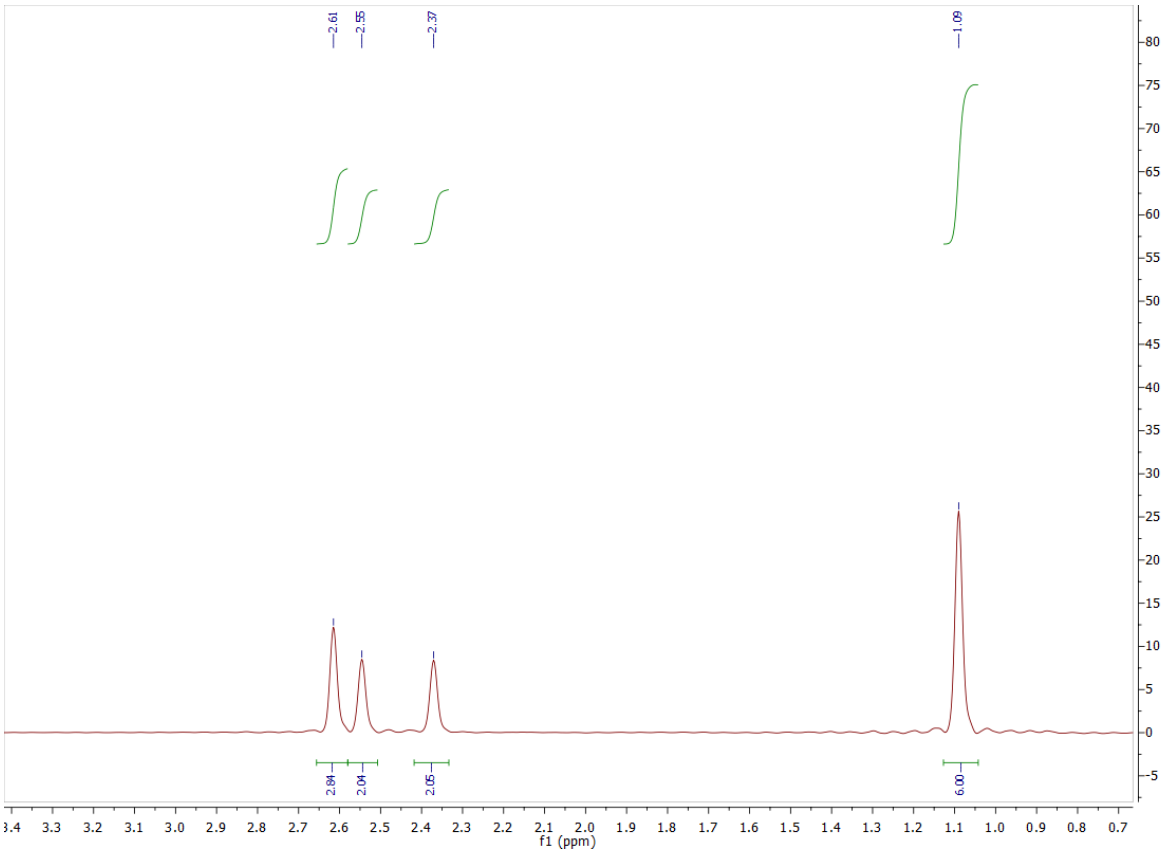
2.61
2.55
2.37
1.09
2.84
2.04
2.05
6.00
f1 (ppm)

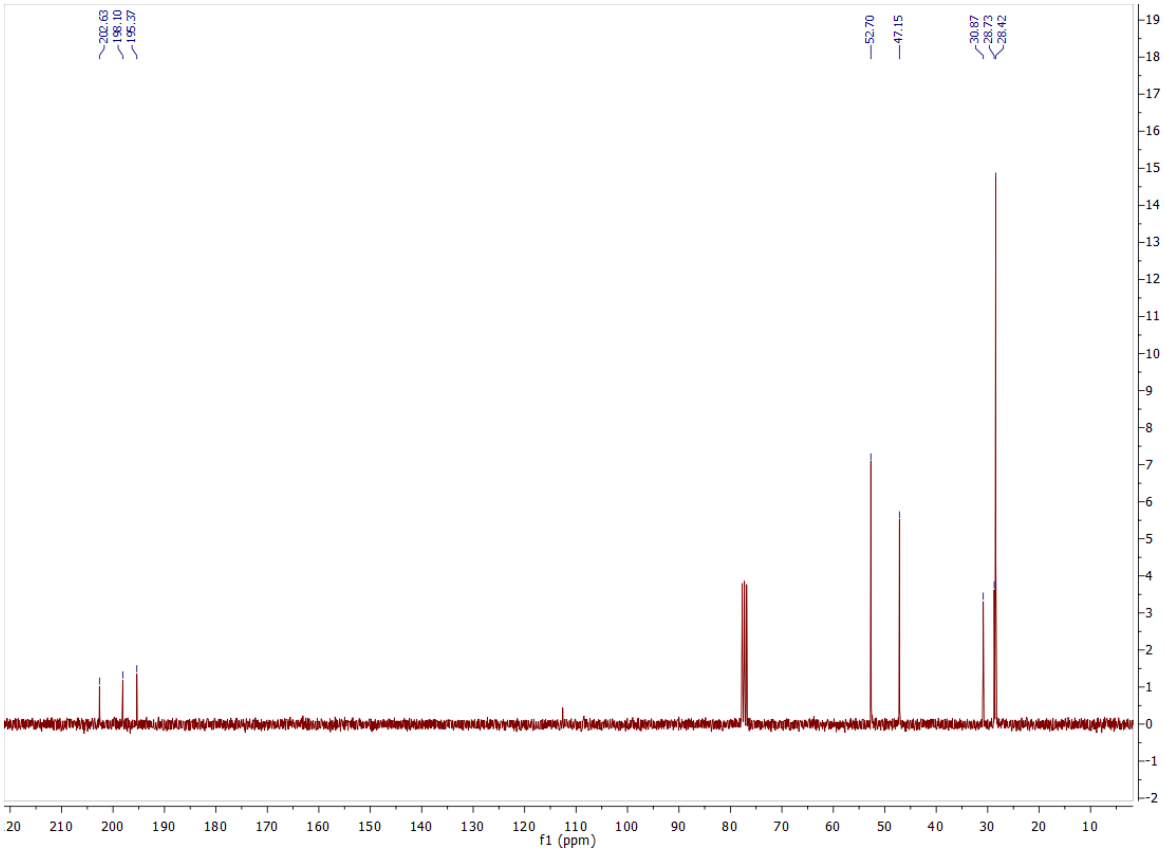
202.63
198.10
195.37
52.70
47.15
30.87
28.73
28.42
f1 (ppm)

5.3.1.6. Synthesis of Fmoc-Lys(Dde)-OH

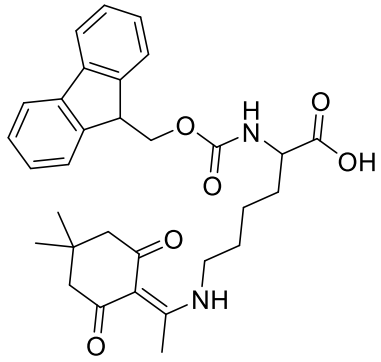

6

TFA (84 µL, 1.1 mmol) is added to a stirred Fmoc-Lys-OH (4.04 g, 10.7 mmol) and Dde-OH (compound 5) (5.84 g, 32.1 mmol) suspension in EtOH (95 mL), at RT. The mixture is heated under reflux for 60 h, following the progress by TLC. After the 60 h, the solvents are evaporated and the consequent orange residue is dissolved in EtOAc (75 mL). Then, the organic solution is washed with 1 M $KHSO_4$ solution (3 x 100 mL), dried over $MgSO_4$ and concentrated under vacuum. The crude is purified by column chromatography, using as eluent DCM:MeOH (8:1), to afford the final pure ***compound 6*** as a brown solid (3.6 g, 6.77 mmol, 63.2% yield).

Rf: 0.20, DCM:MeOH (2:1)

HPLC (SODNEW, λ=254): purity 100%, retention time: 3.7 min.

m/z (ES+) 533.3 (100%) [M+H]+

^{1}H NMR (400 MHz, $CDCl_3$) δ 13.31 (s, 1H), 7.74 (d, *J* = 7.6 Hz, 2H), 7.58 (t, *J* = 7.7 Hz, 2H), 7.37 (t, *J* = 7.5 Hz, 2H), 7.32 – 7.23 (m, 2H), 5.78 (d, *J* = 8.2 Hz, 1H), 4.45 (q, *J* = 7.2, 6.7 Hz, 1H), 4.36 (d, *J* = 7.2 Hz, 2H), 4.19 (t, *J* = 7.0 Hz, 1H), 3.39 (d, *J* = 6.0 Hz, 2H), 2.53 (s, 2H), 2.35 (s, 4H), 2.04 – 1.91 (m, 1H), 1.86 – 1.45 (m, 5H), 1.00 (s, 6H).

^{13}C NMR (100 MHz, $CDCl_3$) δ 198.39, 174.74, 174.21, 156.33, 144.04, 143.88, 141.43, 127.86, 127.20, 125.27, 120.12, 108.04, 67.22, 53.61, 52.61, 47.31, 43.42, 32.09, 30.27, 28.50, 28.34, 22.58, 18.27.

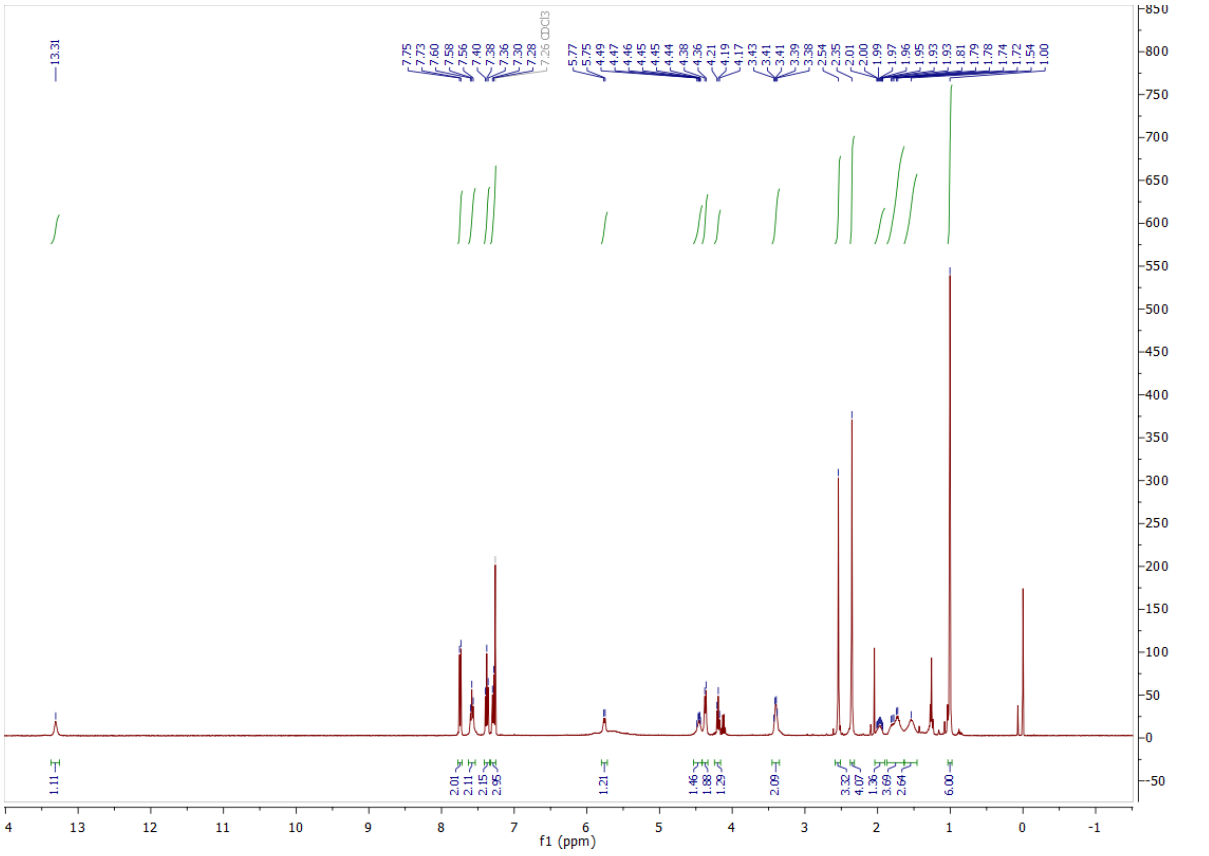
13.31
7.75
7.73
7.60
7.58
7.56
7.40
7.38
7.36
7.30
7.28
CDCl3
5.77
5.75
4.49
4.47
4.46
4.45
4.45
4.44
4.38
4.36
4.21
4.19
4.17
3.43
3.41
3.39
3.38
2.54
2.35
2.01
2.00
1.99
1.97
1.96
1.95
1.93
1.93
1.81
1.79
1.78
1.74
1.72
1.54
1.00
1.11
2.01
2.11
2.15
2.95
1.21
1.46
1.88
1.29
2.09
3.32
4.07
1.36
3.69
2.64
6.00
f1 (ppm)

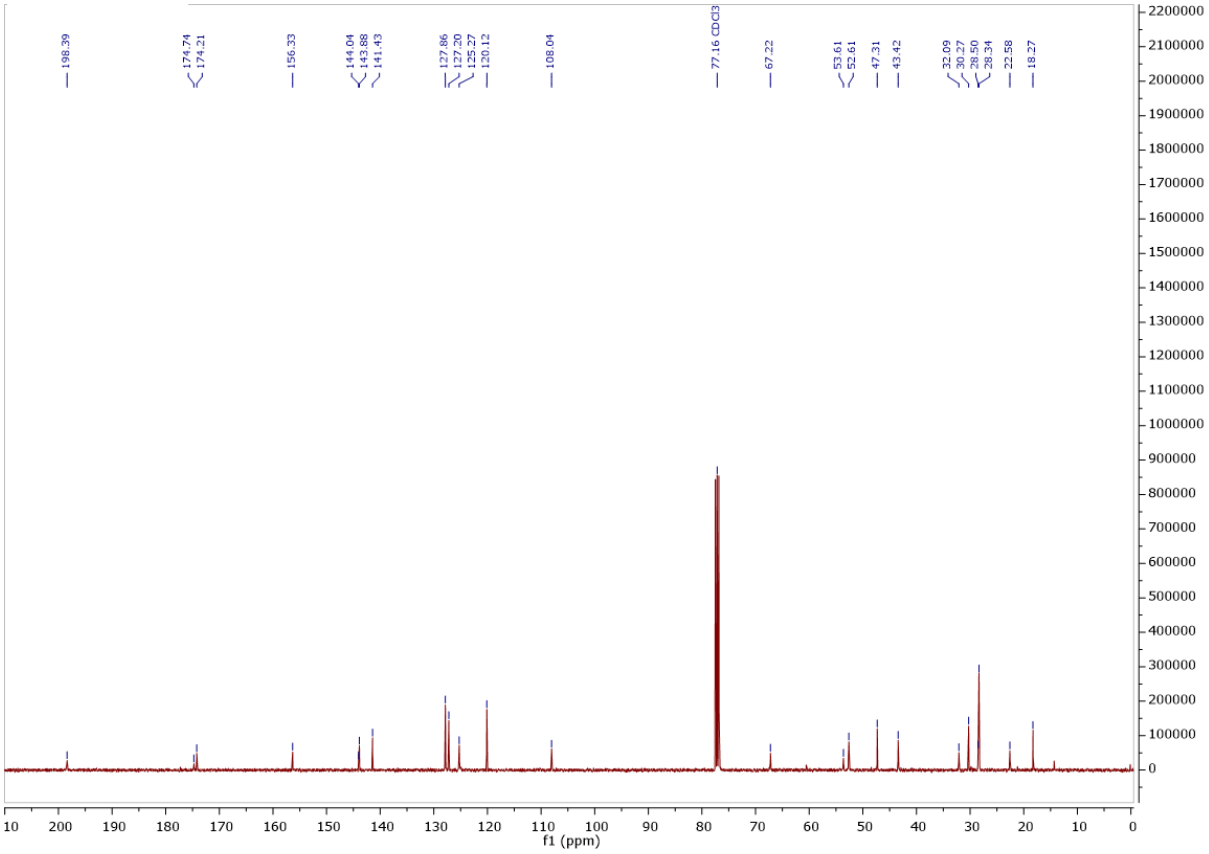
198.39
174.74
174.21
156.33
144.04
143.88
141.43
127.86
127.20
125.27
120.12
108.04
77.16
CDCl3
67.22
53.61
52.61
47.31
43.42
32.09
30.27
28.50
28.34
22.58
18.27
f1 (ppm)

5.3.2. Synthesis of 500 nm amino-functionalised cross-linked polystyrene NPs

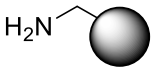

Washed styrene (5.5 mL) was mixed with AIBN (386 µmol), sonicating the mixture upon dissolution. Then, VBAH (371.7 µmol) and washed DVB (279 µmol) were added to the same vial containing styrene and AIBN, sonicating again upon obtaining a homogeneus mixture. Separatedly, PVP (50 mg, M_w = 29.000) was disolved in a purged mixture of EtOH:H_2O (90 mL), mixing with a mechanic stirrer upon dissolution in a the 90 mL reactor. Subsequently, the mixture of styrene, AIBN, DVB and VBAH was added to the reactor. The mixture was then sonicated for 5 min or upon homogeneus disolution. Afterward, the mixture was stirred with mechanical stirring for 1 h, at RT, at 10 rpm, under argon atmosphere for the first 5 min. Later, the mixture was heated up to 68 ºC, keeping the same conditions (10 rpm) for 4 h. After that time, the mixture was cooled for 30 min and then transferred to 15 mL Falcon tubes. NPs were collecting by centrifugation at 11,000*g* for 15 min at RT. Finally, supernatant was removed by washing with cycles of centrifugation-dispersion in MeOH (2 x 10 mL) and H_2O (2 x 10 mL), affording amino-functionalised cross-linked polystyrene NPs that were suspended in H_2O via sonication.

Size: 500 nm.

Loading: 58 µmol/g.

Solid content: 2%, 2 mg NPs in 100 µL of suspension.

5.3.3. Synthesis of 900-1200 nm amino-functionalised cross-linked polystyrene NPs

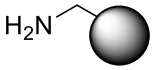

125 mL of H_2O were added to an Erlenrmeyer flask, under argon atmosphere, and then heated up to 80-90 ºC for 30 min, and cooled under argon atmosphere to RT. After that, 70 mL of this H_2O were transferred to the 90 mL reactor, under argon atmosphere. Subsequently, $MgSO_4$ (0.158 mmol) previously dissolved in argon purged H_2O were added to the reactor. Separatedly, in a vial, VBAH (1.56 mmol) and 5.5 mL of previously washed styrene (48 mmol) were dissolved by sonication. Thereupon, 140 µL of previouly washed DVB (983 µmol) and the VBAH-styrene mixture were transferred to the reactor, adding 19

mL of purged H_2O. This addition was performed at RT, without stirring, and under argon atmosphere, for 30 min. After that, the mixture was heated up to 80 ºC with mechanical stirring at 10 rpm, when initiator V_{50} (258 µmol), previously dissolved in 1 mL of argon purged H_2O, was added. The mixture was stirred at 80 ºC, for 4 h, at 10 rpm and 9 rpm, under argon atmosphere, affording NPs of 900 nm and 1200 nm, respectively. After that time, the mixture was cooled for 30 min and then transferred to 15 mL Falcon tubes. NPs were collecting by centrifugation at 11,000*g* for 15 min at RT. Finally, supernatant was removed by washing with cycles of centrifugation-dispersion in MeOH (2 x 10 mL) and H_2O (2 x 10 mL), affording amino-functionalised cross-linked polystyrene NPs that were suspended in H_2O via sonication.

Size: 900 nm – 1200 nm.

Loading: 70 µmol/g – 35 µmol/g.

Solid content: 2.5% – 4% , 2 mg NPs in 100 µL of suspension.

5.3.4. Non-fluorescent NPs

5.3.4.1. Synthesis of PEGlyated NPs

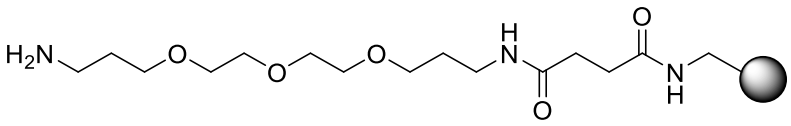

To synthesise **H_2N-PEG-NP_{500}**, 500-nm NPs (loading: 58 µmol/g, solid content: 2%) were used. These NPs were first conditioned by washing them three times with 1 mL of DMF each time through suspension-centrifugation (13,400 rpm, 3 min) cycles. Next, to conjugate a polyethylene glycol (PEG) spacer to the NPs, fluorenylmethyloxycarbonyl-4,7,10-trioxa-1,13-tridecanediamine succinic acid (Fmoc–PEG–OH) (75 eq.) was dissolved in DMF (1 mL) with OxymaPure (75 eq.) and DIC (75 eq.). The mixture was stirred at room temperature for 10 min. Then, the solution was added to the dry NPs, and the suspension was stirred at 60 °C and 1,400 rpm for 2 h. Subsequently, the NPs were washed with three cycles of suspension-centrifugation (13,400 rpm, 3 min) to obtain Fmoc-PEGylated NPs. Fmoc group was removed using a 20% piperidine/DMF solution (3 x 20 min) and sequential washing steps, as described above.

5.3.4.2. Synthesis of Glycine NPs

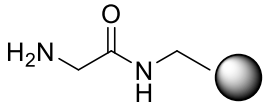

To synthesise **H_2N-Gly-NP_{500}**, 500-nm NPs (loading: 58 µmol/g, solid content: 2%) were used. These NPs were first conditioned by washing them three times with 1 mL of DMF each time through suspension-centrifugation (13,400 rpm, 3 min) cycles. Next, to conjugate a glycine spacer to the NPs, fluorenylmethyloxycarbonyl-Glycine (Fmoc–Gly–OH) (75 eq.) was dissolved in DMF (1 mL) with OxymaPure (75 eq.) and DIC (75 eq.). The mixture was stirred at room temperature for 10 min. Then, the solution was added to the dry NPs, and the suspension was stirred at 60 °C and 1,400 rpm for 2 h. Subsequently, the NPs were washed with three cycles of suspension-centrifugation (13,400 rpm, 3 min) to obtain Fmoc-Gly NPs. Fmoc group was removed using a 20% piperidine/DMF solution (3 x 20 min) and sequential washing steps, as described above.

5.3.5. Fluorescently-decorated NPs

5.3.5.1. Synthesis of Sulfo-Cy5-coupled NPs

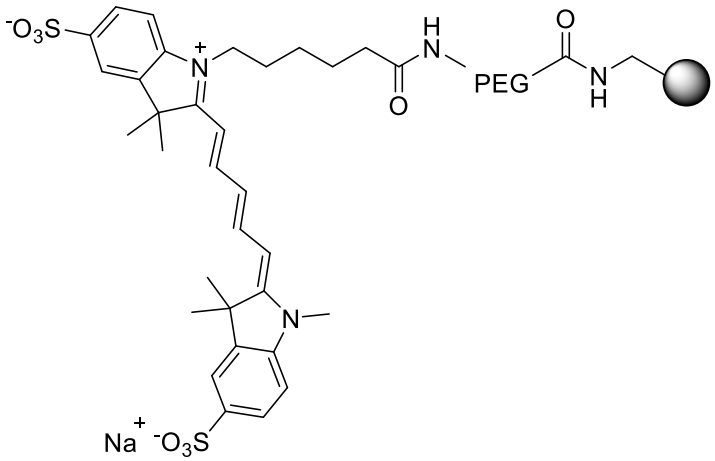

To synthesise sulfo-cyanine 5 **(sulfo-Cy5)-coupled NPs**, 500-nm NPs (loading: 58 µmol/g, solid content: 2%) were used. These NPs were first conditioned by washing them three times with 1 mL of DMF each time, through suspension-centrifugation (13,400 rpm, 3 min) cycles. Next, to conjugate a polyethylene glycol (PEG) spacer to the NPs, fluorenylmethyloxycarbonyl-4,7,10-trioxa-1,13-tridecanediamine succinic acid (Fmoc–PEG–OH) (75 eq.) was dissolved in DMF (1 mL) with OxymaPure (75 eq.) and DIC (75 eq.). The mixture was stirred at room temperature for 10 minutes. Then, the solution was added to the dry NPs, and the suspension was stirred at 60 °C and 1,400 rpm for 2 h. Subsequently, the

NPs were washed with three cycles of suspension-centrifugation (13,400 rpm, 3 min) to obtain Fmoc-PEGylated NPs. Fmoc group was removed using a 20% piperidine/DMF solution (3 x 20 min) and sequential washing steps, as described above. These two steps were repeated *n* times to incorporate *n* PEG spacer units as desired.

Four different sets of Sulfo-Cy5-coupled NPs were synthesised with decreasing concentrations of the fluorophore (Sulfo-Cy5 NHS ester) from a stock solution in DMF (1 mg/mL, 1.313 mM). The different sets were prepared with solutions of the dye at concentrations of 0.1 mg/mL (1.3 x 10^{-4} M), 0.01 mg/mL (1.3 x 10^{-5} M), 0.001 mg/mL (1.3 x 10^{-6} M), and 0.0001 mg/mL (1.3 x 10^{-7} M). Then, 1 mL of each sulfo-Cy5 NHS ester solution was mixed separately with 2 µL of DIPEA, and the mixtures were added to the corresponding dry PEGylated NPs and suspended. The suspensions were stirred at RT at 1,000 rpm for 14 h in the dark. The following day, the NPs were washed with three cycles of suspension-centrifugation with DMF (13,400 rpm, 3 min), MeOH (13,400 rpm, 5 min) and H_2O (13,400 rpm, 8 min), before finally being suspended in H_2O.

5.3.5.2. Synthesis of Fmoc-Lys(Cy5)-NPs

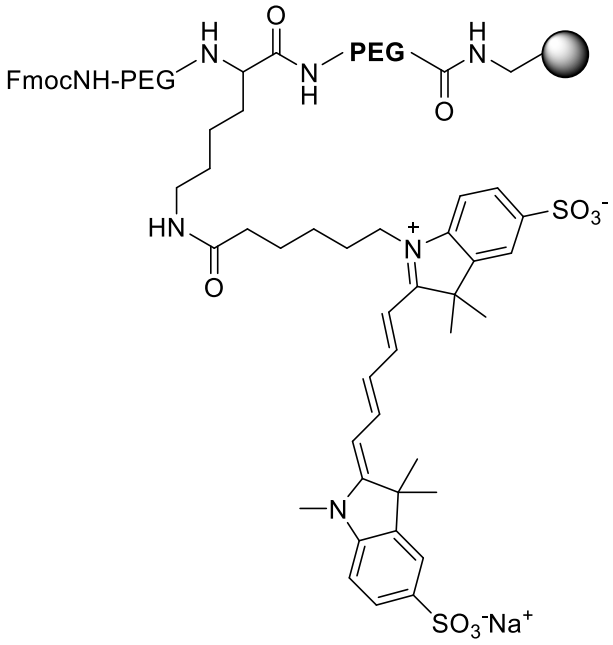

Two Fmoc-Lys(Cy5) NPs, with different polystyrene NPs sizes were synthesised: **Fmoc-Lys(Cy5)-NP$_{500}$** and **Fmoc-Lys(Cy5)-NP$_{900}$**.

To synthesise **Fmoc-Lys(Cy5)-NP$_{500}$**, 460-nm NPs (loading: 64 µmol/g, solid content: 2.5%) were used; and for **Fmoc-Lys(Cy5)-NP$_{900}$**, 900-nm NPs (loading: 70 µmol/g, solid content: 3.3%) were used. These NPs were first conditioned by washing them three times with 1 mL of DMF through suspension-centrifugation (13,400 rpm, 3 min) cycles. Next, to

conjugate the PEG spacer to the NPs, Fmoc–PEG–OH (50 eq.) was dissolved in DMF (1 mL) with OxymaPure (50 eq.) and DIC (50 eq.). The mixture was stirred at RT for 10 min. Then, the solution was added to the dry NPs, and the suspension was left to stir at 60 °C and 1,400 rpm for 2 h. Subsequently, the NPs were washed with three cycles of suspension-centrifugation (13,400 rpm, 3 min) to obtain Fmoc-PEGylated NPs. Fmoc group was removed using a 20% piperidine/DMF solution (3 x 20 min) and sequential washing steps, as described previously.

In the next step, NH_2-PEGlylated NPs were added to a mixture of Fmoc-Lysine-Dde(OH) (50 eq.), OxymaPure (50 eq.) and DIC (50 eq.), previously stirred for 10 min at RT, and suspended. The suspension was stirred at 60 °C and 1,400 rpm for 2 h. Subsequently, the NPs were washed with three cycles of suspension-centrifugation (13,400 rpm, 3 min) to obtain Fmoc-Lysine-Dde-PEGylated NPs. Fmoc group was removed using a 20% piperidine/DMF solution (3 x 20 min) and sequential washing steps, as described previously. Then, a mixture of Fmoc–PEG–OH (50 eq.), OxymaPure (50 eq.) and DIC (50 eq.), previously stirred for 10 min at RT, was added to the NH_2-Lysine-Dde-PEGylated NPs, and the suspension was stirred at 60 °C and 1,400 rpm for 2 h. Afterwards, the NPs were washed by three cycles of suspension-centrifugation (13,400 rpm, 3 min) to obtain Fmoc-PEG-Lysine-Dde-PEGylated NPs.

The Dde protecting group was then removed by treating the NPs with hydroxylamine HCl (0.4 mmol) and imidazole (0.3 mmol) in a mixture of NMP and DMF (4:1) [204], to obtain Fmoc-PEG-Lysine(NH_2)-PEGylated NPs. Subsequently, the NPs were washed with three cycles of suspension-centrifugation (13,400 rpm, 3 min). Then a sulfo-Cy5 NHS ester solution (0.1 mg/mL, 1.313 mM concentration) was mixed separately with 2 µL of DIPEA and added to the dry Fmoc-PEG-Lysine(NH_2)-PEGylated NPs. The particles were suspended and then stirred at RT at 1,400 rpm for 14 h in the dark. Finally, the **Fmoc-Lys(Cy5)-NP_{500}** and **Fmoc-Lys(Cy5)-NP_{900}** were washed with three cycles of suspension-centrifugation with DMF (13,400 rpm, 3 min), MeOH (13,400 rpm, 5 min) and H_2O (13,400 rpm, 8 min), before finally being suspended in H_2O.

5.3.5.3. Synthesis of Strp-Lys(Cy5)-NPs

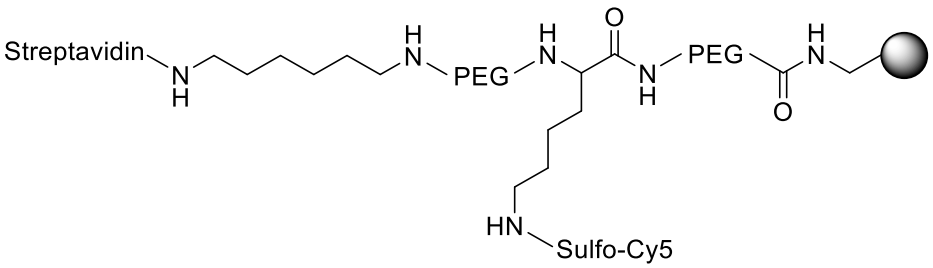

To synthesise **Strp-Lys(Cy5) NPs**, 1,200-nm NPs (loading: 35 µmol/g, solid content: 4%) were used. The NPs were first conditioned by washing them three times with 1 mL of DMF through suspension-centrifugation (13,400 rpm, 3 min) cycles. Next, to conjugate the PEG spacer to the NPs, Fmoc–PEG–OH (50 eq.) was dissolved in DMF (1 mL) with OxymaPure (50 eq.) and DIC (50 eq.). The mixture was stirred at RT for 10 min. Then, the solution was added to the dry NPs, and the suspension was left to stir at 60 °C and 1,400 rpm for 2 h. Subsequently, the NPs were washed with three cycles of suspension-centrifugation (13,400 rpm, 3 min) to obtain Fmoc-PEGylated NPs. Fmoc group was removed using a 20% piperidine/DMF solution (3 x 20 min) and sequential washing steps, as described previously.

In the next step, NH_2-PEGlylated NPs were added to a mixture of Fmoc-Lysine-Dde(OH) (50 eq.), OxymaPure (50 eq.) and DIC (50 eq.), previously stirred for 10 min at RT, and suspended. The suspension was stirred at 60 °C and 1,400 rpm for 2 h. Subsequently, the NPs were washed with three cycles of suspension-centrifugation (13,400 rpm, 3 min) to obtain Fmoc-Lysine-Dde-PEGylated NPs. Fmoc group was removed using a 20% piperidine/DMF solution (3 x 20 min) and sequential washing steps, as described previously. Then, a mixture of Fmoc–PEG–OH (50 eq.), OxymaPure (50 eq.) and DIC (50 eq.), previously stirred for 10 min at RT, was added to the NH_2-Lysine-Dde-PEGylated NPs, and the suspension was stirred at 60 °C and 1,400 rpm for 2 h. Afterwards, the NPs were washed by three cycles of suspension-centrifugation (13,400 rpm, 3 min) to obtain Fmoc-PEG-Lysine-Dde-PEGylated NPs.

The Dde protecting group was then removed by treating the NPs with hydroxylamine HCl (0.4 mmol) and imidazole (0.3 mmol) in a mixture of NMP and DMF (4:1) [204], to obtain Fmoc-PEG-Lysine(NH_2)-PEGylated NPs. Subsequently, the NPs were washed with three cycles of suspension-centrifugation (13,400 rpm, 3 min). Then a sulfo-Cy5 NHS ester solution (0.1 mg/mL, 1.313 mM concentration) was mixed separately with 2 µL of DIPEA and added to the dry Fmoc-PEG-Lysine(NH_2)-PEGylated NPs. The particles were suspended and then stirred at RT at 1,400 rpm for 14 h in the dark, to obtain Fmoc-PEG-Lysine(Cy5)-PEGylated NPs. Subsequently, the NPs were washed with three cycles of suspension-

centrifugation (13,400 rpm, 3 min). Afterwards, Fmoc group deprotection step was carried out by using a 20% piperidine/DMF solution (3 x 20 min) and sequential washing steps, as described previously. Next, the NPs were washed with sequential suspension-centrifugation cycles with PBS (pH 7.4), NaOH (500 mM), and H_2O, before the NPs were finally suspended in a 25% (v/v) glutaraldehyde solution in water. The suspension was shaken at 1,000 rpm at RT for 15 h. Subsequently, the NPs were washed with sequential suspension-centrifugation cycles with PBS (pH 7.4), and a 1 mg/mL Streptavidin solution in PBS, before mixing at RT at 1,000 rpm for 15 h. The NPs were then washed with two cycles of suspension-centrifugation with PBS (pH 7.4). Next, the NPs were suspended in a 20 mM solution of $NaBH_3CN$ in PBS:EtOH (3:1), and the mixture was shaken at 1,000 rpm for 2 h at RT. The reaction was stopped by adding a quenching solution (40 mM ethanolamine in 1% BSA solution in PBS), after a washing suspension-centrifugation step with PBS (pH 7.4). The suspension was quickly centrifuged, and the NPs were washed with three cycles of suspension-centrifugation with PBS (pH 7.4) to afford **Strp-Lys(Cy5) NPs**, before being finally suspended in PBS (pH 7.4).

5.3.5.4. Synthesis of ATTO 647N-coupled NPs

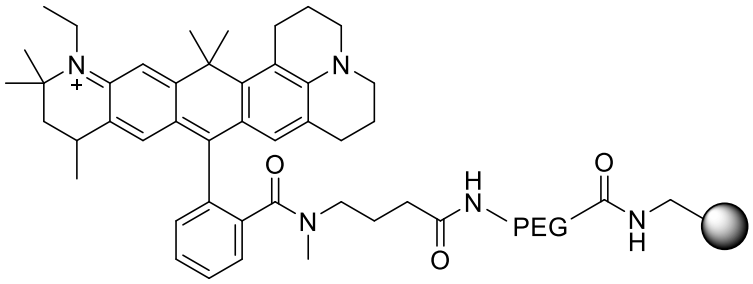

To synthesise **Atto 647N (A647)-coupled NP_{500}**, 500-nm NPs (loading: 58 µmol/g, solid content: 2%) were used. These NPs were first conditioned by washing them three times with 1 mL of DMF each time through suspension-centrifugation (13,400 rpm, 3 min) cycles. Next, to conjugate the PEG spacer to the NPs, Fmoc–PEG–OH (75 eq.) was dissolved in DMF (1 mL) with OxymaPure (75 eq.) and DIC (75 eq.). The mixture was stirred at RT for 10 min. Then, the solution was added to the dry NPs, and the suspension was left to stir at 1,400 rpm at 60 °C for 2 h. Subsequently, the NPs were washed with three successive suspension-centrifugation cycles (13,400 rpm, 3 min) to obtain Fmoc-PEGylated NPs. Fmoc group was removed by treating the NPs with a 20% piperidine/DMF solution (3 x 20 min) and sequential washing steps, as described above.

Four different sets of A647-coupled NPs were synthesised with decreasing concentrations of the fluorophore (Atto 647N NHS ester) from a stock solution in DMF (1 mg/mL, 1.313 mM). The different sets were prepared with solutions of the dye at

concentrations of 0.1 mg/mL (1.3 x 10^{-4} M), 0.01 mg/mL (1.3 x 10^{-5} M), 0.001 mg/mL (1.3 x 10^{-6} M), and 0.0001 mg/mL (1.3 x 10^{-7} M). To afford A647-coupled NPs, 1 mL of each Atto 647N NHS ester solution (0.1 mg/mL, 1.2 mM) were mixed separately with 2 µL of DIPEA and then added to the dry PEGylated NPs, and suspended. The suspensions were stirred at 1,000 rpm at RT for 14 h in the dark. The following day, the NPs were washed with three successive suspension-centrifugation cycles with DMF (13,400 rpm, 3 min), MeOH (13,400 rpm, 5 min), and H_2O (13,400 rpm, 8 min), before finally being suspended in H_2O.

5.3.5.5. Synthesis of Fmoc-Lys(A647)-NPs

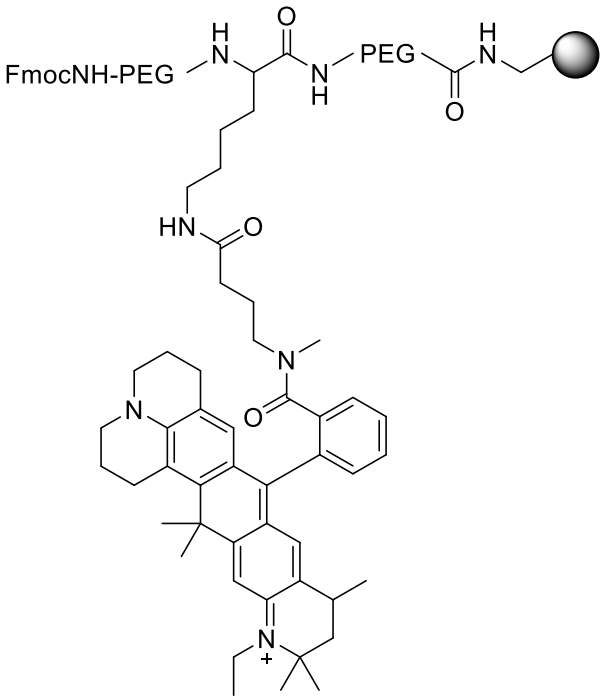

Three Fmoc-Lys(A647) NPs, with different polystyrene particles sizes were synthesised: **Fmoc-Lys(A647)-NP$_{900}$**, **Fmoc-Lys(A647)-NP$_{2500}$** and **Fmoc-Lys(A647)-NP$_{5000}$**. For the last two particles, commercially available crosslinked-polystyrene particles were employed.

To synthesise **Fmoc-Lys(A647)-NP$_{900}$**, 900-nm NPs (loading: 64 µmol/g, solid content: 2.5%) were used; for **Fmoc-Lys(A647)-NP$_{2500}$**, 2.48-µm particles (loading: 42.6 µmol/g, solid content: 1%) were used; and for **Fmoc-Lys(A647)-NP$_{5000}$**, 5 µm particles (loading: ~0.8 mmol/g, solid content: 4%) were used. These particles were first conditioned by washing them three times with 1 mL of DMF through suspension-centrifugation (13,400 rpm, 3 min) cycles. Next, to conjugate the PEG spacer to the particles, Fmoc–PEG–OH (50 eq.) was dissolved in DMF (1 mL) with OxymaPure (50 eq.) and DIC (50 eq.). The mixture was stirred at RT for 10 min. Then, the solution was added to the dry particles, and the suspension was left to stir at 60 °C and 1,400 rpm for 2 h. Subsequently, the particles were washed with three

cycles of suspension-centrifugation (13,400 rpm, 3 min) to obtain Fmoc-PEGylated NPs. Fmoc group was removed using a 20% piperidine/DMF solution (3 x 20 min) and sequential washing steps, as described previously.

In the next step, NH_2-PEGlylated NPs were added to a mixture of Fmoc-Lysine-Dde(OH) (50 eq.), OxymaPure (50 eq.) and DIC (50 eq.), previously stirred for 10 min at RT, and suspended. The suspension was stirred at 60 °C and 1,400 rpm for 2 h. Subsequently, the particles were washed with three cycles of suspension-centrifugation (13,400 rpm, 3 min) to obtain Fmoc-Lysine-Dde-PEGylated NPs. Fmoc group was removed using a 20% piperidine/DMF solution (3 x 20 min) and sequential washing steps, as described previously. Then, a mixture of Fmoc–PEG–OH (50 eq.), OxymaPure (50 eq.) and DIC (50 eq.), previously stirred for 10 min at RT, was added to the NH_2-Lysine-Dde-PEGylated NPs, and the suspension was stirred at 60 °C and 1,400 rpm for 2 h. Afterwards, the particles were washed by three cycles of suspension-centrifugation (13,400 rpm, 3 min) to obtain Fmoc-PEG-Lysine-Dde-PEGylated NPs.

The Dde protecting group was then removed by treating the particles with hydroxylamine HCl (0.4 mmol) and imidazole (0.3 mmol) in a mixture of NMP and DMF (4:1) [204] to obtain Fmoc-PEG-Lysine(NH_2)-PEGylated NPs. Subsequently, the particles were washed with three cycles of suspension-centrifugation (13,400 rpm, 3 min). Then an ATTO 647N NHS ester solution (0.1 mg/mL, 1.313 mM concentration) was mixed separately with 2 µL of DIPEA and added to the dry Fmoc-PEG-Lysine(NH_2)-PEGylated NPs. The particles were suspended and then stirred at RT at 1,400 rpm for 14 h in the dark. Finally, the **Fmoc-Lys(A647)-NP$_{900}$**, **Fmoc-Lys(A647)-NP$_{1200}$** and **Fmoc-Lys(A647)-NP$_{5000}$** were washed with three cycles of suspension-centrifugation with DMF (13,400 rpm, 3 min), MeOH (13,400 rpm, 5 min) and H_2O (13,400 rpm, 8 min), before finally being suspended in H_2O.

5.3.6. Metallofluorescent NPs

5.3.6.1. Synthesis of (Pd^{2+}, Cu^{+}, Ni^{2+})-Sulfo-Cy5-coupled NPs

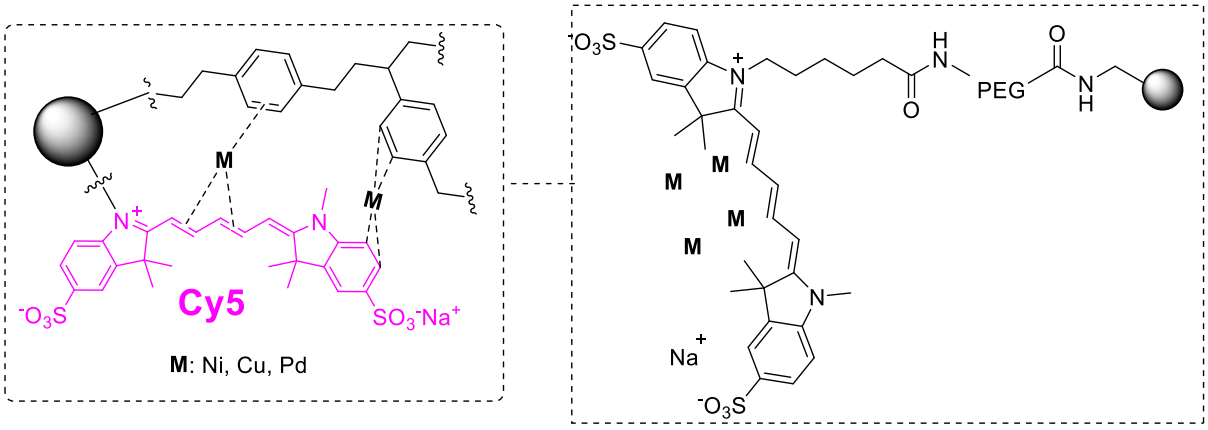

To synthesise **M^{+}-Sulfo-Cy5-coupled NP_{500}** using Pd^{2+}, Cu^{+} and Ni^{2+} as metal ions (M^{+}), 460-nm NPs (loading: 64 µmol/g, solid content: 2.5%) were used. The NPs were first conditioned by washing them three times with 1 mL of DMF each time through suspension-centrifugation (13,400 rpm, 3 min) cycles. Next, to conjugate the PEG spacer to the NPs, Fmoc–PEG–OH (75 eq.) was dissolved in DMF (1 mL) with OxymaPure (75 eq.) and DIC (75 eq.). The mixture was stirred at RT for 10 min. Then, the solution was added to the dry NPs, and the suspension was left to stir at 1,400 rpm at 60 °C for 2 h. Subsequently, the NPs were washed with three successive suspension-centrifugation cycles (13,400 rpm, 3 min) to obtain Fmoc-PEGylated NPs. Fmoc group was removed using a 20% piperidine/DMF solution (3 x 20 min) and sequential washing steps, as described above.

Next, 1 mL of a sulfo-Cy5 NHS ester solution (0.1 mg/mL, 1.313 mM) was mixed separately with 2 µL of DIPEA before being added to the dry PEGylated NPs, which were then suspended. The suspension was stirred at 1,000 rpm at RT for 14 h in the dark. Afterwards, the NPs were washed with three cycles of suspension-centrifugation with DMF (13,400 rpm, 3 min). Next, 100 µL of a 10 mM metal ion solution ($Pd(OAc)_2$, $NiCl_2$ or CuBr) in DMF was added to the dry nanoparticels, and they were stirred at 1,000 rpm at RT for 14 h in the dark. Upon completion of the reaction, the NPs were washed with three successive suspension-centrifugation cycles with DMF (13,400 rpm, 3 min), MeOH (13,400 rpm, 5 min) and H_2O (13,400 rpm, 8 min), before finally being suspended in H_2O.

5.3.6.2. Synthesis of Pd^0-Sulfo-Cy5 NPs

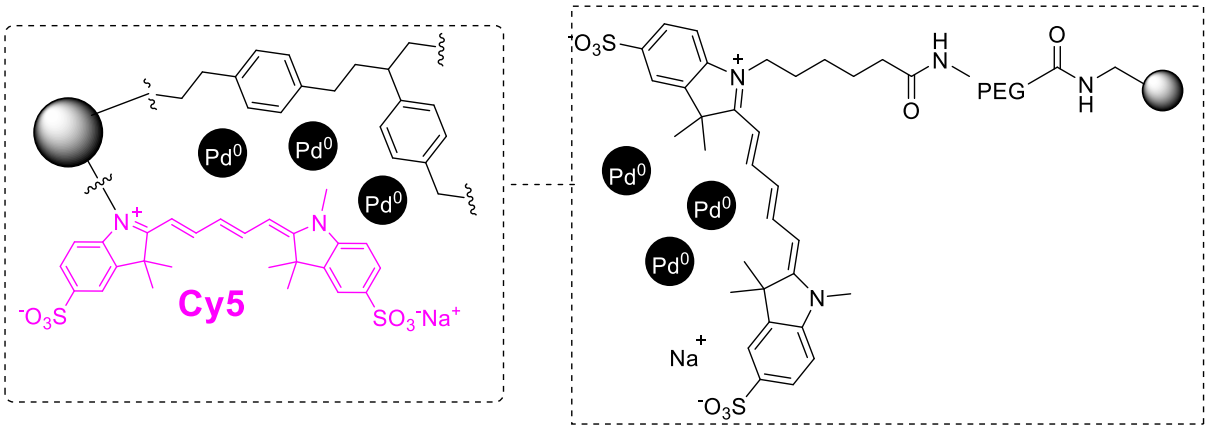

To obtain **Pd^0-Sulfo-Cy5-NP_{500}**, the ionic Pd^{2+} contained in Pd^{2+}-Sulfo-Cy5 NPs was *in situ* reduced to Pd^0 by adding a 10% Hydrazine (55% w/v) in MeOH solution [181]. The reaction mixture was left to stir at RT for 30 min. The NPs were then washed with three suspension-centrifugation cycles with MeOH (13,400 rpm, 5 min) and H_2O (13,400 rpm, 8 min), before finally being suspended in H_2O.

5.3.6.3. Synthesis of Pd-isotopes-Sulfo-Cy5 NPs

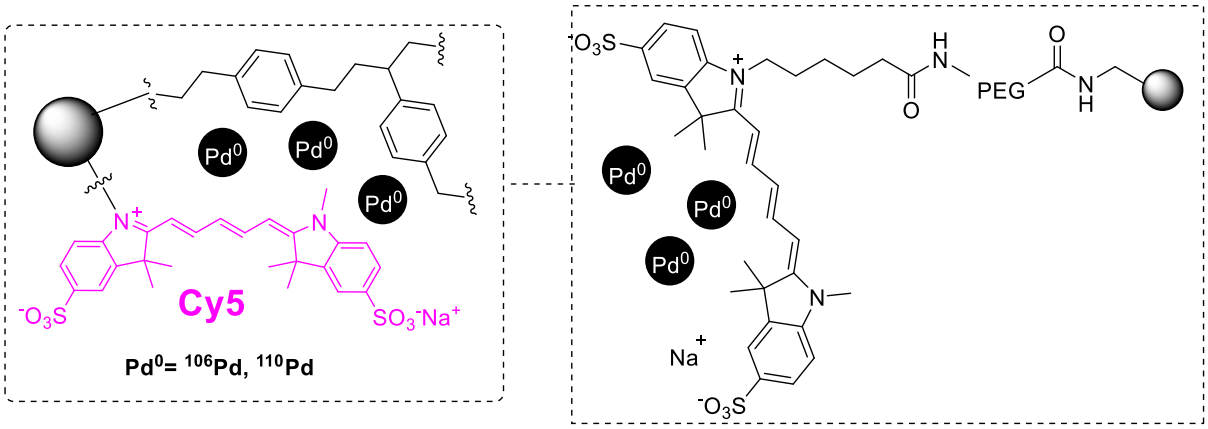

Several types of Pd-isotopes-Sulfo-Cy5 NPs were synthesised: **^{106}Pd-Sulfo-Cy5-NP_{500}** and **^{110}Pd-Sulfo-Cy5-NP_{500}**.

To synthesise **^{106}Pd-Sulfo-Cy5-NP_{500}** and **^{110}Pd-Sulfo-Cy5-NP_{500}**, 500-nm NPs (loading: 64 µmol/g, solid content: 2.5%) were used. The NPs were first conditioned by washing them three times with 1 mL of DMF each time through suspension-centrifugation (13,400 rpm, 3 min) cycles. Next, to conjugate the PEG spacer to the NPs, Fmoc–PEG–OH (75 eq.) was dissolved in DMF (1 mL) with OxymaPure (75 eq.) and DIC (75 eq.). The mixture was stirred at RT for 10 min. Then, the solution was added to the dry NPs, and the suspension was left

to stir at 1,400 rpm at 60 °C for 2 h. Subsequently, the NPs were washed with three successive suspension-centrifugation cycles (13,400 rpm, 3 min) to obtain Fmoc-PEGylated NPs. Fmoc group was removed using a 20% piperidine/DMF solution (3 x 20 min) and sequential washing steps, as described above.

Next, 1 mL of a sulfo-Cy5 NHS ester solution (0.1 mg/mL, 1.313 mM) was mixed separately with 2 µL of DIPEA before being added to the dry PEGylated NPs, which were then suspended. The suspension was stirred at 1,000 rpm at RT for 14 h in the dark. Afterwards, the NPs were washed with three cycles of suspension-centrifugation with DMF (13,400 rpm, 3 min), MeOH (13,400 rpm, 5 min) and H_2O (13,400 rpm, 8 min). Next, a 1 mM $^{106}Pd(NO_3)_2$ or $^{110}Pd(NO_3)_2$ solution in H_2O was added to the dry NPs, and they were stirred at 1,000 rpm at RT for 14 h in the dark. Upon completion of the reaction, the NPs were washed with three cycles of suspension-centrifugation with H_2O (13,400 rpm, 8 min) and MeOH (13,400 rpm, 5 min). Afterwards, Pd^{2+} isotopes contained in the NPs were *in situ* reduced to Pd^0 by adding a 10% Hydrazine (55% w/v) in MeOH solution. The reaction mixture was left to stir at RT for 30 min. The NPs were then washed with three suspension-centrifugation cycles with MeOH (13,400 rpm, 5 min) and H_2O (13,400 rpm, 8 min), before finally being suspended in H_2O.

5.3.7. NPs characterisation

5.3.7.1. FACS

The fluorescent emission of the particles carrying red dyes (either Cy5 or A647) was assessed using flow cytometry analysis with a BD FACSCanto II (Becton Dickinson & Co., NJ, USA) equipped with a solid-state Coherent Sapphire blue laser refrigerated by air (488 nm and 20 mW power), a JDS Uniphase HeNe red laser (633 nm and 17 mW) and eight detectors (six fluorescence detectors and two morphologic parameters). The emission fluorescence was detected in the APC channel (660/20-nm) and FITC channel (530/30-nm). To analyse the samples, 2 µL of the NPs were transferred to Flow Cytometry tubes containing 200 µL of PBS. Then, the suspension was sonicated for 5 s before being uploaded into the BD FACSCanto II.

5.3.7.2. XPS

Palladium presence was determined by monitoring the profile of Pd 3d photoemission. XPS spectra were obtained using a Kratos Axis Ultra-DLD X-ray photoelectron spectrometer equipped with an Al monochromatic X-ray source, over powdered nanoparticle samples. General spectra were obtained with a pass energy of 160 eV, the X-ray source was operated at 75 W, the high-resolution spectra were obtained with a pass energy of 20 eV and the X-

ray source was operated at 225 W. To analyse the samples, 5 µL of NPs suspended in MeOH were added onto a slide and dried at RT. Then, the slide was given to the lab technician at the Centro de Instrumentación Científica (CIC) at the University of Granada.

5.3.7.3. Fluorogenic chemical reaction

The effective reduction of Pd^{2+} to Pd^{0} within the NPs was performed by probing the catalytic activity of these particles, using a reaction catalysed by Pd^{0}, i.e., removing allyloxycarbonyl protecting groups [181],[182]. The non-fluorescent bis-allyloxycarbonyl rhodamine is transformed into fluorescent rhodamine dye once the protecting groups are removed. For that, NPs are suspended in a solution of bis-allyloxycarbonyl rhodamine 110 in PBS pH 7.4 and incubated for 1 h, at RT. Subsequently, fluorescence is analysed.

5.3.7.4. HRTEM-EDX

Transmission electron microscopy experiments were carried out using an ultra-high-resolution FEI Titan G2 microscope with an XFEG Field Emission Gun operating at 300 kV. The microscope was fitted with a high-angle annular dark field (HAADF) detector to operate in scanning transmission electron microscopy (STEM) mode and with an FEI microanalysis system for EDX. The microscope reached maximum resolutions of 0.8 Å in TEM mode and 2 Å in STEM mode. To analyse the samples, 5 µL of the NPs were suspended in 1 mL of absolute EtOH and supported on Ultra-Thin Carbon 200 mesh Cu grids, except for the NPs carrying Cu, which were supported on Ultra-Thin Carbon 200 mesh Au grids.

5.3.7.5. HRSEM

SEM experiments were carried out in a Field Electron Scanning Microscope (FESEM) Zeiss SUPRA40VP, equipped with an EDX Microanalysis System with a high surface X-Max 50 mm detector, and with STEM mode. To analyse the sample, there were used the same platform that was used for HRTEM-EDX.

5.3.7.6. CyTOF

Mass cytometry analysis was performed using a Helios updated CyTOF2 (DVS Sciences, Fluidigm Co., CA, USA). This instrument used an inductively coupled plasma time-of-flight mass spectrometer (ICP-TOF-MS) to detect a mass range of 75-209 amu in 135 different channels at an average event rate of 500 events/s, a highest rate of 2,000 events/s, and a sensitivity of 0.3% for ^{159}Tb. To analyse the samples, 2 µL of the NPs were diluted in EQ Four Elements Calibration Beads solution (Fluidigm) prior to loading them into the Helios updated CyTOF®2.

5.3.8. Metallofluorescent NPs and live cells uptake

5.3.8.1. Cell viability

For viability assays, MDA-MB-231 cell line was used. To assess whether the metallofluorescent NPs were toxic for the cells, 3,000 cells/well were seeded in a 96-well plates and left overnight to stabilise. The stabilised cells were then nanofected with 20,000, 10,000, 5,000, 2,500, 1,250, 625, and 0 NP/cell with different metallofluorescent NPs, control fluorescent NPs and non-fluorescent NPs, in serum-free DMEM to avoid the formation of a protein corona. After 8 h, the serum concentration was restored to normal levels, and the cells were allowed to grow for 6 days. Viability/proliferation was measured by means of a MTT assay (550 nm with reference at 650 nm).

5.3.8.2. FACS

For flow cytometry assays, 5 x 10^5 MDA-MB-231 cells were seeded in 24-well plates and stabilised in an incubator for 18 h. Subsequently 2,000, 1,000, 500, 250, 125, and 0 **metallofluorescent NPs**/cell, **Sulfo-Cy5-coupled-NP$_{500}$**/cell or **PEGylated-NP$_{500}$**/cell were incubated for 8 h in serum-free DMEM to evaluate cellular uptake. After washing with PBS, living cells were trypsinised for 5 min, washed twice with PBS, fixed with paraformaldehyde (2% v/v), washed again with PBS, and collected in a Flow Cytometer tubes. Cells were analysed by Flow Cytometry with a BD FACSCanto II flow cytometer.

5.3.8.3. Confocal Microscopy

For confocal microscopy experiments, 1.5 x 10^3 cells were seeded on poly-L-lysine (Sigma-Aldrich) pre-treated coverslips, stabilised overnight, and nanofected with 3,000 **Pd^0-Sulfo-Cy5-NP$_{500}$**/cell or 3,000 **Sulfo-Cy5-coupled-NP$_{500}$**/cell in duplicate. After 8 h, the coverslips were collected, washed twice in PBS, and mounted with Mowiol® mounting medium (Sigma-Aldrich) on a slide. The NPs in the fixed MDA-MB-231 cells were localised using a scanning confocal inverted microscope LSM 710 Axio Observer (Carl Zeiss, Jena, Germany). The images were acquired with a Plan-Apochromat 63×/1.4 OIL DIC M27 immersion objective and software ZEN 2010 (Carl Zeiss, Jena, Germany). Later, the images were processed with Software ZEN 2010 Black Edition. Confocal images of MDA-MB-231 cells nanofected with either **Sulfo-Cy5-coupled-NP$_{500}$** or **Pd^0-Sulfo-Cy5-coupled-NP$_{500}$** NPs were obtained using the following settings: 1) a 488-nm Argon excitation laser (25 mW) at 2% power, an emission bandpass of 493-599 nm, and a pinhole of 1.0 Airy Unit (0.8 µm optical section); and 2) a 633-nm HeNe excitation laser (5.0 mW) at 18% power, an emission wavelength range of 635-759 nm, and a pinhole of 1.0 Airy Unit (0.8 µm optical section).

5.3.8.4. Mass Cytometry

For Mass Cytrometry assays, 10^6 MDA-MB-231 cells were seeded in 6-well plates and stabilised for 18 h in an incubator. Subsequently, 1,000, 500, 250, 100, 50 and 0 **Pd^0-Sulfo-Cy5-coupled-NP_{500}**/cell were incubated for 8 h in serum-free DMEM. After washing them with PBS, living cells were trypsinised for 5 min, washed twice with PBS (5 min, 450*g*), and collected in a Flow Cytometry tube. Subsequently, cells were incubated with 330 µL of Cell-ID™ Intercalator-Ir (125 µM) into MaxPar® Fix and Perm Buffer (dilution 1:1,000) at 4 °C overnight to identify nucleated cells by CyToF® analysis. After two washing steps with 660 µL MaxPar® Cell Staining Buffer, cells were washed twice with MaxPar® Water. The cell concentration was adjusted to 5 x 10^5 cells/mL with MaxPar® Water immediately prior to CyToF®2 data acquisition and filtered twice into cell strainer cap tubes. The data were acquired on CyToF®2 for a minimum time of 20 min. Results were analysed using the Cytobank Community online software (Cytobank Inc., CA, USA) and compared to the results of FlowJo analysis software. Thresholds were set according to negative controls (0 NPs/cell) to obtain percentages of palladium-particle containing cells.

5.3.9. Live cell barcoding

5.3.9.1. Viability Pd isotopes conjugated NPs

Cell viability was assessed by Resazurin assay. MDA-MB-231 cells were seeded in 96-wells plates at a density 3,000 cells/well. After 24h of cell culture stabilisation, different NPs suspensions (in medium) at the desired concentrations are added to the cells. After 72 h of incubation, 100 µL of medium are removed from the wells and 100 µL of fresh medium are added again to the plates prior to adding 20 µL of a solution of resazurin 0.5 mM (5 µL of resazurin 0.1 M in 25 mL of medium) to the wells, in darkness. Afterwards, the 96-wells plates are wrapped in foiled and incubated at 37 ºC within 2 and 4 h. Thereupon, viability of the cells are measured in GloMax®-Multi Detection System recording the fluorescence emission with a 580-640 nm filter.

5.3.9.2. Pd isotopes conjugated NPs MNF50

Cell uptake of Pd isotopes conjugated NPs was evaluated by FACS and CyTOF. For that, MDA-MB-231 cells were seeded in 24-wells plates at a density 50,000 cells/well. After 18 h of stabilisation, the cells are nanofected by adding a set of nanoparticle's suspensions (in medium) at the desired concentrations (50, 100, 250, 500, 750, 1,000, 2,500, 5,000, 7,500, and 10,0000 NPs/cell). The cells are incubated with the NPs for 3 h. Afterwards, the cells are trypsinised and then medium is added to neutralise the trypsine. Then, the cells are transferred to Flow Cytometer tubes and mixed with 2 mL of PBS prior their centrifugation at

450*g* for 5 min. The supernatant is discarded and 200 µL of 2% paraformaldehyde (PFA) are then added. After pipetting up and down, the cells suspension is incubated at room temperature for 10 min. Subsequently, 2 mL of PBS are added and the cells are centrifuged at 450*g* for 5 min. At last, the supernatant is partially discarded, resuspending the cells in the last drop and keeping the tubes at 4 ºC and protected from the light, upon FACS analysis.

When the MNF50 is assessed by CyTOF, 1 million MDA-MB-231 cells are seeded in 6-well plates, and a ratio of 50, 250, 500, 1,000, and 2,000 NPs/cell are used to nanofect the cells for 3 h. Then, it is followed the same procedure than in FACS until the last centrifugation, where instead of partially discarding the supernatant, it is totally discarded. After that, 330 µL of Fix and Perm Buffer containing 1 µL of Ir cell marker per mL of buffer, are added and mixed with the cells, letting it to incubate at 4 ºC for 14 h. After that, 660 µL of CSM are added and mixed with the cell suspension. Subsequently, the cells are centrifuged at 450*g* for 5 min, the supernatant is discarded and the cells are suspended in another 660 µL prior centrifuging at 450*g* for 5 min again. Afterwards, the supernatant is discarded and the cells are suspended in 660 µL of Maxpar® water and centrifuged at 450*g* for 5 min. At last, the supernatant is removed and the cells are suspended in 0.1X beads solution (Maxpar®) prior being analysed by CyTOF.

5.3.9.3. MDA-MB-231 dual cell barcoding and mixture analysis

MDA-MB-231 cells were seeded in 6-well plate at a density 1 x 10^6 cells/well and stabilised for 18 h. The next day, the plates were separated for the independent live cell barcoding, one set of cells were barcoded with **^{106}Pd-Cy5-NP** and the other set of cells with **^{110}Pd-Cy5-NP**. Thus, there were prepared two different suspensions of the aforementioned NPs (in medium), one containing each Pd-conjugated NPs, and the suspensions were added to corresponding set of cells at a ratio of 2,000 NPs/cell for 3 h, to afford MDA-MB-231 cells barcoded with **^{106}Pd** and MDA-MB-231 cells barcoded with **^{110}Pd**. Afterwards, the cells are trypsinised and then medium is added to neutralise the trypsine, to reach a final volume of 2 mL. Then, the barcoded cells are mixed in different proportions (100%-0%, 75%-25%, 50%-50%, 25%-75%, and 0%-100%) by adding the amount of barcoded cell suspensions into Flow Cytometer tubes, to obtain a final volume of 2 mL, accordingly to the desired percentage of each barcoded cell.

Subsequently, the mixture of barcoded cells is mixed with 2 mL of PBS prior their centrifugation at 450*g* for 5 min. The supernatant is discarded and 200 µL of 2% paraformaldehyde (PFA) are then added. After pipetting up and down, the cells suspension is incubated at room temperature for 10 min. Subsequently, 2 mL of PBS are added and the cells are centrifuged at 450*g* for 5 min, discarding the supernatant. After that, 330 µL of Fix

and Perm Buffer containing 1 µL of Ir cell marker per mL of buffer, are added and mixed with the cells, letting it to incubate at 4 ºC for 14 h. After that, 660 µL of CSM are added and mixed with the cell suspension. Subsequently, the cells are centrifuged at 450*g* for 5 min, the supernatant is discarded and the cells are suspended in another 660 µL of CSM prior centrifuging at 450*g* for 5 min again. Afterwards, the supernatant is discarded and the cells are suspended in 660 µL of Maxpar® water and centrifuged at 450*g* for 5 min. At last, the supernatant is removed and the cells are suspended in 0.1X beads solution (Maxpar®) prior being analysed by CyTOF.

5.3.9.4. Antibodies to metal-polymers conjugations

To conjugate the antibodies to metal-polymers, it was followed the protocol "Maxpar® Antibody Labeling Kit" from Fluidigm, but slightly modified in terms of centrifugation time, of centrifugation speed and buffer volumes. Conjugation times and amount of polymer, metal and antibodies were not changed.

5.3.9.5. Ovarian cancer barcoding

5.3.9.5.1 PoC

To perform live cell barcoding using metallofluorescent NPs two different Pd-isotopes-Sulfo-Cy5-NPs: **^{106}Pd-Sulfo-Cy5-coupled-NP$_{500}$** and **^{110}Pd-Sulfo-Cy5-coupled-NP$_{500}$** were synthesised. Besides, three ovarian cancer cell lines: **TYK-nu**, **Kuramochi** and **OVCAR-4** were used. The vast majority of these experiments were performed during my three month stay in Professor Nolan's group, at Stanford University (Stanford, CA, USA), under the direct supervision of Wendy Fantl, who kindly provided with the cells and isotopes-labelled antibodies needed.

For live cell barcoding, **^{106}Pd-Sulfo-Cy5-coupled-NP$_{500}$** and **^{110}Pd-Sulfo-Cy5-coupled-NP$_{500}$** were mixed to afford **$^{106\text{-}110}$Pd-Sulfo-Cy5-coupled-NP$_{500}$**. Firstly, TYK-nu, Kuramochi and OVCAR-4 were seeded in 6 well plates, 1.5 x 10^6 cells/well, and stabilised in an incubator for 18 h. Then, **^{106}Pd-Sulfo-Cy5-coupled-NP$_{500}$**, **^{110}Pd-Sulfo-Cy5-coupled-NP$_{500}$** and **$^{106\text{-}110}$Pd-Sulfo-Cy5-coupled-NP$_{500}$** were added to TYK-nu, Kuramochi and OVCAR-4 cell lines, respectively, at a reason of 1,500 NPs/cell. The NPs were incubated for 6 h. After that, the cells were washed with PBS, trypsinised for 8 min and complete medium was added. The cells were transferred to Flow Cytometry tubes, spun down (300*g* – 5 min) and washed once with serum-free RPMI. Then, the cells were resuspended in 1 mL of serum-free RPMI and 1 mL of a homemade 50 µM CisPlatin solution in serum-free RPMI was added for 1 min, subsequently, 2 mL of complete RPMI were added and the cells were spun down and washed once with serum-free RPMI. Then, the cells were resuspended again in 1 mL of

serum-free RPMI and were counted using a TC10™ Automated Cell Counter (Bio-Rad), assessing the viability with Trypan Blue. Afterwards, the cells were fixed using 100 µL of 16% PFA (10 min) and washed twice with 2.5x CSM (centrifugations at 4 ºC). Afterwards, the cells were washed twice with 2.5x CSM (centrifugations at 4ºC). At last, 1 mL of a solution containing Cell-ID™ Intercalator-Ir (1:5000 dilution) and 1.6% PFA in PBS was added to the cells, being incubated for 14 h at 4 ºC.

The cells were washed once with 2.5x CSM and twice with CyTOF water (centrifugations at 4 ºC) and counted on a TC10™ Automated Cell Counter. Then, CyTOF water was removed and the cells were resuspended in a homemade 1x Normalisation beads solution before loading them in a CyTOF®2 instrument [279]. Data were analysed using the Cytobank Community online software

5.3.9.5.2 Live cell barcoding

For live cell barcoding, **^{106}Pd-Sulfo-Cy5-coupled-NP$_{500}$** and **^{110}Pd-Sulfo-Cy5-coupled-NP$_{500}$** were mixed to afford **$^{106\text{-}110}$Pd-Sulfo-Cy5-coupled-NP$_{500}$**. Firstly, TYK-nu and OVCAR-4 were seeded in 6 well plates (8 replicates of TyK-nu and 16 of OVCAR-4), 1.5 x 10^6 cells/well, and stabilised in an incubator for 18 h. Then, **^{106}Pd-Sulfo-Cy5-coupled-NP$_{500}$** were added to TYK-nu cells, **^{110}Pd-Sulfo-Cy5-coupled-NP$_{500}$** were added to OVCAR-4 cells (8 replicates) and **$^{106\text{-}110}$Pd-Sulfo-Cy5-coupled-NP$_{500}$** were added to OVCAR-4 cells (8 replicates) as well, at a reason of 1,500 NPs/cell. Therefore, 3 different barcodes could be afforded, BC-1, BC-2, and BC-3, respectively.

NPs were incubated for 6 h. After that, the cells were washed with PBS, trypsinised for 8 min and complete medium was added. The cells were transferred to Flow Cytometry tubes, spun down (300*g* – 5 min) and washed once with serum-free RPMI. Then, the cells were resuspended in 1 mL of serum-free RPMI and 1 mL of a homemade 50 µM CisPlatin solution in serum-free RPMI was added for 1 min, subsequently, 2 mL of complete RPMI were added and the cells were spun down and washed once with serum-free RPMI. Then, the cells were resuspended again in 1 mL of serum-free RPMI and were counted using a TC10™ Automated Cell Counter (Bio-Rad), assessing the viability with Trypan Blue. Afterwards, the cells were fixed using 100 µL of 16% PFA (10 min) and washed twice with 2.5x CSM (centrifugations at 4 ºC). At last, the cells were kept at 4 ºC.

Subsequently, there were generated four pooled tubes containing a mixture of BC-1 TYK-nu, BC-2 OVCAR-4, and BC-3 OVCAR-4 cell lines (1:1:1), resulting in a total of 16 tubes (4 tubes of each barcoded cell and 4 tubes of a mixture of cells). 2.5x CSM was then removed from the tubes, leaving a residual volume of 50 µL. After that, 5 µL of Fc-Block™ solution

(BD Biosciences) was added to the cells for 10 min, at RT, without shaking. Subsequently, cell surface Ab staining was carried out by adding 45 µL of the Surface Ab-isotopes cocktail to the tubes and shaking them for 45 min at RT. Next, the cells were washed twice with 2.5x CSM and 8 tubes were also washed once more with PBS, performing all the centrifugations at 4 ºC. Then, the 8 tubes with 2.5x CSM were kept at 4 ºC, whilst 1 mL of cold MeOH was added to the 8 tubes that had been washed with PBS, leaving them on ice for 10 min to permeabilise the cells. After the 10 min incubation, these cells were washed once with PBS and twice with 2.5x CSM (centrifugations at 4 ºC). Subsequently, the intracellular antigens were stained by adding 50 µL of the Intracellular Ab-isotopes cocktail and leaving it shaking for 1 h at RT. Afterwards, the cells were washed twice with 2.5x CSM (centrifugations at 4 ºC). At last, 2.5x CSM solvent was removed from all the tubes (16 in total) and 1 mL of a solution containing Cell-ID™ Intercalator-Ir (1:5000 dilution) and 1.6% PFA in PBS was added to the cells, being incubated for 14 h at 4 ºC.

Cells were washed once with 2.5x CSM and twice with CyTOF water (centrifugations at 4 ºC) and counted on a TC10™ Automated Cell Counter. Then, CyTOF water was removed and the cells were resuspended in a homemade 1x Normalisation beads solution before loading them in a CyTOF®2 instrument [279]. Data were analysed using the Cytobank Community online software.

CHAPTER VI

6. Appendices

6.1. Appendix 1 – PhD research outcome

The results of this Doctoral Thesis have led to:

(i) The publication of two scientific articles in relevant journals in the field of this Doctoral Thesis:

- **Antonio Delgado-Gonzalez**, Emilio Garcia-Fernandez, Teresa Valero, M. Victoria Cano-Cortes, Maria J. Ruedas-Rama, Asier Unciti-Broceta, Rosario M. Sanchez-Martin, Juan Jose Diaz-Mochon, and Angel Orte. Metallofluorescent nanoparticles for multimodal applications, *ACS Omega*, volume 3, pages 144 – 153, 2018.

- **Antonio Delgado-Gonzalez**, Agustin Robles-Remacho, Antonio Marin-Romero, Simone Detassis, Barbara Lopez-Longarela, F. Javier Lopez-Delgado, Diego de Miguel-Perez, Juan J. Guardia-Monteagudo, Mario Antonio Fara, Mavys Tabraue-Chavez, Salvatore Pernagallo, Rosario M. Sanchez-Martin, Juan J. Diaz-Mochon. PCR-Free and Chemistry-based Technology for miR-21 rapid detection directly from tumour cells, *Talanta*, volume 200, pages 51 – 56, 2019.

(ii) The application for an international patent:

- **Delgado González Antonio**, Sánchez Martín Rosario María, Díaz Mochón Juan José, Valero Griñán María Teresa, Orte Gutiérrez Ángel, García Fernández Emilio. Dual Probres for Flow Cytometry and Mass Cytometry. WO2018224719 (A1) — 2018-12-13 (Source: European Patent Office (EPO)).

(iii) 12 publications in Congresses, highlighting the oral communications in 7th EuCheMS Chemistry Congress in 2018, and in Nanotech France in 2018, and the posters in Bioorthogonal & Bioresponsive RSC Symposium in 2017, and in International Symposium Precision Medicine Based on Liquid Biopsies “From Detection to Dissection” in 2016.

Furthermore, collaboration with Dr. Asier Uniciti-Broceta, from the University of Edinburgh, has led to the publication of another scientific article:

- Teresa Valero, **Antonio Delgado-González**, Juan Diego Unciti-Broceta, Victoria Cano-Cortés, Ana Pérez-López, Asier Unciti-Broceta, Rosario Sánchez-Martín. Drug ‘clicking’on cell-penetrating fluorescent nanoparticles for in cellulo chemical proteomics. *Bioconjugate Chemistry*, volume 29(9), 3154 – 310, 2018

6.1.1. Publication 1 – PCR-free and chemistry-based technology for miR-21 rapid detection directly from tumour cells

Talanta 200 (2019) 51–56

Contents lists available at ScienceDirect

Talanta

journal homepage: www.elsevier.com/locate/talanta

PCR-free and chemistry-based technology for miR-21 rapid detection directly from tumour cells

Antonio Delgado-Gonzalez[a,b], Agustin Robles-Remacho[a,b], Antonio Marin-Romero[a,b,c], Simone Detassis[d], Barbara Lopez-Longarela[c], F. Javier Lopez-Delgado[c], Diego de Miguel-Perez[a,e], Juan J. Guardia-Monteagudo[c], Mario Antonio Fara[c], Mavys Tabraue-Chavez[c], Salvatore Pernagallo[c], Rosario M. Sanchez-Martin[a,b], Juan J. Diaz-Mochon[a,b,*]

[a] Pfizer/Universidad de Granada/Junta de Andalucia Centre for Genomics and Oncological Research (GenYo), PTS Granada, Avenida de la Ilustracion, 114, 18016 Granada, Spain
[b] Department of Medicinal and Organic Chemistry, Faculty of Pharmacy, University of Granada – Campus Cartuja, 18071 Granada, Spain
[c] DestiNA Genomica S.L. PTS Granada, Avenida de la Innovación 1, Edificio BIC, 18100 Armilla, Granada, Spain
[d] Laboratory of RNA Biology and Biotechnology, Centre for Integrative Biology, University of Trento, Trento, Italy
[e] Department of Legal Medicine, Toxicology and Physical Antropology, Faculty of Medicine, University of Granada, Avenida de la Investigación 11, 18016 Granada, Spain

ARTICLE INFO

Keywords:
Dynamic chemistry
Peptide nucleic acid (PNA)
Nucleic acid testing (NAT)
MiRNA quantification
Flow Cytometry (FACS)
Fluorescence Microplate

ABSTRACT

miRNAs are well known for being implicated in a myriad of biological situations, including those related to serious diseases. Amongst miRNAs, miRNA-21 has the spotlight as it is reported to be up-regulated in multiple severe pathological conditions, being its quantification a key point in medicine. To date, most of the techniques for miRNA quantification have shown to be less effective than expected; thus, we herein present a novel, rapid, cost-effective, robust and PCR-free approach, based on dynamic chemistry, for the identification and quantification of miRNA directly from tumour cells using both FACS and a fluorescent microplate. This dynamic chemistry novel application involves bead based reagents and allows quantifying the number of miR-21 molecules presented in MDA-MB-468 and H1975 tumour cells.

1. Introduction

MicroRNAs (miRNAs) are small non-coding RNAs of 18–24 nucleotides in length that regulate gene expression by directly interacting with the 3′ untranslated region (UTR) of a target gene. This interaction leads to degradation and/or translational repression of that gene [1–4]. miRNAs are implicated in the regulation of cell growth, differentiation, and apoptosis (and their deregulation is associated with multiple serious diseases [4].

Since the discovery of miRNAs, miR-21 has become one of the most studied and cited miRNAs, as it has been reported to be up-regulated in a lot of pathological conditions, such as glioblastoma, pancreatic cancer, breast cancer, lung cancer, and colon cancer. Besides, miR-21 up-regulation is directly related to cell proliferation, migration and invasion, and to the generation of chemoresistance in lung cancer [5], in breast cancer [5] and in ovarian cancer [6]. For that, it is considered an OncomiR [7]. Thus, miR-21 has emerged as one of the miRNA most frequently associated with poor outcome in cancer, being considered as a very promising therapeutic target for cancer [8,9]. As a matter of fact, CRISPR/CAS9 based gene therapies targeting miR-21 are being developed nowadays [6,7].

To date, miRNA analysis is mostly done by standard RT-qPCR. However, these tools are not particularly suitable for detecting small RNA species, since they require elongation of the target molecules (ligation step with an extension sequence), conversion of the target molecule into cDNA, as well as amplification steps. There are other approaches which are based on just a hybridisation step between targets and capture probes which tend to be long and increase the probability of obtaining false positives [10]. Therefore, the rapid and cost-effective detection and quantification of miRNAs, which will represent a huge advance and amelioration in diagnosis as it provides a high valuable knowledge to physicians, is still an unmet need. Real-time monitoring of miRNAs will become a key tool in personalised medicine [11].

An alternative approach for nucleic acid testing by dynamic chemistry (also known as Chem-NAT), which harnesses Watson-Crick base pairing to template a dynamic reaction on a strand of abasic peptide

* Corresponding author.
E-mail address: juanjose.diaz@genyo.es (J.J. Diaz-Mochon).

https://doi.org/10.1016/j.talanta.2019.03.039
Received 6 December 2018; Received in revised form 5 March 2019; Accepted 7 March 2019
Available online 08 March 2019
0039-9140/

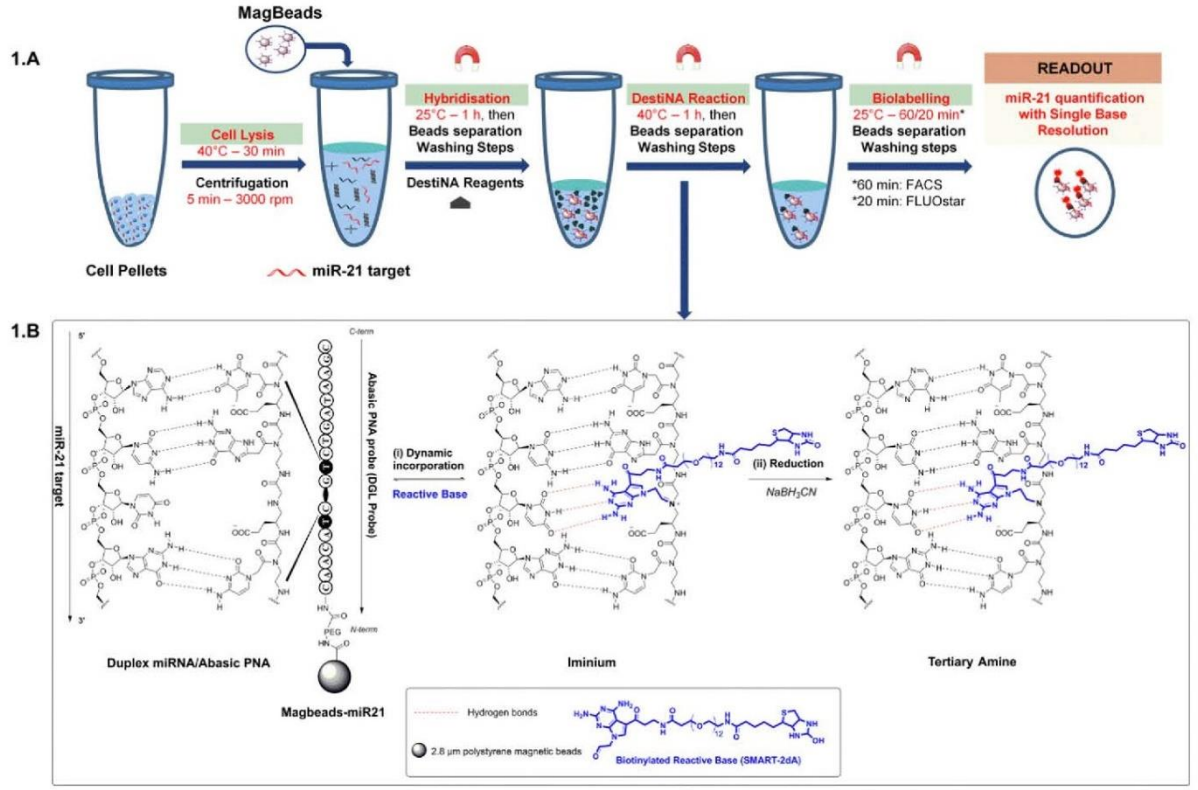

Fig. 1. Direct detection of miRNAs from tumour cells using dynamic chemistry (Chem-NAT). **A)** Workflow scheme: 1) Lysis of the cell pellets; 2) Magnetic beads (Magbeads) functionalised with abasic PNA probes (DGL probes) are added to the supernatant and a hybridisation step takes place; then, washings are performed; 3) biotinylated SMART-NB and reducing agent are added for the dynamic incorporation step, and washing steps are performed; 4) Afterwards and previous to the readout step, the biotinylated SMART-NB is labelled with Streptavidin-Phycoerythrin (SAPE) conjugate or Streptavidin-β-Galactosidase conjugates; and washing steps are performed; 5) Readout by Flow Cytometry or by a Plate Reader. **B)** Schematic representation of the dynamic incorporation step where the specific biotinylated SMART-NB is incorporated into the abasic position of the PNA.

nucleic acid (PNA) probes [12] and using reactive nucleobases (SMART-NBs) has been developed by our group. During the past years, we have validated this approach to detect DNA mutations [13–16] and miRNAs without the need of using PCR [17–20]. Hence, new applications that fitted into the actual chemical biological and biomedicine demands are being developed. Herein, we aimed to develop a novel PCR-free method, based on Chem-NAT, for the rapid detection and quantification of miR-21 directly from tumour cell lines.

In our work, we have selected two widely and commonly used cancer cell lines, obtained by cell culturing, MDA-MB-468 (breast cancer mammalian cell line) and H1975 (lung cancer cell line), both overexpressing miR-21, and Peripheral Blood Mononuclear Cells (PBMCs) as control cell line due to its miR-21 lack of expression. For the purpose of quantification the levels of miRNA presented in those cells, magnetic microspheres (**Dynabeads m270**) were covalently bound to abasic PNA complementary to miR-21 to afford **Magbeads-miR21**, comprising both dynamic chemistry and bead-based reagents. This combination has been shown to be very effective and promising for miRNA detection from biological sources [19,20]. To develop the protocol for miR-21 direct detection and quantification from cell lines, we firstly focused on the detection of miR-21 using fluorescence-activated cell sorting (FACS) as the reading platform. Afterwards, and once the protocol to use Chem-NAT with bead-based reagents to detect miR-21 was validated using FACS, we aimed to go one step further and quantify the number of miR-21 per cell. We decided to use a fluorescent microplate reader (FLUOstar Omega) rather than FACS to do miR-21 quantification as it offers higher throughput capacity.

This new application allows using cell pellets directly, avoiding miRNA isolation and purification steps, which reduces the possibility of contamination, and using fluorescent-based readout platforms (Fig. 1). This new proof-of-concept opens up the possibility for not only single-point miRNA quantification but for multiple points quantification, enabling miRNA level changes to be detected, and quantified, within cell-based assays. This approach, although it requires optimisation and further experiments, could represent a starting point for real monitoring of miRNA, what, as aforementioned, becomes a key tool in personalised medicine.

2. Materials and Methods

2.1. General

DGL probes were designed and synthesised by DestiNA Genomica S.L. (Spain), following standard solid phase chemistry protocols, using an INTAVIS MultiPrep Synthesizer (Intavis AG Gmb H, Germany). Mimic sequences of miRNA were purchased from Integrated DNA Technologies (IDT) as ssDNA (Table 1).

The microspheres Dynabeads® M-270 Carboxylic Acid were purchased from Thermofisher Scientific. 1-ethyl-3-(3-dimethylaminopropyl) carbodiimide (EDC) was purchased from Sigma-Aldrich.

Table 1
Sequences used in the experiments.

Sequence ID	Name	Peptide with abasic position (N'-C')
1	DGL-miR21	xxC A A C A Tglu C *GL* G Tglu C T G A T A A G C
		ssDNA sequence (5'-3')
2	ssDNA-21	TAGCTTATCAGACTGATGTTGA
3	ssDNA-21-2G	TAGCTTATCAGACGGATGTTGA
		miR-21 sequence (5'-3')
4	miR-21	UAGCUUAUCAGACUGAUGUUGA

xx = amino-PEG-linker; Tglu = thymidine containing a propanoic acid side chain at the gamma position; *GL* = abasic "blank" monomer containing a propanoic acid side chain at the gamma position. In yellow, the nucleotides located in front of the PNA abasic position.

Streptavidin-R-Phycoerythrin (SAPE) conjugate was purchased from Fisher. miRNeasy Mini Kit was purchased from Qiagen (Cat No.: 217004); TaqMan™ Advanced miRNA cDNA Synthesis Kit (Cat. No.: A28007) and TaqMan™ Universal PCR Master Mix (Cat. No.: 4304437) were both purchased from Thermofisher Scientific.

Dulbecco's modified Eagle's medium, RPMI 1640 medium and Trypsin-EDTA 0.05% were purchased from Gibco.

PBS-Tween® 0.1%, DestiNA Stablitech proprietary lysis buffer and Buffer A (2X SSC and 0.1% SDS buffer (pH 6)) are homemade.

The thermoshaker (Biometra TS1 ThermoShaker), magnet rack (MagnaRack™) and 96-black well plates (Nunc™ MicroWell™) were purchased from ThermoFisher Scientific. 7900 Fast Real-Time PCR System was purchased from Applied Biosystems. The Automated Peptide Synthesizer is a property of DestiNA Genomica SL., as well as the Smart-Nucleobases. FLUOstar Omega was purchased from BMG Labtech. Flow Cytometer BD FACSCanto II ™ was purchased from BD Biosciences.

2.2. Magbeads-miR21

DGL-miR21 coupling to Dynabeads M-270 Carboxylic Acid® to achieve Magbeads-miR21 was done following established protocols described elsewhere [19,20].

2.3. Cell culturing and cell pelleting

MDA-MB-468 cell line was maintained in Dulbecco's modified Eagle's medium supplemented with L-alanyl-L-glutamine, penicillin/streptomycin, pyruvate, HEPES buffer and 10% (v/v), fetal bovine serum (FBS) in a standard incubator (95% humidity, 5% CO_2, 37 °C) and subcultured twice per week. H1975 cell line was maintained in RPMI 1640 medium supplemented with L-alanyl-L-glutamine, penicillin/streptomycin, pyruvate, HEPES buffer and 10% (v/v) fetal bovine serum (FBS) in a standard incubator (95% humidity, 5% CO2, 37 °C) and subcultured twice per week. Peripheral Blood Mononuclear Cells (PBMC) were obtained from 10 mL of venous blood samples that were collected from healthy volunteers in EDTA tubes (BD, Franklin Lakes, NJ, USA), isolating them by density gradient centrifugation (for 45 min at 700 RFC without brake) using Histopaque-119 (Sigma Aldrich, UK). PBMC were then washed with PBS1X, counted in a Bright-Line™ Hemacytometer (Sigma-Aldrich, UK) and pelleted in serial concentrations by centrifugation for 10 min at 350 RCF.

For cell pelleting, cells were grown to 70–80% confluence in a T75 flask. Then, the medium was removed, the cells were washed with PBS and they were trypsinised with Trypsin-EDTA 0.05% for 10 min; after that, they were neutralised with the correspondent medium, and they were counted using a Neubauer chamber. According to the number of cells required, specific volumes were transferred to 15 mL Falcon tubes and they were centrifuged for 5 min at 1100 rpm. The supernatants were removed and the cell pellets were suspended in 1 mL of cold PBS and transferred to 1.5 mL eppendorf tubes. The eppendorf tubes were then centrifuged for 5 min at 1100 rpm, subsequently, the supernatants were removed and the cell pellets were suspended in cold PBS and centrifuged again. At last, the supernatants were removed and the cell pellets were stored at − 80 °C.

2.4. Flow Cytometry (FACS) and FLUOstar Omega procedures

110 µL of a mixture of a lysis buffer are added to the cell pellets and the tubes are stirred at 1200 rpm, for 1 h at 40 °C. Then, the tubes are centrifuged at 3000 rpm for 5 min, transferring 100 µL to new 1.5 mL eppendorf tubes.

Afterwards, the cell lysates are incubated with 250,000 **Magbeads-miR21** at 1200 rpm, for 1 h at room temperature. Then, the tubes are centrifuged for 10 s at 6000 rpm and placed on a magnet for 10 s and the supernatants are removed. Subsequently, 200 µL of Buffer A are added to the tubes and the Magbeads-miR21 are suspended, as a washing step. After that, the Magbeads-miR21 are centrifuged for 10 s and 6000 rpm and placed on a magnet and the supernatants are removed. This washing step is done three times.

Then, the dried Magbeads-miR21 are suspended in buffer A, and the Smart-Nucleobase and reducing agent $NaBH_3CN$ are added, to reach a final 50 µL volume. Then, Smart-Nucleobase dynamic incorporation takes place when the mixture is stirred at 1200 rpm for 1 h at 41 °C. Subsequently, 150 µL of PBS-Tween®20 0.1% are added to each tube and the washing steps described above are performed, but using PBS-Tween®20 0.1% instead of Buffer A.

For FACS, the dried Magbeads-miR21 are suspended in 100 µL of PBS-Tween®20 0.1% and 20 µL of 60 µg/mL Streptavidin-R-Phycoerythrin conjugate (SAPE) in PBS-Tween®20 0.1% are added. The mixture is stirred at 1200 rpm, for 1 h at room temperature in darkness. Afterwards, the Magbeads-miR21 are washed as described above and finally suspended in 200 µL of Buffer A and transferred to cytometry tubes.

For FLUOstar Omega, the dried Magbeads-21 are suspended in 100 µL of Streptavidin-β-Galactosidase (SbG), and the mixture is stirred at 1200 rpm, for 20 min at room temperature. Afterwards, the Magbeads-miR21 are washed as described above. Subsequently, the Magbeads-miR21 are suspended in 200 µL of PBS-Tween®20 0.1% and transferred to a black 96 well plate, which is placed on a magnet for 1 min, removing the supernatants then. Finally, 200 µL of substrate Resorufin-β-D-Galactopyranoside are added to each well and mixed with the Magbeads-miR21, letting a 10 min fluorescent reaction described elsewhere [20] to take place inside the FLUOstar Omega.

2.5. miR-21 spike-in calibration curve

A calibration curve was done using spike-in solutions of synthetic mimic of miR-21 (500 pM, 250 pM, 125 pM, 62.5 pM, 31.25 pM and

0 pM). For that, two master-mix solutions were prepared: 1) Master-mix 1, containing 500 pM of synthetic mimic miR-21 and 250,000 Magbeads-miR21 in lysis buffer; and 2) Master-mix 2, containing 250,000 Magbeads-miR21 in lysis buffer.

From Master-mix 1, serial dilution solutions were prepared by mixing them with Master-mix 2, affording 6 solutions covering the concentration range indicated above, with a total volume of 100 µL for each solution. Then, a hybridisation step took place at 1200 rpm, for 1 h at room temperature. Afterwards, washing steps, dynamic incorporation step, labelling step and relative fluorescence measurement by FLUOstar Omega were performed as previously mentioned (Section 2.4).

3. Results and discussion

3.1. Flow Cytometry (FACS)

Cell lines were lysated and incubated with **Magbeads-miR21** for miR-21 hybridisation (Hybridisation - Fig. 1). After pelleting out and washing **Magbeads-miR21** from the cell lysate buffer, dynamic chemistry reaction was performed, using biotinylated aldehyde-modified SMART-NBs, which could be covalently attached to the abasic probe into the abasic position, through the templating role of complementary miRNA strand (DestiNA reaction – Fig. 1). Finally, bead labelling was performed using Streptavidin-R-Phycoerythrin conjugate (SAPE), which allowed the fluorescent labelling of the biotinylated **Magbeads-miR21** (Biolabelling – Fig. 1) and their analysis by FACS (Readout – Fig. 1). For this study, we designed a DGL probe which was complementary to mature miR-21, positioning the abasic position in front of a uracil so that it would template the incorporation of a reactive adenine (Table 1). In order to increase the dynamic reaction efficiency, a biotinylated SMART-NB containing the 2-diamino-deazapurine as nucleobase analogue of adenine was used. It is well known that 2,6-diaminopurine:thymine/uracil base pair proceed through three hydrogen bonds rather than the two that occurs between natural adenine and thymine/uracil, increasing their base pair stability. Moreover, Brown et al. demonstrated that modified 7-deaza *2*,6-diaminopurines significantly stabilize DNA duplexes [21]. Therefore, we prepared the SMART-Nucleobase containing the 2-diamino deazapurine analogue (**SMART-2dA**), which, as expected, incorporated more efficiently than standard SMART-Adenine in the presence of a uracil template (data not shown). As the negative control, biotinylated SMART-Cytosine was used [19,20]. FACS data were analysed and Mean fluorescence intensities (MFI) was chosen as the readout parameter per each experimental condition. MFI obtained from cell lysates of both cancer cell lines MDA-MB-468 and H1975 were significantly higher than values obtained when PMBC cells were analysed (Fig. 2). These data show the high specificity of the dynamic chemistry approach as when using the biotinylated SMART-Cytosine rather than SMART-2dA, fluorescence signals were equal to background levels, as uracil do not template the incorporation of a cytosine nucleobase.

3.2. miR-21 calibration curve

As aforementioned, a calibration curve spiking synthetic miR21 at different concentrations was done (500 pM, 250 pM, p.M., 125 pM, 62.5 pM, 31.25 pM and 0 pM.The protocol for miR-21 quantification directly from tumour cells using a microplate reader is the same than the one described above until the biolabelling step (Fig. 1). In this case, biolabelling was performed with Streptavidin-β-Galactosidase (SbG) rather than SAPE, which creates a fluorescent solution upon enzymatic hydrolysis of resorufin-β-D-galactopyranoside (RGP). Relative fluorescence units (RFU) were recorded during a 9 min period with a FLUOstar Omega instrument (Readout - Fig. 1) equipped with 544 ± 10 nm excitation and 590 ± 10 nm emission filters and the slope of the linear region of the reaction time course was calculated. Resorufin

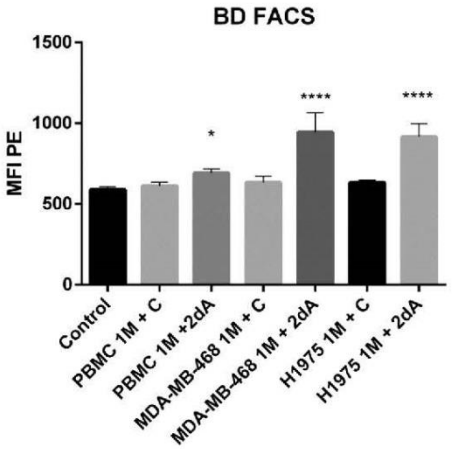

Fig. 2. BD FACS results. Mean Fluorescence Intensity (MFI) of PE channel (585/42 nm) for 1 million MDA-MB-468, H1975, and PBMCs, with SMART-C and SMART-2dA using BD FACS. One-Way ANOVA analysis was performed comparing the cell samples (n = 4) with a control: Magbeads-miR21 that did not undergo any chemical reaction. As expected, MDA-MB-468 and H1975 tumour cells with 2dA showed a strong MFI increase compared with the control ($p < 0.0001$), being "extremely significant".

fluorescence signals are directly proportional to the amount of SbG presented in the Magbeads-miR21 [20]. To ensure the analytical capability of this platform and in order to correlate the amount of miR-21 presented in cells with the Units of Fluorescence by Second (RFU/s) produced in the kinetic measurement, a titration curve using a synthetic miR-21 was carried out calculating a LoD of 35.84 ± 2.4 pM in 100 µL of hybridisation volume (3.58 fmol), corresponding to 2.16E + 9 molecules of synthetic mimic miR-21 (Fig. 3).

3.3. FLUOstar Omega

In order to determine the amount of miR-21 in cancer cell lines, 100,000 cells of MDA-MB-468 and H1975 were evaluated in quadruplicate. One million of PBMC, in triplicate, were tested as negative control. RFU/s values for each condition were determined and the concentration of miR-21 per condition was calculated using the calibration curve previously established. As expected, the calculated concentration of miR-21 presented in 1 million PBMCs was below the LoD of the assay. Knowing the concentration of miR-21 for each condition, the reaction volume and the number of cells, the number of miR-21

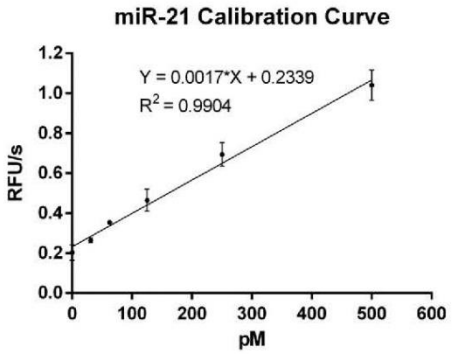

Fig. 3. miR-21 calibration curve by synthetic miR-21 spike-in. Dots represent Mean+SEM (n = 3) at different synthetic miR-21 concentration (500 pM, 250 pM, 125 pM, 62.5 pM, 31.25 pM and 0 pM).

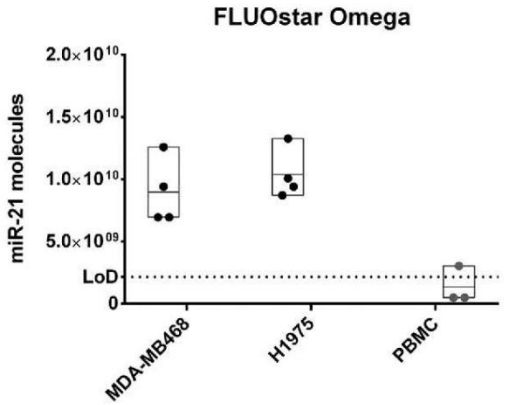

Fig. 4. FLUOstar Omega results. In black dots, the total number of miR-21 molecules calculated by FLUOstar Omega for 100,000 MDA-MB-468 and H1975 cells (n = 4). In grey dots, total number of miR-21 molecules corresponding to 1 million PBMCs (n = 3).

molecules per cell could be calculated (see ESI for formula). In the case of MDA-MB-468 cells, 89,834 ± 16% copies of miR-21 per cell were obtained while in the case of H1975 the copies number per cell were 104,003 ± 11% (Fig. 4). These numbers are coherent with our RT-qPCR data which showed a higher expression of miR-21 in H1975 than in MDA-MB-468 (see ESI for RT-qPCR data). These numbers also fall within expected ranges reported in literature for some of the tumour cell lines [22].

4. Conclusions

We have presented a new Chem-NAT application which allows quantifying the number of miRNA per cell, without the need for miRNA isolation, following an easy-to-implement protocol in any cell biology lab. Concretely, we were able to detect and quantify the number of molecules of miR-21 per cell, a key miRNA involved in tumorigenic processes, in two tumour cancer cell lines, MDA-MB-468 and H1975, in less than 3 h and a half. Likewise, we have also confirmed that the expression of miR-21 in PBMCs is so low that it is hardly detectable, as the signals obtained were below the LoD of our assay. Additionally, we have developed the implementation of the Chem-NAT with two bead-based readout platforms, one based on direct fluorescence detection (FACS) and the other based on an enzyme-assisted fluorescence assay (FLUOstar Omega microplate reader).

Although further experimentation and optimisation has still to be done, this application could be implemented in routine practice during the first phases of drug development for miRNA level monitoring. This novel use of the Chem-NAT technology for cell based assays is the latest addition to the Chem-NAT set of applications, as it has already been used to detect circulating miRNAs found in body fluids with the goal of creating IVD assays for the liquid biopsy market [18–20]. Moreover, the technology is suitable to both detect and quantify any other RNA molecules such as rRNA, lncRNA and circRNA without the need of isolating nor reverse transcript them and with single base resolution. Actually, some of these assays are under development in our group.

Acknowledgements

This research was supported by the Regional Government, Spain (BIO-1778) and the Ministry of Economy and Competitiveness, Spain (BIO2016-80519-R – FJLD is supported by Torres Quevedo fellowship, Spain PTQ-16-08597). ADG and ARR are supported by Spanish Ministry of Education, Spain (PhD scholarships FPU14/02181 and FPU15/06418, respectively). AMR thanks DestiNA Genomics, Spain and the University of Granada, Spain for a PhD scholarship (P26 Knowledge Transfer Programme) DMP acknowledges the University of Granada for his predoctoral research contract. SD's work was supported by intramural funding from the University of Trento, Italy. DestiNA's staff and SD thank the miRNADisEASY Consortium (EU, European Union H2020-MSCA-RISE 2015 (Grant no. 690866)). We would also like to thank all the healthy volunteers who participated in this study.

Contribution on each co-author

ADG: Designed, performed most of the experiments and wrote the paper
ARR: PCR experiments
AMR: Protocol optimisation with FLUOstar Omega
SD: Beads conjugation for FACS studies
FJLD: Synthesis of SMART-Nucleobases
DMP: PBMCs collection
JJGM: Probe synthesis and purification
MAF: Designed synthesis pathways for SMART Nucleobases and optimisation of protocols for abasic PNA synthesis
BLL & MTC: miR-21 probes validation and Dynamic incorporation optimisation
SP: Designed the experiments
RMSM: Designed the experiments
JJDM: Designed the experiments, wrote and edited the paper

Conflicts of interest

JJDM is shareholder and Director of DestiNA Genomics Ltd. SP is shareholder of DestiNA Genomics Ltd.

Appendix A. Supporting information

Supplementary data associated with this article can be found in the online version at doi:10.1016/j.talanta.2019.03.039.

References

[1] R.C. Lee, R.L. Feinbaum, V. Ambros, The C. elegans heterochronic gene lin-4 encodes small RNAs with antisense complementarity to lin-14, Cell 75 (1993) 843–854, https://doi.org/10.1016/0092-8674(93)90529-Y.
[2] V. Ambros, The functions of animal microRNAs, Nature (2004), <https://www.nature.com/articles/nature02871> (accessed 17 January 2018).
[3] D.P. Bartel, MicroRNAs: genomics, biogenesis, mechanism, and function, Cell 116 (2004) 281–297, https://doi.org/10.1016/S0092-8674(04)00045-5.
[4] C.E. Stahlhut Espinosa, F.J. Slack, The role of microRNAs in cancer, Yale J. Biol. Med. 79 (2006) 131–140.
[5] C. Gong, Y. Yao, Y. Wang, B. Liu, W. Wu, J. Chen, F. Su, H. Yao, E. Song, Up-regulation of miR-21 mediates resistance to Trastuzumab therapy for breast cancer, J. Biol. Chem. 286 (2011) 19127–19137, https://doi.org/10.1074/jbc.M110.216887.
[6] W. Huo, G. Zhao, J. Yin, X. Ouyang, Y. Wang, C. Yang, B. Wang, P. Dong, Z. Wang, H. Watari, E. Chaum, L.M. Pfeffer, J. Yue, Lentiviral CRISPR/Cas9 vector mediated miR-21 gene editing inhibits the epithelial to mesenchymal transition in ovarian cancer cells, J. Cancer 8 (2017) 57–64, https://doi.org/10.7150/jca.16723.
[7] W. Ji, B. Sun, C. Su, Targeting microRNAs in cancer gene therapy, Genes 8 (2017) 21, https://doi.org/10.3390/genes8010021.
[8] F. Sicard, M. Gayral, H. Lulka, L. Buscail, P. Cordelier, Targeting miR-21 for the therapy of pancreatic cancer, Mol. Ther. 21 (2013) 986–994, https://doi.org/10.1038/mt.2013.35.
[9] K. Gumireddy, D.D. Young, X. Xiong, J.B. Hogenesch, Q. Huang, A. Deiters, Small-molecule inhibitors of microRNA miR-21 function, Angew. Chem. Int. Ed. 47 (2008) 7482–7484, https://doi.org/10.1002/anie.200801555.
[10] E.A. Hunt, D. Broyles, T. Head, S.K. Deo, MicroRNA detection: current technology and research strategies, Annu. Rev. Anal. Chem. 8 (2015) 217–237, https://doi.org/10.1146/annurev-anchem-071114-040343.
[11] N.J. Schork, Personalized medicine: time for one-person trials, Nat. News 520 (2015) 609, https://doi.org/10.1038/520609a.
[12] P.E. Nielsen, M. Egholm, R.H. Berg, O. Buchardt, Sequence-selective recognition of DNA by strand displacement with a thymine-substituted polyamide, Science 254 (1991) 1497–1500, https://doi.org/10.1126/science.1962210.
[13] F.R. Bowler, J.J. Diaz-Mochon, M.D. Swift, M. Bradley, DNA analysis by dynamic chemistry, Angew. Chem. Int. Ed. 49 (2010) 1809–1812, https://doi.org/10.1002/

anie.200905699.
[14] F.R. Bowler, P.A. Reid, A.C. Boyd, J.J. Diaz-Mochon, M. Bradley, Dynamic chemistry for enzyme-free allele discrimination in genotyping by MALDI-TOF mass spectrometry, Anal. Methods 3 (2011) 1656, https://doi.org/10.1039/c1ay05176h.
[15] M. Bradley, J.J. Diaz-Mochon, Nucleobase characterisation, 2014, US8716457B2. ⟨https://patents.google.com/patent/US8716457/en⟩.
[16] M. Angélica Luque-González, M. Tabraue-Chávez, B. López-Longarela, R. María Sánchez-Martín, M. Ortiz-González, M. Soriano-Rodríguez, J. Antonio García-Salcedo, S. Pernagallo, J. José Díaz-Mochón, Identification of trypanosomatids by detecting single nucleotide fingerprints using DNA analysis by dynamic chemistry with MALDI-ToF, Talanta 176 (2018) 299–307, https://doi.org/10.1016/j.talanta.2017.07.059.
[17] S. Pernagallo, G. Ventimiglia, C. Cavalluzzo, E. Alessi, H. Ilyine, M. Bradley, J.J. Diaz-Mochon, Novel biochip platform for nucleic acid analysis, Sensors 12 (2012) 8100–8111, https://doi.org/10.3390/s120608100.
[18] S. Venkateswaran, M.A. Luque-González, M. Tabraue-Chávez, M.A. Fara, B. López-Longarela, V. Cano-Cortes, F.J. López-Delgado, R.M. Sánchez-Martín, H. Ily M. Bradley, S. Pernagallo, J.J. Díaz-Mochón, Novel bead-based platform fo detection of unlabelled nucleic acids through single nucleobase labelling, Talanta 161 (2016) 489–496, https://doi.org/10.1016/j.talanta.2016.08.072.
[19] D.M. Rissin, B. López-Longarela, S. Pernagallo, H. Ilyine, A.D.B. Vliegenthart, J.W. Dear, J.J. Díaz-Mochón, D.C. Duffy, Polymerase-free measurement of microRNA-122 with single base specificity using single molecule arrays: detection of drug-induced liver injury, PLOS ONE 12 (2017) e0179669, https://doi.org/10.1371/journal.pone.0179669.
[20] A.M. Romero, A.R. Remacho, M. Tabraue-Chávez, R.M. Sánchez-Martín, J.J.G. Monteagudo, M.A. Fara, F.J. López-Delgado, S. Pernagallo, J.J. Diaz-Mochon, A. PCR-free, technology to detect and quantify microRNAs directly from human plasma, Analyst (2018), https://doi.org/10.1039/C8AN01397G.
[21] J. Booth, W.J. Cummins, T. Brown, An analogue of adenine that forms an "A:T" base pair of comparable stability to G:C, Chem. Commun 0 (2004) 2208–2209, https://doi.org/10.1039/B409155H.
[22] Y. Song, D. Kilburn, J.H. Song, Y. Cheng, C.T. Saeui, D.G. Cheung, C.M. Croce, K.J. Yarema, S.J. Meltzer, K.J. Liu, T.-H. Wang, Determination of absolute expres- profiles using multiplexed miRNA analysis, PLOS ONE 12 (2017) e0180988, s://doi.org/10.1371/journal.pone.0180988.

6.1.2. Publication 2 – Metallofluorescent Nanoparticles for Multimodal Applications

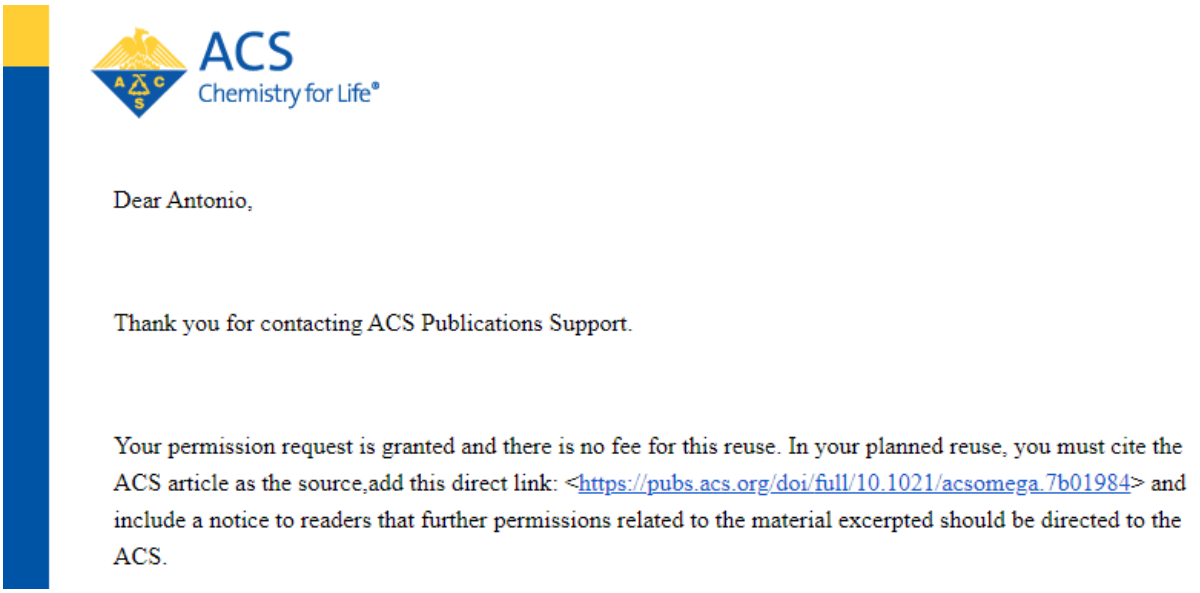

ACS Chemistry for Life®

Dear Antonio,

Thank you for contacting ACS Publications Support.

Your permission request is granted and there is no fee for this reuse. In your planned reuse, you must cite the ACS article as the source,add this direct link: <https://pubs.acs.org/doi/full/10.1021/acsomega.7b01984> and include a notice to readers that further permissions related to the material excerpted should be directed to the ACS.

ACS OMEGA

Article

Cite This: ACS Omega 2018, 3, 144−153

Metallofluorescent Nanoparticles for Multimodal Applications

Antonio Delgado-Gonzalez,[†,‡] Emilio Garcia-Fernandez,[§] Teresa Valero,[†,‡,⊥] M. Victoria Cano-Cortes,[‡] Maria J. Ruedas-Rama,[§] Asier Unciti-Broceta,[∥] Rosario M. Sanchez-Martin,[†,‡] Juan J. Diaz-Mochon,[*,†,‡] and Angel Orte[*,§]

[†]Department of Medicinal and Organic Chemistry, Faculty of Pharmacy, and [§]Department of Physical Chemistry, Faculty of Pharmacy, University of Granada, Campus Cartuja, 18071 Granada, Spain

[‡]GENYO, Pfizer-University of Granada-Junta de Andalucía Centre for Genomics and Oncological Research, Avda. Ilustracion 114. PTS, 18016 Granada, Spain

[∥]Cancer Research UK Edinburgh Centre, Institute of Genetics and Molecular Medicine, The University of Edinburgh, Crewe Road South, Edinburgh EH4 2XR, U.K.

S *Supporting Information*

ABSTRACT: Herein, we describe the synthesis and application of cross-linked polystyrene-based dual-function nano- and microparticles containing both fluorescent tags and metals. Despite containing a single dye, these particles exhibit a characteristic dual-band fluorescence emission. Moreover, these particles can be combined with different metal ions to obtain hybrid metallofluorescent particles. We demonstrate that these particles are easily nanofected into living cells, allowing them to be used for effective fingerprinting in multimodal fluorescence-based and mass spectrometry-based flow cytometry experiments. Likewise, the in situ reductions of the metal ions enable other potential uses of the particles as heterogeneous catalysts.

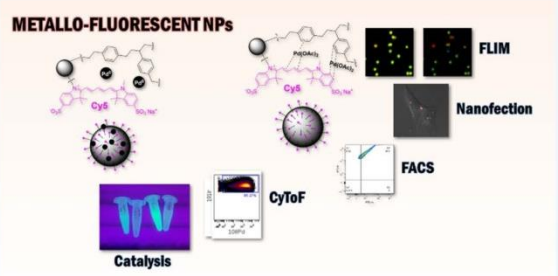

INTRODUCTION

Recent advances in materials science and nanotechnology have actively fostered the development of smart nanomaterials capable of tackling key challenges in nanomedicine, including advanced diagnostics tools, imaging agents, and therapeutic modalities. The use of varied synthetic and surface chemistry approaches has enabled the rapid development of biocompatible particles comprising different materials, such as polymers, semiconductors, gold, magnetite, and carbon, among many others, for a variety of applications, for example, from biolabeling and sensing to targeted drug delivery.[1−5] In this context, multimodal nanoparticles (NPs) can be rationally designed to carry out a myriad of different functions. These multimodal particles contain components that facilitate their use in different imaging techniques, such as fluorescence microscopy, magnetic resonance imaging, and positron emission tomography−computed tomography.[5,6] Similarly, particles featuring imaging capabilities for diagnostics and the ability to carry therapeutic agents have expanded the field of theranostics.[6]

Among a wide variety of imaging techniques available, fluorescence microscopy methods have become the tools of choice in most biological labs to study biomolecules and physiological processes at the intracellular level. These methods provide real-time, in situ, dynamic information of these processes in a simple and minimally invasive manner. Under these conditions, fluorescence detection platforms based on NPs can achieve enhanced sensitivity, stability, and biological compatibility compared with other traditional approaches.[2,7] For instance, very bright entities can be obtained by encapsulating organic fluorophores into particle matrices or by covalently attaching multiple fluorophores onto particles. Because particles can be decorated with thousands of units of a particular dye, issues such as photobleaching are minimized. This improves particle stability and facilitates intricate experiments, such as single-particle tracking.[8]

Additional applications of fluorescent NPs beyond live cell imaging include foreign gene expression at the single cell level (e.g., DNA-functionalized NPs) and fluorescence-based flow cytometry (e.g., fluorescence-activated cell sorting, FACS). To this end, the local nanofection of cells with targeted NPs enables the tracking and barcoding of cells in FACS experiments.[9]

Although these features make fluorescent NPs very attractive tools for cell biology, they still present a few drawbacks. One disadvantage is that the number of simultaneous parameters that can be studied in FACS experiments is frequently limited because of the spectral characteristics of the fluorescent dyes

Received: December 13, 2017
Accepted: December 25, 2017
Published: January 5, 2018

DOI: 10.1021/acsomega.7b01984
ACS Omega 2018, 3, 144−153

Table 1. Design of Different Particles Prepared in This Work

entry	particle[a]	diameter/nm	spacer	dye	additional components
1	NH_2-PEG-NP_{500}	500	PEG		
2	Cy5-PEG-NP_{500}	500	PEG	Cy5	
3	Cy5-PEG_2-NP_{500}	500	$(PEG)_2$	Cy5	
4	Cy5-PEG_3-NP_{500}	500	$(PEG)_3$	Cy5	
5	Fmoc-Lys(Cy5)-NP_{500}	460	lysine	Cy5	
6	Fmoc-Lys(Cy5)-NP_{900}	900	lysine	Cy5	
7	Strp-Lys(Cy5)-NP_{1200}	1200	lysine	Cy5	streptavidin
8	Pd(0)-Cy5-PEG-NP_{500}	500	PEG	Cy5	Pd(0)
9	Pd(II)-Cy5-PEG-NP_{500}	500	PEG	Cy5	Pd(II)

[a]All NPs were covalently bound to their cargo through amide bonds. PEG = 1-amino-4,7,10-trioxa-13-tridecanamine succinamyl.

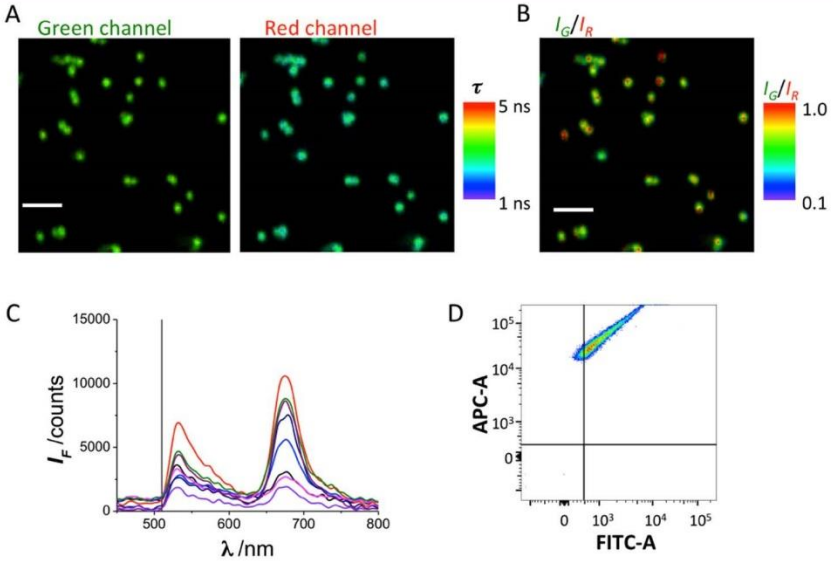

Figure 1. (A) Dual-color FLIM images of **Cy5-PEG-NP_{500}** in the green and red emission channels. The pseudocolor scale indicates the average fluorescence lifetime of the emission in each pixel. The scale bar represents 2.5 μm. (B) I_G/I_R ratio image of the images shown in (A). The pseudocolor scale indicates the I_G/I_R value in each pixel. (C) Fluorescence emission spectra of different particles in the image. (D) FACS correlogram of detected fluorescence in the red (APC-A) and green (FITC-A) channels of **Cy5-PEG-NP_{500}** particles.

and the limited excitation and detection capabilities of available instruments. Another issue that has not been extensively studied is the physicochemical interactions between solid-supported fluorophores and polymeric chains of NPs. These interactions can lead to unique fluorescence profiles different than those of free fluorophores in solution, giving rise to unexpected cross-talk channel interactions.

Recently, our capacity to perform complex multiplexing studies was expanded by combining flow cytometry with precise mass spectrometry detection using metal atoms as markers instead of fluorophores. This novel mass cytometry technique (termed cytometry by time of flight, CyToF) can simultaneously analyze up to 40 different cell parameters through the use of several metal atoms and isotopes.[10,11] However, the manifestation of unexpected spectral properties resulting from interactions between the structural components of solid supports and conjugated dye units has not been comprehensively investigated.

We aimed to study fluorophore–polymer interactions to better understand unexpected fluorescence profiles found in Cy5-functionalized polystyrene NPs. This study allowed us to develop a new type of multimodal cell-penetrating NPs that simultaneously carry a well-established red fluorophore and metal ions for the multiplex tagging of live cells. These novel NPs can be used simultaneously in FACS and CyToF as a new and versatile method for cell barcoding.

RESULTS AND DISCUSSION

Fluorescent, Dual-Band-Emitting Particles. We synthesized cross-linked polystyrene nano- and microparticles (Figure S1 in the Supporting Information) conjugated with the sulfo-Cy5 dye (Table 1, entries 2 to 9, and Scheme S1), a member of the cyanine family, for use in fluorescence microscopy and flow cytometry applications. Remarkably, fluorescence analyses of the resulting NPs showed two distinctive emission bands under the same excitation wavelength: the characteristic red fluorescence emission band of the Cy5 dye and an unexpected band within the green range of the spectrum. The dual-band behavior of these particles was confirmed using different techniques: fluorescence confocal microscopy, dual-color fluorescence lifetime imaging microscopy (FLIM) with spectrographic capabilities (Figure S2), and FACS flow cytometry. FLIM images of **Cy5-PEG-NP_{500}** clearly showed fluorescence emission from the particles in both green and red channels

DOI: 10.1021/acsomega.7b01984
ACS Omega 2018, 3, 144−153

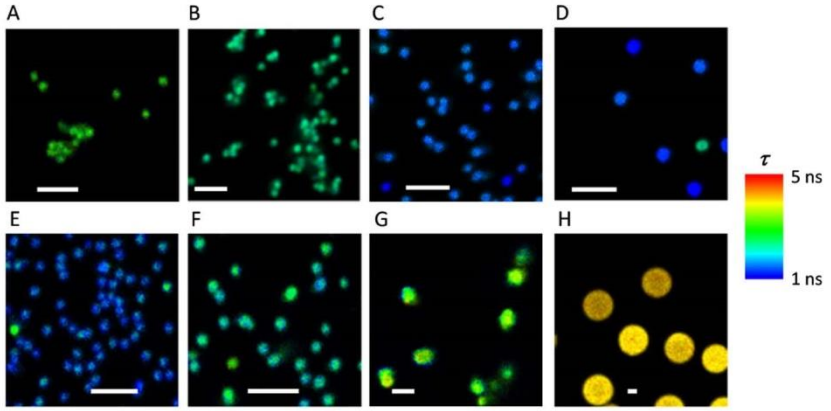

Figure 2. FLIM images in the red emission channel of Cy5- and A647-loaded particles. The pseudocolor scale indicates the average fluorescence lifetime in each pixel. The scale bars represent 2.5 μm. (A) **Cy5-PEG-NP$_{500}$**; (B) **Cy5-PEG$_2$-NP$_{500}$**; (C) **Fmoc-Lys(Cy5)-NP$_{900}$**; (D) **Strp-Lys(Cy5)-NP$_{1200}$**; (E) **A647-PEG-NP$_{500}$**; (F) **Fmoc-Lys(A647)-NP$_{900}$**; (G) **Fmoc-Lys(A647)-NP$_{2500}$**; and (H) **Fmoc-Lys(A647)-NP$_{5000}$**.

when excited at 470 nm (Figure 1A). The ratio of fluorescence intensities between the green and red channels (I_G/I_R) was 0.5 ± 0.1, averaged over different images with several particles. We also reconstructed I_G/I_R images to identify particles exhibiting high green fluorescence (Figure 1B). Emission spectra obtained directly from some of the particles found in the image field of view also showed the dual-band behavior with two maxima, one centered at approximately 670 nm (characteristic of free Cy5) and a second band centered at approximately 530 nm (Figure 1C). These particles were also analyzed using an FACS instrument at excitations of 488 and 633 nm. Events (particles) were recorded in the red allophycocyanin (APC) and green fluorescein isothiocyanate (FITC) channels. Plotting these events in a fluorescence correlogram showed that the green and red channel events were proportionally correlated (Figure 1D). To confirm that the green fluorescence signal did not originate from other components of the particles, unlabeled particles, that is, **NH$_2$-PEG-NP$_{500}$**, were prepared using the same protocol (except for the Cy5 conjugation). FLIM analysis showed no detectable fluorescence from the NPs, whereas FACS analysis showed events only in the random noise quadrant (Figure S3).

To expand the applicability of our particles, we substituted the polyethylene glycol (PEG) spacer with a lysine unit, which enabled the production of bivalent particles featuring a first arm that could be conjugated to other polypeptides or proteins, such as streptavidin through its Nα amino group, and a second arm that could be conjugated to sulfo-Cy5 dyes through its Nε amino group. Thus, in these particles, that is, **Fmoc-Lys(Cy5)-NP$_{500}$**, **Fmoc-Lys(Cy5)-NP$_{900}$**, and **Strp-Lys(Cy5)-NP$_{1200}$**, the Cy5 units were conjugated to the lysine side chains without PEG spacers (Schemes S2 and S3). These particles also exhibited the dual-band green/red emission behavior (Figure S4), thereby confirming that PEG molecules were not involved in the generation of the green fluorescent band. Notably, this effect was less prominent for larger particles. This can be attributed to the lower density of the polymer network in the larger particles, which minimized the interactions that cause the green fluorescence. Therefore, particle size is an important factor in controlling the dual-band emission of Cy5-labeled particles.

On the basis of these results, we first hypothesized that dye aggregation could account for the altered spectral features. Indeed, H- and J-aggregation of cyanine dyes are known to cause changes in their spectroscopic properties by altering their topological arrangements; furthermore, aggregation can be driven by high dye concentrations. Aggregation can also be fostered by certain templating structures. For example, H- and J-aggregates of cyanine dyes have been detected in the major and minor grooves of double-stranded DNA,[12] in NPs,[13] and in other structures. To test this hypothesis, we synthesized a set of **Cy5-PEG-NP$_{500}$** particles with different loadings of Cy5. The concentration of the N-hydroxysuccinimide (NHS) ester, the activated acid form of the dye in the reaction, ranged from 1.3 × 10^{-4} to 1.3 × 10^{-7} M. FACS experiments clearly showed that when the concentration of the dye in the reaction chamber was 1.3 × 10^{-6} M or lower, the emission in the green channel decreased to noise levels (Figure S5). The percentage of detected events showing notable green fluorescence decreased from 94% at the highest concentration of fluorophore to 5% at the lowest concentration. However, additional effects can be seen in the FACS results. A decrease in the concentration of the red dye by 1 order of magnitude caused a notable decrease in the red emission. However, the green emission did not decrease by the same factor and was more persistent. This effect resulted in an increased ratio of green fluorescence to red fluorescence at lower dye loadings. We further investigated this effect in dual-channel fluorescence confocal microscopy experiments. The results showed the same trend in the I_G/I_R ratio, that is, an increased ratio with decreased dye loading (Figure S6). Thus, the hypothesis of dye aggregation independently causing green emission was disproved. In such a case, a reduction of the green emission with respect to that of the red emission was expected as the dye concentration decreased. Therefore, we considered the possibility of an intermolecular interaction between the Cy5 moiety and the NP components. The close proximity of the cyanine dye aromatic rings and conjugated system (alternating double bonds) to the polystyrene aromatic groups was considered to promote $\pi-\pi$ stacking interactions, causing a charge transfer that would result in the green emissive transition. Figure S7 in the Supporting Information shows the aromatic interactions that could cause the green fluorescence

DOI: 10.1021/acsomega.7b01984
ACS Omega 2018, 3, 144−153

Scheme 1. Reduction Reaction To Prepare Pd(0)-Cy5-PEG-NP$_{500}$

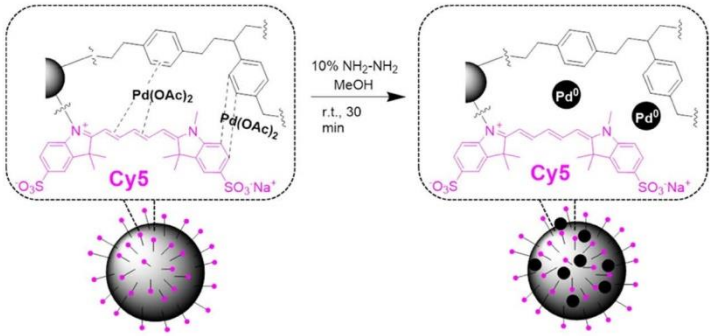

emission. Additional insights into this model is described in the next section.

An additional effect that may be behind the different trends in the relative emissions in the green and the red spectral regions is the presence of fluorescence resonance energy transfer (FRET) from the green emission emitters (i.e., the donors) to the red dyes (i.e., the acceptors; Figure S7). The FRET process would result in a lower green fluorescence when high loadings of the acceptor Cy5 dye are present. This energy transfer explains why a decrease in the number of acceptors resulted in an apparent increase in green emission. Experimental proof for the presence of FRET was obtained by investigating the average fluorescence lifetime, τ, profiles of the red-emitting dyes in the particles using FLIM microscopy. To test the potential energy transfer from green emission emitters to the red dyes, we employed a 470 nm excitation laser and collected FLIM images in the red channel (Figure S2). For small particles carrying Cy5 with short linkers, such as **Cy5-PEG-NP$_{500}$** (Figure 1A) and **Cy5-PEG$_2$-NP$_{500}$**, the Cy5 τ value was surprisingly longer than that of the dye in solution (1.0 ns).[14] For **Cy5-PEG-NP$_{500}$**, the average τ value was 2.3 ns, and for **Cy5-PEG$_2$-NP$_{500}$**, it was 1.9 ns (Figure 2A,B, respectively). This enhancement in the fluorescence lifetime correlated with the appearance of the green fluorescence emission. Interestingly, as the linker was lengthened, the fluorescence lifetime decreased. Similarly, for larger particles, the green emission was considerably reduced, and the fluorescence lifetime of Cy5 approached that of the dye in solution. For example, the average τ values of Cy5 in **Fmoc-Lys(Cy5)-NP$_{900}$** and **Strp-Lys(Cy5)-NP$_{1200}$** were 1.4 and 1.2 ns, respectively (Figure 2C,D), similar to those of the dye in solution. This behavior was primarily due to the energy transfer from the green-emitting donors to the Cy5 red fluorophores, acting as acceptors. Indeed, spectral analyses showed a clear overlap between the green emission of the aggregates in the absorption region of free Cy5 (Figures 1 and S8). This overlap may have fostered FRET between the two fluorescent forms. FRET resulted in an increased fluorescence lifetime of the acceptor dye, that is, Cy5, because the excitation source of the dye was not a direct laser pulse but the donor species. Thus, the fluorescence decay of the acceptor was a convolution of its natural decay law with that of the donor.[15] Therefore, when the acceptor was at larger distances or when there was a lower surface loading of the acceptor in large particles, the FRET process was impeded, and the dye fluorescence value returned to its unaffected state.

We then investigated whether the unexpected green fluorescence emission observed was specific to the Cy5 dye. We synthesized particles according to the same protocol (see the Supporting Information and Scheme S4), except that the Cy5 dye was substituted with another red fluorophore, Atto 647N (A647). A647 is spectrally equivalent to Cy5 (Figure S8) but has a different chemical structure. Cy5 is a carbocyanine dye, whereas A647 is a carbopyronin dye.[16] Dual-channel FLIM and FACS studies of A647-loaded NPs showed negligible green fluorescence emission (Figure S9), exhibiting I_G/I_R values generally below 0.1 (Figure S10). Similar to previous experiments, we prepared particles using different loadings of the A647 dye. FACS measurements showed that the number of events exhibiting green fluorescence was always lower than 10% (Figure S11). Thus, we confirmed that the unexpected green fluorescence and the dual-band behavior of the particles were specific effects of the chemical structure of the Cy5 dye and likely due to stacking interactions between the dye and the aromatic-rich network of the particle (Figure S7). Moreover, we confirmed that this effect was not related to any factor in the synthesis of the conjugates.

FLIM imaging also showed opposite behaviors in the Cy5- and A647-loaded particles. The fluorescence lifetime τ of the A647 dye in the NPs remarkably varied from one particle to another but followed a different trend. In small particles (**A647-PEG-NP$_{500}$**), the average τ value was 1.3 ns (Figure 2E), which was much shorter than the reported value of τ of the dye in solution (3.5 ns),[17] providing evidence for a quenching process. In large particles carrying polypeptide chains, the A647 lifetime indicated a quenching behavior; the quenching effect reduced as the size of the particles increased. The average τ value was 1.8 ns in **Fmoc-Lys(A647)-NP$_{900}$** (Figure 2F) and 2.8 ns in **Fmoc-Lys(A647)-NP$_{2500}$** (Figure 2G). For **Fmoc-Lys(A647)-NP$_{5000}$** (Figure 2H), the average lifetime of the dye of 3.7 ns was close to that of the free dye in solution. This quenching effect was likely related to a homo-FRET process between different moieties of the dye on the NPs that were brought close together. The homomolecular energy transfer was facilitated by the spectral overlap between the emission and absorption of the dye (Figure S8). As the interdye distance lengthened due to increased particle area, the homo-FRET quenching was reduced. This showed the valuable information that FLIM provides to probe the environment of the dyes used in fluorescence microscopy.[18]

Metallofluorescent Particles for Flow Cytometry and Catalysis. The next step was to construct metallofluorescent particles to produce multimodal particles for fingerprinting in

DOI: 10.1021/acsomega.7b01984
ACS Omega 2018, 3, 144−153

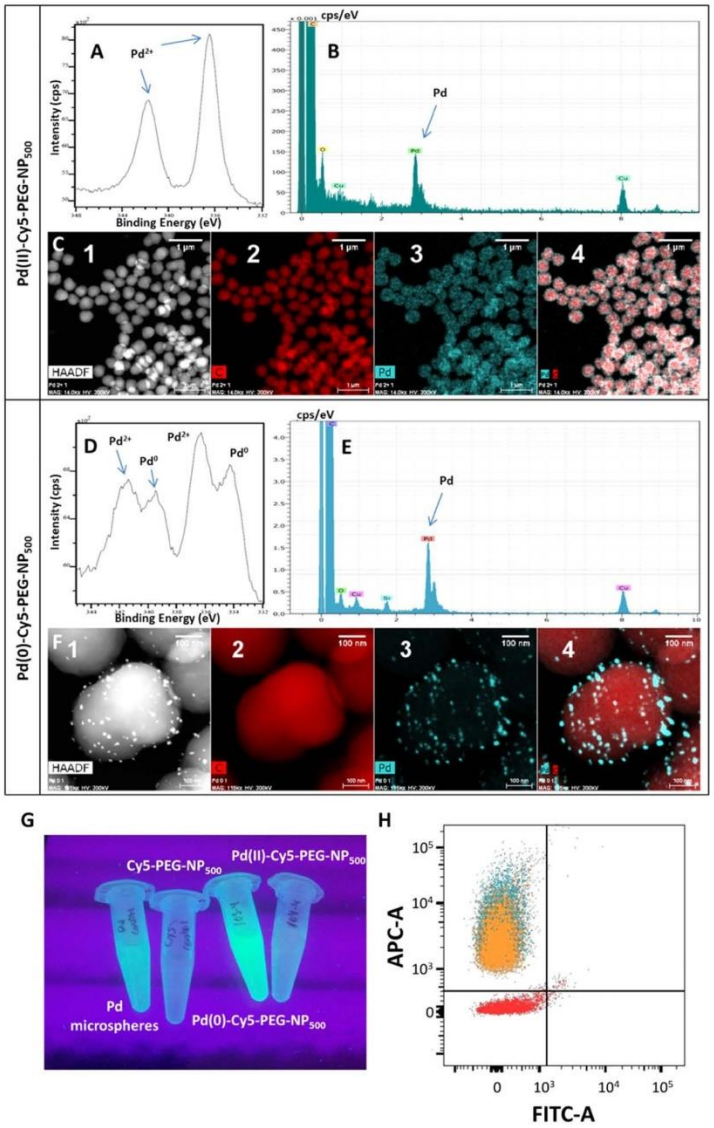

Figure 3. (A–C) XPS and EDX–HRTEM analysis of **Pd(II)-Cy5-PEG-NP$_{500}$** particles. (D–F) XPS and EDX–HRTEM analyses of **Pd(0)-Cy5-PEG-NP$_{500}$** particles. (A,D) XPS high-resolution spectra for Pd. (B,E) EDX analyses showing the presence of Pd in **Pd(II)-Cy5-PEG-NP$_{500}$** and **Pd(0)-Cy5-PEG-NP$_{500}$**. (C,F) EDX–HRTEM composite: high-angle annular dark field (HAADF) (1), carbon (2), palladium (3), and the stacked image palladium–carbon (4). (G) Evidence of the Pd(0)-catalytic activity of **Pd(0)-Cy5-PEG-NP$_{500}$** particles from the fluorogenic reaction consisting of the removal of allyloxycarbonyl groups. The fluorogenic emission is compared with a control using Pd microspheres as a catalyst. **Cy5-PEG-NP$_{500}$** and **Pd(II)-Cy5-PEG-NP$_{500}$** particles are not capable of catalyzing the reaction. (H) FACS counting of **Pd(II)-Cy5-PEG-NP$_{500}$** (cyan), **Pd(0)-Cy5-PEG-NP$_{500}$** (orange), and blank control **NH$_2$-PEG-NP$_{500}$** (red) particles.

fluorescence-based and mass spectrometry-based approaches. Palladium polystyrene NPs have been previously prepared by coordinating palladium ions with free amino groups and aromatic rings of polymer networks.[19] Herein, we exploited the conjugated polymethine chain of the Cy5 dye to create, with the polystyrene aromatic rings, an electron-rich network to coordinate metal ions. **Cy5-PEG-NP$_{500}$** was mixed with Pd(OAc)$_2$, and after 24 h of incubation, excess metal ions were washed away, leaving only metal ions that had been effectively coordinated with the particles, thereby yielding **Pd(II)-Cy5-PEG-NP$_{500}$** (Scheme S5). An in situ reduction of the Pd^{2+} ions to Pd(0) via hydrazine treatment (Schemes 1 and S6)[20] was employed to obtain **Pd(0)-Cy5-PEG-NP$_{500}$**.

The metallofluorescent NPs were then analyzed by energy-dispersive X-ray spectroscopy and high-resolution transmission electron microscopy (EDX–HRTEM) (Figures 3, S13, and S14). Both sets of particles, **Pd(II)-Cy5-PEG-NP$_{500}$** and **Pd(0)-Cy5-PEG-NP$_{500}$**, clearly presented Pd(II) and Pd(0), respectively, in the structure. The presence of the metal was evident when compared with the EDX–HRTEM results of the control **Cy5-PEG-NP$_{500}$** particles (Figure S12). An additional test to prove the effective reduction of Pd(II) to Pd(0) within

DOI: 10.1021/acsomega.7b01984
ACS Omega 2018, 3, 144–153

the NPs was performed by probing the catalytic activity of these particles, using a well-known reaction catalyzed by Pd(0), that is, removing allyloxycarbonyl protecting groups.[20,21] We used a fluorogenic version of this reaction, wherein the nonfluorescent bis-allyloxycarbonyl rhodamine was transformed into fluorescent rhodamine 110 once the protecting groups were removed (Scheme S9). The **Pd(0)-Cy5-PEG-NP$_{500}$** particles were capable of catalyzing the fluorogenic reaction (Figure 3G) to an even larger extent than the Pd microspheres used as controls.[20] This improved catalytic activity can be explained by the fact that Pd(0) nanoclusters were found within the NPs (Figures 3F and S14), thereby exhibiting a larger specific area than the Pd(0) microspheres. By contrast, **Pd(II)-Cy5-PEG-NP$_{500}$** and **Cy5-PEG-NP$_{500}$**, that is, particles carrying the Pd^{2+} cation and particles not carrying any metal at all, respectively, were not capable of facilitating the removal of the allyloxycarbonyl groups.

As another control, **H_2N-NP$_{500}$** and **Ac-HN-NP$_{500}$** (Table S1 and Schemes S7 and S8) were used to confirm if the electron-rich polymethine chain played a role in coordinating Pd ions. The **H_2N-NP$_{500}$** and **Ac-HN-NP$_{500}$** particles possessed glycine spacers, but the former presented an electron-rich environment due to the free amino groups, whereas the latter presented aromatic rings as electron-rich groups because they contained amide groups rather than free amines. These particles were treated with $Pd(OAc)_2$, following the same protocol as that described for fabricating **Pd(II)-Cy5-PEG-NP$_{500}$** and **Pd(0)-Cy5-PEG-NP$_{500}$**. All sets of particles, with and without Cy5, were characterized by X-ray photoelectron spectroscopy (XPS) (Figure S15). The XPS spectra showed that **Ac-HN-NP$_{500}$** contained lower levels of Pd(II) and traces of Pd(0), whereas the treated **H_2N-NP$_{500}$** contained similar levels of Pd(II) and Pd(0) compared with **Pd(II)-Cy5-PEG-NP$_{500}$** (Figures 3A and S15) and **Pd(0)-Cy5-PEG-NP$_{500}$** (Figures 3D and S15), respectively. This indicated that polystyrene rings were not sufficient to strongly coordinate Pd ions and require additional electron-rich functional groups to enhance coordination of Pd species to NPs. Polymethine groups of the Cy5 dye coupled to polystyrene NPs offered an optimal environment to coordinate metals such as Pd.

Interestingly, the coordination of Pd^{2+} ions in the electron-rich network of the conjugated double bonds of the cyanine dye and the polystyrene rings was found to have an effect on the green fluorescence emission caused by the direct interaction between these moieties of the NPs. Indeed, FACS experiments showed that the green fluorescence emission was completely removed upon coordination of Pd^{2+} ions (Figures 3H and 4), supporting the proposed model for the $\pi-\pi$-stacking interaction causing the green emission (Figure S7) and the model for the coordination of Pd^{2+} (Figure 5A). Moreover, the reduction of Pd^{2+} to Pd(0) in the **Pd(0)-Cy5-PEG-NP$_{500}$** particles did not considerably change the fluorescent properties of the particle (Figures 3H and 4), confirming that the reduction did not alter the spatial arrangement of the metal (Figure 5A). Two others metal ions, Ni^{2+} and Cu^{+}, were also used to produce more metallofluorescent NPs following the same approach. A dim quenching effect of the Cy5 fluorescence in the red channel was observed by FACS for all metal particles (Figure S16). Most importantly, the presence of these metal ions caused the fluorescence emission in the green channel to mostly disappear when analyzed by FACS, suggesting a similar coordination mechanism as that of Pd^{2+} ions.

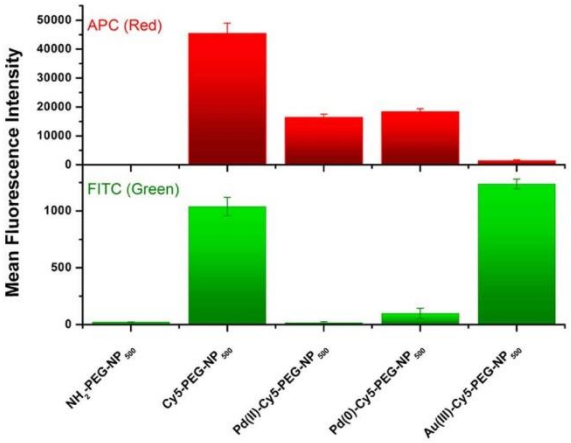

Figure 4. APC (red) and FITC (green) channels mean fluorescence intensities from FACS experiments of **NH_2-PEG-NP$_{500}$**, **Cy5-PEG-NP$_{500}$**, **Pd(II)-Cy5-PEG-NP$_{500}$**, **Pd(0)-Cy5-PEG-NP$_{500}$**, and NPs incubated with $HAuC_4{\cdot}3H_2O$ [**Au(III)-Cy5-PEG-NP$_{500}$**].

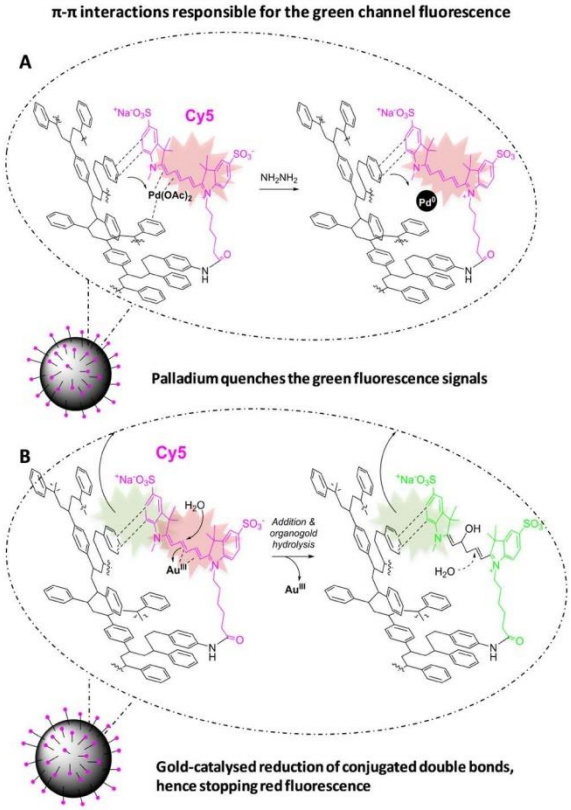

Figure 5. $\pi-\pi$ interactions taking place within polystyrene and Cy5. (A) $Pd(OAc)_2$ and Pd(0) particles hinder the $\pi-\pi$ interactions. (B) Gold catalyzes the reduction of Cy5-conjugated double bonds.

To provide further insights into the role of the polymethine chain in the interactions behind the manifestation of green fluorescence from red-emitting dyes, we studied whether the interruption of the electronic conjugation of the system could affect the fluorescent properties of the NPs. To this end, we

DOI: 10.1021/acsomega.7b01984
ACS Omega 2018, 3, 144−153

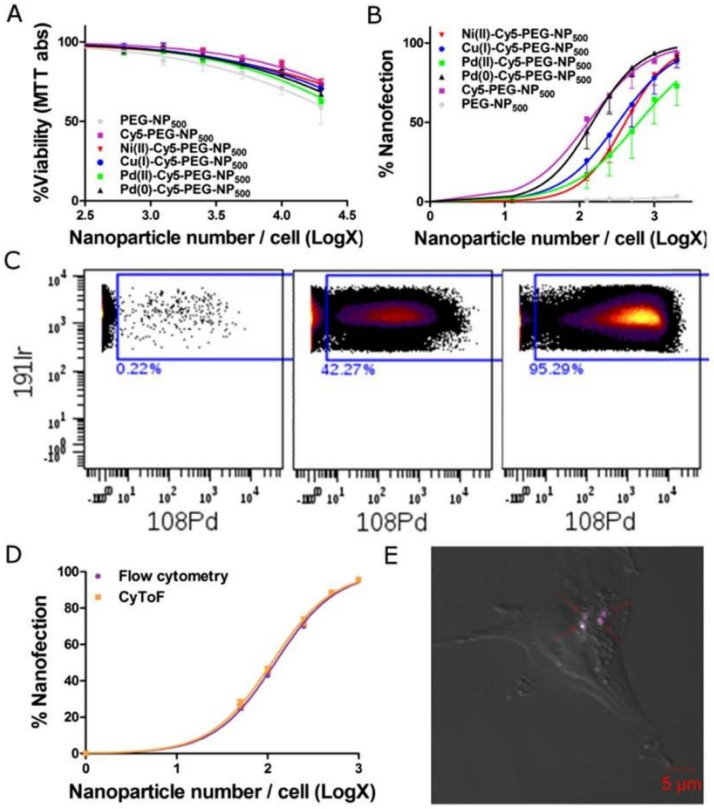

Figure 6. (A) Cellular viability (MTT assay) of MDA-MB-231 cells nanofected for 6 days with metallofluorescent NPs expressed as a percentage of the control nonnanofected cells. Data are reported as the mean ± SEM of four independent experiments conducted in triplicate. (B) Analysis of metallofluorescent NP cellular uptake by MDA-MB-231 cells at different ratios per cell measured using flow cytometry. Data are reported as the mean ± SEM of four independent experiments. (C) Representative CyToF scatterplots of the **Pd(0)-Cy5-PEG-NP$_{500}$** uptake percentage as the number of NPs increases (0, 100, and 1000 NPs/cell). ^{191}Ir was used for nuclei staining. (D) Comparison of **Pd(0)-Cy5-PEG-NP$_{500}$** uptake curves in the same cells using flow cytometry and CyToF. Data are reported as the mean ± SEM of four independent experiments. Two-way ANOVA analysis followed by Bonferroni post hoc test showed no differences between techniques. (E) Confocal microscopy image of a representative nanofected cell at a ratio of 3000 **Pd(0)-Cy5-PEG-NP$_{500}$**/cell. Arrows point to single NPs in the cell cytoplasm.

tested the effect of gold ions ($HAuCl_4 \cdot 3H_2O$) over the Cy5 fluorophore. Au(III) ions are capable of catalyzing addition reactions to alkenes.[22] We found that Au(III) ions catalyzed the breakage of the polymethine chain conjugation in Cy5, as evidenced by an immediate color loss from blue to transparent, when Au(III) was added to an aqueous solution of the dye. This color loss was supported by the total disappearance of the typical Cy5 absorption spectrum, after treatment with Au(III) (Figure S17). With these properties in mind, we treated **Cy5-PEG-NP$_{500}$** particles with $HAuCl_4 \cdot 3H_2O$. Following treatment, NPs were washed and analyzed by FACS and XPS. Remarkably, the FACS analysis showed the disappearance of the red fluorescence signal, whereas the green fluorescence signal remained unmodified compared with untreated **Cy5-PEG-NP$_{500}$** (Figure 4). XPS analyses of these particles showed traces of gold. This indicated that the disappearance of red fluorescence was not due to metal quenching but due to gold catalyzing addition reactions to the conjugated double bonds of the Cy5 dye, thereby breaking the electronic conjugation of the polymethine chain (Figure 5B). However, green fluorescence signals were unaltered, suggesting that this signal comes from aromatic interactions between the heterocyclic moieties of the dye and polystyrene chains without intervention from the polymethine chain (Figure 5B). With these experiments, we clearly identified the source of the double-band fluorescence emission behavior in Cy5-loaded NPs.

We previously reported the versatility of cross-linked polystyrene-based nano-/microparticles for the nanofection of a plethora of cell lines and primary cultures.[9,20,23] To prove the feasibility of using these novel metallofluorescent NPs to nanofect mammalian cells in live cell cultures, breast cancer cell line MDA-MB-231 was used. Cells were incubated with these particles for up to 6 days before measuring cell viability. Cells nanofected with metallofluorescent particles presented viability similar to those nanofected with the control, **NH$_2$-PEG-NP$_{500}$**, even at high NP loadings (Figure 6A). This indicated that the metal ions did not leach out in the cells. The efficient uptake of the metallofluorescent NPs was also confirmed by FACS analysis. As shown in Figure 6B, a greater number of NPs employed during nanofection resulted in a higher percentage of cells containing the metallofluorescent NPs. The multiplicity of nanofection 50 (MNF50) values[24] of the different metallofluorescent particles was the same order of magnitude as that of the control **Cy5-PEG-NP$_{500}$** (Figure 6B).

To validate the multimodal applications of the metallofluorescent NPs and confirm that these particles transported

DOI: 10.1021/acsomega.7b01984
ACS Omega 2018, 3, 144−153

metals into cells, **Pd(0)-Cy5-PEG-NP$_{500}$** was used at different concentrations. MDA-MB-231 cells were incubated with **Pd(0)-Cy5-PEG-NP$_{500}$**, split into two aliquots, and analyzed using flow cytometry and CyToF. For cells analyzed using CyToF, a DNA marker labeled with iridium was used to record instances, when both iridium (cell nuclei marker) and palladium (present in NPs) were present in the nanofected cells as a positive event (Figures 6C and S18). CyToF dot plots confirmed that cells were nanofected with particles carrying Pd(0) without any evident toxic effects. Moreover, a comparison of the percentages of nanofected cells (Figure 6D) showed no differences between the values from flow cytometry detection and those from CyToF detection. These results confirmed that **Pd(0)-Cy5-PEG-NP$_{500}$** was a suitable dual marker for flow cytometry and CyToF in living cells and did not negatively affect the cell growth. Moreover, an NP size of 500 nm guaranteed cellular uptake and the complete burning and ionization of the beads in the inductively coupled plasma (ICP) torch for CyToF. As shown in Figures 6E and S19, these particles were detectable by confocal microscopy, enabling localization or colocalization studies and the direct counting of NPs in a cell (Figure S20). The practical combination of red-emitting particles with different metals served to provide different fingerprinting options for CyToF applications, facilitating cell barcoding for cell-based multiplexing assays.

■ CONCLUSIONS

The synthesis and characterization of multimodal particles featuring fluorophores and metals were reported. We validated the use of these particles as cell trackers detectable by fluorescence microscopy, CyToF, and FACS. The Cy5-labeled particles presented characteristic dual-band emission, in which the fluorescence originated exclusively from a single dye in two different states. This characteristic emission profile may be considered a fingerprint of our particles for FACS and fluorescence microscopy experiments. The particles carrying both Cy5 and metal cations enabled multiplex fingerprinting and cell barcoding using tandem FACS and CyToF. Finally, the possibility of reducing Pd^{2+} ions to Pd(0) in situ provides new possibilities for multimodal particles, such as carrying a red fluorophore for fluorescence applications while acting as in situ catalysts for Pd chemistry.

■ EXPERIMENTAL SECTION

Multimodal, Red-Emitting Particles and Metallofluorescent NPs. We prepared an extensive series of modified particles, including red-emitting fluorophores, such as sulfo-Cy5 or A647. The fluorophores were attached to the particles via PEG spacers of different lengths or via spacers suitable for secondary modifications, including those featuring either Fmoc-protected amino acids or streptavidin. Additionally, different metallofluorescent particles containing the red fluorophore sulfo-Cy5 and different metal isotopes were prepared by exploiting the chelating properties of π bonds in the dye and PEG units to the metals. Tables 1 and S1 summarize the nomenclature and design of the particles prepared in this work. The initial 500, 900, and 1200 nm aminomethyl cross-linked polystyrene NPs (Figure S1) were synthesized according to our established protocols.[9] Then, different reactions allowed the incorporation of the fluorescent dyes and other modifications. Further details on the synthetic steps of all particle structures developed in this work can be found in the Supporting Information (Schemes S1−S8).

General Method for Metallofluorescent Particle Loading. All chemical reactions were performed over dried NPs. When the reactions were finished, the NPs were washed three times using suspension−centrifugation cycles. The 500, 900, and 1200 nm aminomethyl cross-linked polystyrene NPs were functionalized with chemical spacers, such as Fmoc-protected PEG and Fmoc-lysine-Dde(OH), using oxyma and *N*,*N*′-diisopropylcarbodiimide (DIC), at 60 °C for 2 h. Subsequent Fmoc and Dde removal was performed using a 20% piperidine solution in dimethylformamide (DMF) and using a mixture of hydroxylamine hydrochloride/imidazole in *N*-methyl-2-pyrrolidone/DMF.[25] The fluorophore conjugation step was carried out using a sulfo-Cy5 NHS ester solution in DMF with *N*,*N*-diisopropylethylamine at room temperature for 14 h. Afterward, the fluorescent NPs were mixed with a palladium diacetate ($Pd(OAc)_2$) solution in DMF and were stirred at room temperature for 14 h. To generate the in situ reduction of Pd^{2+} into Pd^0, the Pd^{2+} metallofluorescent NPs were mixed with a 10% hydrazine solution in methanol at room temperature for 30 min.[20,21] Finally, to obtain streptavidin-conjugated NPs, the fluorescent NPs were functionalized with a 25% glutaraldehyde solution in H_2O and a streptavidin solution in phosphate buffer saline (PBS), at room temperature for 14 h. Subsequently, the NPs were mixed with a $NaBH_3CN$ solution in PBS/EtOH (3:1) and washed with ethanolamine in bovine serum albumin solution in PBS.

Fluorescence Lifetime Imaging Microscopy (FLIM) and Spectroscopy. A MicroTime 200 (PicoQuant GmbH, Germany) was used to collect FLIM images in two different detection channels, green and red, after a 470 nm pulsed excitation. The system was equipped with an Andor Shamrock 303i-A spectrograph and an ultrasensitive Andor Newton electron multiplying CCD camera to simultaneously collect the entire fluorescence emission spectrum from different points of the images. Further instrumental details can be found in the Supporting Information and Figure S2.

Confocal Fluorescence Microscopy. A Leica DMi8 confocal microscope was used for dual-color fluorescence imaging, equipped with a Lumencore solid-state white light source, a PL Apo CS2 oil immersion objective (63×, 1.4 NA), and an Andor Zyla CSMOS camera for imaging. The green channel was collected with a 480/40 nm excitation bandpass filter, a 505 nm dichroic mirror, and a 527/30 nm emission bandpass filter, whereas the red channel was obtained using a 620/60 nm bandpass filter for the excitation, a 660 nm dichroic mirror, and a 700/75 nm bandpass emission filter.

Fluorescence-Activated Cell Sorting (FACS). The fluorescence emission of the particles carrying red dyes (either Cy5 or A647) was assessed using flow cytometry analysis with BD FACSCanto II (Becton Dickinson & Co., NJ, USA) equipped with a solid-state Coherent Sapphire blue laser refrigerated by air (488 nm and 20 mW power), a JDS uniphase HeNe red laser (633 nm and 17 mW), and eight detectors (six fluorescence detectors and two morphologic parameters). The red emission fluorescence was detected in the APC channel (660/20 nm). Unexpected "green emission" was measured using the FITC channel (530/30 nm).

Mass Cytometry. Mass cytometry analysis was performed using Helios CyTOF2 (DVS Sciences, Fluidigm Co., CA, USA). This instrument used an ICP time-of-flight mass spectrometer to detect a mass range of 75−209 amu in 135

DOI: 10.1021/acsomega.7b01984
ACS Omega 2018, 3, 144−153

different channels at an average event rate of 500 events/s, a highest rate of 2000 events/s, and a sensitivity of 0.3% for ^{159}Tb.

X-ray Photoelectron Spectroscopy. The presence of palladium was determined by monitoring the profile of Pd 3d photoemission. XPS spectra were obtained using a Kratos Axis Ultra-DLD X-ray photoelectron spectrometer equipped with an Al monochromatic X-ray source, over powdered nanoparticle samples. General spectra were obtained with a pass energy of 160 eV, the X-ray source was operated at 75 W, the high-resolution spectra were obtained with a pass energy of 20 eV, and the X-ray source was operated at 225 W.

High-Resolution Transmission Electron Microscopy (HRTEM) and Energy-Dispersive X-ray (EDX) Analyses. Transmission electron microscopy experiments were carried out using an ultrahigh-resolution FEI Titan G2 microscope with an XFEG field emission gun operating at 300 kV. The microscope was fitted with a high-angle annular dark field (HAADF) detector to operate in scanning transmission electron microscopy (STEM) mode and with an FEI microanalysis system for EDX. The microscope reached maximum resolutions of 0.8 Å in the TEM mode and 2 Å in the STEM mode. To analyze samples, the NPs were suspended in absolute ethanol and supported on ultra-thin carbon 200 mesh Cu grids.

■ ASSOCIATED CONTENT

Supporting Information

The Supporting Information is available free of charge on the ACS Publications website at DOI: 10.1021/acsomega.7b01984.

Table of synthesized particles; experimental details on the synthesis and loading of polystyrene NPs, metallofluorescent NPs, and glycine and capped glycine NPs, fluorescence lifetime imaging microscopy (FLIM) and spectroscopy, additional results of Cy5-carrying NPs, scheme of stacking interactions causing green fluorescence and FRET, additional results of Atto 647N-carrying NPs, fluorogenic reaction catalyzed by Pd(0), additional results of metallofluorescent NPs, Au(III) ions catalyze the breakage of the polymethine chain of Cy5, and live cell metallofluorescent particle uptake (PDF)

■ AUTHOR INFORMATION

Corresponding Authors

*E-mail: juandiaz@ugr.es (J.J.D.-M.).
*E-mail: angelort@ugr.es. Phone: (+34) 958243825 (A.O.).

ORCID

Maria J. Ruedas-Rama: 0000-0003-0853-187X
Asier Unciti-Broceta: 0000-0003-1029-2855
Angel Orte: 0000-0003-1905-4183

Present Address

[⊥]School of Pharmacy, University of Bradford, Bradford, West Yorkshire, BD7 1DP, United Kingdom (T.V.).

Author Contributions

The manuscript was written through contributions of all authors. All authors have given approval to the final version of the manuscript.

Notes

The authors declare no competing financial interest.

■ ACKNOWLEDGMENTS

This work was funded by the Consejeria de Economia, Innovacion, Ciencia y Empleo (Junta de Andalucia, grant BIO-1778), the Spanish Ministry of Economy and Competitiveness (grants BIO2016-80519-R and CTQ2014-56370-R) and the Fundación Ramón Areces. A.D.-G. acknowledges scholarships from the Spanish Ministry of Education (grant FPU14/02181) and the University of Granada, PhD programme in Biomedicine. T.V. thanks the Talentia Postdoc Fellowship Programme (grant 267226, co-funded by the Andalusian Knowledge Agency and the 7th Framework Program of the European Union). A.U.-B. is grateful to the EPSRC (EP/N021134/1) for funding. The authors thank the staff at the microscopy facility of the Centre for Integrative Biology (CIBIO) of the University of Trento (Italy), the staff at the electron microscopy facilities of the Centre for Scientific Instrumentation (CIC) of the University of Granada, and the staff at the Flow Cytometry unit at the Pfizer-University of Granada-Junta de Andalucia Centre for Genomics and Oncological Research (GENYO).

■ REFERENCES

(1) Freeman, R.; Willner, I. *Chem. Soc. Rev.* **2012**, *41*, 4067−4085.
(2) Ruedas-Rama, M. J.; Walters, J. D.; Orte, A.; Hall, E. A. H. *Anal. Chim. Acta* **2012**, *751*, 1−23.
(3) Yeh, Y.-C.; Creran, B.; Rotello, V. M. *Nanoscale* **2012**, *4*, 1871−1880.
(4) Blanco, E.; Shen, H.; Ferrari, M. *Nat. Biotechnol.* **2015**, *33*, 941−951.
(5) Chen, G.; Roy, I.; Yang, C.; Prasad, P. N. *Chem. Rev.* **2016**, *116*, 2826−2885.
(6) Lee, D.-E.; Koo, H.; Sun, I.-C.; Ryu, J. H.; Kim, K.; Kwon, I. C. *Chem. Soc. Rev.* **2012**, *41*, 2656−2672.
(7) Goesmann, H.; Feldmann, C. *Angew. Chem., Int. Ed.* **2010**, *49*, 1362−1395.
(8) Kusumi, A.; Tsunoyama, T. A.; Hirosawa, K. M.; Kasai, R. S.; Fujiwara, T. K. *Nat. Chem. Biol.* **2014**, *10*, 524−532.
(9) Sanchez-Martin, R. M.; Muzerelle, M.; Chitkul, N.; How, S. E.; Mittoo, S.; Bradley, M. *ChemBioChem* **2005**, *6*, 1341−1345.
(10) Tanner, S. D.; Baranov, V. I.; Ornatsky, O. I.; Bandura, D. R.; George, T. C. *Cancer Immunol. Immunother.* **2013**, *62*, 955−965.
(11) Spitzer, M. H.; Nolan, G. P. *Cell* **2016**, *165*, 780−791.
(12) Armitage, B. A. *Top. Curr. Chem.* **2005**, *253*, 55−76.
(13) Lim, I.-I. S.; Goroleski, F.; Mott, D.; Kariuki, N.; Ip, W.; Luo, J.; Zhong, C.-J. *J. Phys. Chem. B* **2006**, *110*, 6673−6682.
(14) Buschmann, V.; Weston, K. D.; Sauer, M. *Bioconjugate Chem.* **2003**, *14*, 195−204.
(15) Zhao, M.; Huang, R.; Peng, L. *Opt. Express* **2012**, *20*, 26806−26827.
(16) Stennett, E. M. S.; Ciuba, M. A.; Levitus, M. *Chem. Soc. Rev.* **2014**, *43*, 1057−1075.
(17) ATTO 647N Product Datasheet. http://www.atto-tec.com (accessed March 2017).
(18) Ruedas-Rama, M.; Alvarez-Pez, J.; Crovetto, L.; Paredes, J.; Orte, A. *Advanced Photon Counting*; Kapusta, P., Wahl, M., Erdmann, R., Eds.; Springer International Publishing, 2015; pp 191−223.
(19) Weiss, J. T.; Dawson, J. C.; Fraser, C.; Rybski, W.; Torres-Sánchez, C.; Bradley, M.; Patton, E. E.; Carragher, N. O.; Unciti-Broceta, A. *J. Med. Chem.* **2014**, *57*, 5395−5404.
(20) Unciti-Broceta, A.; Johansson, E. M. V.; Yusop, R. M.; Sánchez-Martín, R. M.; Bradley, M. *Nat. Protoc.* **2012**, *7*, 1207−1218.
(21) Yusop, R. M.; Unciti-Broceta, A.; Johansson, E. M. V.; Sánchez-Martín, R. M.; Bradley, M. *Nat. Chem.* **2011**, *3*, 239−243.
(22) Rezsnyak, C. E.; Autschbach, J.; Atwood, J. D.; Moncho, S. *J. Coord. Chem.* **2013**, *66*, 1153−1165.

DOI: 10.1021/acsomega.7b01984
ACS Omega 2018, 3, 144−153

(23) Unciti-Broceta, A.; Díaz-Mochón, J. J.; Sánchez-Martín, R. M.; Bradley, M. *Acc. Chem. Res.* **2012**, *45*, 1140−1152.
(24) Unciti-Broceta, J. D.; Cano-Cortés, V.; Altea-Manzano, P.; Pernagallo, S.; Díaz-Mochón, J. J.; Sánchez-Martín, R. M. *Sci. Rep.* **2015**, *5*, 10091.
(25) Díaz-Mochón, J. J.; Bialy, L.; Bradley, M. *Org. Lett.* **2004**, *6*, 1127−1129.

DOI: 10.1021/acsomega.7b01984
ACS Omega 2018, 3, 144−153

6.2. Appendix 2 – Scheme 1

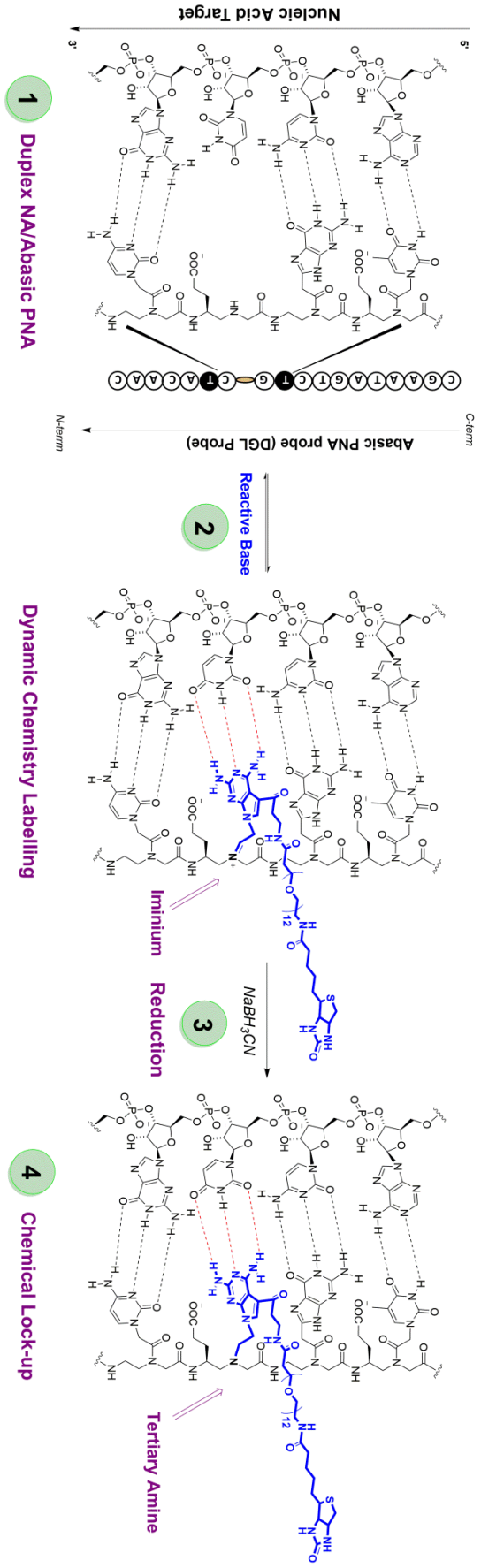

6.3. Appendix 3 – Figure 24

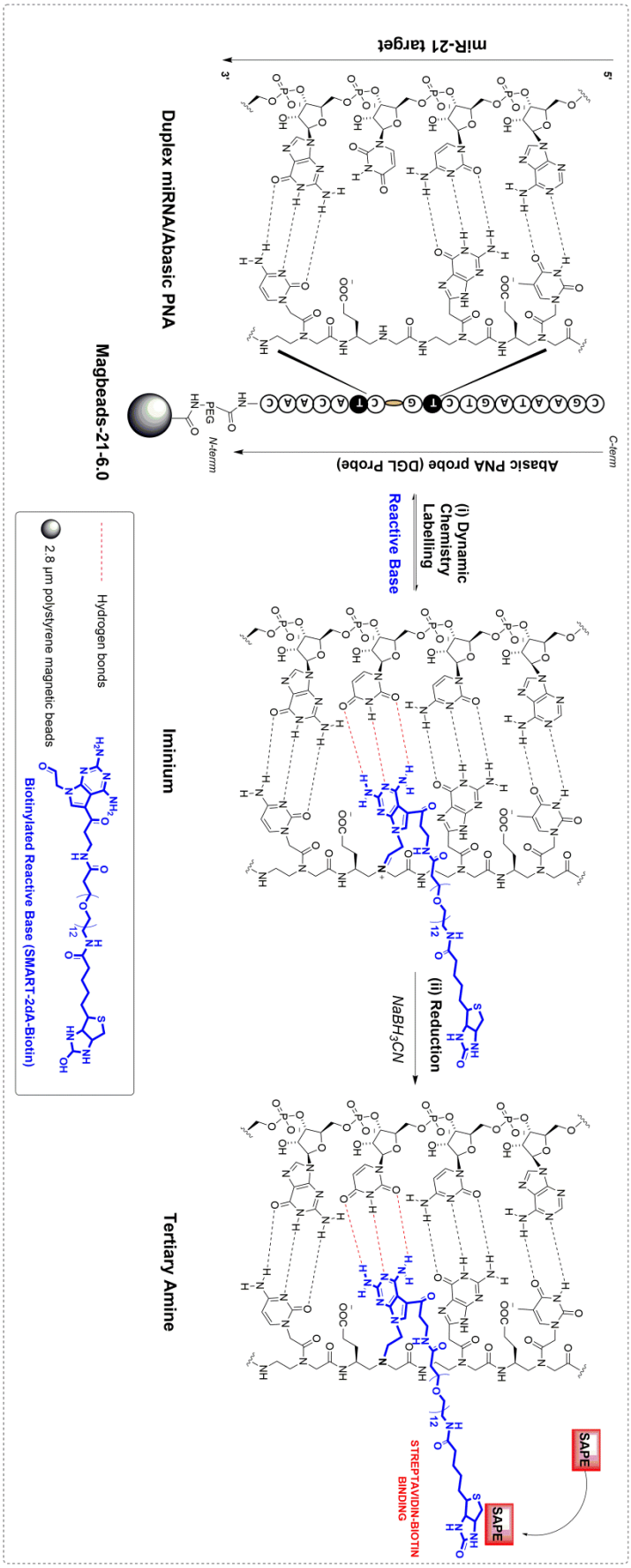

6.4. Appendix 4 – Short-term stay at the University of Edinburgh

While nucleic acid analysis by dynamic chemistry has been validated for end-point reading, the large number of real-time readers placed in many molecular biology labs makes very appealing the idea to adapt this novel chemistry for real-time applications. Thus, during the short-term stay it was proposed the development of novel BODIPY labelled Smart-NBs for nucleic acid detection by dynamic chemistry through real-time fluorescence reading. These BODIPYs-labelled to the Smart-NBs would not present a high fluorescent signal *per se*. Nevertheless, upon dynamic chemistry reaction between the nucleic acid of study and the DGL probe, BODIPY-labelled Smart-NB incorporation occurs. Due to the interaction between the BODIPY and the hydrophobic microenvironment (PNA-Nucleic Acid duplex), a high fluorescent signal would be released, enabling its identification through Real-Time Fluorescence approach (Figure 84).

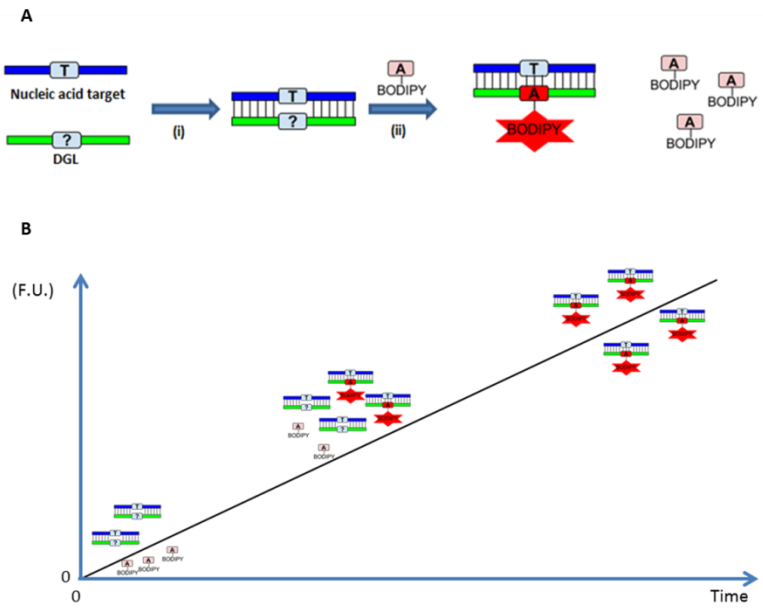

Figure 85. A) Once BODIPY labelled SMART-Nucleobase is incoporated into the PNA-Nucleic Acid dúplex [steps (i) and (ii)] a high fluorescent signal will be realised whilst if BODIPY labelled SMART-Nucleobases is not incorporated, the fluorescence will be much lower. **B)** Real-Time Fluoresence approach reading: at T0 there is not BODIPY labelled SMART-Nucleobase incorporation (not appreciable fluorescence), but when the time elapses, owe to a higher dynamic incorporation, an important fluorescence increase is obtained

As a result, a synthetic route (not shown – unpublished) was designed for the synthesis of near infrared (NIR) BODIPY-labelled Smart-NBs. This led to the synthesis of two stable final NIR BODIPY compounds amongst 16 different compounds.

6.5. Appendix 5 – Rights and Permissions

6.5.1. Figure 1

Figure 3.b and 3.c from “Biotech baby boom”, John Hodgson, *Nature Biotechnology* **37**, 502–512 (2019). Reference number 18.

Copyright Clearance Center RightsLink®

Home | Account Info | Help | LIVE CHAT

SPRINGER NATURE

Title: Biotech’s baby boom
Author: John Hodgson
Publication: Nature Biotechnology
Publisher: Springer Nature
Date: May 3, 2019
Copyright © 2019, Springer Nature

Logged in as:
Antonio Delgado-Gonzalez
LOGOUT

Order Completed

Thank you for your order.

This Agreement between Mr. Delgado-Gonzlaez A ("You") and Springer Nature ("Springer Nature") consists of your license details and the terms and conditions provided by Springer Nature and Copyright Clearance Center.

Your confirmation email will contain your order number for future reference.

printable details

License Number	4611850312207
License date	Jun 18, 2019

6.5.2. Figure 35 and Figure 36

Figures 2 and 4 from “A deep profiler’s guide to cytometry”, Sean C. Bendall,Garry P. Nolan,Mario Roederer,Pratip K. Chattopadhyay, *Trends in Immunology* **33(7)**, 323–332 (2012). Reference number 216.

Copyright Clearance Center RightsLink®

Home | Account Info | Help | LIVE CHAT

Title: A deep profiler's guide to cytometry
Author: Sean C. Bendall,Garry P. Nolan,Mario Roederer,Pratip K. Chattopadhyay
Publication: Trends in Immunology
Publisher: Elsevier
Date: July 2012
Published by Elsevier Ltd.

Logged in as:
Antonio Delgado-Gonzalez
Account #: 3001470900
LOGOUT

Order Completed

Thank you for your order.

This Agreement between Mr. Delgado-Gonzlaez A ("You") and Elsevier ("Elsevier") consists of your license details and the terms and conditions provided by Elsevier and Copyright Clearance Center.

Your confirmation email will contain your order number for future reference.

printable details

License Number	4613150496814
License date	Jun 20, 2019

CHAPTER VII

7. Bibliography

[1] Verma, A. S.; Agrahari, S.; Rastogi, S.; Singh, A. Biotechnology in the Realm of History. *J. Pharm. Bioallied Sci.* **2011**, *3* (3), 321.

[2] Watson, J. D.; Crick, F. H. C. Molecular Structure of Nucleic Acids: A Structure for Deoxyribose Nucleic Acid. *Nature* **1953**, *171* (4356), 737.

[3] Franklin, R. E.; Gosling, R. G. Evidence for 2-Chain Helix in Crystalline Structure of Sodium Deoxyribonucleate. *Nature* **1953**, *172* (4369), 156.

[4] Franklin, R. E.; Gosling, R. G. Molecular Configuration in Sodium Thymonucleate. *Nature* **1953**, *171* (4356), 740.

[5] Wilkins, M. H. F.; Seeds, W. E.; Stokes, A. R.; Wilson, H. R. Helical Structure of Crystalline Deoxypentose Nucleic Acid. *Nature* **1953**, *172* (4382), 759.

[6] Grunberg-Manago, M.; Ochoa, S. ENZYMATIC SYNTHESIS AND BREAKDOWN OF POLYNUCLEOTIDES; POLYNUCLEOTIDE PHOSPHORYLASE1. *J. Am. Chem. Soc.* **1955**, *77* (11), 3165–3166.

[7] Bessman, M. J.; Lehman, I. R.; Simms, E. S.; Kornberg, A. Enzymatic Synthesis of Deoxyribonucleic Acid II. GENERAL PROPERTIES OF THE REACTION. *J. Biol. Chem.* **1958**, *233* (1), 171–177.

[8] Lehman, I. R.; Bessman, M. J.; Simms, E. S.; Kornberg, A. Enzymatic Synthesis of Deoxyribonucleic Acid I. PREPARATION OF SUBSTRATES AND PARTIAL PURIFICATION OF AN ENZYME FROM ESCHERICHIA COLI. *J. Biol. Chem.* **1958**, *233* (1), 163–170.

[9] Cobb, M. Who Discovered Messenger RNA? *Curr. Biol.* **2015**, *25* (13), R526–R532.

[10] Nirenberg, M. W.; Matthaei, J. H. THE DEPENDENCE OF CELL- FREE PROTEIN SYNTHESIS IN E. COLI UPON NATURALLY OCCURRING OR SYNTHETIC POLYRIBONUCLEOTIDES. *Proc. Natl. Acad. Sci. U. S. A.* **1961**, *47* (10), 1588–1602.

[11] Marshall, R. E.; Caskey, C. T.; Nirenberg, M. Fine Structure of RNA Codewords Recognized by Bacterial, Amphibian, and Mammalian Transfer RNA. *Science* **1967**, *155* (3764), 820–826.

[12] Shimomura, O.; Johnson, F. H.; Saiga, Y. Extraction, Purification and Properties of Aequorin, a Bioluminescent Protein from the Luminous Hydromedusan, Aequorea. *J. Cell. Comp. Physiol.* **1962**, *59*, 223–239.

[13] Starting off DNA with RNA. *Nature* **1972**, *239* (5366), 7.

[14] Cohen, S. N.; Chang, A. C. Y.; Boyer, H. W.; Helling, R. B. Construction of Biologically Functional Bacterial Plasmids In Vitro. *Proc. Natl. Acad. Sci. U. S. A.* **1973**, *70* (11), 3240–3244.

[15] Köhler, G.; Milstein, C. Continuous Cultures of Fused Cells Secreting Antibody of Predefined Specificity. *Nature* **1975**, *256* (5517), 495.

[16] Sanger, F.; Nicklen, S.; Coulson, A. R. DNA Sequencing with Chain-Terminating Inhibitors. *Proc. Natl. Acad. Sci. U. S. A.* **1977**, *74* (12), 5463–5467.

[17] Venter, J. C.; Adams, M. D.; Myers, E. W.; Li, P. W.; Mural, R. J.; Sutton, G. G.; Smith, H. O.; Yandell, M.; Evans, C. A.; Holt, R. A.; et al. The Sequence of the Human Genome. *Science* **2001**, *291* (5507), 1304–1351.

[18] Initial Sequencing and Analysis of the Human Genome. *Nature* **2001**, *409* (6822), 860.

[19] Gibson, D. G.; Glass, J. I.; Lartigue, C.; Noskov, V. N.; Chuang, R.-Y.; Algire, M. A.; Benders, G. A.; Montague, M. G.; Ma, L.; Moodie, M. M.; et al. Creation of a Bacterial Cell Controlled by a Chemically Synthesized Genome. *Science* **2010**, *329* (5987), 52–56.

[20] Jinek, M.; Chylinski, K.; Fonfara, I.; Hauer, M.; Doudna, J. A.; Charpentier, E. A Programmable Dual-RNA-Guided DNA Endonuclease in Adaptive Bacterial Immunity. *Science* **2012**, *337* (6096), 816–821.

[21] Ran, F. A.; Hsu, P. D.; Wright, J.; Agarwala, V.; Scott, D. A.; Zhang, F. Genome Engineering Using the CRISPR-Cas9 System. *Nat. Protoc.* **2013**, *8* (11), 2281–2308.

[22] Hodgson, J. Biotech's Baby Boom. *Nat. Biotechnol.* **2019**, *37* (5), 502.

[23] Binnig, G.; Rohrer, H.; Gerber, Ch.; Weibel, E. Surface Studies by Scanning Tunneling Microscopy. *Phys. Rev. Lett.* **1982**, *49* (1), 57–61.

[24] Drexler, K. E. Molecular Engineering: An Approach to the Development of General Capabilities for Molecular Manipulation. *Proc. Natl. Acad. Sci.* **1981**, *78* (9), 5275–5278.

[25] Drexler, K. E. Molecular Machinery and Manufacturing with Applications to Computation. Thesis, Massachusetts Institute of Technology, 1991.

[26] Kroto, H. W.; Heath, J. R.; O'Brien, S. C.; Curl, R. F.; Smalley, R. E. C 60 : Buckminsterfullerene. *Nature* **1985**, *318* (6042), 162.

[27] Brus, L. E. Electron–Electron and Electron-hole Interactions in Small Semiconductor Crystallites: The Size Dependence of the Lowest Excited Electronic State. *J. Chem. Phys.* **1984**, *80* (9), 4403–4409.

[28] Iijima, S. Helical Microtubules of Graphitic Carbon. *Nature* **1991**, *354* (6348), 56.

[29] Lee, H. J.; Ho, W. Single-Bond Formation and Characterization with a Scanning Tunneling Microscope. *Science* **1999**, *286* (5445), 1719–1722.

[30] Omabegho, T.; Sha, R.; Seeman, N. C. A Bipedal DNA Brownian Motor with Coordinated Legs. *Science* **2009**, *324* (5923), 67–71.

[31] Gu, H.; Chao, J.; Xiao, S.-J.; Seeman, N. C. Dynamic Patterning Programmed by DNA Tiles Captured on a DNA Origami Substrate. *Nat. Nanotechnol.* **2009**, *4* (4), 245–248.

[32] Gu, H.; Chao, J.; Xiao, S.-J.; Seeman, N. C. A Proximity-Based Programmable DNA Nanoscale Assembly Line. *Nature* **2010**, *465* (7295), 202–205.

[33] Dietrich-Buchecker, C. O.; Sauvage, J. P.; Kintzinger, J. P. Une Nouvelle Famille de Molecules : Les Metallo-Catenanes. *Tetrahedron Lett.* **1983**, *24* (46), 5095–5098.

[34] Dietrich-Buchecker, C. O.; Sauvage, J. P.; Kern, J. M. Templated Synthesis of Interlocked Macrocyclic Ligands: The Catenands. *J. Am. Chem. Soc.* **1984**, *106* (10), 3043–3045.

[35] Anelli, P. L.; Spencer, N.; Stoddart, J. F. A Molecular Shuttle. *J. Am. Chem. Soc.* **1991**, *113* (13), 5131–5133.

[36] Koumura, N.; Zijlstra, R. W. J.; Delden, R. A. van; Harada, N.; Feringa, B. L. Light-Driven Monodirectional Molecular Rotor. *Nature* **1999**, *401* (6749), 152.

[37] Yoshida, M.; Lahann, J. Smart Nanomaterials. *ACS Nano* **2008**, *2* (6), 1101–1107.

[38] Lee, D.-E.; Koo, H.; Sun, I.-C.; Ryu, J. H.; Kim, K.; Kwon, I. C. Multifunctional Nanoparticles for Multimodal Imaging and Theragnosis. *Chem. Soc. Rev.* **2012**, *41* (7), 2656–2672.

[39] Chen, G.; Roy, I.; Yang, C.; Prasad, P. N. Nanochemistry and Nanomedicine for Nanoparticle-Based Diagnostics and Therapy. *Chem. Rev.* **2016**, *116* (5), 2826–2885.

[40] Sun, X.; Lei, Y. Fluorescent Carbon Dots and Their Sensing Applications. *TrAC Trends Anal. Chem.* **2017**, *89*, 163–180.

[41] Tabish, T. A.; Zhang, S. Graphene Quantum Dots: Syntheses, Properties, and Biological Applications☆. In *Comprehensive Nanoscience and Nanotechnology (Second Edition)*; Andrews, D. L., Lipson, R. H., Nann, T., Eds.; Academic Press: Oxford, 2016; pp 171–192.

[42] Wiley, B.; Sun, Y.; Chen, J.; Cang, H.; Li, Z.-Y.; Li, X.; Xia, Y. Shape-Controlled Synthesis of Silver and Gold Nanostructures. *MRS Bull.* **2005**, *30* (5), 356–361.

[43] Dreaden, E. C.; Alkilany, A. M.; Huang, X.; Murphy, C. J.; El-Sayed, M. A. The Golden Age: Gold Nanoparticles for Biomedicine. *Chem. Soc. Rev.* **2012**, *41* (7), 2740–2779.

[44] Yeh, Y.-C.; Creran, B.; Rotello, V. M. Gold Nanoparticles: Preparation, Properties, and Applications in Bionanotechnology. *Nanoscale* **2012**, *4* (6), 1871–1880.

[45] Singh, L. P.; Bhattacharyya, S. K.; Kumar, R.; Mishra, G.; Sharma, U.; Singh, G.; Ahalawat, S. Sol-Gel Processing of Silica Nanoparticles and Their Applications. *Adv. Colloid Interface Sci.* **2014**, *214*, 17–37.

[46] Chen, G.; Qiu, H.; Prasad, P. N.; Chen, X. Upconversion Nanoparticles: Design, Nanochemistry, and Applications in Theranostics. *Chem. Rev.* **2014**, *114* (10), 5161–5214.

[47] Chen, G.; Ågren, H.; Ohulchanskyy, T. Y.; Prasad, P. N. Light Upconverting Core-Shell Nanostructures: Nanophotonic Control for Emerging Applications. *Chem. Soc. Rev.* **2015**, *44* (6), 1680–1713.

[48] Bioimaging: Applications. In *Introduction to Biophotonics*; John Wiley & Sons, Ltd, 2004; pp 255–310.

[49] Wilchek, M.; Bayer, E. A. The Avidin-Biotin Complex in Bioanalytical Applications. *Anal. Biochem.* **1988**, *171* (1), 1–32.

[50] Pounder, R. J.; Stanford, M. J.; Brooks, P.; Richards, S. P.; Dove, A. P. Metal Free Thiol–Maleimide 'Click' Reaction as a Mild Functionalisation Strategy for Degradable Polymers. *Chem. Commun.* **2008**, No. 41, 5158–5160.

[51] Rostovtsev, V. V.; Green, L. G.; Fokin, V. V.; Sharpless, K. B. A Stepwise Huisgen Cycloaddition Process: Copper(I)-Catalyzed Regioselective "Ligation" of Azides and Terminal Alkynes. *Angew. Chem. Int. Ed.* **2002**, *41* (14), 2596–2599.

[52] Baskin, J. M.; Bertozzi, C. R. Copper-Free Click Chemistry. In *Click Chemistry for Biotechnology and Materials Science*; John Wiley & Sons, Ltd, 2009; pp 29–51.

[53] Jewett, J. C.; Bertozzi, C. R. Cu-Free Click Cycloaddition Reactions in Chemical Biology. *Chem. Soc. Rev.* **2010**, *39* (4), 1272–1279.

[54] Migneault, I.; Dartiguenave, C.; Bertrand, M. J.; Waldron, K. C. Glutaraldehyde: Behavior in Aqueous Solution, Reaction with Proteins, and Application to Enzyme Crosslinking. *BioTechniques* **2004**, *37* (5), 790–802.

[55] Laurent, S.; Forge, D.; Port, M.; Roch, A.; Robic, C.; Vander Elst, L.; Muller, R. N. Magnetic Iron Oxide Nanoparticles: Synthesis, Stabilization, Vectorization, Physicochemical Characterizations, and Biological Applications. *Chem. Rev.* **2008**, *108* (6), 2064–2110.

[56] Ruffert, C. Magnetic Bead—Magic Bullet. *Micromachines* **2016**, *7* (2), 21.

[57] Neurauter, A. A.; Bonyhadi, M.; Lien, E.; Nøkleby, L.; Ruud, E.; Camacho, S.; Aarvak, T. Cell Isolation and Expansion Using Dynabeads®. In *Cell Separation: Fundamentals, Analytical and Preparative Methods*; Kumar, A., Galaev, I. Y., Mattiasson, B., Eds.; Advances in Biochemical Engineering/Biotechnology; Springer Berlin Heidelberg: Berlin, Heidelberg, 2007; pp 41–73.

[58] Horwood, N. J.; Udagawa, N.; Elliott, J.; Grail, D.; Okamura, H.; Kurimoto, M.; Dunn, A. R.; Martin, T.; Gillespie, M. T. Interleukin 18 Inhibits Osteoclast Formation via T Cell Production of Granulocyte Macrophage Colony-Stimulating Factor. *J. Clin. Invest.* **1998**, *101* (3), 595–603.

[59] Wubbolts, R.; Leckie, R. S.; Veenhuizen, P. T. M.; Schwarzmann, G.; Möbius, W.; Hoernschemeyer, J.; Slot, J.-W.; Geuze, H. J.; Stoorvogel, W. Proteomic and Biochemical Analyses of Human B Cell-Derived Exosomes POTENTIAL IMPLICATIONS FOR THEIR FUNCTION AND MULTIVESICULAR BODY FORMATION. *J. Biol. Chem.* **2003**, *278* (13), 10963–10972.

[60] Smith, C. Striving for Purity: Advances in Protein Purification. *Nat. Methods* **2005**, *2* (1), 71.

[61] Rissin, D. M.; López-Longarela, B.; Pernagallo, S.; Ilyine, H.; Vliegenthart, A. D. B.; Dear, J. W.; Díaz-Mochón, J. J.; Duffy, D. C. Polymerase-Free Measurement of MicroRNA-122 with Single Base Specificity Using Single Molecule Arrays: Detection of Drug-Induced Liver Injury. *PLOS ONE* **2017**, *12* (7), e0179669.

[62] Graham, H.; Chandler, D. J.; Dunbar, S. A. The Genesis and Evolution of Bead-Based Multiplexing. *Methods* **2019**.

[63] Coppock, M. B.; Stratis-Cullum, D. N. A Universal Method for the Functionalization of Dyed Magnetic Microspheres with Peptides. *Methods* **2019**, *158*, 12–16.

[64] Cardoso, S. P.; Chong, W.; Lucas, G.; Green, A.; Navarrete, C. Determination of Human Neutrophil Antigen-1, -3, -4 and -5 Allele Frequencies in English Caucasoid Blood Donors Using a Multiplex Fluorescent DNA-Based Assay. *Vox Sang.* **2013**, *105* (1), 65–72.

[65] Spierings, G.; Dunbar, S. A. Pharmacogenetics Using Luminex® XMAP® Technology: A Method for Developing a Custom Multiplex Single Nucleotide Polymorphism Mutation Assay. In *Pharmacogenomics: Methods and Protocols*; Innocenti, F., van Schaik, R. H. N., Eds.; Methods in Molecular Biology; Humana Press: Totowa, NJ, 2013; pp 115–126.

[66] Gonsalves, S.; Mahony, J.; Rao, A.; Dunbar, S.; Juretschko, S. Multiplexed Detection and Identification of Respiratory Pathogens Using the NxTAG® Respiratory Pathogen Panel. *Methods* **2019**, *158*, 61–68.

[67] Sorensen, K. Individualized MiRNA Assay Panels Using Optically Encoded Beads. In *Next-Generation MicroRNA Expression Profiling Technology: Methods and Protocols*; Fan, J.-B., Ed.; Methods in Molecular Biology; Humana Press: Totowa, NJ, 2012; pp 131–141.

[68] Kim, J. S.; Taitt, C. R.; Ligler, F. S.; Anderson, G. P. Multiplexed Magnetic Microsphere Immunoassays for Detection of Pathogens in Foods. *Sens. Instrum. Food Qual. Saf.* **2010**, *4* (2), 73–81.

[69] Vordenbäumen, S.; Lueking, A.; Budde, P.; Zucht, H.-D.; Goehler, H.; Brinks, R.; Fischer-Betz, R.; Richter, J.; Bleck, E.; Detert, J.; et al. Sequential High-Content Profiling of the IgG-Autoantibody Repertoire Reveals Novel Antigens in Rheumatoid Arthritis. *Arthritis Res. Ther.* **2016**, *18* (1), 235.

[70] Velu, V. K. Circulating MicroRNAs as Biomarkers in Health and Disease. *J. Clin. Diagn. Res.* **2012**.

[71] Bhattacharya, S.; Mariani, T. J. Array of Hope: Expression Profiling Identifies Disease Biomarkers and Mechanism. *Biochem. Soc. Trans.* **2009**, *37* (4), 855–862.

[72] Mitchell, P. S.; Parkin, R. K.; Kroh, E. M.; Fritz, B. R.; Wyman, S. K.; Pogosova-Agadjanyan, E. L.; Peterson, A.; Noteboom, J.; O'Briant, K. C.; Allen, A.; et al. Circulating MicroRNAs as Stable Blood-Based Markers for Cancer Detection. *Proc. Natl. Acad. Sci. U. S. A.* **2008**, *105* (30), 10513–10518.

[73] Kawaguchi, T.; Komatsu, S.; Ichikawa, D.; Tsujiura, M.; Takeshita, H.; Hirajima, S.; Miyamae, M.; Okajima, W.; Ohashi, T.; Imamura, T.; et al. Circulating MicroRNAs: A Next-Generation Clinical Biomarker for Digestive System Cancers. *Int. J. Mol. Sci.* **2016**, *17* (9).

[74] Chi, K. R. The Tumour Trail Left in Blood. *Nature* **2016**, *532* (7598), 269–271.

[75] Bettegowda, C.; Sausen, M.; Leary, R. J.; Kinde, I.; Wang, Y.; Agrawal, N.; Bartlett, B. R.; Wang, H.; Luber, B.; Alani, R. M.; et al. Detection of Circulating Tumor DNA in Early- and Late-Stage Human Malignancies. *Sci. Transl. Med.* **2014**, *6* (224), 224ra24-224ra24.

[76] Arroyo, J. D.; Chevillet, J. R.; Kroh, E. M.; Ruf, I. K.; Pritchard, C. C.; Gibson, D. F.; Mitchell, P. S.; Bennett, C. F.; Pogosova-Agadjanyan, E. L.; Stirewalt, D. L.; et al. Argonaute2 Complexes Carry a Population of Circulating MicroRNAs Independent of Vesicles in Human Plasma. *Proc. Natl. Acad. Sci.* **2011**, *108* (12), 5003–5008.

[77] Vickers, K. C.; Palmisano, B. T.; Shoucri, B. M.; Shamburek, R. D.; Remaley, A. T. MicroRNAs Are Transported in Plasma and Delivered to Recipient Cells by High-Density Lipoproteins. *Nat. Cell Biol.* **2011**, *13* (4), 423–433.

[78] Lohr, J. G.; Adalsteinsson, V. A.; Cibulskis, K.; Choudhury, A. D.; Rosenberg, M.; Cruz-Gordillo, P.; Francis, J. M.; Zhang, C.-Z.; Shalek, A. K.; Satija, R.; et al. Whole-Exome Sequencing of Circulating Tumor Cells Provides a Window into Metastatic Prostate Cancer. *Nat. Biotechnol.* **2014**, *32* (5), 479–484.

[79] Im, H.; Shao, H.; Park, Y. I.; Peterson, V. M.; Castro, C. M.; Weissleder, R.; Lee, H. Label-Free Detection and Molecular Profiling of Exosomes with a Nano-Plasmonic Sensor. *Nat. Biotechnol.* **2014**, *32* (5), 490–495.

[80] Valadi, H.; Ekström, K.; Bossios, A.; Sjöstrand, M.; Lee, J. J.; Lötvall, J. O. Exosome-Mediated Transfer of MRNAs and MicroRNAs Is a Novel Mechanism of Genetic Exchange between Cells. *Nat. Cell Biol.* **2007**, *9* (6), 654–659.

[81] Nilsson, R. J. A.; Balaj, L.; Hulleman, E.; van Rijn, S.; Pegtel, D. M.; Walraven, M.; Widmark, A.; Gerritsen, W. R.; Verheul, H. M.; Vandertop, W. P.; et al. Blood Platelets Contain Tumor-Derived RNA Biomarkers. *Blood* **2011**, *118* (13), 3680–3683.

[82] Wang, H.; Peng, R.; Wang, J.; Qin, Z.; Xue, L. Circulating MicroRNAs as Potential Cancer Biomarkers: The Advantage and Disadvantage. *Clin. Epigenetics* **2018**, *10* (1), 59.

[83] Bray, F.; Ferlay, J.; Soerjomataram, I.; Siegel, R. L.; Torre, L. A.; Jemal, A. Global Cancer Statistics 2018: GLOBOCAN Estimates of Incidence and Mortality Worldwide for 36 Cancers in 185 Countries. *CA. Cancer J. Clin.* **2018**, *68* (6), 394–424.

[84] Wozniak, M. B.; Scelo, G.; Muller, D. C.; Mukeria, A.; Zaridze, D.; Brennan, P. Circulating MicroRNAs as Non-Invasive Biomarkers for Early Detection of Non-Small-Cell Lung Cancer. *PLOS ONE* **2015**, *10* (5), e0125026.

[85] Sathipati, S. Y.; Ho, S.-Y. Identifying a MiRNA Signature for Predicting the Stage of Breast Cancer. *Sci. Rep.* **2018**, *8* (1), 16138.

[86] Rodríguez-Martínez, A.; de Miguel-Pérez, D.; Ortega, F. G.; García-Puche, J. L.; Robles-Fernández, I.; Exposito, J.; Martorell-Marugan, J.; Carmona-Sáez, P.; Garrido-

Navas, M. del C.; Rolfo, C.; et al. Exosomal MiRNA Profile as Complementary Tool in the Diagnostic and Prediction of Treatment Response in Localized Breast Cancer under Neoadjuvant Chemotherapy. *Breast Cancer Res.* **2019**, *21* (1), 21.

[87] Masuda, T.; Hayashi, N.; Kuroda, Y.; Ito, S.; Eguchi, H.; Mimori, K. MicroRNAs as Biomarkers in Colorectal Cancer. *Cancers* **2017**, *9* (9).

[88] Danese, E.; Minicozzi, A. M.; Benati, M.; Paviati, E.; Lima-Oliveira, G.; Gusella, M.; Pasini, F.; Salvagno, G. L.; Montagnana, M.; Lippi, G. Reference MiRNAs for Colorectal Cancer: Analysis and Verification of Current Data. *Sci. Rep.* **2017**, *7* (1), 8413.

[89] Shivapurkar, N.; Weiner, L. M.; Marshall, J. L.; Madhavan, S.; Deslattes Mays, A.; Juhl, H.; Wellstein, A. Recurrence of Early Stage Colon Cancer Predicted by Expression Pattern of Circulating MicroRNAs. *PloS One* **2014**, *9* (1), e84686.

[90] Kanwal, R.; Plaga, A. R.; Liu, X.; Shukla, G. C.; Gupta, S. MicroRNAs in Prostate Cancer: Functional Role as Biomarkers. *Cancer Lett.* **2017**, *407*, 9–20.

[91] Lee, R. C.; Feinbaum, R. L.; Ambros, V. The C. Elegans Heterochronic Gene Lin-4 Encodes Small RNAs with Antisense Complementarity to Lin-14. *Cell* **1993**, *75* (5), 843–854.

[92] Ambros, V. The functions of animal microRNAs https://www.nature.com/articles/nature02871 (accessed Jan 17, 2018).

[93] Bartel, D. P. MicroRNAs: Genomics, Biogenesis, Mechanism, and Function. *Cell* **2004**, *116* (2), 281–297.

[94] Stahlhut Espinosa, C. E.; Slack, F. J. The Role of MicroRNAs in Cancer. *Yale J. Biol. Med.* **2006**, *79* (3–4), 131–140.

[95] Alles, J.; Fehlmann, T.; Fischer, U.; Backes, C.; Galata, V.; Minet, M.; Hart, M.; Abu-Halima, M.; Grässer, F. A.; Lenhof, H.-P.; et al. An Estimate of the Total Number of True Human MiRNAs. *Nucleic Acids Res.* **2019**, *47* (7), 3353–3364.

[96] Detassis, S.; Grasso, M.; Del Vescovo, V.; Denti, M. A. MicroRNAs Make the Call in Cancer Personalized Medicine. *Front. Cell Dev. Biol.* **2017**, *5*.

[97] Krichevsky, A. M.; Gabriely, G. MiR-21: A Small Multi-Faceted RNA. *J. Cell. Mol. Med.* **2009**, *13* (1), 39–53.

[98] Ji, W.; Sun, B.; Su, C. Targeting MicroRNAs in Cancer Gene Therapy. *Genes* **2017**, *8* (1), 21.

[99] Esquela-Kerscher, A.; Slack, F. J. Oncomirs — MicroRNAs with a Role in Cancer. *Nat. Rev. Cancer* **2006**, *6* (4), 259.

[100] Sicard, F.; Gayral, M.; Lulka, H.; Buscail, L.; Cordelier, P. Targeting MiR-21 for the Therapy of Pancreatic Cancer. *Mol. Ther.* **2013**, *21* (5), 986–994.

[101] Gumireddy, K.; Young, D. D.; Xiong, X.; Hogenesch, J. B.; Huang, Q.; Deiters, A. Small-Molecule Inhibitors of MicroRNA MiR-21 Function. *Angew. Chem. Int. Ed.* **2008**, *47* (39), 7482–7484.

[102] Ciafrè, S. A.; Galardi, S.; Mangiola, A.; Ferracin, M.; Liu, C.-G.; Sabatino, G.; Negrini, M.; Maira, G.; Croce, C. M.; Farace, M. G. Extensive Modulation of a Set of MicroRNAs in Primary Glioblastoma. *Biochem. Biophys. Res. Commun.* **2005**, *334* (4), 1351–1358.

[103] Gabriely, G.; Wurdinger, T.; Kesari, S.; Esau, C. C.; Burchard, J.; Linsley, P. S.; Krichevsky, A. M. MicroRNA 21 Promotes Glioma Invasion by Targeting Matrix Metalloproteinase Regulators. *Mol. Cell. Biol.* **2008**, *28* (17), 5369–5380.

[104] Volinia, S.; Calin, G. A.; Liu, C.-G.; Ambs, S.; Cimmino, A.; Petrocca, F.; Visone, R.; Iorio, M.; Roldo, C.; Ferracin, M.; et al. A MicroRNA Expression Signature of Human Solid Tumors Defines Cancer Gene Targets. *Proc. Natl. Acad. Sci. U. S. A.* **2006**, *103* (7), 2257–2261.

[105] Zhu, S.; Wu, H.; Wu, F.; Nie, D.; Sheng, S.; Mo, Y.-Y. MicroRNA-21 Targets Tumor Suppressor Genes in Invasion and Metastasis. *Cell Res.* **2008**, *18* (3), 350–359.

[106] Nam, E. J.; Yoon, H.; Kim, S. W.; Kim, H.; Kim, Y. T.; Kim, J. H.; Kim, J. W.; Kim, S. MicroRNA Expression Profiles in Serous Ovarian Carcinoma. *Clin. Cancer Res. Off. J. Am. Assoc. Cancer Res.* **2008**, *14* (9), 2690–2695.

[107] Wang, P.; Zou, F.; Zhang, X.; Li, H.; Dulak, A.; Tomko, R. J.; Lazo, J. S.; Wang, Z.; Zhang, L.; Yu, J. MicroRNA-21 Negatively Regulates Cdc25A and Cell Cycle Progression in Colon Cancer Cells. *Cancer Res.* **2009**, *69* (20), 8157–8165.

[108] Medina, P. P.; Nolde, M.; Slack, F. J. OncomiR Addiction in an *in Vivo* Model of MicroRNA-21-Induced Pre-B-Cell Lymphoma. *Nature* **2010**, *467* (7311), 86–90.

[109] Li, T.; Li, D.; Sha, J.; Sun, P.; Huang, Y. MicroRNA-21 Directly Targets MARCKS and Promotes Apoptosis Resistance and Invasion in Prostate Cancer Cells. *Biochem. Biophys. Res. Commun.* **2009**, *383* (3), 280–285.

[110] Liu, Z.-L.; Wang, H.; Liu, J.; Wang, Z.-X. MicroRNA-21 (MiR-21) Expression Promotes Growth, Metastasis, and Chemo- or Radioresistance in Non-Small Cell Lung Cancer Cells by Targeting PTEN. *Mol. Cell. Biochem.* **2013**, *372* (1–2), 35–45.

[111] Gong, C.; Yao, Y.; Wang, Y.; Liu, B.; Wu, W.; Chen, J.; Su, F.; Yao, H.; Song, E. Up-Regulation of MiR-21 Mediates Resistance to Trastuzumab Therapy for Breast Cancer. *J. Biol. Chem.* **2011**, *286* (21), 19127–19137.

[112] Huo, W.; Zhao, G.; Yin, J.; Ouyang, X.; Wang, Y.; Yang, C.; Wang, B.; Dong, P.; Wang, Z.; Watari, H.; et al. Lentiviral CRISPR/Cas9 Vector Mediated MiR-21 Gene Editing Inhibits the Epithelial to Mesenchymal Transition in Ovarian Cancer Cells. *J. Cancer* **2017**, *8* (1), 57–64.

[113] Geretto, M.; Pulliero, A.; Rosano, C.; Zhabayeva, D.; Bersimbaev, R.; Izzotti, A. Resistance to Cancer Chemotherapeutic Drugs Is Determined by Pivotal MicroRNA Regulators. *Am. J. Cancer Res.* **2017**, *7* (6), 1350–1371.

[114] Lujambio, A.; Lowe, S. W. The Microcosmos of Cancer. *Nature* **2012**, *482* (7385), 347–355.

[115] Schork, N. J. Personalized Medicine: Time for One-Person Trials. *Nat. News* **2015**, *520* (7549), 609.

[116] Wark, A. W.; Lee, H. J.; Corn, R. M. Multiplexed Detection Methods for Profiling MicroRNA Expression in Biological Samples. *Angew. Chem. Int. Ed.* **2008**, *47* (4), 644–652.

[117] Shen, Y.; Tian, F.; Chen, Z.; Li, R.; Ge, Q.; Lu, Z. Amplification-Based Method for MicroRNA Detection. *Biosens. Bioelectron.* **2015**, *71*, 322–331.

[118] de Planell-Saguer, M.; Rodicio, M. C. Analytical Aspects of MicroRNA in Diagnostics: A Review. *Anal. Chim. Acta* **2011**, *699* (2), 134–152.

[119] Cissell, K. A.; Deo, S. K. Trends in MicroRNA Detection. *Anal. Bioanal. Chem.* **2009**, *394* (4), 1109–1116.

[120] Tentori, A. M.; Nagarajan, M. B.; Kim, J. J.; Zhang, W. C.; Slack, F. J.; Doyle, P. S. Quantitative and Multiplex MicroRNA Assays from Unprocessed Cells in Isolated Nanoliter Well Arrays. *Lab. Chip* **2018**.

[121] Li, X.; Rout, P.; Xu, R.; Li, P.; Tchounwou, P. B.; Ma, Y.; Liu, Y.-M. Quantification of MicroRNAs by Coupling Cyclic Enzymatic Amplification with Microfluidic Voltage-Assisted Liquid Desorption Electrospray Ionization Mass Spectrometry. *Anal. Chem.* **2018**.

[122] Detassis, S.; Grasso, M.; Tabraue-Chávez, M.; Marín-Romero, A.; López-Longarela, B.; Ilyine, H.; Ress, C.; Ceriani, S.; Erspan, M.; Maglione, A.; et al. New Platform for the Direct Profiling of MicroRNAs in Biofluids. *Anal. Chem.* **2019**, *91* (9), 5874–5880.

[123] Repasky, G. A.; Chenette, E. J.; Der, C. J. Renewing the Conspiracy Theory Debate: Does Raf Function Alone to Mediate Ras Oncogenesis? *Trends Cell Biol.* **2004**, *14* (11), 639–647.

[124] Schubbert, S.; Shannon, K.; Bollag, G. Hyperactive Ras in Developmental Disorders and Cancer. *Nat. Rev. Cancer* **2007**, *7* (4), 295–308.

[125] Mitin, N.; Rossman, K. L.; Der, C. J. Signaling Interplay in Ras Superfamily Function. *Curr. Biol. CB* **2005**, *15* (14), R563-574.

[126] Karnoub, A. E.; Weinberg, R. A. Ras Oncogenes: Split Personalities. *Nat. Rev. Mol. Cell Biol.* **2008**, *9* (7), 517–531.

[127] Aoki, Y.; Niihori, T.; Kawame, H.; Kurosawa, K.; Ohashi, H.; Tanaka, Y.; Filocamo, M.; Kato, K.; Suzuki, Y.; Kure, S.; et al. Germline Mutations in HRAS Proto-Oncogene Cause Costello Syndrome. *Nat. Genet.* **2005**, *37* (10), 1038–1040.

[128] Ellis, R. W.; DeFeo, D.; Furth, M. E.; Scolnick, E. M. Mouse Cells Contain Two Distinct Ras Gene MRNA Species That Can Be Translated into a P21 Onc Protein. *Mol. Cell. Biol.* **1982**, *2* (11), 1339–1345.

[129] Porru, M.; Pompili, L.; Caruso, C.; Biroccio, A.; Leonetti, C. Targeting KRAS in Metastatic Colorectal Cancer: Current Strategies and Emerging Opportunities. *J. Exp. Clin. Cancer Res. CR* **2018**, *37* (1), 57.

[130] Aghagolzadeh, P.; Radpour, R. New Trends in Molecular and Cellular Biomarker Discovery for Colorectal Cancer. *World J. Gastroenterol.* **2016**, *22* (25), 5678–5693.

[131] Tan, C.; Du, X. KRAS Mutation Testing in Metastatic Colorectal Cancer. *World J. Gastroenterol. WJG* **2012**, *18* (37), 5171–5180.

[132] Stolze, B.; Reinhart, S.; Bulllinger, L.; Fröhling, S.; Scholl, C. Comparative Analysis of KRAS Codon 12, 13, 18, 61, and 117 Mutations Using Human MCF10A Isogenic Cell Lines. *Sci. Rep.* **2015**, *5*, 8535.

[133] Tomasini, P.; Walia, P.; Labbe, C.; Jao, K.; Leighl, N. B. Targeting the KRAS Pathway in Non-Small Cell Lung Cancer. *The Oncologist* **2016**, *21* (12), 1450–1460.

[134] Bellon, E.; Ligtenberg, M. J. L.; Tejpar, S.; Cox, K.; de Hertogh, G.; de Stricker, K.; Edsjö, A.; Gorgoulis, V.; Höfler, G.; Jung, A.; et al. External Quality Assessment for KRAS Testing Is Needed: Setup of a European Program and Report of the First Joined Regional Quality Assessment Rounds. *The Oncologist* **2011**, *16* (4), 467–478.

[135] Matsuda, K. Chapter Two - PCR-Based Detection Methods for Single-Nucleotide Polymorphism or Mutation: Real-Time PCR and Its Substantial Contribution Toward Technological Refinement. In *Advances in Clinical Chemistry*; Makowski, G. S., Ed.; Elsevier, 2017; Vol. 80, pp 45–72.

[136] Vossen, R. H. A. M.; Aten, E.; Roos, A.; Dunnen, J. T. den. High-Resolution Melting Analysis (HRMA)—More than Just Sequence Variant Screening. *Hum. Mutat.* **2009**, *30* (6), 860–866.

[137] Mahdieh, N.; Rabbani, B. An Overview of Mutation Detection Methods in Genetic Disorders. *Iran. J. Pediatr.* **2013**, *23* (4), 375–388.

[138] Pourzand, C.; Cerutti, P. Genotypic Mutation Analysis by RFLP/PCR. *Mutat. Res.* **1993**, *288* (1), 113–121.

[139] Orum, H. PCR Clamping. *Curr. Issues Mol. Biol.* **2000**, *2* (1), 27–30.

[140] Zuo, Z.; Jabbar, K. J. COLD-PCR: Applications and Advantages. In *Clinical Applications of PCR*; Luthra, R., Singh, R. R., Patel, K. P., Eds.; Methods in Molecular Biology; Springer New York: New York, NY, 2016; pp 17–25.

[141] Vogelstein, B.; Kinzler, K. W. Digital PCR. *Proc. Natl. Acad. Sci. U. S. A.* **1999**, *96* (16), 9236–9241.

[142] Quan, P.-L.; Sauzade, M.; Brouzes, E. DPCR: A Technology Review. *Sensors* **2018**, *18* (4).

[143] Nordgård, O.; Oltedal, S.; Janssen, E. A. M.; Gilje, B.; Kørner, H.; Tjensvoll, K.; Smaaland, R. Comparison of a PNA Clamp PCR and an ARMS/Scorpion PCR Assay for the Detection of K-Ras Mutations. *Diagn. Mol. Pathol.* **2012**, *21* (1), 9–13.

[144] Bolton, L.; Reiman, A.; Lucas, K.; Timms, J.; Cree, I. A. KRAS Mutation Analysis by PCR: A Comparison of Two Methods. *PLOS ONE* **2015**, *10* (1), e0115672.

[145] MATSUNAGA, M.; KANETA, T.; MIWA, K.; ICHIKAWA, W.; FUJITA, K.-I.; NAGASHIMA, F.; FURUSE, J.; KAGE, M.; AKAGI, Y.; SASAKI, Y. A Comparison of Four Methods for Detecting KRAS Mutations in Formalin-Fixed Specimens from Metastatic Colorectal Cancer Patients. *Oncol. Lett.* **2016**, *12* (1), 150–156.

[146] Hunt, E. A.; Broyles, D.; Head, T.; Deo, S. K. MicroRNA Detection: Current Technology and Research Strategies. *Annu. Rev. Anal. Chem.* **2015**, *8* (1), 217–237.

[147] Bowler, F. R.; Diaz-Mochon, J. J.; Swift, M. D.; Bradley, M. DNA Analysis by Dynamic Chemistry. *Angew. Chem. Int. Ed.* **2010**, *49* (10), 1809–1812.

[148] Bowler, F. R.; Reid, P. A.; Boyd, A. C.; Diaz-Mochon, J. J.; Bradley, M. Dynamic Chemistry for Enzyme-Free Allele Discrimination in Genotyping by MALDI-TOF Mass Spectrometry. *Anal. Methods* **2011**, *3* (7), 1656.

[149] Nielsen, P. E.; Egholm, M.; Berg, R. H.; Buchardt, O. Sequence-Selective Recognition of DNA by Strand Displacement with a Thymine-Substituted Polyamide. *Science* **1991**, *254* (5037), 1497–1500.

[150] Heemstra, J. M.; Liu, D. R. Templated Synthesis of Peptide Nucleic Acids via Sequence-Selective Base-Filling Reactions. *J. Am. Chem. Soc.* **2009**, *131* (32), 11347–11349.

[151] Dragulescu-Andrasi, A.; Rapireddy, S.; Frezza, B. M.; Gayathri, C.; Gil, R. R.; Ly, D. H. A Simple γ-Backbone Modification Preorganizes Peptide Nucleic Acid into a Helical Structure. *J. Am. Chem. Soc.* **2006**, *128* (31), 10258–10267.

[152] Moggio, L.; Romanelli, A.; Gambari, R.; Bianchi, N.; Borgatti, M.; Fabbri, E.; Mancini, I.; di Blasio, B.; Pedone, C.; Messere, A. Alternate PNA-DNA Chimeras (PNA-DNA)n: Synthesis, Binding Properties and Biological Activity. *Biopolymers* **2007**, *88* (6), 815–822.

[153] Sharma, C.; Awasthi, S. K. Versatility of Peptide Nucleic Acids (PNAs): Role in Chemical Biology, Drug Discovery, and Origins of Life. *Chem. Biol. Drug Des.* **2016**.

[154] Park, H.; Germini, A.; Sforza, S.; Corradini, R.; Marchelli, R.; Knoll, W. Effect of Ionic Strength on PNA-DNA Hybridization on Surfaces and in Solution. *Biointerphases* **2007**, *2* (2), 80–88.

[155] Costa, N. T. S. D.; Heemstra, J. M. Evaluating the Effect of Ionic Strength on Duplex Stability for PNA Having Negatively or Positively Charged Side Chains. *PLOS ONE* **2013**, *8* (3), e58670.

[156] Berkessel, A. Diversity-Based Approaches to Selective Biomimetic Oxidation Catalysis. In *Advances in Inorganic Chemistry*; van Eldik, R., Reedijk, J., Eds.; Academic Press, 2006; Vol. 58, pp 1–28.

[157] Bradley, M.; Diaz-Mochon, J. J. Nucleobase Characterisation. US8716457B2, May 6, 2014.

[158] Angélica Luque-González, M.; Tabraue-Chávez, M.; López-Longarela, B.; María Sánchez-Martín, R.; Ortiz-González, M.; Soriano-Rodríguez, M.; Antonio García-Salcedo, J.; Pernagallo, S.; José Díaz-Mochón, J. Identification of Trypanosomatids by Detecting Single Nucleotide Fingerprints Using DNA Analysis by Dynamic Chemistry with MALDI-ToF. *Talanta* **2018**, *176*, 299–307.

[159] Pernagallo, S.; Ventimiglia, G.; Cavalluzzo, C.; Alessi, E.; Ilyine, H.; Bradley, M.; Diaz-Mochon, J. J. Novel Biochip Platform for Nucleic Acid Analysis. *Sensors* **2012**, *12* (6), 8100–8111.

[160] Venkateswaran, S.; Luque-González, M. A.; Tabraue-Chávez, M.; Fara, M. A.; López-Longarela, B.; Cano-Cortes, V.; López-Delgado, F. J.; Sánchez-Martín, R. M.; Ilyine, H.; Bradley, M.; et al. Novel Bead-Based Platform for Direct Detection of Unlabelled Nucleic Acids through Single Nucleobase Labelling. *Talanta* **2016**, *161*, 489–496.

[161] Romero, A. M.; Remacho, A. R.; Tabraue-Chávez, M.; Sánchez-Martín, R. M.; Monteagudo, J. J. G.; Fara, M. A.; López-Delgado, F. J.; Pernagallo, S.; Diaz-Mochon, J. J. A PCR-Free Technology to Detect and Quantify MicroRNAs Directly from Human Plasma. *Analyst* **2018**.

[162] Tabraue-Chávez, M.; Luque-González, M. A.; Marín-Romero, A.; Sánchez-Martín, R. M.; Escobedo-Araque, P.; Pernagallo, S.; Díaz-Mochón, J. J. A Colorimetric Strategy Based on Dynamic Chemistry for Direct Detection of Trypanosomatid Species. *Sci. Rep.* **2019**, *9* (1), 3696.

[163] Delgado-Gonzalez, A.; Robles-Remacho, A.; Marin-Romero, A.; Detassis, S.; Lopez-Longarela, B.; Lopez-Delgado, F. J.; de Miguel-Perez, D.; Guardia-Monteagudo, J. J.; Fara, M. A.; Tabraue-Chavez, M.; et al. PCR-Free and Chemistry-Based Technology for MiR-21 Rapid Detection Directly from Tumour Cells. *Talanta* **2019**, *200*, 51–56.

[164] Booth, J.; Cummins, W. J.; Brown, T. An Analogue of Adenine That Forms an “A:T” Base Pair of Comparable Stability to G:C. *Chem. Commun.* **2004**, *0* (19), 2208–2209.

[165] Song, Y.; Kilburn, D.; Song, J. H.; Cheng, Y.; Saeui, C. T.; Cheung, D. G.; Croce, C. M.; Yarema, K. J.; Meltzer, S. J.; Liu, K. J.; et al. Determination of Absolute Expression Profiles Using Multiplexed MiRNA Analysis. *PLOS ONE* **2017**, *12* (7), e0180988.

[166] Loos, C.; Syrovets, T.; Musyanovych, A.; Mailänder, V.; Landfester, K.; Nienhaus, G. U.; Simmet, T. Functionalized Polystyrene Nanoparticles as a Platform for Studying Bio–Nano Interactions. *Beilstein J. Nanotechnol.* **2014**, *5* (1), 2403–2412.

[167] Baptista, P. V.; Doria, G.; Quaresma, P.; Cavadas, M.; Neves, C. S.; Gomes, I.; Eaton, P.; Pereira, E.; Franco, R. Chapter 11 - Nanoparticles in Molecular Diagnostics. In *Progress in Molecular Biology and Translational Science*; Villaverde, A., Ed.; Nanoparticles in Translational Science and Medicine; Academic Press, 2011; Vol. 104, pp 427–488.

[168] Liu, Y.; Miyoshi, H.; Nakamura, M. Nanomedicine for Drug Delivery and Imaging: A Promising Avenue for Cancer Therapy and Diagnosis Using Targeted Functional Nanoparticles. *Int. J. Cancer* **2007**, *120* (12), 2527–2537.

[169] Gennet, N.; Alexander, L. M.; Sánchez-Martín, R. M.; Behrendt, J. M.; Sutherland, A. J.; Brickman, J. M.; Bradley, M.; Li, M. Microspheres as a Vehicle for Biomolecule Delivery to Neural Stem Cells. *New Biotechnol.* **2009**, *25* (6), 442–449.

[170] Tsakiridis, A.; Alexander, L. M.; Gennet, N.; Sanchez-Martin, R. M.; Livigni, A.; Li, M.; Bradley, M.; Brickman, J. M. Microsphere-Based Tracing and Molecular Delivery in Embryonic Stem Cells. *Biomaterials* **2009**, *30* (29), 5853–5861.

[171] Tseng, C. M.; Lu, Y. Y.; El-Aasser, M. S.; Vanderhoff, J. W. Uniform Polymer Particles by Dispersion Polymerization in Alcohol. *J. Polym. Sci. Part Polym. Chem.* **1986**, *24* (11), 2995–3007.

[172] Delair, T.; Marguet, V.; Pichot, C.; Mandrand, B. Synthesis and Characterization of Cationic Amino Functionalized Polystyrene Latexes. *Colloid Polym. Sci.* **1994**, *272* (8), 962–970.

[173] Sanchez-Martin, R. M.; Muzerelle, M.; Chitkul, N.; How, S. E.; Mittoo, S.; Bradley, M. Bead-Based Cellular Analysis, Sorting and Multiplexing. *ChemBioChem* **2005**, *6* (8), 1341–1345.

[174] Sánchez-Martín, R. M.; Alexander, L.; Bradley, M. Multifunctionalized Biocompatible Microspheres for Sensing. *Ann. N. Y. Acad. Sci.* **2008**, *1130* (1), 207–217.

[175] Alexander, L. M.; Sánchez-Martín, R. M.; Bradley, M. Knocking (Anti)-Sense into Cells: The Microsphere Approach to Gene Silencing. *Bioconjug. Chem.* **2009**, *20* (3), 422–426.

[176] Borger, J. G.; Cardenas-Maestre, J. M.; Zamoyska, R.; Sanchez-Martin, R. M. Novel Strategy for Microsphere-Mediated DNA Transfection. *Bioconjug. Chem.* **2011**, *22* (10), 1904–1908.

[177] Manuel Cardenas-Maestre, J.; Panadero-Fajardo, S.; Maria Perez-Lopez, A.; M. Sanchez-Martin, R. Sulfhydryl Reactive Microspheres for the Efficient Delivery of Thiolated Bioactive Cargoes. *J. Mater. Chem.* **2011**, *21* (34), 12735–12743.

[178] Unciti-Broceta, A.; Díaz-Mochón, J. J.; Sánchez-Martín, R. M.; Bradley, M. The Use of Solid Supports to Generate Nucleic Acid Carriers. *Acc. Chem. Res.* **2012**, *45* (7), 1140–1152.

[179] Sanchez-Martin, R. M.; Alexander, L.; Muzerelle, M.; Cardenas-Maestre, J. M.; Tsakiridis, A.; Brickman, J. M.; Bradley, M. Microsphere-Mediated Protein Delivery into Cells. *ChemBioChem* **2009**, *10* (9), 1453–1456.

[180] Sánchez-Martín, R. M.; Cuttle, M.; Mittoo, S.; Bradley, M. Microsphere-Based Real-Time Calcium Sensing. *Angew. Chem. Int. Ed.* **2006**, *45* (33), 5472–5474.

[181] Unciti-Broceta, A.; Johansson, E. M. V.; Yusop, R. M.; Sánchez-Martín, R. M.; Bradley, M. Synthesis of Polystyrene Microspheres and Functionalization with Pd(0) Nanoparticles to Perform Bioorthogonal Organometallic Chemistry in Living Cells. *Nat. Protoc.* **2012**, *7* (6), 1207–1218.

[182] Yusop, R. M.; Unciti-Broceta, A.; Johansson, E. M. V.; Sánchez-Martín, R. M.; Bradley, M. Palladium-Mediated Intracellular Chemistry. *Nat. Chem.* **2011**, *3* (3), 239–243.

[183] Valero, T.; Delgado-González, A.; Unciti-Broceta, J. D.; Cano-Cortés, V.; Pérez-López, A.; Unciti-Broceta, A.; Sánchez-Martín, R. Drug 'Clicking' on Cell-Penetrating Fluorescent Nanoparticles for in Cellulo Chemical Proteomics. *Bioconjug. Chem.* **2018**.

[184] M. Alexander, L.; Pernagallo, S.; Livigni, A.; M. Sánchez-Martín, R.; M. Brickman, J.; Bradley, M. Investigation of Microsphere-Mediated Cellular Delivery by Chemical, Microscopic and Gene Expression Analysis. *Mol. Biosyst.* **2010**, *6* (2), 399–409.

[185] Singh, A. K. Chapter 4 - Experimental Methodologies for the Characterization of Nanoparticles. In *Engineered Nanoparticles*; Singh, A. K., Ed.; Academic Press: Boston, 2016; pp 125–170.

[186] Stetefeld, J.; McKenna, S. A.; Patel, T. R. Dynamic Light Scattering: A Practical Guide and Applications in Biomedical Sciences. *Biophys. Rev.* **2016**, *8* (4), 409–427.

[187] Carter, M.; Shieh, J. Chapter 5 - Microscopy. In *Guide to Research Techniques in Neuroscience (Second Edition)*; Carter, M., Shieh, J., Eds.; Academic Press: San Diego, 2015; pp 117–144.

[188] Lee, S.; Rao, S. P.; Moon, M. H.; Giddings, J. C. Determination of Mean Diameter and Particle Size Distribution of Acrylate Latex Using Flow Field-Flow Fractionation, Photon Correlation Spectroscopy, and Electron Microscopy. *Anal. Chem.* **1996**, *68* (9), 1545–1549.

[189] Pyrz, W. D.; Buttrey, D. J. Particle Size Determination Using TEM: A Discussion of Image Acquisition and Analysis for the Novice Microscopist. *Langmuir* **2008**, *24* (20), 11350–11360.

[190] Epicier, T.; Sato, K.; Tournus, F.; Konno, T. Chemical Composition Dispersion in Bi-Metallic Nanoparticles: Semi-Automated Analysis Using HAADF-STEM. *J. Nanoparticle Res.* **2012**, *14* (9), 1106.

[191] Selvamani, V. Chapter 15 - Stability Studies on Nanomaterials Used in Drugs. In *Characterization and Biology of Nanomaterials for Drug Delivery*; Mohapatra, S. S., Ranjan, S., Dasgupta, N., Mishra, R. K., Thomas, S., Eds.; Micro and Nano Technologies; Elsevier, 2019; pp 425–444.

[192] Weiner, B. B.; Tscharnuter, W. W.; Fairhurst, D. Zeta Potential: A New Approach. In *Canadian Mineral Analysts Meeting*; 1993; p 12.

[193] Herzing, A. A.; Watanabe, M.; Edwards, J. K.; Conte, M.; Tang, Z.-R.; Hutchings, G. J.; Kiely, C. J. Energy Dispersive X-Ray Spectroscopy of Bimetallic Nanoparticles in an Aberration Corrected Scanning Transmission Electron Microscope. *Faraday Discuss.* **2008**, *138* (0), 337–351.

[194] Techane, S. D.; Gamble, L. J.; Castner, D. G. X-Ray Photoelectron Spectroscopy Characterization of Gold Nanoparticles Functionalized with Amine-Terminated Alkanethiols. *Biointerphases* **2011**, *6* (3), 98–104.

[195] Forte, M.; Iachetta, G.; Tussellino, M.; Carotenuto, R.; Prisco, M.; De Falco, M.; Laforgia, V.; Valiante, S. Polystyrene Nanoparticles Internalization in Human Gastric Adenocarcinoma Cells. *Toxicol. In Vitro* **2016**, *31*, 126–136.

[196] Varela, J. A.; Bexiga, M. G.; Åberg, C.; Simpson, J. C.; Dawson, K. A. Quantifying Size-Dependent Interactions between Fluorescently Labeled Polystyrene Nanoparticles and Mammalian Cells. *J. Nanobiotechnology* **2012**, *10* (1), 39.

[197] Khattab, S. N.; Subirós-Funosas, R.; El-Faham, A.; Albericio, F. Oxime Carbonates: Novel Reagents for the Introduction of Fmoc and Alloc Protecting Groups, Free of Side Reactions. *Eur. J. Org. Chem.* **2010**, *2010* (17), 3275–3280.

[198] El-Faham, A.; Al Marhoon, Z.; Abdel-Megeed, A.; Albericio, F. OxymaPure/DIC: An Efficient Reagent for the Synthesis of a Novel Series of 4-[2-(2-Acetylaminophenyl)-2-Oxo-Acetylamino] Benzoyl Amino Acid Ester Derivatives. *Molecules* **2013**, *18* (12), 14747–14759.

[199] Subirós-Funosas, R.; Prohens, R.; Barbas, R.; El-Faham, A.; Albericio, F. Oxyma: An Efficient Additive for Peptide Synthesis to Replace the Benzotriazole-Based HOBt and HOAt with a Lower Risk of Explosion[1]. *Chem. – Eur. J.* **2009**, *15* (37), 9394–9403.

[200] Sheehan, J. C.; Hess, G. P. A New Method of Forming Peptide Bonds. *J. Am. Chem. Soc.* **1955**, *77* (4), 1067–1068.

[201] Sheehan, J.; Cruickshank, P.; Boshart, G. Notes- A Convenient Synthesis of Water-Soluble Carbodiimides. *J. Org. Chem.* **1961**, *26* (7), 2525–2528.

[202] Montalbetti, C. A. G. N.; Falque, V. Amide Bond Formation and Peptide Coupling. *Tetrahedron* **2005**, *61* (46), 10827–10852.

[203] Fields, G. B.; Noble, R. L. Solid Phase Peptide Synthesis Utilizing 9-Fluorenylmethoxycarbonyl Amino Acids. *Int. J. Pept. Protein Res.* **1990**, *35* (3), 161–214.

[204] Díaz-Mochón, J. J.; Bialy, L.; Bradley, M. Full Orthogonality between Dde and Fmoc: The Direct Synthesis of PNA−Peptide Conjugates. *Org. Lett.* **2004**, *6* (7), 1127–1129.

[205] Altea-Manzano, P.; Unciti-Broceta, J. D.; Cano-Cortes, V.; Ruiz-Blas, M. P.; Valero-Griñan, T.; Diaz-Mochon, J. J.; Sanchez-Martin, R. Tracking Cell Proliferation Using a Nanotechnology-Based Approach. *Nanomed.* **2017**, *12* (13), 1591–1605.

[206] Bradley, M.; Alexander, L.; Duncan, K.; Chennaoui, M.; Jones, A. C.; Sánchez-Martín, R. M. PH Sensing in Living Cells Using Fluorescent Microspheres. *Bioorg. Med. Chem. Lett.* **2008**, *18* (1), 313–317.

[207] Cárdenas-Maestre, J. M.; Pérez-López, A. M.; Bradley, M.; Sánchez-Martín, R. M. Microsphere-Based Intracellular Sensing of Caspase-3/7 in Apoptotic Living Cells. *Macromol. Biosci.* **2014**, *14* (7), 923–928.

[208] Castro, V.; Rodríguez, H.; Albericio, F. CuAAC: An Efficient Click Chemistry Reaction on Solid Phase. *ACS Comb. Sci.* **2016**, *18* (1), 1–14.

[209] M. Cardenas-Maestre, J.; M. Sanchez-Martin, R. Efficient Solid Phase Strategy for Preparation of Modified Xanthene Dyes for Biolabelling. *Org. Biomol. Chem.* **2011**, *9* (6), 1720–1722.

[210] Bradley, M.; Alexander, L.; Sanchez-Martin, R. M. Cellular Uptake of Fluorescent Labelled Biotin–Streptavidin Microspheres. *J. Fluoresc.* **2008**, *18* (3–4), 733–739.

[211] Miyaura, N.; Yamada, K.; Suzuki, A. A New Stereospecific Cross-Coupling by the Palladium-Catalyzed Reaction of 1-Alkenylboranes with 1-Alkenyl or 1-Alkynyl Halides. *Tetrahedron Lett.* **1979**, *20* (36), 3437–3440.

[212] Miyaura, Norio.; Suzuki, Akira. Palladium-Catalyzed Cross-Coupling Reactions of Organoboron Compounds. *Chem. Rev.* **1995**, *95* (7), 2457–2483.

[213] Bandura, D. R.; Baranov, V. I.; Ornatsky, O. I.; Antonov, A.; Kinach, R.; Lou, X.; Pavlov, S.; Vorobiev, S.; Dick, J. E.; Tanner, S. D. Mass Cytometry: Technique for Real Time Single Cell Multitarget Immunoassay Based on Inductively Coupled Plasma Time-of-Flight Mass Spectrometry. *Anal. Chem.* **2009**, *81* (16), 6813–6822.

[214] Liu, R.; Wu, P.; Yang, L.; Hou, X.; Lv, Y. Inductively Coupled Plasma Mass Spectrometry-Based Immunoassay: A Review. *Mass Spectrom. Rev.* **2014**, *33* (5), 373–393.

[215] Tanner, S. D.; Ornatsky, O.; Bandura, D. R.; Baranov, V. I. Multiplex Bio-Assay with Inductively Coupled Plasma Mass Spectrometry: Towards a Massively Multivariate Single-Cell Technology. *Spectrochim. Acta Part B At. Spectrosc.* **2007**, *62* (3), 188–195.

[216] Tanner, S. D.; Bandura, D. R.; Ornatsky, O.; Baranov, V. I.; Nitz, M.; Winnik, M. A. Flow Cytometer with Mass Spectrometer Detection for Massively Multiplexed Single-Cell Biomarker Assay. *Pure Appl. Chem.* **2008**, *80* (12), 2627–2641.

[217] Bjornson, Z. B.; Nolan, G. P.; Fantl, W. J. Single-Cell Mass Cytometry for Analysis of Immune System Functional States. *Curr. Opin. Immunol.* **2013**, *25* (4), 484–494.

[218] Roederer, M. Spectral Compensation for Flow Cytometry: Visualization Artifacts, Limitations, and Caveats. *Cytometry* **2001**, *45* (3), 194–205.

[219] Bendall, S. C.; Nolan, G. P. From Single Cells to Deep Phenotypes in Cancer. *Nat. Biotechnol.* **2012**, *30* (7), 639–647.

[220] Bendall, S. C.; Nolan, G. P.; Roederer, M.; Chattopadhyay, P. K. A Deep Profiler's Guide to Cytometry. *Trends Immunol.* **2012**, *33* (7), 323–332.

[221] Ornatsky, O. I.; Lou, X.; Nitz, M.; Sheldrick, W. S.; Baranov, V. I.; Bandura, D. R.; Tanner, S. D. Study of Cell Antigens and Intracellular DNA by Identification of Element-Containing Labels and Metallointercalators Using Inductively Coupled Plasma Mass Spectrometry. *Anal. Chem.* **2008**, *80* (7), 2539–2547.

[222] Ornatsky, O.; Bandura, D.; Baranov, V.; Nitz, M.; Winnik, M. A.; Tanner, S. Highly Multiparametric Analysis by Mass Cytometry. *J. Immunol. Methods* **2010**, *361* (1), 1–20.

[223] Han, G.; Spitzer, M. H.; Bendall, S. C.; Fantl, W. J.; Nolan, G. P. Metal-Isotope-Tagged Monoclonal Antibodies for High-Dimensional Mass Cytometry. *Nat. Protoc.* **2018**, 1.

[224] Abdelrahman, A. I.; Ornatsky, O.; Bandura, D.; Baranov, V.; Kinach, R.; Dai, S.; Thickett, S. C.; Tanner, S.; Winnik, M. A. Metal-Containing Polystyrene Beads as Standards for Mass Cytometry. *J. Anal. At. Spectrom.* **2010**, *25* (3), 260–268.

[225] Kagan, H. B. Introduction: Frontiers in Lanthanide Chemistry. *Chem. Rev.* **2002**, *102* (6), 1805–1806.

[226] Bodenmiller, B.; Zunder, E. R.; Finck, R.; Chen, T. J.; Savig, E. S.; Bruggner, R. V.; Simonds, E. F.; Bendall, S. C.; Sachs, K.; Krutzik, P. O.; et al. Multiplexed Mass Cytometry Profiling of Cellular States Perturbed by Small-Molecule Regulators. *Nat. Biotechnol.* **2012**, *30* (9), 858–867.

[227] Lou, X.; Zhang, G.; Herrera, I.; Kinach, R.; Ornatsky, O.; Baranov, V.; Nitz, M.; Winnik, M. A. Polymer-Based Elemental Tags for Sensitive Bioassays. *Angew. Chem. Int. Ed.* **2007**, *46* (32), 6111–6114.

[228] Majonis, D.; Herrera, I.; Ornatsky, O.; Schulze, M.; Lou, X.; Soleimani, M.; Nitz, M.; Winnik, M. A. Synthesis of a Functional Metal-Chelating Polymer and Steps toward Quantitative Mass Cytometry Bioassays. *Anal. Chem.* **2010**, *82* (21), 8961–8969.

[229] Illy, N.; Majonis, D.; Herrera, I.; Ornatsky, O.; Winnik, M. A. Metal-Chelating Polymers by Anionic Ring-Opening Polymerization and Their Use in Quantitative Mass Cytometry. *Biomacromolecules* **2012**, *13* (8), 2359–2369.

[230] Adlersberg, J. B. The Immunoglobulin Hinge (Interdomain) Region. *Ric. Clin. Lab.* **1976**, *6* (3), 191.

[231] Behbehani, G. K.; Thom, C.; Zunder, E. R.; Finck, R.; Gaudilliere, B.; Fragiadakis, G. K.; Fantl, W. J.; Nolan, G. P. Transient Partial Permeabilization with Saponin Enables Cellular Barcoding Prior to Surface Marker Staining: Transient Partial Permeabilization Cellular Barcoding. *Cytometry A* **2014**, *85* (12), 1011–1019.

[232] Zunder, E. R.; Finck, R.; Behbehani, G. K.; Amir, E. D.; Krishnaswamy, S.; Gonzalez, V. D.; Lorang, C. G.; Bjornson, Z.; Spitzer, M. H.; Bodenmiller, B.; et al. Palladium-Based Mass Tag Cell Barcoding with a Doublet-Filtering Scheme and Single-Cell Deconvolution Algorithm. *Nat. Protoc.* **2015**, *10* (2), 316–333.

[233] Edgar, L. J.; Vellanki, R. N.; Halupa, A.; Hedley, D.; Wouters, B. G.; Nitz, M. Identification of Hypoxic Cells Using an Organotellurium Tag Compatible with Mass Cytometry. *Angew. Chem. Int. Ed.* **2014**, *53* (43), 11473–11477.

[234] Fienberg, H.; Simonds, E. F.; Fantl, W. J.; Nolan, G. P.; Bodenmiller, B. A Platinum-Based Covalent Viability Reagent for Single Cell Mass Cytometry. *Cytom. Part J. Int. Soc. Anal. Cytol.* **2012**, *81* (6).

[235] Hartmann, F. J.; Simonds, E. F.; Bendall, S. C. A Universal Live Cell Barcoding-Platform for Multiplexed Human Single Cell Analysis. *Sci. Rep.* **2018**, *8*.

[236] Mei, H. E.; Leipold, M. D.; Maecker, H. T. Platinum-Conjugated Antibodies for Application in Mass Cytometry. *Cytometry A* **2016**, *89* (3), 292–300.

[237] Park, H.; Edgar, L. J.; Lumba, M. A.; Willis, L. M.; Nitz, M. Organotellurium Scaffolds for Mass Cytometry Reagent Development. *Org. Biomol. Chem.* **2015**, *13* (25), 7027–7033.

[238] Willis, L. M.; Park, H.; Watson, M. W. L.; Majonis, D.; Watson, J. L.; Nitz, M. Tellurium-Based Mass Cytometry Barcode for Live and Fixed Cells. *Cytometry A* **2018**, *93* (7), 685–694.

[239] Majonis, D.; Ornatsky, O.; Weinrich, D.; Winnik, M. A. Dual-Purpose Polymer Labels for Fluorescent and Mass Cytometric Affinity Bioassays. *Biomacromolecules* **2013**, *14* (5), 1503–1513.

[240] Lin, W.; Hou, Y.; Lu, Y.; Abdelrahman, A. I.; Cao, P.; Zhao, G.; Tong, L.; Qian, J.; Baranov, V.; Nitz, M.; et al. A High-Sensitivity Lanthanide Nanoparticle Reporter for Mass Cytometry: Tests on Microgels as a Proxy for Cells. *Langmuir* **2014**, *30* (11), 3142–3153.

[241] Pichaandi, J.; Zhao, G.; Bouzekri, A.; Lu, E.; Ornatsky, O.; Baranov, V.; Nitz, M.; A. Winnik, M. Lanthanide Nanoparticles for High Sensitivity Multiparameter Single Cell Analysis. *Chem. Sci.* **2019**, *10* (10), 2965–2974.

[242] Bendall, S. C.; Simonds, E. F.; Qiu, P.; Amir, E. D.; Krutzik, P. O.; Finck, R.; Bruggner, R. V.; Melamed, R.; Trejo, A.; Ornatsky, O. I.; et al. Single-Cell Mass Cytometry of Differential Immune and Drug Responses Across a Human Hematopoietic Continuum. *Science* **2011**, *332* (6030), 687–696.

[243] Newell, E. W.; Sigal, N.; Bendall, S. C.; Nolan, G. P.; Davis, M. M. Cytometry by Time-of-Flight Shows Combinatorial Cytokine Expression and Virus-Specific Cell Niches within a Continuum of CD8+ T Cell Phenotypes. *Immunity* **2012**, *36* (1), 142–152.

[244] Good, Z.; Borges, L.; Gonzalez, N. V.; Sahaf, B.; Samusik, N.; Tibshirani, R.; Nolan, G. P.; Bendall, S. C. Proliferation Tracing with Single-Cell Mass Cytometry Optimizes Generation of Stem Cell Memory-like T Cells. *Nat. Biotechnol.* **2019**, *37* (3), 259.

[245] Hartmann, F. J.; Babdor, J.; Gherardini, P. F.; Amir, E.-A. D.; Jones, K.; Sahaf, B.; Marquez, D. M.; Krutzik, P.; O'Donnell, E.; Sigal, N.; et al. Comprehensive Immune Monitoring of Clinical Trials to Advance Human Immunotherapy. *Cell Rep.* **2019**, *28* (3), 819-831.e4.

[246] O'Gorman, W. E.; Hsieh, E. W. Y.; Savig, E. S.; Gherardini, P. F.; Hernandez, J. D.; Hansmann, L.; Balboni, I. M.; Utz, P. J.; Bendall, S. C.; Fantl, W. J.; et al. Single-Cell Systems-Level Analysis of Human Toll-like Receptor Activation Defines a Chemokine Signature in Patients with Systemic Lupus Erythematosus. *J. Allergy Clin. Immunol.* **2015**, *136* (5), 1326–1336.

[247] Lujan, E.; Zunder, E. R.; Ng, Y. H.; Goronzy, I. N.; Nolan, G. P.; Wernig, M. Early Reprogramming Regulators Identified by Prospective Isolation and Mass Cytometry. *Nature* **2015**, *521* (7552), 352–356.

[248] Amir, E. D.; Davis, K. L.; Tadmor, M. D.; Simonds, E. F.; Levine, J. H.; Bendall, S. C.; Shenfeld, D. K.; Krishnaswamy, S.; Nolan, G. P.; Pe'er, D. ViSNE Enables Visualization of High Dimensional Single-Cell Data and Reveals Phenotypic Heterogeneity of Leukemia. *Nat. Biotechnol.* **2013**, *31* (6), 545–552.

[249] Good, Z.; Sarno, J.; Jager, A.; Samusik, N.; Aghaeepour, N.; Simonds, E. F.; White, L.; Lacayo, N. J.; Fantl, W. J.; Fazio, G.; et al. Single-Cell Developmental

Classification of B Cell Precursor Acute Lymphoblastic Leukemia at Diagnosis Reveals Predictors of Relapse. *Nat. Med.* **2018**.

[250] Gonzalez, V. D.; Samusik, N.; Chen, T. J.; Savig, E. S.; Aghaeepour, N.; Quigley, D. A.; Huang, Y.-W.; Giangarrà, V.; Borowsky, A. D.; Hubbard, N. E.; et al. Commonly Occurring Cell Subsets in High-Grade Serous Ovarian Tumors Identified by Single-Cell Mass Cytometry. *Cell Rep.* **2018**, *22* (7), 1875–1888.

[251] Behbehani, G. K.; Bendall, S. C.; Clutter, M. R.; Fantl, W. J.; Nolan, G. P. Single-Cell Mass Cytometry Adapted to Measurements of the Cell Cycle. *Cytometry A* **2012**, *81A* (7), 552–566.

[252] Majonis, D.; Ornatsky, O.; Kinach, R.; Winnik, M. A. Curious Results with Palladium- and Platinum-Carrying Polymers in Mass Cytometry Bioassays and an Unexpected Application as a Dead Cell Stain. *Biomacromolecules* **2011**, *12* (11), 3997–4010.

[253] Newell, E. W.; Sigal, N.; Nair, N.; Kidd, B. A.; Greenberg, H. B.; Davis, M. M. Combinatorial Tetramer Staining and Mass Cytometry Analysis Facilitate T-Cell Epitope Mapping and Characterization. *Nat. Biotechnol.* **2013**, *31* (7), 623–629.

[254] Newell, E. W.; Davis, M. M. Beyond Model Antigens: High-Dimensional Methods for the Analysis of Antigen-Specific T Cells. *Nat. Biotechnol.* **2014**, *32* (2), 149–157.

[255] McCarthy, R. L.; Mak, D. H.; Burks, J. K.; Barton, M. C. Rapid Monoisotopic Cisplatin Based Barcoding for Multiplexed Mass Cytometry. *Sci. Rep.* **2017**, *7*.

[256] Wu, X.; DeGottardi, Q.; Wu, I.-C.; Wu, L.; Yu, J.; Kwok, W. W.; Chiu, D. T. Ratiometric Barcoding for Mass Cytometry. *Anal. Chem.* **2018**, *90* (18), 10688–10694.

[257] Delgado-Gonzalez, A.; Garcia-Fernandez, E.; Valero, T.; Cano-Cortes, M. V.; Ruedas-Rama, M. J.; Unciti-Broceta, A.; Sanchez-Martin, R. M.; Diaz-Mochon, J. J.; Orte, A. Metallofluorescent Nanoparticles for Multimodal Applications. *ACS Omega* **2018**, *3* (1), 144–153.

[258] Wang, M.; Silva, G. L.; Armitage, B. A. DNA-Templated Formation of a Helical Cyanine Dye J-Aggregate. *J. Am. Chem. Soc.* **2000**, *122* (41), 9977–9986.

[259] Eisfeld, A.; Briggs, J. S. The J- and H-Bands of Organic Dye Aggregates. *Chem. Phys.* **2006**, *324* (2–3), 376–384.

[260] Würthner, F.; Kaiser, T. E.; Saha-Möller, C. R. J-Aggregates: From Serendipitous Discovery to Supramolecular Engineering of Functional Dye Materials. *Angew. Chem. Int. Ed.* **2011**, *50* (15), 3376–3410.

[261] Kang, J.; Kaczmarek, O.; Liebscher, J.; Dähne, L. Prevention of H-Aggregates Formation in Cy5 Labeled Macromolecules. *Int. J. Polym. Sci.* **2010**, *2010*, 1–7.

[262] Chowdhury, A.; Wachsmann-Hogiu, S.; Bangal, P. R.; Raheem, I.; Peteanu, L. A. Characterization of Chiral H and J Aggregates of Cyanine Dyes Formed by DNA Templating Using Stark and Fluorescence Spectroscopies. *J. Phys. Chem. B* **2001**, *105* (48), 12196–12201.

[263] Ha, T.; Enderle, T.; Ogletree, D. F.; Chemla, D. S.; Selvin, P. R.; Weiss, S. Probing the Interaction between Two Single Molecules: Fluorescence Resonance Energy Transfer between a Single Donor and a Single Acceptor. *Proc. Natl. Acad. Sci.* **1996**, *93* (13), 6264–6268.

[264] Buschmann, V.; Weston, K. D.; Sauer, M. Spectroscopic Study and Evaluation of Red-Absorbing Fluorescent Dyes. *Bioconjug. Chem.* **2003**, *14* (1), 195–204.

[265] Zhao, M.; Huang, R.; Peng, L. Quantitative Multi-Color FRET Measurements by Fourier Lifetime Excitation-Emission Matrix Spectroscopy. *Opt. Express* **2012**, *20* (24), 26806–26827.

[266] Stennett, E. M. S.; Ciuba, M. A.; Levitus, M. Photophysical Processes in Single Molecule Organic Fluorescent Probes. *Chem. Soc. Rev.* **2014**, *43* (4), 1057–1075.

[267] Unciti-Broceta, A.; Torres-Sánchez, C.; Fraser, C.; Patton, E. E.; Weiss, J. T.; Dawson, J. C.; Macleod, K. G.; Bradley, M.; Carragher, N. O.; Rybski, W. Extracellular Palladium-Catalysed Dealkylation of 5-Fluoro-1-Propargyl-Uracil as a Bioorthogonally Activated Prodrug Approach. *Nat. Commun.* **2014**, *5*, 3277.

[268] Weiss, J. T.; Dawson, J. C.; Fraser, C.; Rybski, W.; Torres-Sánchez, C.; Bradley, M.; Patton, E. E.; Carragher, N. O.; Unciti-Broceta, A. Development and Bioorthogonal Activation of Palladium-Labile Prodrugs of Gemcitabine. *J. Med. Chem.* **2014**, *57* (12), 5395–5404.

[269] Medici, S.; Peana, M.; Nurchi, V. M.; Lachowicz, J. I.; Crisponi, G.; Zoroddu, M. A. Noble Metals in Medicine: Latest Advances. *Coord. Chem. Rev.* **2015**, *284*, 329–350.

[270] Yang, S.; Dong, J.; Yao, Z.; Shen, C.; Shi, X.; Tian, Y.; Lin, S.; Zhang, X. One-Pot Synthesis of Graphene-Supported Monodisperse Pd Nanoparticles as Catalyst for Formic Acid Electro-Oxidation. *Sci. Rep.* **2014**, *4*, srep04501.

[271] Smith, E. F.; Garcia, I. J. V.; Briggs, D.; Licence, P. Ionic Liquids in Vacuo; Solution-Phase X-Ray Photoelectron Spectroscopy. *Chem. Commun.* **2005**, *0* (45), 5633–5635.

[272] Downs, R. T.; Bartelmehs, K. L.; Gibbs, G. V.; Boisen, M. B. Interactive Software for Calculating and Displaying X-Ray or Neutron Powder Diffractometer Patterns of Crystalline Materials. *Am. Mineral.* **1993**, *78* (9–10), 1104–1107.

[273] Zemann, J. Crystal Structures, 2nd Edition. Vol. 1 by R. W. G. Wyckoff. *Acta Crystallogr.* **1965**, *18* (1), 139–139.

[274] Rezsnyak, C. E.; Autschbach, J.; Atwood, J. D.; Moncho, S. Reactions of Gold(III) Complexes with Alkenes in Aqueous Media: Generation of Bis-(β-Hydroxyalkyl)Gold(III) Complexes. *J. Coord. Chem.* **2013**, *66* (7), 1153–1165.

[275] Niehörster, T.; Löschberger, A.; Gregor, I.; Krämer, B.; Rahn, H.-J.; Patting, M.; Koberling, F.; Enderlein, J.; Sauer, M. Multi-Target Spectrally Resolved Fluorescence Lifetime Imaging Microscopy. *Nat. Methods* **2016**, *13* (3), 257–262.

[276] Clavadetscher, J.; Indrigo, E.; Chankeshwara, S. V.; Lilienkampf, A.; Bradley, M. In-Cell Dual Drug Synthesis by Cancer-Targeting Palladium Catalysts. *Angew. Chem. Int. Ed.* **2017**, *56* (24), 6864–6868.

[277] Clavadetscher, J.; Hoffmann, S.; Lilienkampf, A.; Mackay, L.; Yusop, R. M.; Rider, S. A.; Mullins, J. J.; Bradley, M. Copper Catalysis in Living Systems and In Situ Drug Synthesis. *Angew. Chem. Int. Ed.* **2016**, n/a-n/a.

[278] Unciti-Broceta, J. D.; Cano-Cortés, V.; Altea-Manzano, P.; Pernagallo, S.; Díaz-Mochón, J. J.; Sánchez-Martín, R. M. Number of Nanoparticles per Cell through a Spectrophotometric Method - A Key Parameter to Assess Nanoparticle-Based Cellular Assays. *Sci. Rep.* **2015**, *5*, 10091.

[279] Finck, R.; Simonds, E. F.; Jager, A.; Krishnaswamy, S.; Sachs, K.; Fantl, W.; Pe'er, D.; Nolan, G. P.; Bendall, S. C. Normalization of Mass Cytometry Data with Bead Standards. *Cytom. Part J. Int. Soc. Anal. Cytol.* **2013**, *83* (5), 483–494.

[280] Delgado-Gonzalez A. et al., Dual Probes for Flow Cytometry and Mass Cytometry. PCT/ES2018070413.

[281] Mei, H. E.; Leipold, M. D.; Schulz, A. R.; Chester, C.; Maecker, H. T. Barcoding of Live Human PBMC for Multiplexed Mass Cytometry. *J. Immunol. Baltim. Md 1950* **2015**, *194* (4), 2022–2031.

[282] Wellings, D. A.; Atherton, E. [4] Standard Fmoc Protocols. In *Methods in Enzymology*; Solid-Phase Peptide Synthesis; Academic Press, 1997; Vol. 289, pp 44–67.

[283] Davoren, P. A.; McNeill, R. E.; Lowery, A. J.; Kerin, M. J.; Miller, N. Identification of Suitable Endogenous Control Genes for MicroRNA Gene Expression Analysis in Human Breast Cancer. *BMC Mol. Biol.* **2008**, *9*, 76.

[284] Ponomaryova, A. A.; Morozkin, E. S.; Rykova, E. Y.; Zaporozhchenko, I. A.; Skvortsova, T. E.; Dobrodeev, A. Y.; Zavyalov, A. A.; Tuzikov, S. A.; Vlassov, V. V.; Cherdyntseva, N. V.; et al. Dynamic Changes in Circulating MiRNA Levels in Response to Antitumor Therapy of Lung Cancer. *Exp. Lung Res.* **2016**, *42* (2), 95–102.